Mass transfer and hydrodynamics in multiphase systems

Pedro Miguel Pacheco Neves Carteado Mena

A thesis submitted in part fulfilment of the requirement for the degree of Doctor in the Faculty of Engineering, University of Porto, Portugal

This thesis was supervised by
Doctor Fernando Alberto Nogueira da Rocha, Departamento de Engenharia Química, Faculdade de Engenharia da Universidade do Porto, Porto, Portugal

And co-supervised by
Professor José António Couto Teixeira, Centro de Engenharia Biológica, Universidade do Minho, Braga, Portugal

Laboratório de Engenharia de Sistemas de Processos
Instituto de Sistemas e Robótica - Porto
Departamento de Engenharia Química
Faculdade de Engenharia
Universidade do Porto
Porto, Portugal

November, 2005

"There is no knowledge without experience"
Albert Einstein

Abstract

The mass transfer and the hydrodynamics of three-phase bubble columns were investigated. The aim was to study the influence of relevant phases characteristics on the gas-liquid mass transfer process and on the hydrodynamic of a bubble column, where gas, liquid and solid phases are in contact. The solid phase and its characteristics are, at the same time, among the most important operational parameters of multiphase reactors, and those which have been poorly explored and understood. Therefore, special focus was given to the solid properties, namely, to the content, size and type, although attention was also given to the liquid phase, particularly, to its viscosity and the presence of surfactants.

Three main studies were performed, the first dedicated to the mass transfer in three-phase systems, the second to the flow regime transition and homogeneous regime stability in two- and three-phase flows and the third focused on local measurements of gas phase characteristics in a three-phase bubble column.

In the first study, it was found that the gas-liquid mass transfer process is strongly influenced by the solids type, loading and size. The volumetric mass transfer coefficient (k_La) and its individual components, the liquid side mass transfer coefficient (k_L) and the gas-liquid interfacial area (a) generally decreased with solids loading and size, although a k_La increase with solid content was also observed. The k_La was measured by the dynamic method and the a and other bubble characteristics through an image analysis technique.

The second study showed that the presence of an electrolyte in the liquid, up to a certain concentration, may stabilize the homogeneous flow regime. Both liquid viscosity and presence of solids have a dual effect on the bubble bed stability, first stabilizing and then destabilizing the homogeneous flow regime. The gas holdup was measured by bed expansion and the flow regime transition was determined by the Drift flux concept. To complement the solids effect study, auxiliary visualization experiments, with a standard and a high speed camera, indicated the importance of hydrodynamic bubble-particle interactions.

In the third study, radial profiles of gas-phase characteristics were obtained, using a monofiber optical probe. Gas holdup and bubble rise velocity profiles are clearly influenced by the solids loading. For higher solid loadings, the negative effect of the solid content on the gas-liquid interfacial was confirmed, and visualization experiments showed that bubble sphericity increases with the solid concentration.

Keywords: Bubble column, flow regimes, hydrodynamics, image analysis, mass transfer, optical probe, solids.

Resumo

Neste trabalho investigou-se a transferência de massa e a hidrodinâmica de colunas de bolhas trifásicas. O objectivo foi estudar a influência de importantes caracteristicas de fases, no processo de transferência de massa gás-líquido e na hidrodinâmica de colunas de bolhas, onde, gas, líquido e solidos estão em contacto. A fase sólida e as suas caracteristicas são, estão ao mesmo tempo, entre os parâmetros operacionais mais importantes e também os que ainda foram pouco explorados e compreendidos. Por isso, foi dada particular atenção às propriedades da fase sólida, nomeadamente a carga, o tamanho e o tipo, embora as propriedades da fase líquida também tenham sido abordadas, particularmente a sua viscosidade e a presença de surfactantes.

Foram realizados três estudos principais, o primeiro dedicado à transferência de massa em sistemas trifásicos, o segundo à transição de regimes de escoamento e à estabilidade do regime homogéneo em sistemas bi e trifásicos e o terceiro debruçado na medição local de caracteristicas da fase gasosa em escoamentos trifásicos.

No primeiro estudo, foi verificado que o processo de transferência de massa gás-líquido é fortemente influenciado pelo tipo de sólidos e também pela sua carga e tamanho. O coeficiente volumétrico de transferência de massa (k_La) e os seus componentes individuais, o coeficiente de transferência de massa do lado do líquido (k_L) e a área interfacial gás-líquido (a), em geral diminuem com a carga e tamanho dos sólidos, embora aumento de k_La com a carga de sólidos também tenha sido observado. O k_La foi medido pelo método dinâmico e o a e outras caracteristicas de bolhas através de uma técnica de análise de imagem.

O segundo estudo, mostrou que a presença de um electrólito no líquido, até determinada concentração, pode estabilizar o regime de escoamento homogéneo. Tanto a viscosidade do líquido como a presença de sólidos podem ter um efeito ambiguo na estabilidade do leito de bolhas, primeiro estabilizando e depois destabilizando o regime de escoamento homogéneo.

A fracção volumica de gás foi medida por expansão de leito e a transição de regimes de escoamento foi determinada pelo método de $DriftFlux$. Como complemento ao estudo do efeito dos sólidos, foram realizadas experiências de visualização, com uma câmara standard e outra de alta velocidade, as quais relevaram a importância das interacções hidrodinâmicas bolha-partícula.

No terceiro estudo, foram medidos perfis radiais de caracteristicas da fase gasosa, utilizando uma monosonda óptica. A fracção vólumica de gas e velocidade de subida das bolhas são claramente influênciadas pela carga de sólidos. Para cargas de sólidos mais elevadas, a área interfacial gás-líquido diminui com a carga de sólidos e as experiências de visualização mostram que a excentricidade das bolhas aumenta com a carga de sólidos.

Palavras chave: Análise de imagem, coluna de bolhas, hidrodinâmica, regimes de escoamento, sólidos, sonda óptica, transferência de massa.

Résumé

Dans ce travail nous avons recherché le transport de masse et l'hydrodynamique de colonnes de bulles triphasiques.

L'objectif a été d'étudier l'influence des caractéristiques importantes de phases dans le processus de transport de masse gaz/liquide et dans l'hydrodynamique de colonnes de bulles dans lequel gaz, liquide et solides sont en contact. La phase solide et ses caractéristiques sont simultanément, à l'intérieur des paramètres opérationnel les plus important, et également ceux qui n'ont pas encore été très explorés ni compris. Pour cette raison nous avons donné plus d'importance aux propriétés de la phase solide, notamment la charge, la taille et le type, néanmoins les propriétés de la phase liquide furent également abordées en particulier sa viscosité et la présence de surfactants.

Trois études principales ont été réalisées, la première concernant le transport le masse dans des systèmes triphasiques, le second concernant le transition de régimes d'écoulement et la stabilité du régime homogène dans des systèmes di et triphasiques et le troisième concernant le mesurage local des caractéristiques de la phase gazeuse dans des écoulements triphasiques.

Dans la première étude nous avons observé que le processus de transport de masse gaz-liquide est fortement influencé par le type des solides ainsi que par sa charge et sa taille. Le coefficient volumétrique de transport de masse (k_La) et ses composants individuels, le coefficient de transport de masse du coté liquide (k_L) et l'aire interfacial gaz-liquide (a), diminuent généralement par rapport á la charge et la taille des solides bien qu'une augmentation de k_La avec la charge des solides ait été également observée. Le k_La a été mesuré au moyen de la méthode dynamique et le a et les autres caractéristiques des bulles au moyen d'une technique d'analyse d'image.

La seconde étude a montré que la présence d'un électrolyte dans le liquide, jusqu'à une certaine concentration, peut stabiliser le régime d'écoulement homogène. Aussi bien

la viscosité de liquide et la présence de solides peuvent avoir un effet ambigu dans la stabilité dans le lit de bulles, d'abord stabilisent puis en déstabilisent le régime découlement homogène. La fraction volumique de gaz a été mesurée par expansion du lit et la transition de régimes d'écoulement a été déterminée par la méthode $Drift\ Flux$.

Des expériences de visualisation, avec une camera standard et une autre à grande vitesse, ont été exécutées comme complément à l'étude de l'effet des solides. Celles-ci ont révélé l'importance des interactions hydrodynamiques bulle-particule.

Dans la troisième étude, des profils radiaux de caractéristiques de la phase gazeuse ont été mesuré avec une monosonde optique. La fraction volumique de gaz et la vitesse de montée des bulles sont nettement influencées par la charge de solides. Pour des charges de solides plus élevées, l'aire interfaciale gaz-liquide diminue avec la charge de solides et les expériences de visualisation montrent que l'excentricité des bulles augment avec la charge de solides.

Mots clé: analyse d'image, colonne de bulles, hydrodynamique, régimes d'écoulement, sonde optique, transport de masse, solides.

à tia Lena
à avó Laura
ao avô Joaquim

Acknowledgements

My first acknowledgement is for my supervisors Professors Fernando Rocha and José Teixeira, who invited me to do this project. I am very grateful, for the interesting topic proposed and also for the support and motivation they gave me, which were extremely important during this research. The second acknowledgements are for Fundação para a Ciência e Tecnologia that financially supported this study during 48 months through a PhD scholarship (contract number BD/3427/2000) and also the European Communities Commission for my fellowship at the Marie Curie Training Site at the Institute of Chemical Process Fundamentals, Prague, Czech Republic (contract no. HPMT-CT-2000-0074), during 9 months.

It has been a long way, in time and space, so I have to acknowledge several people, who had, somehow, participated and contributed to this work. I have worked in three different countries and mainly in four different institutions and I am very pleased for that since I had a chance to meet very interesting people and different ways of thinking, behaving and working.

At Engineering Faculty of University of Porto (FEUP), in Porto, Portugal, I had very good conditions and working atmosphere. Particular thanks go to Professor Romualdo Salcedo, who kindly offered free space at his laboratory and to Vânia, with whom I have shared long days in the lab. I acknowledge also Mr. Nelson Neves for his excellent work in the construction of the experimental apparatus, with his peculiar perfection. Very special thanks to all my colleagues and friends at FEUP, I will take the risk to mention all, in totally arbitrary order: Renato, Pedro, António, Vânia, Isabel, Luis M., Zé Luis, Lúcia, Carina, Rui, Sarah (and her mother), Sofia N., Tiago, Herney, Vasco, João, Sofia S., Filipa, Joana, Marta, Clara, Klára, Nuno F., Ricardo, Hélder, Nuno R., Claudia, Manuela, Tirzhá and Luis.

At the Laboratoire des Sciences du Génie Chimie (LSGC-ENSIC), Nancy, France: I

would like to thank Professor Marie Noel Pons, for welcoming me and for her contribution in the image analysis field. I thank Bruno Salvador, my flatmate, all the friends that I had made there and all my colleagues at ENSIC, namely Virginie and Sebastien.

At the Institute of Chemical Process Fundamentals (ICPF), Prague, Czech Republic: I am truly indebted to Doctor Marek *Captain* Ruzicka, who gave, indeed, one of the most serious contributions for this thesis. I would also like to thank all my colleagues and staff in ICPF, for their kindness and support, especially, Doctor Maria F., Misa, Marek V., Jiri(s), Jarda T., Miro, Rado, Jacob. And to the big bunch of friends that I met there, for the excellent moments we spent together.

At Laboratoire des Ecoulements Géophysiques et Industriel (LEGI), Grenoble, France: I acknowledge Doctor Alain Cartellier and Doctor Philipe Sechet for welcoming me at their lab and for their constant support. Special thanks to Engineer Laurent Terrier, for his precious and skilled technical support. I also thank to my colleagues at LEGI, namely my good friends Stef and Leo. I will not forget family Bolliet and their lovely countryside house, close to Grenoble.

At Biological Engineering Center, University of Minho, Braga, Portugal: I am also indebted to Nuno Reis and António Vicente.

I am grateful also to all my big family, in particular, to my grandmother Leonor, to grandfather Durval, my parents Teresa e Artur and my sister and brothers, Berta, Filipe and Luis. Rita and Olivia are also a part of it. I am deeply indebted to my brother Filipe for his English language revision and suggestions to improve the syntax and readability.

I dedicate this thesis to all my friends around the world, namely the closest ones André, Frederico, Kicas, Nicholas e Philip.

To Sandra, with kiiises.

P.S. Please feel acknowledged too, if your name was not mentioned above (it is physically impossible to refer to you all).

Contents

Abstract **v**

Acknowledgements **xiii**

Nomenclature **xix**

List of Figures **xxv**

List of Tables **xxxiii**

1 Introduction **1**

1.1 Motivation and aim 1

1.2 Thesis Layout 2

2 Mass transfer in three-phase bubble columns **5**

2.1 Introduction 5

2.1.1 Bubble Columns 5

2.1.2 Mass transfer 7

2.2 Experimental technique 18

2.2.1 Experimental facility 18

2.2.2 Experimental method 20

2.2.3 Solids 24

2.3 Results and discussion 27

2.3.1 $k_L a$ evaluation from experimental data 27

2.3.2 Air-water 29

2.3.3 Air-water-calcium alginate beads 30

2.3.4 Air-water-polystyrene beads 34

2.3.5 Effect of polystyrene fine particles on k_La . . . 45
2.3.6 Air-water-hollow glass spheres . . . 46
2.3.7 Bubble characteristics . . . 48
2.3.8 Gas-liquid interfacial area and gas holdup . . . 55
2.3.9 Liquid side mass transfer coefficient . . . 61
2.4 Conclusions . . . 63

3 Flow Regime Transition in bubble columns 65
3.1 Introduction . . . 65
3.1.1 Flow regimes and regime transition . . . 65
3.1.2 Effect of surfactants on regime transition . . . 68
3.1.3 Effect of viscosity on regime transition . . . 70
3.1.4 Effect of solids on regime transition . . . 71
3.2 Experiments and data treatment . . . 74
3.2.1 Experimental technique and errors . . . 74
3.2.2 Evaluation of the critical point . . . 78
3.2.3 Criteria for transition . . . 84
3.2.4 Visualization experiments . . . 87
3.3 Results and discussion . . . 88
3.3.1 Surfactants . . . 88
3.3.2 Viscosity . . . 92
3.3.3 Solids . . . 107
3.4 Conclusions . . . 120

4 Local gas-phase characteristics in three-phase systems 123
4.1 Introduction . . . 123
4.2 Experimental . . . 125
4.2.1 Experimental conditions . . . 125
4.2.2 Optical probe response for three phase systems . . . 125
4.2.3 Optical Probe Measurements . . . 126
4.2.4 Visualization Measurements . . . 128
4.3 Results and discussion . . . 129
4.3.1 Validity of the optical probe response for three phase systems . . . 129
4.3.2 Optical Probe results . . . 132

4.3.3 Visualization results - Bubble sphericity 142
4.4 Conclusions 144

5 General conclusions and suggestions for future work 147
5.1 General conclusions 147
5.2 Suggestions for future work 150

Appendices 151

A Image Analysis 151
A.1 Image descriptors 151
A.2 Image Processing 158
A.3 Images of different systems 164

B Determination of gas-liquid interfacial area 171

C Solubility of oxygen in freshwater 173

Nomenclature

Roman symbols

A	total interfacial area
A'	column aspect ratio
A_{sup}	mean superficial area of the bubbles
a	gas-liquid interfacial area per unit of volume
a'	bubble drift coefficient
a_{mean}	mean gas-liquid interfacial area
B	major axis of an elliptical object
B_1	empirical parameter in Eq. 3.9
B'_i	coefficient of u_0^*/u_0 power series (i=1,2,3,...)
b	linear regression slope ($y_{est} = c + bx$)
b_1	linear regression optimum slope for the left hand side
b_2	linear regression optimum slope for the right hand side
b_i	coefficient of μ^*/μ power series (i=1,2,3,...)
C	bubble drag coefficient
C'	parameter of the correlation for the optical probe calibration
C_g	solute concentration in the gas
C_g^i	solute concentration at the interface in the gas side
C_L	solute concentration in the liquid
C_L^i	solute concentration at the interface in the liquid side
C_L^*	solute concentration in the liquid phase in equilibrium with the solute concentration in the gas phase
C_L^0	dissolved oxygen concentration at $t = 0$
C_S	solid concentration, content, loading

$Circ$	circularity
c	linear regression parameter ($y_{est} = c + bx$)
c_1	empirical parameter in Eq. 3.12
D	diffusion coefficient
D'	parameter of the correlation for the optical probe calibration
D_C	bubble column diameter
d	diameter
E	structuring element
e_G	voidage, gas holdup
F	Feret diameter
F^*	Test F parameter
F_{max}	maximum Feret diameter
$F_{max} + 90^o$	maximum Feret diameter+90^o
F_{min}	minimum Feret diameter
f	volumetric concentration of the particles, solids volume fraction
f'	bubbles frequency
g	gravity
H	Henry's constant
h	layer height in bubble column
h_0	clear liquid height
K_L	global liquid side mass transfer coefficient
k_G	individual gas-side mass transfer coefficient
k_L	individual liquid-side mass transfer coefficient
k_La	volumetric mass transfer coefficient
k_1	empirical parameter in Eq. 3.12
k_2	empirical parameter in Eq. 3.12
L	minor axis of an elliptical object
m	slope at the origin of Eq. $k_La = mu_G^n$
n	exponent of Eq. $k_La = mu_G^n$
$n_{det.bubbles}$	number of detected bubbles
N	mass transfer rate
N'	molar flux of a solute
N_b	number of bubbles in the column at a certain instant of time

n_{p_1}	number of points for linear regression for the left hand side
n_{p_2}	number of points for linear regression for the right hand side
P	object perimeter
p	exponent of Richardson and Zaki (1954) formula (Eq. 3.16)
Q_b	bubble flow rate
Q_G	gas flow rate
Q_{O_2}	amount of oxygen transferred per unit volume of reactor
R	column radius
R_{xy}	linear regression coefficient
r	radial probe position
r_1	radius of the ellipse major axis
r_2	radius of the ellipse minor axis
S	projected area of an object
s	fractional rate of surface renewal
Sp	sphericity
t_a	arriving time
t_{acq}	acquisition time in the optical probe measurements
t_G	residence time
t_m	rising time
t_s	rising time of a bubble through the column
U	bubble slip speed
U_0	bubble terminal speed
u	mean bubble rise speed (mean velocity of gas phase in the column)
u_G	superficial gas velocity
u_s	speed of small bubbles (Eq. 3.8)
V	volume
v	velocity

Greek symbols

ΔC	concentration difference between the ends of the film
ΔP	pressure drop across the plate (Eq. 3.11)
δ	thickness of the film

κ	hydrodynamic diffusivity of bubbles
μ	dynamic viscosity
Ω_1	robustness
Ω_2	biggest concavity
ω_1	number of erosions to totally erase the object
ω_2	number of erosions necessary to erase the object 'CBP-Obj'
ρ	density
σ	interfacial tension (liquid surface tension)
τ	retention time
θ	contact time
φ	relative free area ratio

Indices and exponents

b	bubble
C	critical
eq	equivalent
f	fluid
G	gas
L	liquid
p	particle
S	solid
ref	reference
$*$	effective
%	dimensionless

Acronyms

CBP	convex bounding polygon
CFD	Computer fluid dynamics
CI	concavity index
$g-l$	gas-liquid

$g-l-s$	gas-liquid-solid
$g-s$	gas-solid
HoR	homogeneous flow regime
HeR	heterogeneous flow regime
Obj	object
$R-Z$	Richardson and Zaki

Dimensionless numbers

Eo	Eötvös number	$Eo = \Delta\rho g d^2/\sigma$
Mo	Morton number	$Mo = \Delta\rho g \mu^4/(\sigma^3\rho^2)$
Re	Reynolds number	$Re = \rho d v/\mu$
We	Weber number	$We = \rho d v^2/\sigma$

List of Figures

2.1 Bubble column. 19

2.2 Needles plate for gas sparging. 20

2.3 Experimental set-up (1: N_2, 2: Air, 3: Rotameter, 4: Manometer, 5: Humidifier, 6: Digital camera, 7: Bubble column, 8: O_2 probe, 9: O_2 concentration meter, 10: PC, 11: Diffuser glass, 12: Halogen lamp, 13: Thermostatic bath). 21

2.4 Image processing scheme. 23

2.5 Calcium alginate beads: (a) $d_{eq} = 2.1\ mm$; (b) $d_{eq} = 1.2\ mm$. 25

2.6 Granulometric analysis of polystyrene beads. 26

2.7 Granulometric analysis of hollow glass spheres. 26

2.8 Dissolved oxygen concentration variation for air-water-P424 "washed"beads and $u_G = 2.2\ mm/s$. 27

2.9 Test F application for the experimental results for air-water-P424 "washed"beads and $u_G = 2.2\ mm/s$. 29

2.10 Dependence of k_La on superficial gas velocity for air-water system. 30

2.11 Dependence of k_La on superficial gas velocity u_G, for different calcium alginate concentrations. Experimental data and proposed correlation ($d_p = 1.2\ mm$). 31

2.12 Dependence of k_La on superficial gas velocity for different calcium alginate concentrations. Experimental data and proposed correlation ($d_p = 2.1\ mm$). 32

2.13 Comparison of experimental data and correlation for air-water-calcium alginate three-phase systems. 33

2.14 Dependence of k_La on superficial gas velocity for different P124N ($d_p = 1100\ \mu m$) concentrations. Experimental data and proposed correlation ("New"particles). 35

2.15 Comparison of experimental data and correlation for air-water-P124N (d_p = 1100 μm) three-phase systems ("New"particles). 35
2.16 Dependence of k_La on superficial gas velocity for different P324N (d_p = 769.8 μm) concentrations. Experimental data and proposed correlation ("New"particles). 36
2.17 Comparison of experimental data and correlation for air-water-P324N (d_p = 769.8 μm) three-phase systems ("New"particles). 37
2.18 Dependence of k_La on superficial gas velocity for different P424N (d_p = 591.2 μm) concentrations. Experimental data and proposed correlation ("New"particles). 37
2.19 Comparison of experimental data and correlation for air-water-P424N (d_p = 591.2 μm) three-phase systems ("New"particles). 38
2.20 Dependence of k_La on superficial gas velocity for different P124W ($d_p = 1100$ μm) concentrations. Experimental data and proposed correlation ("Washed"particles). 39
2.21 Comparison of experimental data and correlation for air-water-P124W (d_p = 1100 μm) three-phase systems ("Washed"particles). 40
2.22 Dependence of k_La on superficial gas velocity for different P324W (d_p = 769.8 μm) concentrations. Experimental data and proposed correlation ("Washed"particles). 41
2.23 Comparison of experimental data and correlation for air-water-P324W (d_p = 769.8 μm) three-phase systems ("Washed"particles). 42
2.24 Dependence of k_La on superficial gas velocity for different P424W (d_p = 591.2 μm) concentrations. Experimental data and proposed correlation ("Washed"particles). 43
2.25 Comparison of experimental data and correlation for air-water-P424W (d_p = 591.2 μm) three-phase systems ("Washed"particles). 43
2.26 Effect of polystyrene particle size on mass transfer coefficient (P124 d_p = 1100 μm; P324 d_p = 769.8 μm and P424 d_p = 591.2 μm). 44
2.27 Effect of polystyrene fine particles on k_La for air-water-polystyrene systems (P124 d_p = 1100 μm; P324 d_p = 769.8 μm and P424 d_p = 591.2 μm). . . . 45
2.28 Dependence of k_La on superficial gas velocity for different hollow glass spheres concentrations. Experimental data and proposed correlation. 46

2.29 Experimental volumetric mass transfer coefficient as a function of hollow glass spheres loading. 47
2.30 Examples of images of air-water system: (a) $u_G = 1.5\ mm/s$ (b) $u_G = 1.7\ mm/s$ (c) $u_G = 2.0\ mm/s$ (d) $u_G = 2.2\ mm/s$ (e) $u_G = 2.5\ mm/s$ (f) $u_G = 2.7\ mm/s$. 49
2.31 Examples of images of air-water-calcium alginate 5 $vol\%$ ($d_{eq} = 2.1\ mm$) system: (a) $u_G = 1.5\ mm/s$ (b) $u_G = 1.7\ mm/s$ (c) $u_G = 2.0\ mm/s$ (d) $u_G = 2.2\ mm/s$ (e) $u_G = 2.5\ mm/s$ (f) $u_G = 2.7\ mm/s$. 50
2.32 Examples of images of air-water-calcium alginate 10 $vol\%$ ($d_{eq} = 2.1\ mm$) system: (a) $u_G = 1.5\ mm/s$ (b) $u_G = 1.7\ mm/s$ (c) $u_G = 2.0\ mm/s$ (d) $u_G = 2.2\ mm/s$ (e) $u_G = 2.5\ mm/s$ (f) $u_G = 2.7\ mm/s$. 51
2.33 Examples of images of air-water-calcium alginate 5 $vol\%$ ($d_{eq} = 1.2\ mm$) system: (a) $u_G = 1.5\ mm/s$ (b) $u_G = 1.7\ mm/s$ (c) $u_G = 2.0\ mm/s$ (d) $u_G = 2.2\ mm/s$ (e) $u_G = 2.5\ mm/s$ (f) $u_G = 2.7\ mm/s$. 52
2.34 Examples of images of air-water-calcium alginate 10 $vol\%$ ($d_{eq} = 1.2\ mm$) system: (a) $u_G = 1.5\ mm/s$ (b) $u_G = 1.7\ mm/s$ (c) $u_G = 2.0\ mm/s$ (d) $u_G = 2.2\ mm/s$ (e) $u_G = 2.5\ mm/s$ (f) $u_G = 2.7\ mm/s$. 53
2.35 F_{max}/F_{min} for the different experimental conditions. 54
2.36 Bubble examples for different superficial gas velocities and solid concentrations ($d_p = 1.2\ mm$). 55
2.37 Experimental gas-liquid interfacial area and same of the literature correlations for air-water system. 57
2.38 Experimental gas-liquid interfacial area and literature correlation for air-water-calcium alginate beads systems (alg.I - $d_p = 1.2\ mm$, alg.II - $d_p = 2.1\ mm$). 58
2.39 Experimental gas holdup and literature correlations for air-water system. . 59
2.40 Experimental gas holdup and literature correlation for air-water-alg.I system. 60
2.41 Experimental gas holdup and literature correlation for air-water-alg.II system. 60
2.42 Experimental liquid side mass transfer coefficient and literature correlations for air-water system. 61
2.43 Experimental liquid side mass transfer coefficients for air-water and air-water-calcium alginate systems (alg.I - $d_p = 1.2\ mm$, alg.II - $d_p = 2.1\ mm$). 62

3.1 (a) Dispersion behaviour in the homogeneous and heterogeneous flow regimes (Zahradnik et al., 1997). (b) Time-averaged radial profiles of liquid velocity and voidage. 66
3.2 Dependence of voidage on superficial gas velocity. 67
3.3 Scheme of the experimental set-up (1: Bubble column, 2: Gas chamber, 3: Perforated plate, 4: Rotameters, 5: On/Off valves, 6: Pressure reducer). . 75
3.4 Layer height as a function of superficial gas velocity. 78
3.5 Dependence of gas holdup on superficial gas velocity. 79
3.6 Slip speed graph. 80
3.7 Determination of the bubble terminal velocity U_0 and the bubble drift coefficient a'. 81
3.8 Drift flux plot (j versus e_G). 82
3.9 Drift flux plot (j versus u_G). 82
3.10 Slip velocity graph (U versus e_G). 83
3.11 Slip velocity graph (U versus u_G). 83
3.12 Primary data: voidage e_G vs superficial gas velocity u_G. (a) $|CaCl_2| = 0 - 0.03\ mol/L$ and (b) $|CaCl_2| = 0.03 - 0.1\ mol/L$. 89
3.13 Main result: homogeneous regime stability measured by critical values of (a) voidage e_{G_C} and (b) superficial gas velocity u_{G_C}. 91
3.14 Voidage e_G vs superficial gas velocity u_G. Viscosity range: 1-5 $mPa.s$. . . . 93
3.15 Homogeneous regime stability measured by critical values of (a) voidage e_{G_C} and (b) superficial gas velocity u_{G_C}. 94
3.16 Primary data: voidage e_G vs superficial gas velocity u_G. Viscosity range: 0.946-5.480 $mPa.s$. 96
3.17 Primary data: voidage e_G vs liquid viscosity μ. 97
3.18 Primary data: slip speed U vs superficial gas velocity u_G. Viscosity range: 0.946-5.480 $mPa.s$. 98
3.19 Primary data: retention time τ vs superficial gas velocity u_G, for 0 and 6 $vol\%$ of glycerol. 99
3.20 Secondary data: Richardson-Zaki exponent p vs liquid viscosity μ. 100
3.21 Secondary data: Slip speed parameters (a) terminal bubble velocity U_0 and (b) bubble drift coefficient a'. 101

3.22 Secondary data: Comparison between Ruzicka et al. (2001b) (Eq. 3.3) and Richardson and Zaki (1954) (Eq. 3.16) formulas for the bubble slip speed U. Example for air-water system. 102

3.23 Main result: homogeneous regime stability measured by critical values of (a) voidage e_{G_C} and (b) superficial gas velocity u_{G_C}. 104

3.24 Main result: Linear fit of critical voidage e_{G_C} for low viscosities. 105

3.25 Primary data: voidage e_G vs superficial gas velocity u_G. (a) solid content 0-5 $vol\%$ and (b) solid content 5-30 $vol\%$. 108

3.26 Primary data: effect of solid content C_S on (a) voidage e_G and (b) mean bubble speed U. 109

3.27 Secondary data: drift flux plot of drift flux j vs voidage e_G (a) $C_S = 0\%$, (b) $C_S = 3\%$ and (c) $C_S = 30\%$. 110

3.28 Main result: homogeneous regime stability measured by critical values of (a) voidage e_{G_C} and (b) superficial gas velocity u_{G_C}. 112

3.29 Bubble deflection from the vertical direction after collision with a solid particle.116

3.30 Bubble rotation caused by collision with a solid particle. 117

3.31 Bubble shape oscillation caused by collision with two solid particles. 118

3.32 Bubble coalescence induced by collision with a swarm of solid particles. . . 119

4.1 Experimental set-up for investigation of the optical probe response in three phase systems (1: Bubble column, 2: Optical probe, 3: Y junction, 4: Light emitter, 5: Light receiver and converter, 6: Oscilloscope, 7: PC1, 8: On/off valve, 9: Pressure reducer, 10: Rotameter, 11: High speed camera, 12: PC2, 13: Diffuser glass, 14: Halogen lamp). 126

4.2 Experimental set-up for optical probe measurements (1: Bubble column, 2: Optical probe, 3: Y junction, 4: Light emitter, 5: Light receiver and converter, 6: Oscilloscope, 7: PC, 8: On/off valve, 9: Pressure reducer, 10: Rotameter). 127

4.3 Typical signal of a bubble signature. t_G - residence time, t_m - rising time. . 128

4.4 Experimental set-up for visualization measurements (1: Bubble column, 2: Digital camera, 3: PC, 4: Diffuser glass, 5: Halogen lamp, 6: On/off valve, 7: Pressure reducer, 8: Rotameter). 129

4.5 High amplitude signal observed for bubbles after probe tip hitting by a solid: A - solid piercing (seq A1-A3 in Fig. 4.6). B and C - bubble piercing (seq B1-B3 and C1-C3 in Fig. 4.6). 130
4.6 High speed camera image sequences of particle and bubble piercing: A1-A3 particle piercing; B1-B3 bubble piercing; C1-C3 bubble piercing. 131
4.7 Probe signal during particle and bubble piercing (long time acquisition). . 132
4.8 Radial gas holdup profile for: (a) $u_G = 1.6\ cm/s$; (b) $u_G = 2.7\ cm/s$; (c) $u_G = 3.8\ cm/s$; (d) $u_G = 4.6\ cm/s$. The symbols depicted in (a), for $vol\%$ of solids, are valid for the other subfigures. 134
4.9 Comparison between the present study and regime transition study presented in Chapter 3. 136
4.10 Integrated gas holdup as a function of superficial gas velocity. 137
4.11 Comparison between gas holdup obtained by optical probe and by bed expansion. 137
4.12 Calibration curve of the monofiber optical probe. 138
4.13 Bubble rise velocity profile for: (a) $u_G = 1.6\ cm/s$; (b) $u_G = 2.7\ cm/s$; (c) $u_G = 3.8\ cm/s$; (d) $u_G = 4.6\ cm/s$. The symbols depicted in (a), for $vol\%$ of solids, are valid for the other subfigures. 139
4.14 Comparison between bubble flow and gas flow. 140
4.15 Interfacial area as a function of solids loading. 142
4.16 Examples of images of air-water-calcium alginate systems: (a) $u_G = 1.6\ cm/s$; $C_S = 0\ vol\%$ (b) $u_G = 4.6\ cm/s$; $C_S = 0\ vol\%$ (c) $u_G = 1.6\ cm/s$; $C_S = 10\ vol\%$ (d) $u_G = 4.6\ cm/s$; $C_S = 10\ vol\%$ (e) $u_G = 1.6\ cm/s$; $C_S = 20\ vol\%$ (f) $u_G = 4.6\ cm/s$; $C_S = 20\ vol\%$ (g) $u_G = 1.6\ cm/s$; $C_S = 30\ vol\%$ (h) $u_G = 4.6\ cm/s$; $C_S = 30\ vol\%$. 143
4.17 Bubble sphericity as a function of superficial gas velocity. 144

A.1 Feret diameter. 152
A.2 Maximum and minimum Feret diameters. 153
A.3 Maximum Feret diameter+90^o. 154
A.4 Equivalent diameter. 154
A.5 Elongation parameters. 155
A.6 Circularity. 155

A.7 Convex bounding polygon. 156
A.8 Biggest concavity. 157
A.9 Bubbles sphericity. 157
A.10 Threshold. 158
A.11 Example of threshold. 159
A.12 Example of label. 159
A.13 Example of hole fill. 160
A.14 Example of border kill. 160
A.15 Structuring element. 161
A.16 Erosion of order 1. 161
A.17 Erosion of order 6. 162
A.18 Dilation of order 4. 162
A.19 Example of reconstruction. 163
A.20 Example of ultimate. 164
A.21 Examples of images of air-water-glycerol ($\mu = 5\ cP$) system: (a) $u_G = 1.5\ mm/s$ (b) $u_G = 1.7\ mm/s$ (c) $u_G = 2.0\ mm/s$ (d) $u_G = 2.2\ mm/s$ (e) $u_G = 2.5\ mm/s$ (f) $u_G = 2.7\ mm/s$. 165
A.22 Examples of images of air-water-pvc system ($0.5\ wt\%$; $160 < d_p < 180\ \mu m$): (a) $u_G = 0.4\ mm/s$ (b) $u_G = 0.6\ mm/s$ (c) $u_G = 0.9\ mm/s$ (d) $u_G = 1.2\ mm/s$ (e) $u_G = 1.5\ mm/s$ (f) $u_G = 1.7\ mm/s$ (g) $u_G = 2.0\ mm/s$ (h) $u_G = 2.2\ mm/s$ (i) $u_G = 2.5\ mm/s$ (j) $u_G = 2.7\ mm/s$. 166
A.23 Examples of images of air-water-ion exchange resin system ($1\ vol\%$; $d_p = 0.8\ mm$): (a) $u_G = 0.4\ mm/s$ (b) $u_G = 0.6\ mm/s$ (c) $u_G = 0.9\ mm/s$ (d) $u_G = 1.2\ mm/s$ (e) $u_G = 1.5\ mm/s$ (f) $u_G = 1.7\ mm/s$ (g) $u_G = 2.0\ mm/s$ (h) $u_G = 2.2\ mm/s$ (i) $u_G = 2.5\ mm/s$ (j) $u_G = 2.7\ mm/s$. 167
A.24 Examples of images of air-water system ("high"superficial gas velocities): (a) $u_G = 3.4\ mm/s$ (b) $u_G = 6.6\ mm/s$ (c) $u_G = 8.7\ mm/s$. 168
A.25 Examples of images of air-water-calcium alginate system 5 $vol\%$ ($d_{eq} = 2.1\ mm$) ("high"superficial gas velocities): (a) $u_G = 3.4\ mm/s$ (b) $u_G = 6.6\ mm/s$ (c) $u_G = 8.7\ mm/s$. 169
A.26 Examples of images of air-water-calcium alginate system 5 $vol\%$ ($d_{eq} = 1.2\ mm$) ("high"superficial gas velocities): (a) $u_G = 2.4\ mm/s$ (b) $u_G = 4.2\ mm/s$ (c) $u_G = 5.8\ mm/s$. 169

A.27 Examples of images of air-water-alumina (Al_2O_3) system (0.5 $wt\%$; $\bar{d}_p$ = 78 μm) ("high"superficial gas velocities): (a) u_G = 2.4 mm/s (b) u_G = 4.2 mm/s (c) $u_G = 5.8$ mm/s. 170
A.28 Examples of images of air-water-gibbsite ($Al(HO)_3$) system (0.5 $wt\%$; $\bar{d}_p$ = 86 μm) ("high"superficial gas velocities): (a) $u_G = 5.8$ mm/s (b) u_G = 7.3 mm/s (c) $u_G = 8.7$ mm/s. 170

C.1 Solubility of oxygen in freshwater (Velz, 1970). 174

List of Tables

2.1 Volume statistics of particle diameter 25
2.2 Optimum parameters 28
2.3 Superficial area and volume of elongated and flattened spheroids 55

3.1 Aqueous $CaCl_2$ solutions 76
3.2 Aqueous glycerol solutions 76
3.3 Viscosities of the aqueous glycerol solutions 77

4.1 Comparison of experimental conditions between the regime transition study (Chapter 3) and the present study. 135

Chapter 1

Introduction

1.1 Motivation and aim

Many research groups working with bubble columns, slurry columns, fluidized beds, airlift reactors and flotation columns, are interested in the complex gas-liquid-solid (g-l-s) systems. Their wide application in various industrial processes such as chemical, petrochemical, biochemical and environmental is an unquestionable proof of their increasing importance. The presence of the solid phase can influence the gas-liquid (g-l) mixture in different ways such as bubble rise and formation, radial and axial profiles, mixing and dispersion, gas holdup and flow regimes and mass transfer. Despite all the research efforts, the knowledge about the effects of solids on gas-liquid systems and their respective physical mechanisms are far from being clarified. A clear understanding of the mass transfer and the hydrodynamics of the gas-liquid-solid systems is needed to improve the design and operation of the processes where these systems are used.

In multiphase systems, appearing in bubble column reactors, gas-liquid mass transfer is, most frequently, the rate determining step for the overall process. Therefore, the knowledge of gas-liquid mass transfer rates characterized by volumetric liquid side mass transfer coefficients (k_La) is required for a reliable design of such reactors. Also, a complete understanding of the effect of the operating parameters on each component of k_La (the liquid side mass transfer coefficient, k_L, and the interfacial area, a) is needed. The presence of solids is an important parameter that can have either a beneficial or undesirable influence on the mass transfer process. So, the effect of solid characteristics such as size, loading and surface properties on gas-liquid mass transfer has been challenging for

researchers.

Bubble column reactors have different behaviour in homogeneous and heterogeneous regimes, thus, the dependencies of the rates of mass, heat and momentum transfer on the design and operating parameters (such as reactor geometry, gas and liquid flow rates and proprieties of the contacting phases) are also very different. Therefore, for a rational reactor design and operation, it is of crucial importance to know the range of parameters over which a certain regime prevails. In spite of all the efforts that have been done, many basic questions concerning the effect of important design and operational parameters as well as system properties, such as solid phase and its characteristics, on regime stability and on flow regime transition remain unanswered. These knowledge gaps restrict the ability to design and operate gas-liquid and gas-liquid-solid contacting and reacting systems.

Moreover, the operation and design of g-l and g-l-s reactors still relies, to a large extent, on empirical rules and correlations, which in turn are based on measurements performed under conditions relevant to industry. Even more modern approaches like computer fluid dynamics (CFD), which are used to help in the design of multiphase reactors, need data on local and transient flow characteristics to build physical models. Therefore, reliable measuring techniques are required for a rational design and description of multiphase reactors. Currently, intrusive phase detection probes (such as optical probes) are very attractive for industry and research, since they are able to measure not only phase concentrations but also bubble velocities and other phase and flow characteristics. This information is of crucial importance in describing and modelling multiphase flows.

Therefore, the aim of this work is to give an useful contribution to the knowledge and understanding of multiphase gas-liquid-solid systems, focusing on the gas-liquid mass transfer process and on the hydrodynamics of the three-phase flows. In order to do that the thesis was structured as follows.

1.2 Thesis Layout

The thesis has three main chapters (Chapter 2, 3 and 4) where the work is presented and discussed, and in last chapter (Chapter 5) the general conclusions and future work suggestions are refered. Each of the main chapters, is basically composed by: an introduction, with the respective state-of-the-art revision; an experimental section, where the

experimental details and techniques are explained; results and discussion section(s); and finally a conclusions section.

In Chapter 2, the gas-liquid mass transfer process in three-phase systems is investigated in a three-phase bubble column. The purpose of this study was to analyse the effect of relevant solid properties (such as solid type, loading and size) on the volumetric mass transfer coefficient and on its individual components.

In Chapter 3, the influence of important operating parameters on the flow regime transition and on the stability of the homogeneous regime in bubble column is studied. The parameters investigated were: the presence of a surfactant (electrolyte) in the liquid phase, the viscosity of the liquid and the presence of a solid phase.

In Chapter 4, the local structure of the multiphase flow is investigated with a monofiber optical probe, in order to determine the variations of the bubble flow properties along the bubble column cross section.

Chapter 2

Mass transfer in three-phase bubble columns

2.1 Introduction

2.1.1 Bubble Columns

In many operations of chemical industry processes, one or more components of a gas phase are absorbed into a liquid phase. The phase contacting is often required to trigger reactions among components of the two phases. The complexity and diversity of industrial processes implied that different types of gas-liquid contactors were developed and constructed. As examples there are: bubble columns, pipes/tubes, mechanical agitated tanks, packed columns, plate/tray columns, spray towers, jet (loop) reactors, tubular/ventury ejectors and motionless mixers (Lee and Tsui, 1999). Bubble columns are contactors in which a gas or a mixture of gases in the form of a dispersed phase of bubbles moves in a continuous liquid phase. In the liquid, there can also be a suspended or fluidized, reactive or catalytic solid. Thus, in fact, there exist two- or three-phase bubble columns (Deckwer and Schumpe, 1987). Bubble columns can be of different types such as single stage, multi stage, multi channel, with motionless mixers, loop reactors, jet reactors, downflow bubble columns, three-phase fluidized-bed reactors and slurry reactors.

The main features of the bubble columns are: low to moderate mixing intensity, the mixing is induced mainly by the gas (unless liquid is introduced into the column as a jet), large liquid holdup, long liquid residence time, variable extent of backmixing in the liquid.

The principal advantages of using bubble columns comparing to other contactors are:

1. Simple construction and low capital cost
2. Minimal maintenance due to the absence of moving parts
3. Higher interfacial areas and overall mass transfer coefficients can be achieved
4. Ability to handle solids without erosion or plugging problems
5. Easy temperature control
6. Slow reactions can be performed due to high liquid residence time
7. No sealing problems
8. Higher heat transfer rates per unit volume of reactor can be obtained

As main disadvantages we can point out:

1. Gas high pressure drop caused by high static head of liquid
2. Bubble coalescence, which decreases gas-liquid (g-l) interfacial area
3. Substantial backmixing in both phases

Bubble column applications are not limited to chemical industry, they can be found in biochemical operations, separation of mixtures by rectification, absorption, wastewater treatment (W.-H. Hong, 1989) and petrochemical industry. Bubble columns are also gaining increasing importance in the field of biotechnology (Alvarez et al., 2000). Practical examples of processes performed in bubble columns are various oxidations (e.g. oxidation of acetaldehyde to acetic acid), separation of oily water, coal liquefaction, various hydrogenations (e.g. benzene to cyclohexane), Ficher-Tropsch systhesis, methanol from synthesis gas, production of single cell protein and culture of animal cells.

Parameters such as phase holdup, flow regime, bubble size distribution, coalescence characteristics, gas-liquid interfacial area, interfacial mass transfer coefficients, heat transfer coefficients and dispersion coefficients influence the bubble column reactors design. The adjustable parameter which affects more all the above mentioned non-adjustable parameters is the column diameter. The mass transfer coefficient is believed to be the most

important design variable, followed by the gas holdup and the axial dispersion coefficient (Shah et al., 1982).

2.1.2 Mass transfer

Theoretical mass transfer models

1. Stagnant-film model

The case of mass transfer through gas-liquid interface is considered. The stagnant-film model assumes that the mass transfer resistance depends on the velocity of the solute diffusive transport in each contacting phases and it is localized near the interface between two stagnant liquid and gas film with finite thickness, δ_L and δ_G. There is a thermodynamic equilibrium between interfacial phase concentrations, thus the interface itself does not represent a mass transfer resistance. The mass transfer through the stagnant film is processed by molecular diffusion in steady state in which the local flux across each element of area is constant. Furthermore, there is no accumulation of diffusing species within the film and the films present linear concentration profiles. In this case, the molar flux, N', of the diffusing species through the film of thickness, δ, is given by the simplified expression of Fick's first law:

$$N' = \frac{D}{\delta}\Delta C \tag{2.1}$$

where D is diffusion coefficient and ΔC is the concentration difference between the ends of the film. The liquid side mass transfer coefficient is given by:

$$k_L = \frac{D}{\delta_L} \tag{2.2}$$

2. Penetration Theory (Higbie,1935)

Higbie emphasized that in many situations the contact times between phases are too short for the steady state to be achieved. It is assumed that if θ is the time that a liquid particle is subject to unsteady-state diffusion (or penetration), then the liquid side mass transfer coefficient is given by:

$$k_L = 2\sqrt{\frac{D}{\pi\theta}} \tag{2.3}$$

3. Surface-Renewal Theory (Danckwerts,1951)

The surface-renewal theory is an extension of the previous theory that allows eddies of fluid to be exposed at the surface for varying lengths of time. On the assumption that the change of a surface element being replaced is independent of its age, the liquid side mass transfer coefficient is given by:

$$k_L = \sqrt{Ds} \tag{2.4}$$

where s is the fractional rate of surface renewal (Treybal, 1968; Perry and Green, 1984).

In the Stagnant-Film Model, the liquid side mass transfer coefficient (k_L) is proportional to the diffusion coefficient (D), while the other models considered here predict a square-root dependency on D. For all the models presented here there is an unknown parameter namely: δ_L for the Stagnant-Film Model, θ for the Penetration Theory and s for the Surface-Renewal Theory, which constrains their application.

Mass transfer resistances

When a gas has low solubility in a liquid, the gas side mass transfer resistance is negligible compared to the liquid side resistance. This is shown below for the particular case of air-water oxygen (O_2) mass transfer. The mass transfer rate (N) can be expressed in the following different ways:

$$N = k_G A \left(C_g - C_g^i\right) \tag{2.5}$$

$$N = k_L A \left(C_L^i - C_L\right) \tag{2.6}$$

$$N = K_L A \left(C_L^* - C_L\right) \tag{2.7}$$

where A is the total interfacial area. C_g and C_g^i are the solute concentrations in the gas and in the interface, respectively. C_L, C_L^i and C_L^* are the solute concentrations in the liquid, in the interface and in the liquid phase in equilibrium with the solute concentration in the gas phase C_g, respectively. And k_G, k_L and K_L represent the individual gas side mass coefficient, the individual liquid side mass coefficient and the global liquid side mass transfer coefficient, respectively. As the solute has low solubility in the liquid then Henry's law can be used:

$$C_L^* = HC_g \tag{2.8}$$

$$C_L^i = HC_g^i \tag{2.9}$$

where H is the Henry constant. Using equations 2.5-2.9 the following expression is obtained:

$$\frac{1}{K_L A} = \frac{1}{k_L A} + \frac{H}{k_G A} \tag{2.10}$$

The left hand side represents the total mass transfer resistance, the first term of the right hand side is the liquid side resistance and the second term is the gas side resistance. By Higbie's penetration theory and surface-renewal theory $k \propto \sqrt{D}$. At 25^oC, $D_{O_2-air} = 0.1937\ cm^2/s$, $D_{O_2-water} = 2.10 \times 10^{-5}\ cm^2/s$ (Cussler, 1984; Sherwood et al., 1975) and $H_{O_2} = 3.1 \times 10^{-2}$ (Perry and Green, 1984). As a result,

$$\frac{1}{k_L A} = 3098 \frac{H}{k_G A} \tag{2.11}$$

Therefore, the gas side resistance can be neglected, compared to the liquid side resistance. Thus, the O_2 mass transfer rate from the bubbles to the water can now be expressed as,

$$N_{O_2} = k_L A \left(C_L^* - C_L\right) \tag{2.12}$$

The amount of oxygen transferred per unit volume of reactor (Q_{O_2}) is defined as,

$$Q_{O_2} = k_L \frac{A}{V} \left(C_L^* - C_L\right) = k_L a \left(C_L^* - C_L\right) \tag{2.13}$$

where a is the gas-liquid interfacial area per unit of volume and $k_L a$ represents the volumetric mass transfer coefficient. The dissolved oxygen concentration variation with time is equal to the molar flux defined in equation 2.13.

$$\frac{dC}{dt} = k_L a \left(C_L^* - C_L\right) \tag{2.14}$$

Equation 2.14 expresses the oxygen mass balance in the liquid phase. Considering the liquid phase homogeneous and C_L^0 the dissolved oxygen concentration at $t = 0$, the integration of the last equation leads to:

$$\ln\left(C_L^* - C_L\right) = \ln\left(C_L^* - C_L^0\right) - k_L a \cdot t. \tag{2.15}$$

If C_L^0 and C_L^* (oxygen solubility) are known, then the volumetric mass transfer coefficient can be determined by plotting $ln(C_L^* - C_L)$ against time.

Volumetric liquid-side mass transfer coefficient - $k_L a$

In the particular case of oxygen absorption, the standard procedure is to first measure the dissolved oxygen concentration and then a method is applied to extract the volumetric liquid-side mass transfer coefficient ($k_L a$).

In the measurement of oxygen concentrations in the liquid phase, different probes were already tested and used:

- **Polarographic electrodes**

  These electrodes are the most commonly used to measure the dissolved oxygen concentration in the liquid. Oxygen is consumed by reduction on the cathode and the current is used as a measure of the oxygen fugacity (amperometric principle) (Terasaka et al., 1998). The probe is connected to the respective meter/analyzer where the oxygen concentrations are displayed. A good mixing near the membrane interface should be provided and the dynamics of the electrode should have a negligible effect on the $k_L a$ results (Freitas and Teixeira, 2001).

- **Optical probe**

  In viscous solutions, the liquid film resistance on the polarographic electrode membrane becomes important and the electrode readings are systematically low. To avoid

this limitation an optical oxygen sensor was developed at TU, Hannover, Germany. This sensor has no oxygen consumption, thus no minimum liquid turbulence is required. Optical sensors are based on a change of the optical properties such as absorption or luminescence of an indicator dye caused by chemical substances. The optical fiber tip was coated with tris(4,7-diphenyl-1,10-phenanthrolin)-ruthenium(II)-chloride (RuBPP), an oxygen sensitive dye, embedded in silicone. The measurement principle is the change in fluorescence intensity of RuBPP as a consequence of fluorescence quenching by molecular oxygen. The reduction of fluorescence with increasing oxygen partial pressure is converted on the basis of Stern-Volmer kinetics to give a signal which is directly proportional to the oxygen concentration (Terasaka et al., 1998; Tservistas et al., 2001).

- **Laser-induced fluorescence (LIF)**
  This technique was used by Schluter et al. (2001) to investigate local mass transfer phenomena. A laser light sheet illuminates a thin layer of carboxymethylcellulose/water solution that contains a fluorescent tracer whose luminosity depends on dissolved oxygen concentration. A high speed camera is used to detect the luminosity. Injecting an oxygen bubble into an oxygen-depleted solution, the oxygen transport from the bubble into the liquid can be detected and the mass transfer rate calculated using a greyscale calibration.

The volumetric liquid-side mass transfer coefficient is often estimated by following methods:

- **Stationary method**
  In this method the mass transfer rate of a solute is obtained in steady state conditions. Two columns are required, one for oxygen absorption where air is injected and another for striping or desorption where nitrogen is fed. A liquid flow circulates continuously between the columns and the steady state is reached when the oxygen absorbed by the liquid in one column is equal to the oxygen removed by the nitrogen in the other column. The steady state concentration of dissolved oxygen is measured (normally with polarographic electrodes) and k_La is determined from mass balance equations (Zahradnik et al., 1992; Thompson and Worden, 1997). If the steady state liquid phase oxygen concentration profiles are measured, the volumetric liquid-side mass transfer coefficient is usually determined by fitting these profiles to the axial

dispersion model (Kim and Kim, 1990; Yang et al., 2001) or to backflow cell model (Patwari et al., 1986; Schumpe et al., 1989).

- **Dynamic method**
  Generally a single column or reactor is necessary when this method is applied. Initially the liquid is deoxygenated by stripping with nitrogen. When the oxygen concentration in the liquid is zero, air is supplied into the column. At this moment the oxygen transfer process from air bubbles to the liquid begins and continues until oxygen concentration in the liquid phase reaches saturation. Dissolved oxygen concentration values are recorded on a PC, through a data acquisition board, and the dissolved oxygen concentration variation with time (t) is obtained (Mena et al., 2005a). The volumetric mass transfer coefficient is determined from the relation expressed by equation 2.15, that results from the mass balance of oxygen in the liquid phase (equation 2.14). This procedure is frequently used in two-phase systems investigations (see e.g. Dudley (1995); Nirdosh et al. (1998)) and also in three-phase reactors (see e.g. Patwari et al. (1986); Ozkan et al. (2000); Freitas and Teixeira (2001)).

Factors affecting k_La

In gas-liquid contactors, the volumetric gas-liquid mass transfer coefficient depends mainly on the superficial gas velocity, sparger design, physicochemical properties of the contacting phases and column dimensions. But, in three-phase bubble columns, k_La can also be affected by the presence of the solids.

Due to their significant differences, three-phase contactors will be divided in **three-phase fluidized beds reactors** and **three-phase slurry reactors**. The main difference between them is the particle size, being in the former of the order of millimeters (mm) and in the latter of the order of micrometers (μm).

In **three-phase fluidized beds reactors**, the dispersed gas phase rises through the continuous liquid phase where the solids are suspended or fluidized. This suspension can be achieved simply by the strength of the bubble bed rise or, more regularly, by liquid circulation. Thus, as mentioned by Shah et al. (1982), the effect of the solid concentration on k_La strongly depends on the gas and liquid velocities. Shah et al. (1982) review

presents a research work about an aeration of a suspension of glass beads ($d_p = 300\ \mu m$) in water, in which it was found a slight increase of k_La for high liquid velocities and low gas velocities, in comparison with the results without solids. Decreasing the liquid velocity and increasing the gas velocity, the solids distribution becomes more and more nonuniform and the k_La values are lower than those without solids.

Freitas and Teixeira (2001) working in an internal-loop airlift reactor, used calcium alginate beads ($d_p = 2.1\ mm$) at concentrations up to 30%v/v suspended in water and aqueous ethanol solutions. They verified that k_La decreases with the increase in solids loading, especially for high superficial gas velocities, as a result of an increase in bubble coalescence. Reductions of 40% and 70% were obtained with the introduction of 20% and 30% of solids, respectively. This negative effect of solids loading on mass transfer rate in airlifts was also reported by Kawase and Hashimoto (1996), Hwang and Lu (1997) and Nicolella et al. (1998). However, an initial increase of k_La with solids loading followed by a decrease with further solids additions is mentioned by Smith and Skimore (1990). Zheng et al. (1995) studied the mass transfer of the three-phase fluidized beds, composed by air,water and glass spheres ($d_p = 0.52$ to $0.755\ mm$) for solids holdup until 20%. It was observed that k_La decreases if the solids concentration increases, independently of the gas velocity.

Dhanuka and Stepanek (1980) measured the mass transfer coefficient and the interfacial area in three phase fluidized beds and observed that k_La decreases with an increase in particle size, due to a decrease in the interfacial area. Zheng et al. (1995) measured the k_La for 5% of solids holdup and noted that increasing the particle size from $d_p = 0.52$ to $0.755\ mm$, k_La decreases, especially for higher gas velocities. The effect of particle size on k_La was also investigated by Kim and Kim (1990) using glass beads as solid phase. In the bubble coalescing beds ($d_p = 1.0$, 1.7, $2.3\ mm$), k_La values are smaller than those for gas-liquid (g-l) system, while in bubble disintegrating beds ($d_p = 3.7$, $6.0\ mm$) k_La values are higher than those without solids. Moreover, increasing the particle size, k_La increases. It was observed that in bubble coalescing beds the interfacial area values are smaller than those in solids-free systems, due to the bubble coalescence in the beds of smaller particles. Similar results were reported by Nguyen-Tien et al. (1985) for a wider range of particle diameter ($d_p = 0.05 - 8\ mm$). For small particles ($d_p \leq 1\ mm$), k_La exhibits a decrea-

sing function of solids volume fraction. This behavior can be explained by the increase in the suspension viscosity which induces bubble coalescence. Larger particles ($d_p \geq 3\ mm$) improve the k_La as a consequence of bubble disintegration leading to higher g-l interfacial areas. The bubble disintegration capability can be reduced by an increase of liquid viscosity as shown by Patwari et al. (1986). Increasing the viscosity of the liquid, a larger particle size is required for an increase in g-l mass transfer rate in comparison with the system without solids. For the same particle size, the relative k_La increase is considerably reduced.

Solids density may also influence the mass transfer rate. A small increase of solids density (from 1023 to 1048 kg/m^3) results in a huge decrease on k_La, due to changes on the solids distribution in the reactor. By increasing the solids density, the solids concentration in the lower sections of the reactor also increases, enhancing bubble coalescence and decreasing the g-l interfacial area (Freitas and Teixeira, 2001).

In **three-phase slurry reactors** the particles are kept in suspension by liquid eddies induced by gas flow and/or mechanical agitation. Numerous investigations have been directed to study the influence of the suspended solid particles on the mass transfer characteristics of slurry reactors. By suspending a small amount of fine particles, Chandrasekaran and Sharma (1977) noted significant increases in g-l interfacial area and k_La due to the bubble coalescence hindering effect of the fine particles. On the contrary, Quicker et al. (1984) concluded that there was no significant effect on g-l interfacial area for low activated carbon concentrations. So, the increase in k_La observed under those conditions has to be attributed to increase in k_L. Sada et al. (1986b) investigated the influence of fine particles ($d_p \leq 10\ \mu m$) on k_La in electrolyte solutions. Different particles were tested (aluminium oxide, calcium hydroxide and calcium carbonate) and it was observed that the effect of the type of suspended particles on k_La for low solids loadings ($\leq 1\ wt\%$) was not significant. The same authors, in a previous work (Sada et al., 1983), measured k_La, a and k_L in a slurry bubble column with suspended magnesium hydroxide particles ($d_p = 2\ \mu m$). For solids concentration range $0.2 - 5\ wt\%$, k_La remains almost constant and then decreases with further increases in the slurry concentration. Sada et al. (1985) continued their investigation with calcium hydroxide particles ($d_p = 7\ \mu m$) suspended in sodium chloride solutions. Experimental results showed that k_La in slurries can be 35% higher than that without solids, independently of the solids loading for slurry concentrations up to 15 $wt\%$.

In another work, Sada et al. (1986a) worked with calcium hydroxide ($d_p = 7\ \mu m$), glass beads (d_p= 40 and 96 μm) and nylon 6 particles ($d_p = 2000\ \mu m$) to study the mass transfer characteristics of a three-phase bubble column. They realized that for high solids loading, k_La is larger than that in a two-phase system, while for solids concentrations lower than 5 $wt\%$ k_La, remains nearly constant. The suspended solids influence on k_La was found to be much smaller in electrolyte solutions than in nonelectrolyte liquid media.

Zahradnik et al. (1992) carried out mass transfer experiments in a sectionalized aerated slurry reactor, using ZnO ($d_p = 2.3\ \mu m$) as solid phase, for concentrations up to 5 $wt\%$. Increasing solids concentration, reduced k_La values were obtained. It was also found that the relation between k_La and gas holdup is independent of solid concentration, which may imply that solids do not affect the g-l mass transfer mechanism. So, the decrease of k_La with solids loading can only be attributed to the decrease of interfacial area as a result of bubble coalescence enhancement.

The effect of solids on k_La in mechanical agitated slurry reactors has also been studied in the past. Yagi and Yoshida (1974) performed oxygen absorptions in a fermenter. They verified that the effect of dead microorganisms on k_L was negligible. However, the presence of such substances caused considerable change in the bubble size distribution, and consequently decreased the gas holdup, the g-l interfacial area, and the k_La. Albal et al. (1983) added glass beads ($d_p = 150\ \mu m$) and oil shale particles ($d_p = 44\ \mu m$) to water in order to study the influence of solids concentration on k_La. The solids loading varied from 0 to 25 $vol\%$. For low solids concentration ($2 - 5\ vol\%$), k_La increased by about $10\% - 30\%$ and then decreased with a further increase in the solids concentration. Several kinds of solids were used by Ozkan et al. (2000) to study the influence of inert fine solid particles on g-l mass transfer. While kieselguhr, activated carbon, Fe_2O_3 and $BaSO_4$ has a pronounced positive effect on k_La, a smooth increase is observed for TiO_2 and $CaCO_3$ slurries up to 1.5 $vol\%$ in water. However, the effects of the same solid particles in n-butanol are moderate. Enhancements in the gas absorption rate in various liquids (water, hexadecane and sunflower oil) by TiO_2 particles ($d_p = 3\ \mu m$) were reported by Dagaonkar et al. (2002). The enhancement factors increase with an increase in solids loading and level off to a constant value at higher solids loadings. The minimum solid loading necessary for maximum enhancement depends on the liquid phase. The discrepancies on the results

presented above may be due to the differences in experimental conditions, such as the loading, size, wettability, density of solids and physicochemical properties of liquid.

As already mentioned above, the presence of solid particles may influence the volumetric mass transfer coefficient (k_La) by affecting either the individual liquid-side mass transfer coefficient (k_L) or gas-liquid interfacial area (a). Therefore, to better understand the effect of solids on k_La, it is of great importance to individualize the mass transfer components. Usually, the gas-liquid interfacial area and the volumetric mass transfer coefficient are measured experimentally and then the individual liquid-side mass transfer coefficient is determined from the knowledge of k_La and a.

Individual liquid-side mass transfer coefficient - k_L

The individual liquid-side mass transfer coefficient can also be determined from measurements with single bubbles, whenever the g-l interfacial area is known. Alternatively, k_L values can be estimated from correlations (Shah et al., 1982).

The solid particles may increase k_L by enhancing turbulence at the gas-liquid interface and inducing surface renewal. On the contrary, k_L values may decrease with the solids presence. In the latter cases, the solid particles limit the diffusion path, blocking the available area for mass transfer. Indeed, both positive and negative effects may occur for the same solids, depending on the solids loading. Yang et al. (2001) used glass beads ($d_p = 0.4\ mm$) as solid phase and solids holdup up to 18%. For low solids holdup, k_L increases and then decreases for further increase of solids content. For low solids fractions, the solids movement enhance the bubble breaking and the liquid phase turbulence, while for higher solid loadings, the solids increase the apparent viscosity of the bed, decreasing k_L, since k_L is inversely proportional to viscosity. Ozkan et al. (2000) working with micron sized particles, also pointed out the opposite effects on k_L of fine particles of high density and size in the order of the film thickness for mass transfer. k_L values might increase due to changes in the film thickness with turbulence or decrease due to diffusion coefficient lowering. As solids volume fraction increase, the covered g-l interface by particles can hinder the gas diffusion, reducing k_L. Sada et al. (1985) referred that k_L depends mainly on the diffusivity of gas in the solution and on the viscosity of the solution. They reported a sudden decrease in k_L for solids loadings under 2 $wt\%$, followed by a constant k_L region. The decrease in k_L is attributed to the decrease in bubble size. It was also verified that in

bubbly flow regime, k_L is nearly independent of the superficial gas velocity, while in the churn turbulent regime k_L increases considerably, probably due to the formation of large bubbles and strong bubble oscillations.

Gas-liquid interfacial area - a

Numerous methods exist for measuring the interfacial area in g-l systems, a few of them may be applied also to g-l-s systems. These methods can be classified as chemical and physical methods. The chemical techniques are based on a reaction of known kinetics in which the absorption rate is a function of the interfacial g-l area, while the physical methods are based on the modification of some physical property. The most employed chemical techniques are the sulfite method, that involves the oxidation of sulfite ions by oxygen (Quicker et al., 1984; Camacho et al., 1991; Vázquez et al., 2000a; Shah et al., 1982) and the CO_2 absorption in alkali (Sada et al., 1985), among those the most common is the Danckwerts method (Alper et al., 1980; Vázquez et al., 2000a,b). The main disadvantages of the chemical methods are their limitations to specific g-l systems and the need to know certain physicochemical properties. The physical techniques are usually divided in non-invasive and invasive. Among the non-invasive techniques the most suitable for measure bubble sizes and g-l interfacial areas are: Photography and image analysis (Mena et al., 2005a), light attenuation, radiography and laser (and phase) Doppler anemometry (Boyer et al., 2002). The invasive techniques used for bubble size and interfacial area measurements are the needle probes and the ultrasound probes. The two main types of needle probes are: optical fibre probes which are widely used (Kiambi et al., 2001; Yang et al., 2001; Zhang et al., 2005; Mena et al., 2005b) and the resistive or conductive probes. The ultrasound probes can be based on attenuation or Doppler techniques. The invasive techniques are particularly useful for highly turbulent systems, specially for nearly industrial operating conditions because in many cases non-invasive techniques become ineffective. For instance, in opaque mediums or in opaque wall reactors, the image analysis is not effective. Also , for high gas holdup or bubble density, the laser Doppler anemometry or PIV are not suitable.

The presence of solid particles may increase, decrease or have a negligible effect on the g-l interfacial area. In some situations, solids particles induce bubble break-up, increasing a, in other cases the solids enhance bubble coalescence which results in bigger bubbles and consequently decreased g-l interfacial areas. Ozkan et al. (2000) indicated that the presence of fine and heavy particles in the liquid film at g-l interface may prevent bubble coales-

cence, increasing the g-l interfacial area. Zahradnik et al. (1992) suggested that increasing solids content intensify bubble coalescence and consequently decrease the interfacial area. Quicker et al. (1984) stated that for low solids loadings, there was no significant effect on a, while at higher solids concentrations the interfacial area decreased with the increase of solids loading. Yang et al. (2001) observed also that the interfacial area decreased with the increase of solids holdup. This was ascribed to the increase of the system apparent viscosity which resulted in increased bubble coalescence rates. Sada et al. (1985) reported an increase in a with the increase of the slurry content for solids concentrations below 2 $wt\%$, while constant a values were observed for solids loadings between 2 and 15 $wt\%$.

Solid particles size may also affect the interfacial area as observed by Kim and Kim (1990). They verified that increasing the particle size, the interfacial area increases due to the reduction of the bubble size. However, Randall et al. (1989) mentioned that an increase in the solid particle size results in larger bubbles.

Another solid property that might influence the interfacial area is the solid density. Increasing solids density may modify the solids distribution in the reactor. The solids concentration in the lower sections of the reactor increases, inducing bubble coalescence and consequently reducing the interfacial area (Freitas and Teixeira, 2001). Randall et al. (1989) also referred that increasing pulp density results in bigger bubbles.

2.2 Experimental technique

In this section the experimental apparatus is presented and the experimental procedure and conditions are described. The different types of solids used in the experiments are characterized.

2.2.1 Experimental facility

The contact device used to perform the mass transfer experiments was the bubble column represented in Fig. 2.1 with the respective dimensions. The device is a perspex cylindrical column covered by a perspex rectangular box. The box has two roles: filling the space between the two columns with the liquid under study so that the optical effects

can be avoided; control the temperature through water circulation. The gas enters first in a gas chamber and then passes through a sparger where the bubbles are formed.

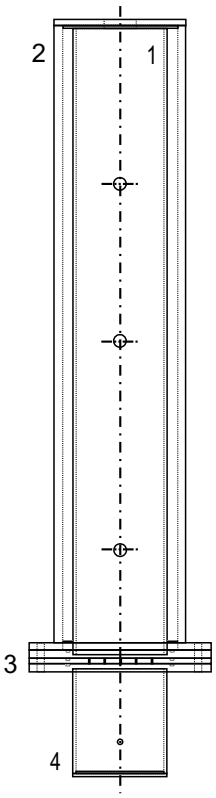

Component	Dimensions	mm
1 – Cylindrical column	Internal diameter	84
	Thickness	3
	High	600
2 – Rectangular box	Width	110
	Thickness	8
	High	600
3 – Sparger	Thickness	5
4 – Gas chamber	Internal diameter	84
	Thickness	3
	High	100

Figure 2.1. Bubble column.

The sparger consists of 13 uniformly spaced needles with an inner diameter of 0.3 mm. A scheme of the gas sparger is shown in Fig. 2.2. The shape and size of the needles ensure the formation of small and well-defined bubbles. The needles disposal enables a uniform bubble distribution along the column which enhances the suspension of low density solids. A concave perspex cylindrical piece, formed by small cones involving each needle, was placed at the column bottom to allow solids circulation in this area and avoid solids deposition.

A complete scheme of the experimental setup is shown in Fig. 2.3. The air flow rate was measured by a KDG Mobrey 2-A-150 R rotameter followed by a manometer, where the pressure was kept at the constant value of 1 bar, and a flow control valve. Before enter

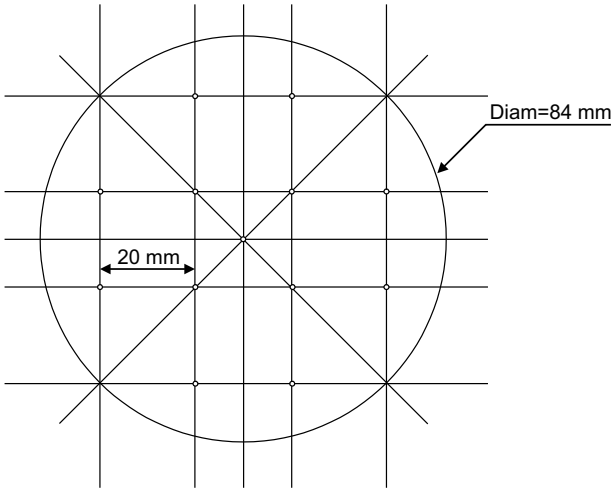

Figure 2.2. Needles plate for gas sparging.

in the bubble column, the air is saturated in a humidifier. A high resolution black and white digital camera Sony XCD-X700 was used in the image analysis experiments. The camera was connected to a Matrox Meteor II/1394 frame grabber. $Visilog^{TM}$ 5.4 (Noésis, les Ulis, France) was the software used for image acquisition and processing. The lightning system is composed by a 200 *watt* halogen lamp and a diffusing glass where the light is scattered. Dissolved oxygen concentration was measured by a Mettler Toledo In Pro 6100 O_2 sensor (polarographic electrode) connected with a Mettler Toledo O_2 4100 dissolved oxygen meter. A data acquisition board was coupled to the O_2 meter, enabling to read the O_2 concentration on-line.

2.2.2 Experimental method

Mass transfer experiments

Oxygen mass transfer runs were performed in two and three-phase systems. Air and water were used as gas and liquid phases, and different types of solids were tested as solid phase. The experiments were performed for several superficial gas velocities (up to 2.7 mm/s). The clear liquid height was $h_0 = 0.2\ m$ for all experiments (no liquid throughput) and the polarographic electrode (O_2 probe) was located 0.1 m from the gas sparger. The dynamic method, described in section 2.1.2, was employed to determine the

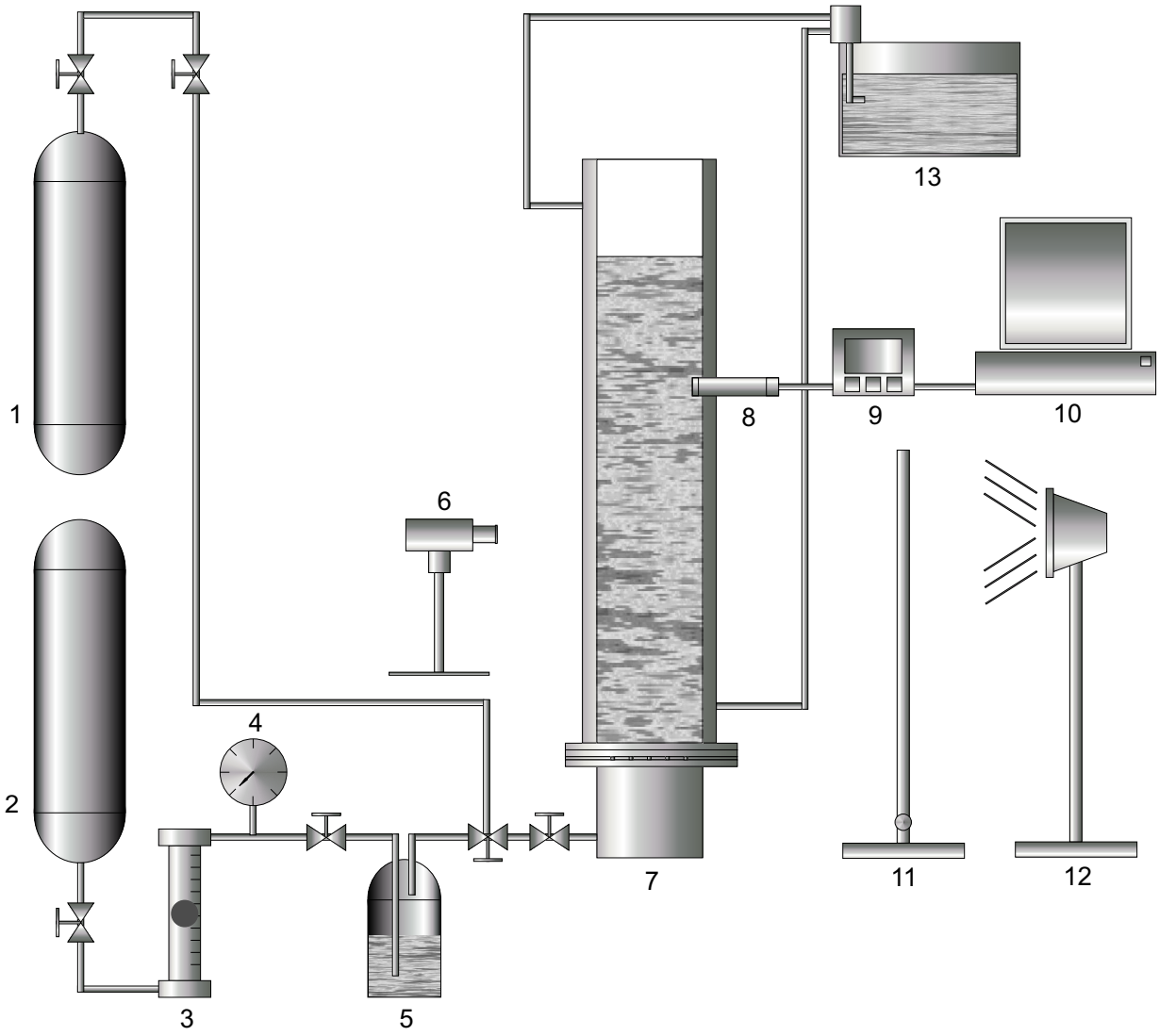

Figure 2.3. Experimental set-up (1: N_2, 2: Air, 3: Rotameter, 4: Manometer, 5: Humidifier, 6: Digital camera, 7: Bubble column, 8: O_2 probe, 9: O_2 concentration meter, 10: PC, 11: Diffuser glass, 12: Halogen lamp, 13: Thermostatic bath).

volumetric liquid-side mass transfer coefficient, k_La.

Image analysis experiments

In order to study the characteristics of the bubbles, images were grabbed with a monochrome video digital camera, which was connected to the frame grabber. Sets of images ($1024x768\ Pixels$) were recorded for different gas velocities, solids loadings and sizes, in

the same conditions used in air-water-calcium alginate beads mass transfer experiments. Then, the images were automatically treated, analyzed and several object descriptors were obtained for each bubble using a program running under $Visilog^{TM}$ 5.4 software (Noésis, les Ulis, France). The image treatment procedure is described below and illustrated in Fig. 2.4 (for air-water-calcium alginate 1 $vol\%$ system and a superficial gas velocity of 0.09 cm/s). The procedure is based on the fact that alginate particles have a higher grey level than the bubbles and lower than the background.

- Find the first peak in the histogram of the original grey-level image. This peak corresponds to the grey level of the bubbles.
- Segment the grey-level image with the previous grey level as limit. Only the bubbles are selected and the solids are eliminated.
- Hole fill - All the holes inside objects are filled.
- Border kill - All the objects touching the frame of the image are eliminated.
- Noise elimination applying a sequence of erosions and reconstruction. Reconstruction retrieves the original shape of the retained objects after a series of erosions that eliminates undesirable small objects.
- Labelling the image. All the objects are detected and identified.
- Ultimate searches for the ultimate eroded set. This enables to count the number of convex objects, even if some of them are touching each other, as long as the pseudo-center of each object is outside other objects.

More details on image processing can be found in Appendix A.2. After the image treatment, several size and shape descriptors can be determined for each bubble: the projected area (S) from which the equivalent diameter (d_{eq}) can be calculated; the Feret diameters distribution, from which the maximum (F_{max}) and minimum (F_{min}) Feret diameters are obtained (the Feret diameter is the smallest distance between two parallel tangents to the object, the tangent position being defined by the angle between them and the horizontal axis); the elongation (F_{max}/F_{min}) is also determined; the convex bounding polygon of each

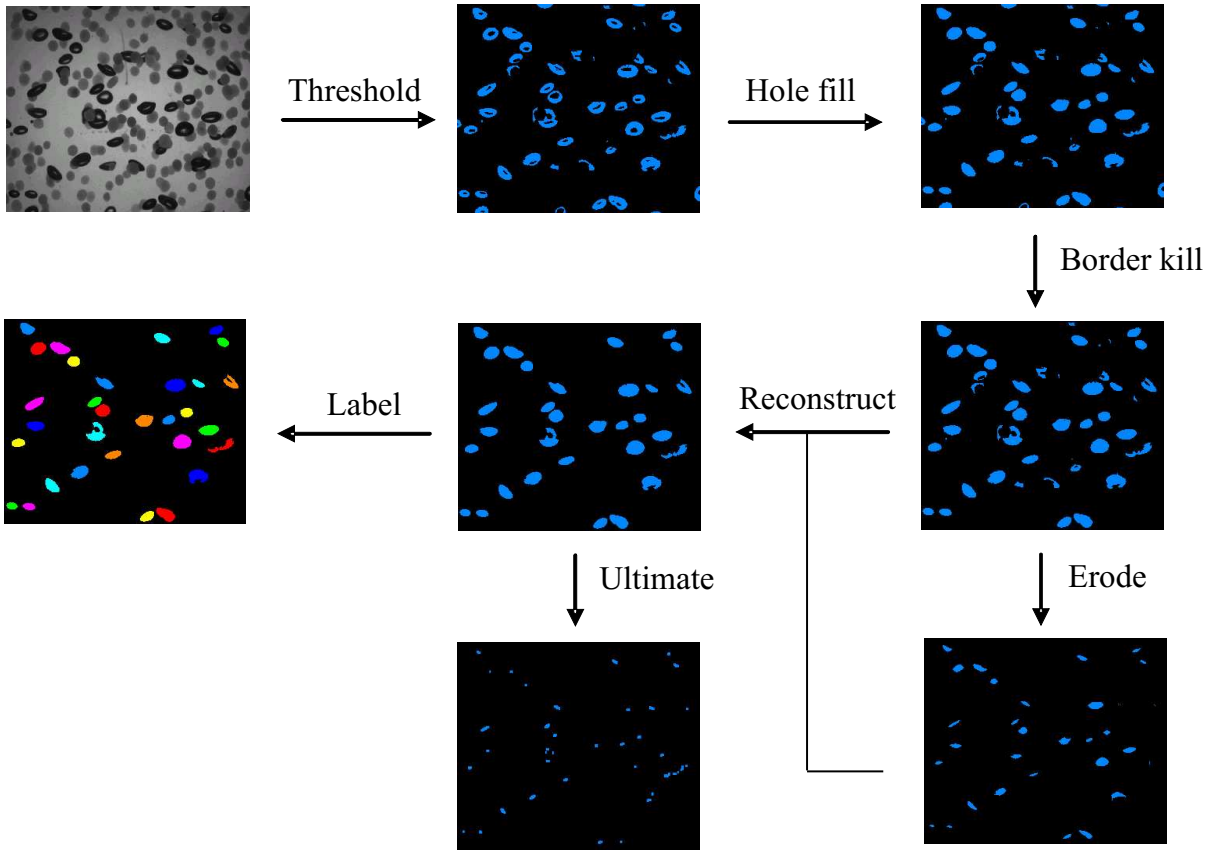

Figure 2.4. Image processing scheme.

object is calculated and the concavity index ($C.I. = S_{Obj}/S_{CBP}$) is obtained, where S_{Obj} and S_{CBP} are the surfaces of the object and of the convex bounding polygon, respectively (see Fig. A.8 in Appendix A.1) (Pons et al., 1997). More details on image descriptors can be found in Appendix A.1. It was found that $C.I. > 0.99$ was a good criterium to distinguish between isolated and overlapping bubbles: overlap induces concavities in the object and decreases the concavity index (C.I.). The change in size due to the depth of view was experimentally studied. It was found that the error in the calculation of the superficial area of the bubbles was less than 2%.

The image analysis technique was applied only for g-l air-water system and air-water-calcium alginate beads three-phase systems (two solid sizes, 5 $vol\%$ and 10 $vol\%$ of solids and superficial gas velocity up to 2.7 mm/s)(see Figs. 2.30-2.34). However, tests at higher gas flow rates and also with different kinds of solids were performed but the automatic image

treatment was unfortunately inefficient. One can find in Appendix A.3 some examples of images of different systems at certain conditions under which the automatic image analysis was found to be inadequate.

2.2.3 Solids

Calcium alginate beads

In order to investigate the solid size effect on mass transfer, two solid particle sizes were produced and used. To produce calcium alginate beads, a 2% (w/v) sodium alginate solution was prepared dissolving sodium alginate in water at a temperature higher than $70^{O}C$, under strong agitation. This mixture was then dropped into a 2% (w/v) calcium chloride solution using a peristaltic pump and calcium alginate beads were formed by ion exchange $Ca^{2+} \leftrightarrow Na^{+}$ (Freitas, 2002). This procedure was employed at the Center of Biological Engineering - IBQF (University of Minho, Portugal) where the bigger particles, with an equivalent diameter $d_{eq} = 2.1\ mm$ (Fig. 2.5(a)), were prepared.

A slightly different and more complex set-up was used at ENSAIA-IPLP (Nancy, France) on the preparation of the smaller beads with an equivalent diameter $d_{eq} = 1.2\ mm$ (Fig. 2.5(b))(Jourdain, 2002). A 0.45 mm outer diameter needle was used to drop the sodium alginate solution and an electric impulse generator working at 9 kV was connected to the chamber in order to create very small drops which resulted in smaller beads.

The equivalent diameter of the beads was measured as follows: several images of a considerable amount of particles were obtained from a digital camera coupled with a microscope (see Fig. 2.5) and then the images were automatically analyzed and the bead size obtained.

The beads are approximately spherical and have a density $\rho_p = 1023\ kg/m^3$. The choice of calcium alginate beads corresponds to our interest in three-phase airlift reactors with immobilized biomass (as calcium alginate is commonly used in biomass immobilization). These solids are well-defined completely wettable objects with reasonable rigidity. Moreover, they do not form agglomerates and are big enough not to affect the surface properties of the gas-liquid interface.

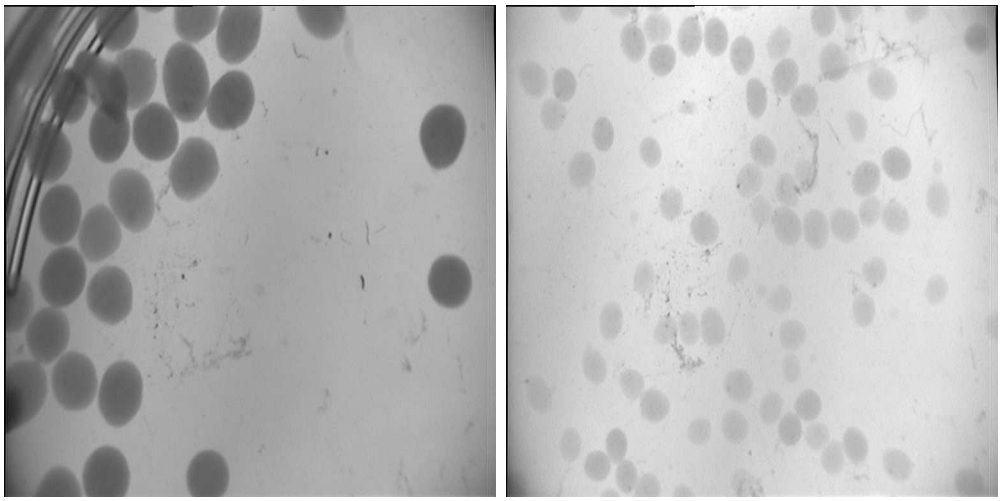

(a) (b)

Figure 2.5. Calcium alginate beads: (a) $d_{eq} = 2.1\ mm$; (b) $d_{eq} = 1.2\ mm$.

Polystyrene beads

The polystyrene beads are white rigid spheres insoluble in water with a density of $\rho_p = 1040 - 1050\ kg/m^3$. Expandable polystyrene (EPS) particles, from BASF, of three different size ranges were tested: *Styropor*® VEP 124 (P124), *Styropor*® VEP 324 (P324) and *Styropor*® EP 424 (P424). A granulometric analysis was performed in *COULTER LS Particle Size Analyzer* in order to estimate the particle sizes. For each particle size range, two concordant measurements (a and b) were carried out (Fig. 2.6) and the mean particle diameters were obtained (see table 2.1).

Table 2.1. Volume statistics of particle diameter

Bead	Mean diameter (μm)
P124	1100
P324	769.8
P424	591.2

Hollow Glass Spheres

The mass transfer experiments with fine particles were done using as solid phase *Spheriçel*® hollow glass spheres. These are white spherical particles, insoluble in water

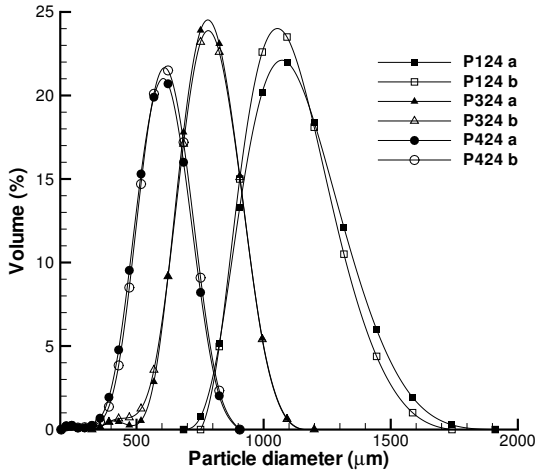

Figure 2.6. Granulometric analysis of polystyrene beads.

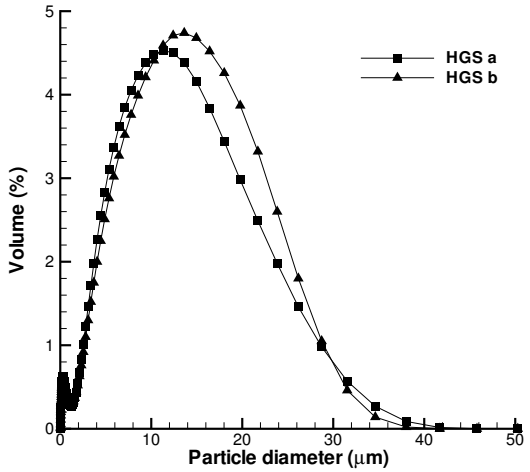

Figure 2.7. Granulometric analysis of hollow glass spheres.

and with density of $\rho_p = 1100\ kg/m^3$. This low density is a consequence of the fact that they are hollow solids, otherwise they would have the usual glass density. A granulometric analysis was also performed and two concordant runs (a and b) were obtained (Fig. 2.7). The mean particle diameter obtained is 9.6 μm.

2.3 Results and discussion

2.3.1 k_La evaluation from experimental data

For each mass transfer experiment, the dissolved oxygen concentration variation with time is obtained. An example of data treatment is presented below, for air-water-P424 "washed" beads and superficial gas velocity $u_G = 2.2\ mm/s$. The dissolved oxygen concentration curve for this particular experiment is plotted in Fig. 2.8. One can distinguish three zones on the graph. Zone I, at the beginning, where the O_2 concentration is nearly constant, followed by an intense mass transfer zone where the O_2 concentration rises fast (Zone II). The last zone (Zone III) appears close to the saturation, when the mass transfer rate starts to decline.

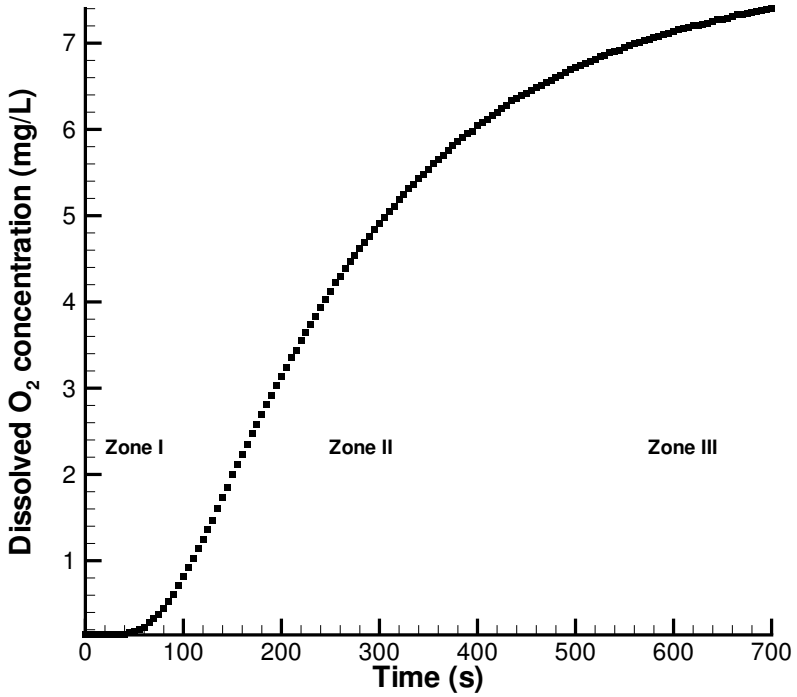

Figure 2.8. Dissolved oxygen concentration variation for air-water-P424 "washed" beads and $u_G = 2.2\ mm/s$.

Plotting $ln(C_L^* - C_L)$ against time (see equation 2.15 in section 2.1), one can determine

k_La from the slope in the linear zone. The solubility of oxygen in water (C_L^*) is taken from a table (see Appendix C) and the slope is determined using the statistical method Test F. This method consists in determining the optimum number of points (n_p) for a linear regression of the experimental data. Initially, a short data interval is considered and the linear regression parameters (c and b) are determined as well as a parameter F^*. This parameter is defined as:

$$F^* = \frac{1}{n_p - 1} \cdot \sqrt{\frac{\sum (y_{est} - y)^2}{\sum y^2}} \tag{2.16}$$

where y is the experimental value and y_{est} is the estimated value ($y_{est} = c + bx$). At each iteration, an increment in n_p is added to the data interval and the parameters c and b are recalculated until the parameter F^* reaches its minimum.

Since the linear region is located somewhere in Zone II, first a fixed initial point is defined within that zone and the Test F is performed to the left and the right hand sides of the initial point (Fig. 2.9). Two optimum slopes and intervals are obtained and the final value of k_La is the weighted average of the slopes:

$$k_La = \left| \frac{n_{p_1} \cdot b_1 + n_{p_2} \cdot b_2}{n_{p_1} + n_{p_2}} \right| \tag{2.17}$$

where n_{p_1}, b_1 and n_{p_2}, b_2 are the optimum number of points and slopes for the left and right hand sides of the initial point, respectively. For this particular case the results are presented in following table:

Table 2.2. Optimum parameters

	Left	Right
$F*$	4.26E-05	8.28E-05
n_p	35	19
c	2.469777	2.431651
b	-0.004081	-0.003964

and finally one obtains the volumetric mass transfer coefficient $k_La = 0.00404\ s^{-1}$.

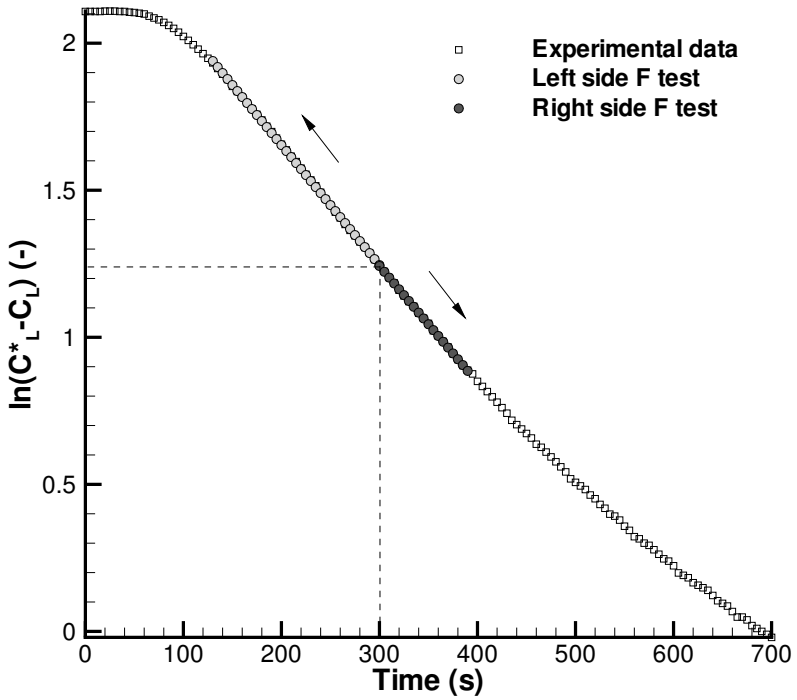

Figure 2.9. Test F application for the experimental results for air-water-P424 "washed" beads and $u_G = 2.2\ mm/s$.

2.3.2 Air-water

Before each three-phase system mass transfer study, air-water two-phase system experiments were performed. In two-phase and also three-phase systems, tap water was the liquid phase. Tests with air-distilled water were conducted and no significant difference was found between air-tap water and air-distilled water, confirming that tap water could be used as liquid phase for all experiments. Experimental volumetric mass transfer coefficients for air-water system were then compared with correlations presented in literature. All the correlations displayed in Fig. 2.10 can be found in Shah et al. (1982), except the one of Sotelo et al. (1994). The majority of the correlations underestimate the experimental values due to differences in the experimental conditions, mainly in superficial gas velocity range and bubble column diameter.

Overestimation is obtained using the semiempirical equation proposed by Sotelo et al.

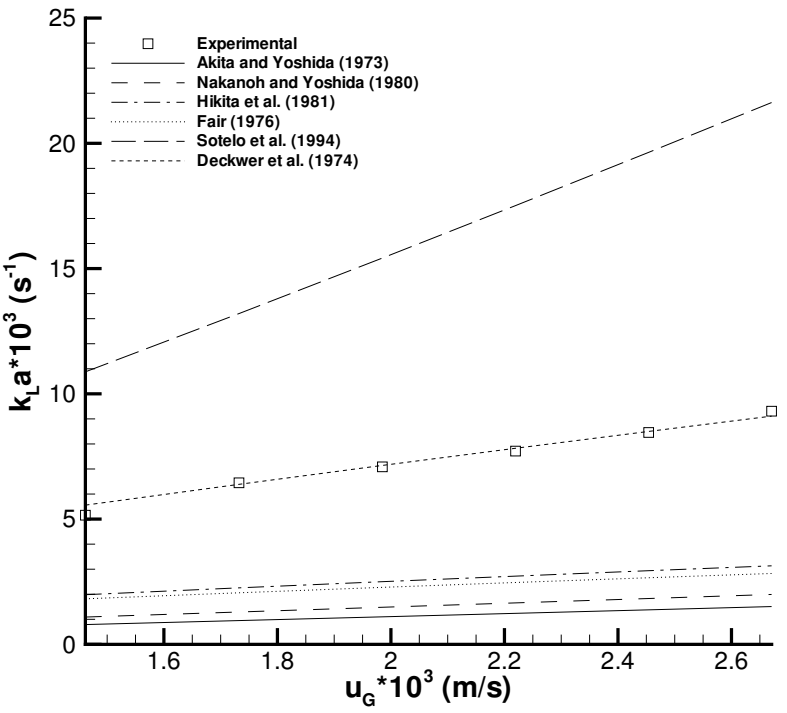

Figure 2.10. Dependence of k_La on superficial gas velocity for air-water system.

(1994) as a consequence of differences in the type of diffuser. A very good agreement is found with the Deckwer et al. (1974) correlation, which is of the form $k_La = mu_G^n$, with parameters m and n equal to 1.174 and 0.82, respectively.

2.3.3 Air-water-calcium alginate beads

Fig. 2.11 shows how k_La varies with superficial gas velocity, u_G, and solid loading, for calcium alginate beads of 1.2mm diameter (alg.I). It can be seen from this figure that k_La increases with superficial gas velocity and decreases with the solid concentration. Furthermore, it seems that the solid effect becomes independent from solid loading for higher gas velocities.

Only one study using calcium alginate beads ($d_p = 2.1\ mm$) as solid phase was found in literature. This study was conducted by Freitas and Teixeira (2001) who worked in a three-phase internal loop airlift reactor and verified that k_La decreases with an increase in

solids loading, especially for high superficial gas velocities. Zheng et al. (1995) although investigating different systems (air-water-glass spheres fluidized beds), also observed that the k_La decreases if the solids concentration increases.

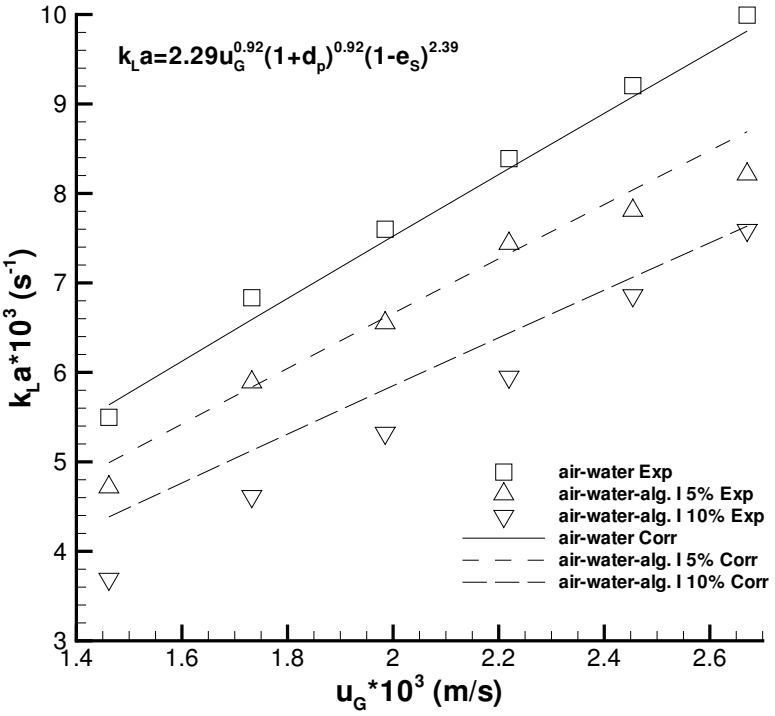

Figure 2.11. Dependence of k_La on superficial gas velocity u_G, for different calcium alginate concentrations. Experimental data and proposed correlation ($d_p = 1.2\ mm$).

Similar experiments were performed using calcium alginate beads with a 2.1 mm size (alg.II). In this case, k_La also increases with superficial gas velocity (Fig. 2.12). The influence of the solids increases with the superficial gas velocity and is independent from the solids concentration. The results in Figs. 2.11 and 2.12 indicate that the smaller particles have a stronger effect on k_La. These results are reproducible with an average relative error of 5%. Moreover, k_La for 2.1 mm particles exhibits similar values (for the smaller solid loading) or higher than those obtained for 1.2 mm.

For glass spheres under 1 mm diameter in a fluidized bed, Zheng et al. (1995) found that k_La increases with gas velocity and decreases with solid concentration and increasing

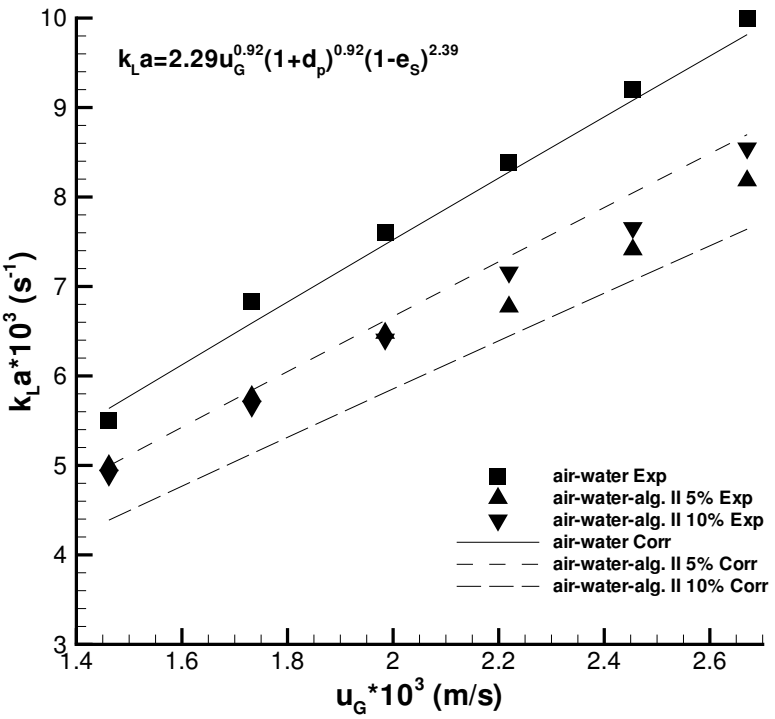

Figure 2.12. Dependence of k_La on superficial gas velocity for different calcium alginate concentrations. Experimental data and proposed correlation ($d_p = 2.1\ mm$).

particle size. For particles above 1mm, the effect of particle size on k_La changes. Kim and Kim (1990) reported that, in that range, k_La increases with an increase in particle size. Above 3mm size, k_La is, higher than in the situation without particles. Comparable results were presented by Nguyen-Tien et al. (1985) for a wider range of particle diameter ($d_p = 0.05 - 8\ mm$). For small particles ($d_p \leq 1\ mm$), k_La exhibits a decreasing function of solids volume fraction while bigger particles ($d_p \geq 3\ mm$) enhance the k_La. The dependence of the mass transfer characteristics on particle size is also highlighted by Patwari et al. (1986) and Schumpe et al. (1989).

An empirical correlation for k_La on the experimental variables superficial gas velocity u_G, particle diameter d_p and solid volume fraction e_S was developed, using the least squares method. Only few correlations devoted to the effect of solids characteristics on k_La can be found in literature. Zheng et al. (1995) correlated k_La with the axial distance from

the distributor, superficial gas and liquid velocities, particle diameter and fractional solid holdup. However, this correlation is not applicable to the present study since we have no liquid input. Among other correlations proposed in the literature (e.g. Midoux et al. (1984); Kim and Kim (1990); Schumpe et al. (1989)), the exponential dependence was found to be the most suitable. Thus, for each type of solid phase investigated, it was obtained a correlation of the following type:

$$k_L a = a_1 u_G^{a_2} (1 + d_p)^{a_3} (1 - e_S)^{a_4}. \tag{2.18}$$

where a_i are empirical parameters, which were determined by the least squares method for each type of solid phase. In the present case of calcium alginate beads as solid phase, the volumetric mass transfer coefficient was correlated with the experimental variables as:

$$k_L a = 2.29 u_G^{0.92} (1 + d_p)^{0.92} (1 - e_S)^{2.39}. \tag{2.19}$$

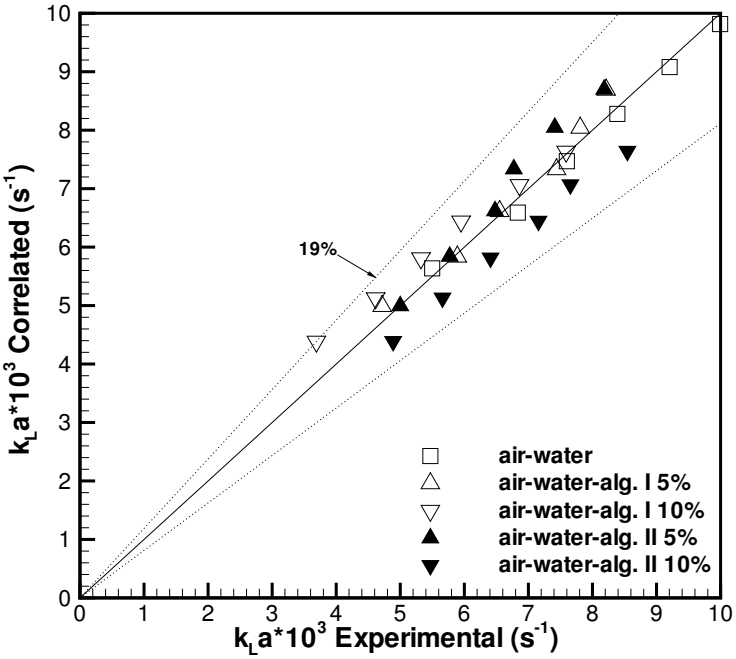

Figure 2.13. Comparison of experimental data and correlation for air-water-calcium alginate three-phase systems.

Figs. 2.11, 2.12 corroborate the good agreement between experimental and correlated values, which is confirmed by the parity plot presented in Fig. 2.13. The maximum and mean deviations between the experimental and correlated results are 19% and 5%, respectively.

2.3.4 Air-water-polystyrene beads

Two sets of experiments were conducted with polystyrene beads as solid phase. The first set, with polystyrene beads used for the first time, was called "new" polystyrene beads. The second, with polystyrene beads being used after "washing" with air and water in the first experiments, was called "washed" polystyrene beads. The main difference between these two sets was that, in the first set (with "New" polystyrene beads), fine polystyrene particles from big beads were being dispersed in the liquid, during the experiments, thus influencing the mass transfer experiments. Consequently, a new set of experiments had to be performed in order to avoid the influence of fine polystyrene particles on the mass transfer results. For each set, the three solid sizes (P124 $d_p = 1100\ \mu m$; P324 $d_p = 769.8\ \mu m$ and P424 $d_p = 591.2\ \mu m$) were investigated, for the solid loading range 0-30%.

"New" polystyrene beads

Using the bigger polystyrene particles (P124N, "N" means "New") it was verified that the volumetric mass transfer coefficient increases with the superficial gas velocity (Fig. 2.14). This influence of u_G on k_La decreases as the solid loading increases, being almost negligible for 25 and 30 $vol\%$ of solids. As observed in the air-water-calcium alginate beads experiments and in many works in the literature, k_La decreases with the solid loading increase, and this effect is enhanced by the presence of the fine particles, which affect negatively k_La. With the experimental mass transfer results for new polystyrene beads as solid phase and the three solid sizes, a general empirical correlation was obtained:

$$k_La = 0.94u_G^{0.80}(1 + d_p)^{0.96}(1 - e_S)^{4.72}. \tag{2.20}$$

A comparison between experimental and correlated values is plotted in Fig. 2.15. The correlation underestimates the experimental k_La, which can be attributed to the influence of the fine polystyrene particles. The maximum and mean absolute deviations between the

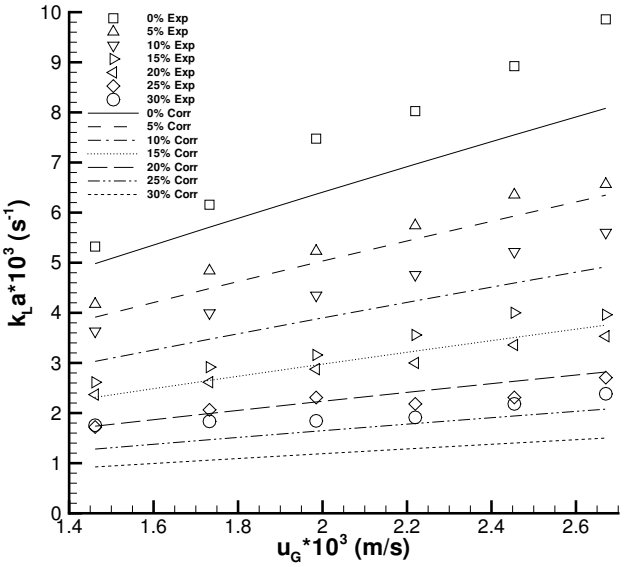

Figure 2.14. Dependence of k_La on superficial gas velocity for different P124N ($d_p = 1100\ \mu m$) concentrations. Experimental data and proposed correlation ("New" particles).

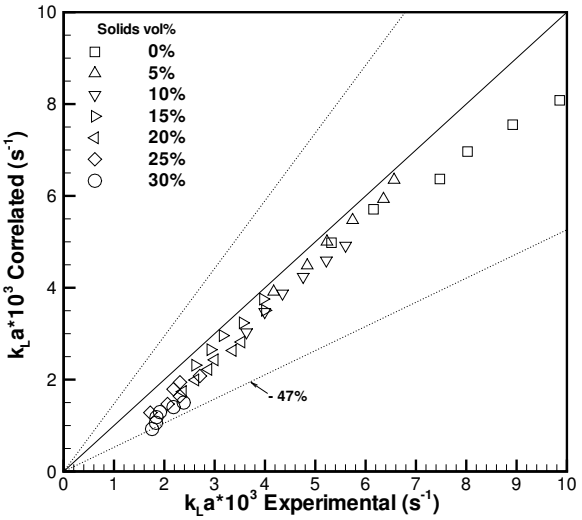

Figure 2.15. Comparison of experimental data and correlation for air-water-P124N ($d_p = 1100$ μm) three-phase systems ("New" particles).

experimental and correlated results are 47% and 17%, respectively.

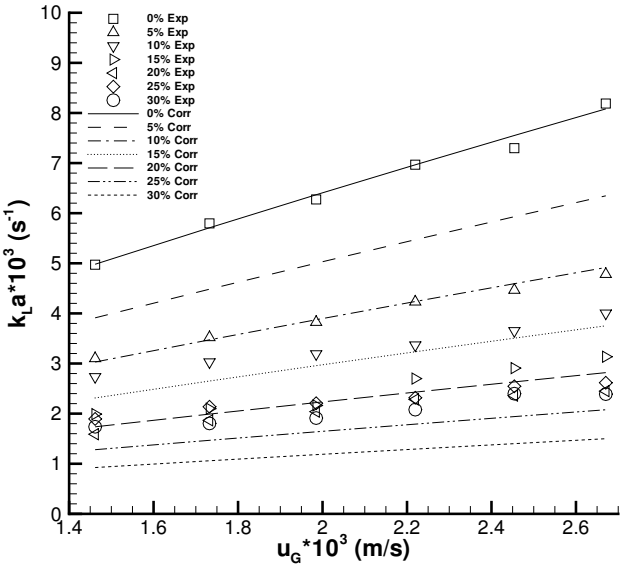

Figure 2.16. Dependence of k_La on superficial gas velocity for different P324N ($d_p = 769.8\ \mu m$) concentrations. Experimental data and proposed correlation ("New" particles).

For intermediate size polystyrene particles (P324N) the volumetric mass transfer coefficient slightly increases with the superficial gas velocity (Fig. 2.16). As for the previous solid size, k_La also decreases with the solid loading increase, but in this case only for solid concentrations up to 20 $vol\%$ and then it keeps almost constant for further solid content increases. Experimental and correlated values are compared in Fig. 2.17. Once again, a poor agreement is observed, which may be due to the presence of the fine polystyrene particles. The maximum and mean absolute deviations between the experimental and correlated results are 47% and 21%, respectively.

Similarly to the previous solid size, for the smaller size polystyrene particles (P424N), k_La also slightly increases with the superficial gas velocity (Fig. 2.18). Increasing solid loading, the volumetric mass transfer coefficient decreases. In Fig. 2.19 a comparison between experimental and correlated values is presented and poor agreement is again observed. The maximum and mean absolute deviations between the experimental and correlated results are 36% and 15%, respectively.

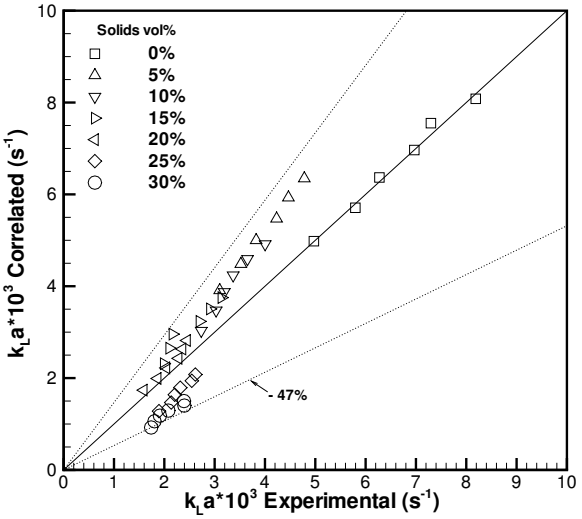

Figure 2.17. Comparison of experimental data and correlation for air-water-P324N ($d_p = 769.8$ μm) three-phase systems ("New" particles).

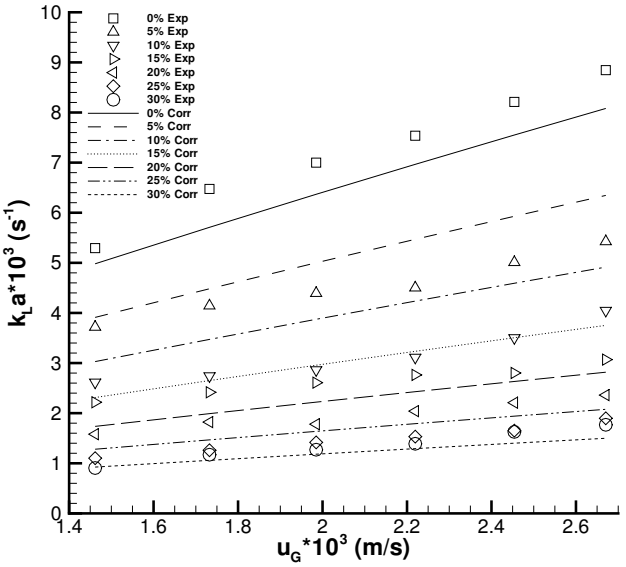

Figure 2.18. Dependence of k_La on superficial gas velocity for different P424N ($d_p = 591.2$ μm) concentrations. Experimental data and proposed correlation ("New" particles).

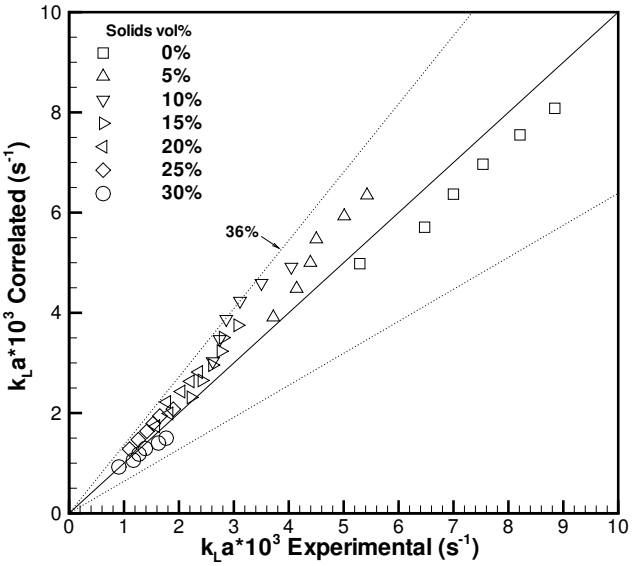

Figure 2.19. Comparison of experimental data and correlation for air-water-P424N ($d_p = 591.2$ μm) three-phase systems ("New" particles).

"Washed" polystyrene beads

For the bigger polystyrene particles (P124W, "W" means "Washed") it was observed that the volumetric mass transfer coefficient increases with the superficial gas velocity (Fig. 2.20). But, in this case of "washed" particles, the influence of u_G on k_La is not significantly affected by the solid loading. However, in the experiments with the "new" polystyrene beads and in other works found in the literature, the effect of u_G on k_La decreases as the solid loading increases. With the experimental mass transfer data for "washed" polystyrene beads as solid phase and the three solid sizes, a general empirical correlation was obtained:

$$k_La = 1.01u_G^{0.82}(1+d_p)^{0.97}(1-e_S)^{2.73}. \tag{2.21}$$

The parity plot is given in Fig. 2.21. As expected, a much better agreement is found for this case of "washed" particles, comparing to the results obtained with the "new" ones.

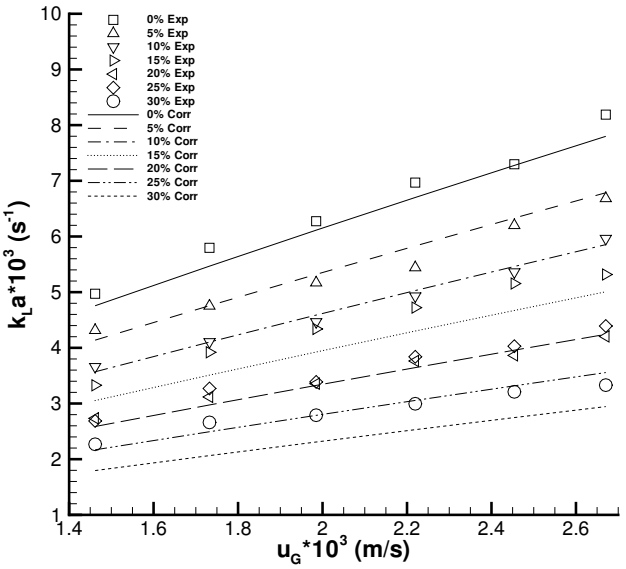

Figure 2.20. Dependence of k_La on superficial gas velocity for different P124W ($d_p = 1100\ \mu m$) concentrations. Experimental data and proposed correlation ("Washed" particles).

The maximum and mean absolute deviations between the experimental and correlated results are only 24% and 8%, respectively.

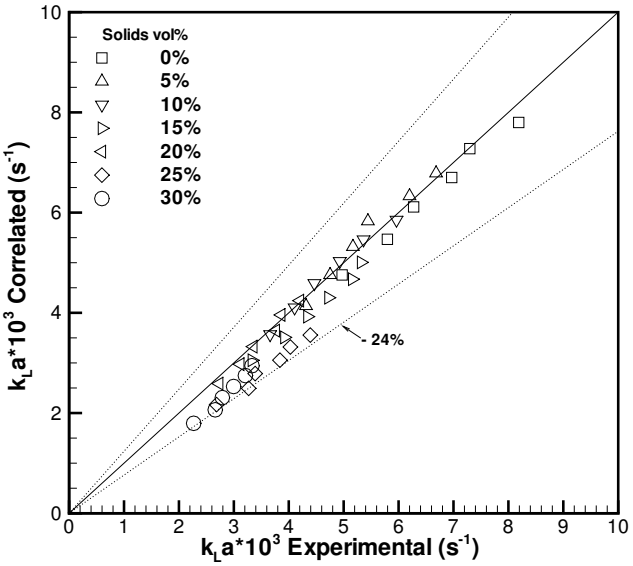

Figure 2.21. Comparison of experimental data and correlation for air-water-P124W ($d_p = 1100$ μm) three-phase systems ("Washed" particles).

The dependencies of the volumetric mass transfer coefficient on the superficial gas velocity and solid content, observed for the air-water-P324W system (Fig. 2.22), were similar to previous solid size. As can be seen in Fig. 2.23, a good agreement between experimental and correlated values is also verified. In this case, the maximum and mean absolute deviations between the experimental and correlated results are 26% and 8%, respectively.

Finally, using the smallest "washed" polystyrene particles as solid phase, comparable general trend as previous ones was observed, but with some anomalies for higher solid content and intermediate superficial gas velocities (Fig. 2.24). As expected, the agreement between experimental and correlated data is not so good in this particular case, with a maximum and mean absolute deviations between the experimental and correlated results of 29% and 11%, respectively (Fig. 2.25).

Summarizing the main results for air-water-polystyrene systems, it was found that the volumetric mass transfer coefficient increases with the superficial gas velocity. This

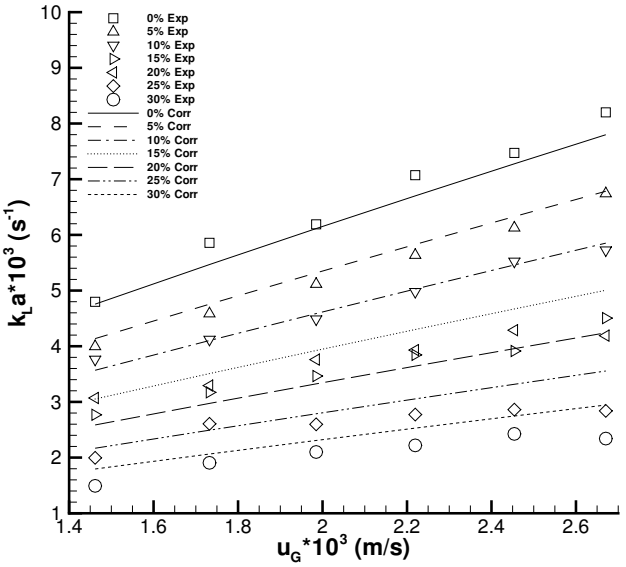

Figure 2.22. Dependence of k_La on superficial gas velocity for different P324W (d_p = 769.8 μm) concentrations. Experimental data and proposed correlation ("Washed" particles).

dependence is generally flattened for increasing solid content. When solid loading increases, the k_La values decrease. With the experimental mass transfer data for "new" and "washed" polystyrene beads as solid phase, and the three solid sizes, two empirical correlations were obtained and a good agreement between correlated and experimental data was verified for the "washed" polystyrene beads.

Shah et al. (1982) refered that the effect of solid concentration on k_La strongly depends on the gas and liquid velocities. In the present study, the liquid velocity is zero, but one noticed that the negative solids influence on k_La is stronger for higher gas velocities. In spite of the low gas holdup ($\approx$ 1%), for higher gas velocities, more bubbles are in the bubble column in a certain instant. Thus, recalling the high solid fraction (up to 30 $vol\%$), the probability of bubble-bubble interaction increases (with both u_G and e_S), which may increase the bubble coalescence rate. The gas-liquid interfacial area decreases which leads to a reduction on the volumetric mass transfer coefficient. Freitas and Teixeira (2001) also observed a k_La reduction with the increase in solids (calcium alginate beads) loading, especially for high superficial gas velocities. This effect was also attributed to an increase in bubble coalescence. According to Nguyen-Tien et al. (1985) for small particles

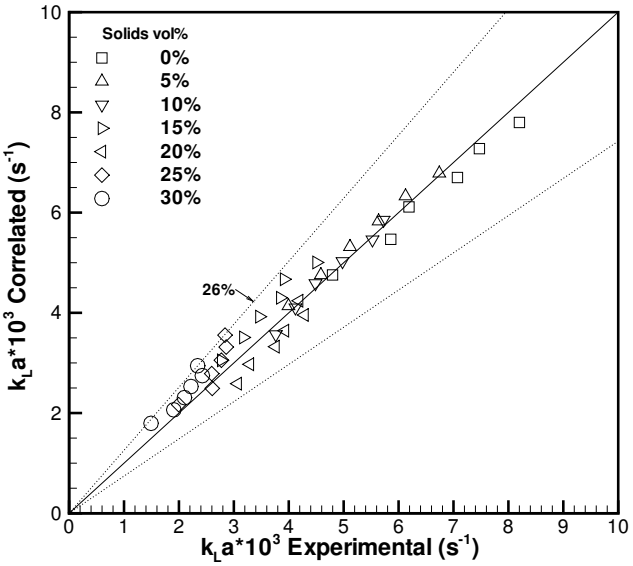

Figure 2.23. Comparison of experimental data and correlation for air-water-P324W ($d_p = 769.8$ μm) three-phase systems ("Washed" particles).

($d_p \leq 1$ mm), k_La decreases with solid volume fraction. This behavior was explained by the increase in the suspension viscosity that causes bubble coalescence. The bigger beads used in the present work had $d_p = 1100$ μm, so we can consider that we are roughly within the particle size range defined above which confirms the agreement between the present results with those presented by Nguyen-Tien et al. (1985).

The effect of solid particle size on the mass transfer coefficient is plotted in Fig. 2.26, individually for the six solid loadings, and for the "washed" polystyrene beads. The influence of solid size is negligible for 5 $vol\%$ of solids. For the rest of solid loadings, the general trend indicates that decreasing solid size results in a reduction of the mass transfer coefficient. Kim and Kim (1990) mentioned a similar influence of particle size on k_La, but an opposite effect was reported by Dhanuka and Stepanek (1980) and Zheng et al. (1995). These differences can be attributed to the differences in experimental conditions and particulary in solid type (namely: hydrophobicity, geometry and density) and particle size range.

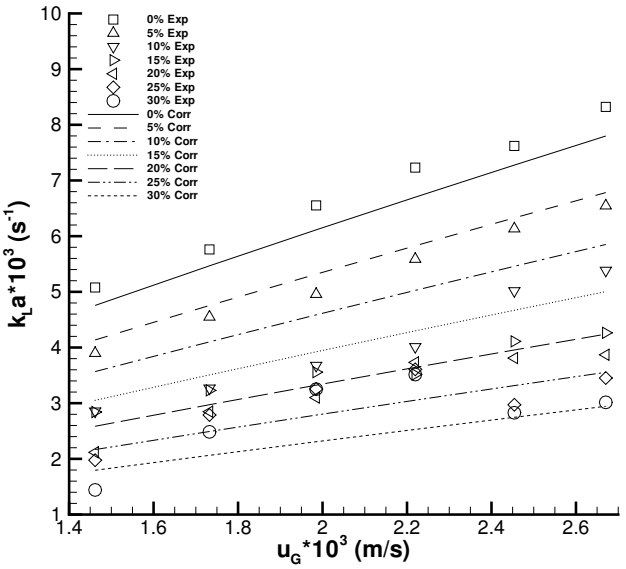

Figure 2.24. Dependence of k_La on superficial gas velocity for different P424W (d_p = 591.2 μm) concentrations. Experimental data and proposed correlation ("Washed" particles).

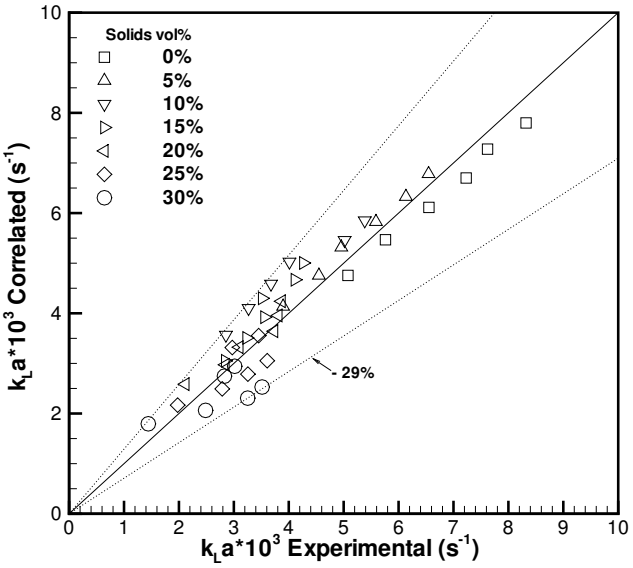

Figure 2.25. Comparison of experimental data and correlation for air-water-P424W (d_p = 591.2 μm) three-phase systems ("Washed" particles).

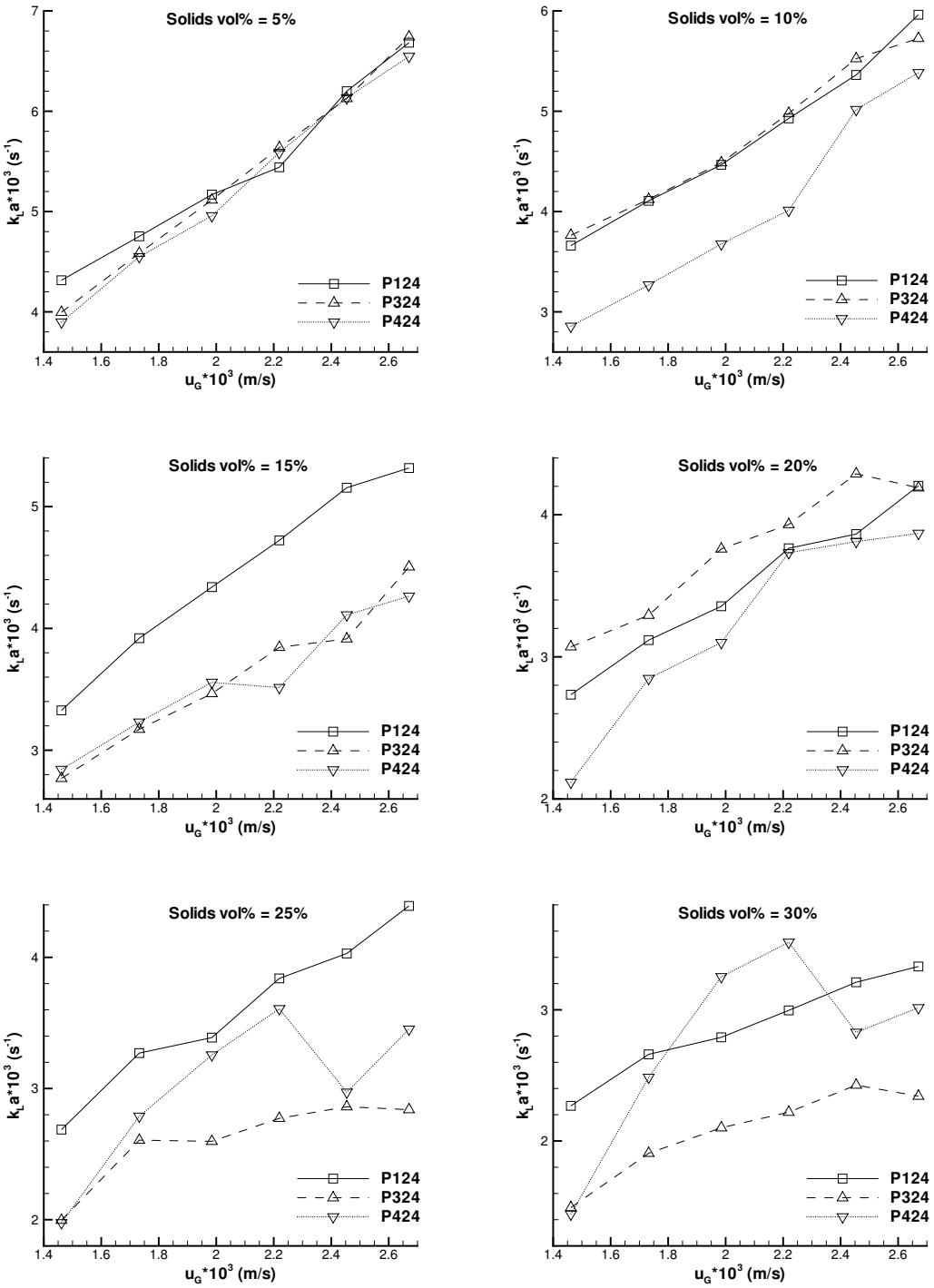

Figure 2.26. Effect of polystyrene particle size on mass transfer coefficient (P124 $d_p = 1100$ μm; P324 $d_p = 769.8$ μm and P424 $d_p = 591.2$ μm).

2.3.5 Effect of polystyrene fine particles on k_La

As already mentioned, during the mass transfer experiments, the "new" polystyrene spheres released very fine particles ($d_p = 0.1\ \mu m$) which were dispersed in the liquid phase. Fig. 2.27 shows a comparison between k_La values for the experiments with "new" and "washed" polystyrene beads.

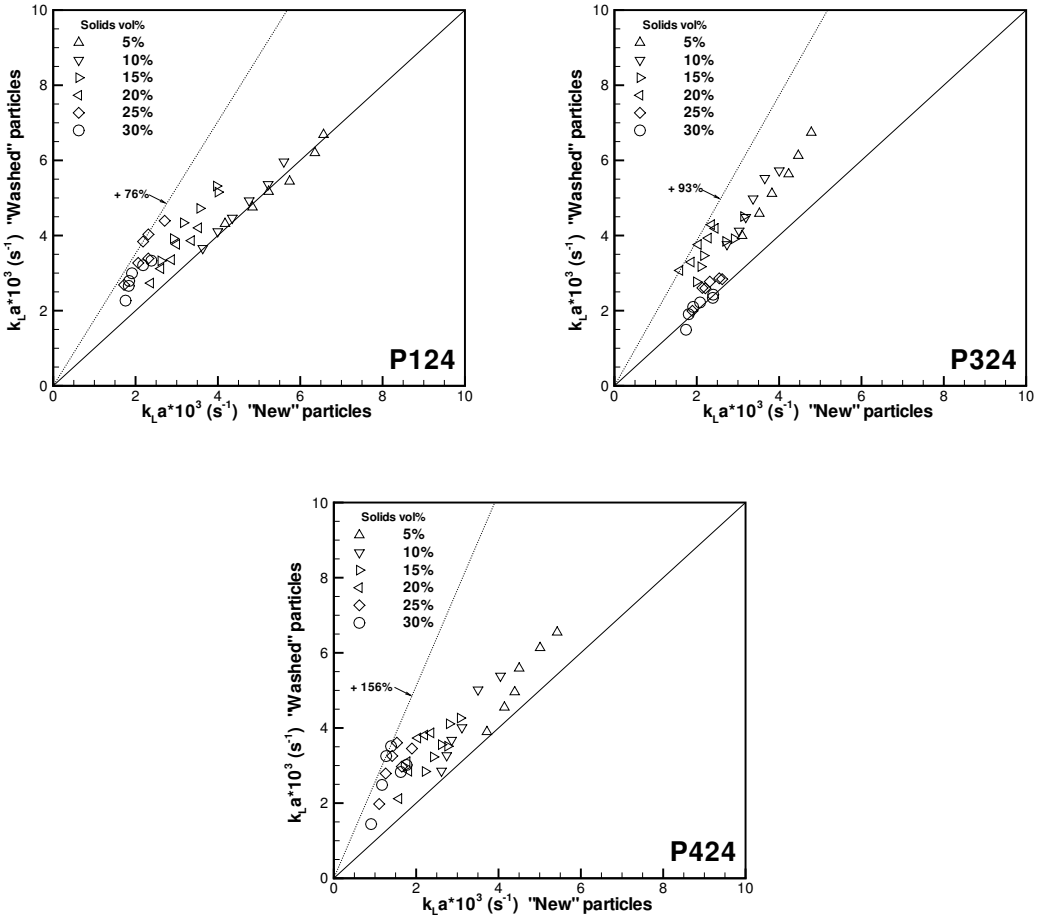

Figure 2.27. Effect of polystyrene fine particles on k_La for air-water-polystyrene systems (P124 $d_p = 1100\ \mu m$; P324 $d_p = 769.8\ \mu m$ and P424 $d_p = 591.2\ \mu m$).

Mass transfer coefficients for "washed" particles experiments are generally substantially higher than those found for correspondent experiments with "new" particles, which means that the fine particles influence negatively the mass transfer process. These particles, whose size is smaller than the liquid film around the bubble ($d_p \leq 20\ \mu m$), are hydrophobic.

Therefore, they tend to stick on the bubble, partially covering its surface and blocking the mass transfer path. So, the liquid side mass transfer coefficient (k_L) is reduced and consequently decreasing the volumetric mass transfer coefficient (k_La).

2.3.6 Air-water-hollow glass spheres

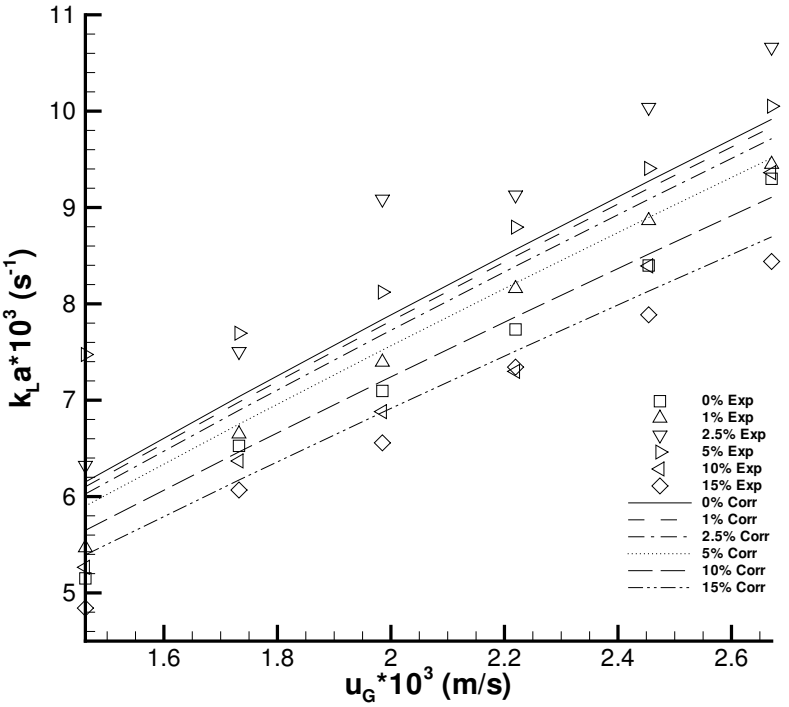

Figure 2.28. Dependence of k_La on superficial gas velocity for different hollow glass spheres concentrations. Experimental data and proposed correlation.

In order to study in more detail the influence of fine particles on k_La, mass transfer experiments were conducted in a slurry composed by 9.6 μm hollow glass spheres as solid phase, for concentrations up to 15 $vol\%$ Fig. 2.28 shows that, as in the fluidized beds previously studied (see subsections 2.3.3 and 2.3.4), the mass transfer coefficient increases with the superficial gas velocity. The same correlation type as Eq. 2.18 was tested but, as expected, without success. The influence of solid phase on mass transfer in three-phase slurry reactors is quite different from that in fluidized beds, since in the former case the

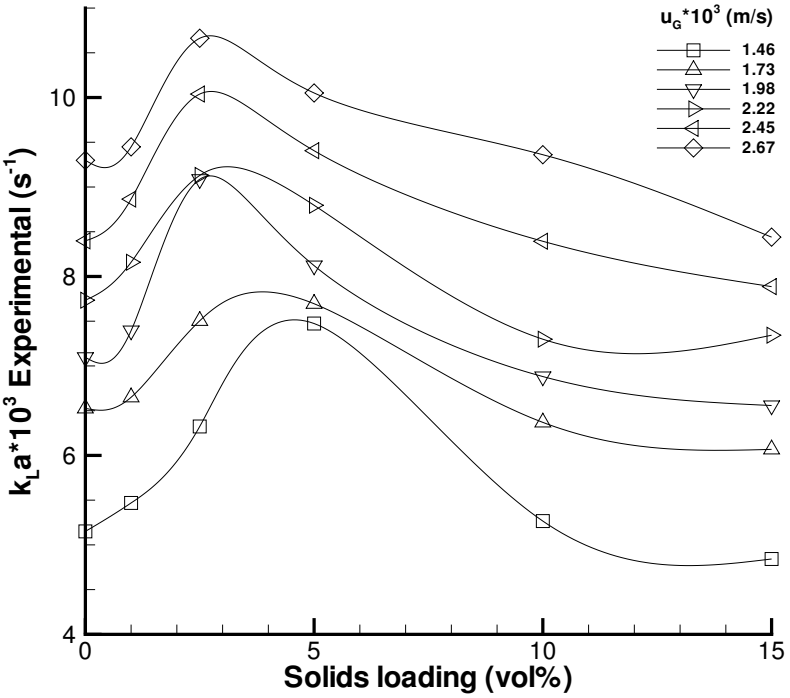

Figure 2.29. Experimental volumetric mass transfer coefficient as a function of hollow glass spheres loading.

particle size is much smaller and consequently the physical mechanisms underling the solid effect on k_La are also different.

A dual effect of solids loading on k_La is shown in Fig. 2.29. For low solids loading ($\leq\sim$ 3 $vol\%$) the mass transfer coefficient increases as the solid content increases and then decreases with further solid additions (Fig. 2.29). Two possible reasons can be pointed out for the enhancement of k_La with the solid loading increase verified for low solid contents: The first is the fact that small solid concentrations do not change significantly the liquid viscosity, but improve the surface renewal and turbulence in the liquid film, increasing k_L and thus k_La. The second is the presence of fine particles in the liquid film at gas-liquid interface which may hinder the coalescence behaviour of water, consequently increasing the gas-liquid interfacial area. On the other hand, higher solid concentrations increase the slurry viscosity and hence decreasing the surface renewal and mobility which results in reduced k_L. In addition, for higher solid contents, the gas-liquid interface will

be covered by fine particles, hindering the oxygen diffusion and reducing k_L. Also, a reduction of gas holdup with the solid content increase is expected, which consequently decreases the g-l interfacial area a. Indeed, as mentioned before, the effective mixture viscosity increases as the solid load increases which will induce the formation of bigger bubbles at the gas distributor, will promote the bubble coalescence and suppress the bubble breakup (Shah et al., 1982). Therefore, both decreases in k_L and in a obviously result in a reduction of the mass transfer coefficient k_La. Similar dual effect of solids on k_La was reported by Ozkan et al. (2000) and Albal et al. (1983). However, reduction of k_La with an increase of solid loading for a certain solid content range was referred by Sada et al. (1983) and Zahradnik et al. (1992), while Chandrasekaran and Sharma (1977), Quicker et al. (1984) and Sada et al. (1985) presented increases in the k_La with the solid loading. Once again, these discrepancies may arise from differences in experimental conditions, such as physicochemical properties of the liquid and also, loading, size, density and wettability of solids. Further investigations are needed on possible mechanisms based in changes in the gas phase (gas holdup, bubble coalescence) and in the environment around bubble (interaction of liquid film and fine particles, surface tension at the bubble, liquid film and particle interfaces, wetting differences, adsoption) (Ozkan et al., 2000).

2.3.7 Bubble characteristics

The results presented in this subsection and in subsections 2.3.8 and 2.3.9 are only from the experiments with air-water system and air-water-calcium alginate beads three-phase systems (two solid sizes, 5 $vol\%$ and 10 $vol\%$ of solids and superficial gas velocity up to 2.7 mm/s). Examples of original images of those systems are presented in Figs. 2.30-2.34.

The shape of the bubbles is influenced by superficial gas velocity, concentration and size of solids. In the range of the superficial gas velocities used here, the bubbles are oblate spheroids more or less elongated according to the operating conditions. Fig. 2.35 shows the F_{max}/F_{min} ratio, which gives the bubble shape. The concentration of solids is the parameter with the strongest effect on the bubble shape. The presence of solids makes the bubbles more rounded, and this effect is more pronounced for the higher solids loading and for the smaller particles, where the bubble sphericity approaches 1. Reese et al. (1996) studied the bubble characteristics in three-phase systems used for pulp and paper processing. They reported that the bubbles in a pulp slurry system are more flattened than

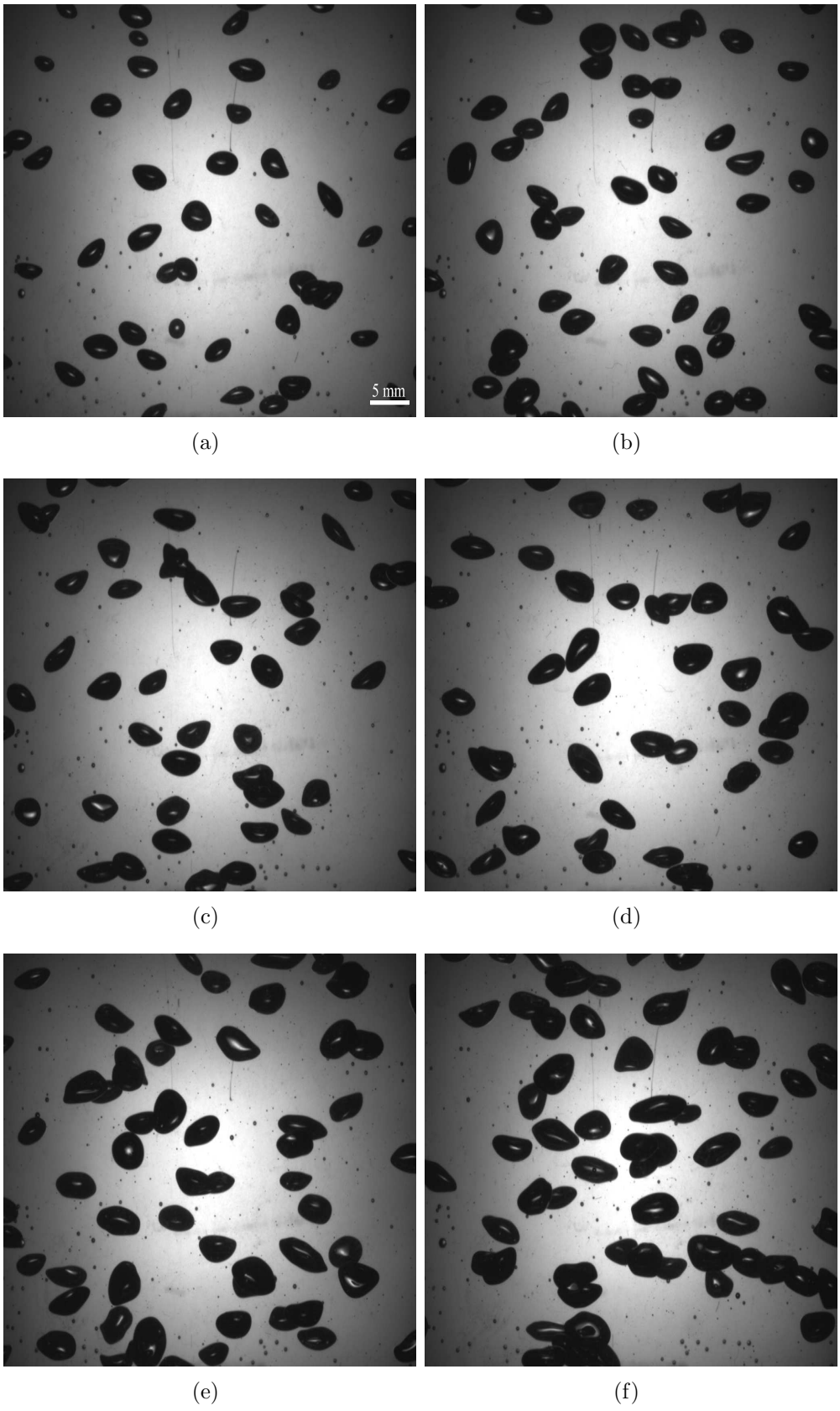

Figure 2.30. Examples of images of air-water system: (a) $u_G = 1.5\ mm/s$ (b) $u_G = 1.7\ mm/s$ (c) $u_G = 2.0\ mm/s$ (d) $u_G = 2.2\ mm/s$ (e) $u_G = 2.5\ mm/s$ (f) $u_G = 2.7\ mm/s$.

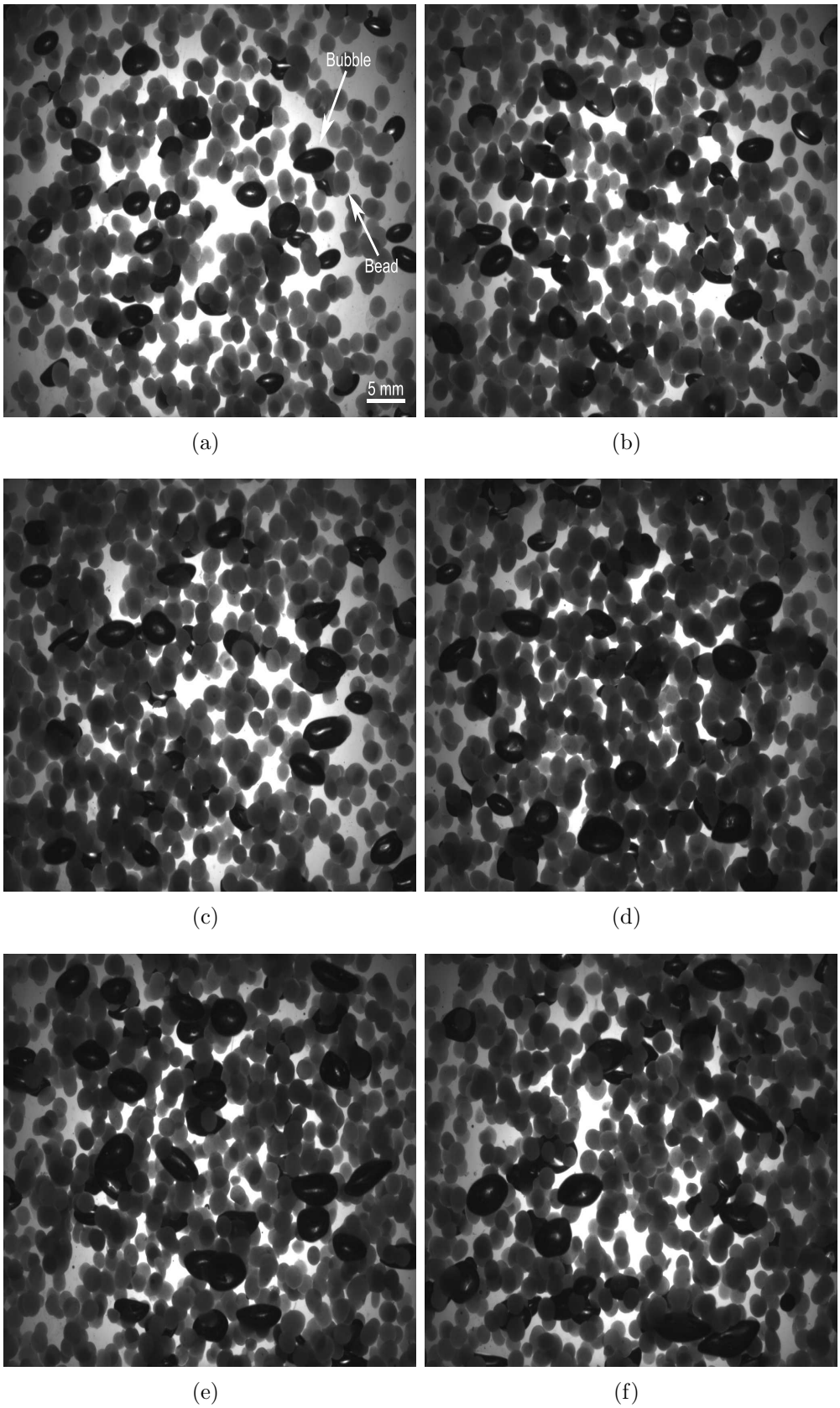

Figure 2.31. Examples of images of air-water-calcium alginate 5 $vol\%$ ($d_{eq} = 2.1\ mm$) system: (a) $u_G = 1.5\ mm/s$ (b) $u_G = 1.7\ mm/s$ (c) $u_G = 2.0\ mm/s$ (d) $u_G = 2.2\ mm/s$ (e) $u_G = 2.5\ mm/s$ (f) $u_G = 2.7\ mm/s$.

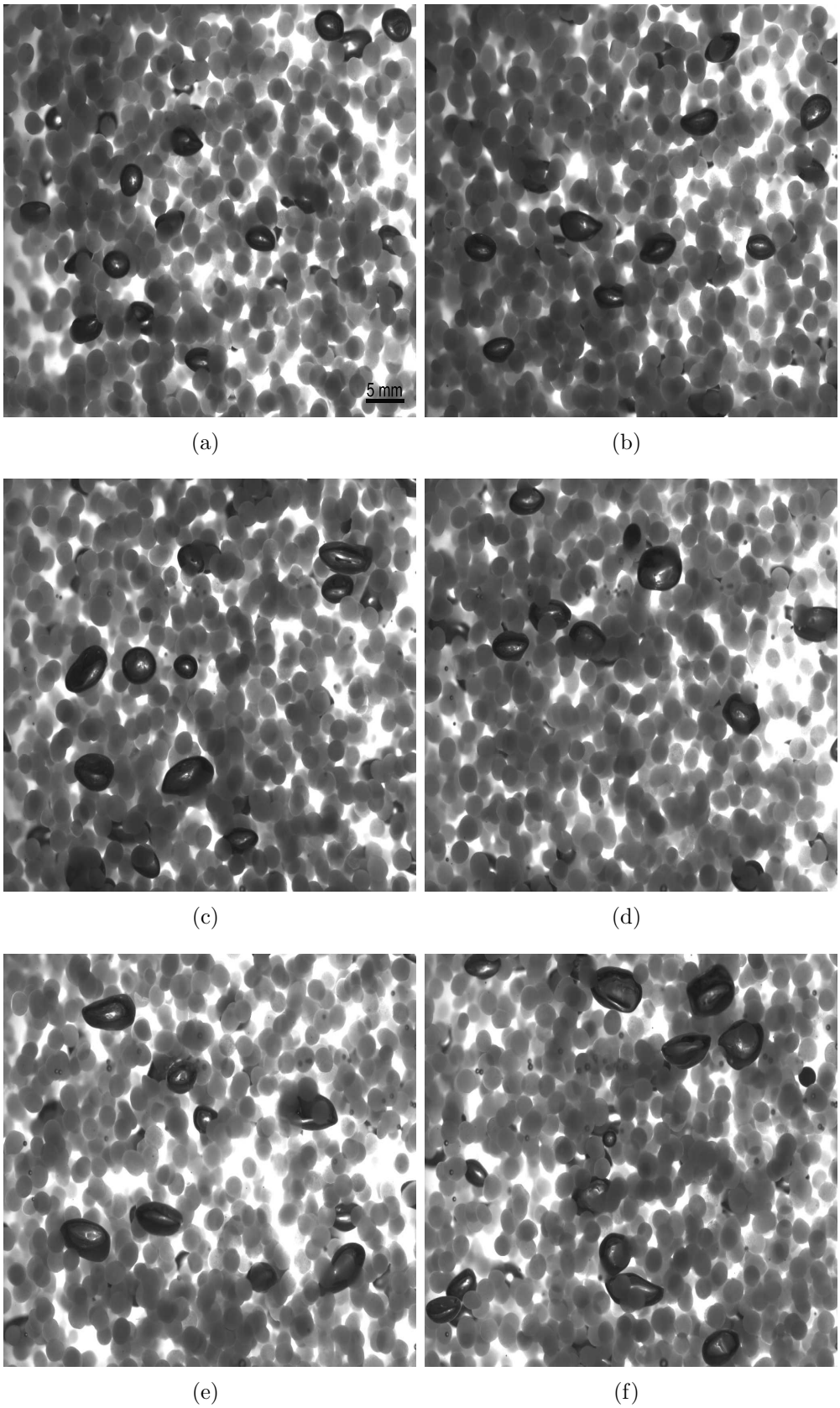

Figure 2.32. Examples of images of air-water-calcium alginate 10 $vol\%$ ($d_{eq} = 2.1\ mm$) system: (a) $u_G = 1.5\ mm/s$ (b) $u_G = 1.7\ mm/s$ (c) $u_G = 2.0\ mm/s$ (d) $u_G = 2.2\ mm/s$ (e) $u_G = 2.5\ mm/s$ (f) $u_G = 2.7\ mm/s$.

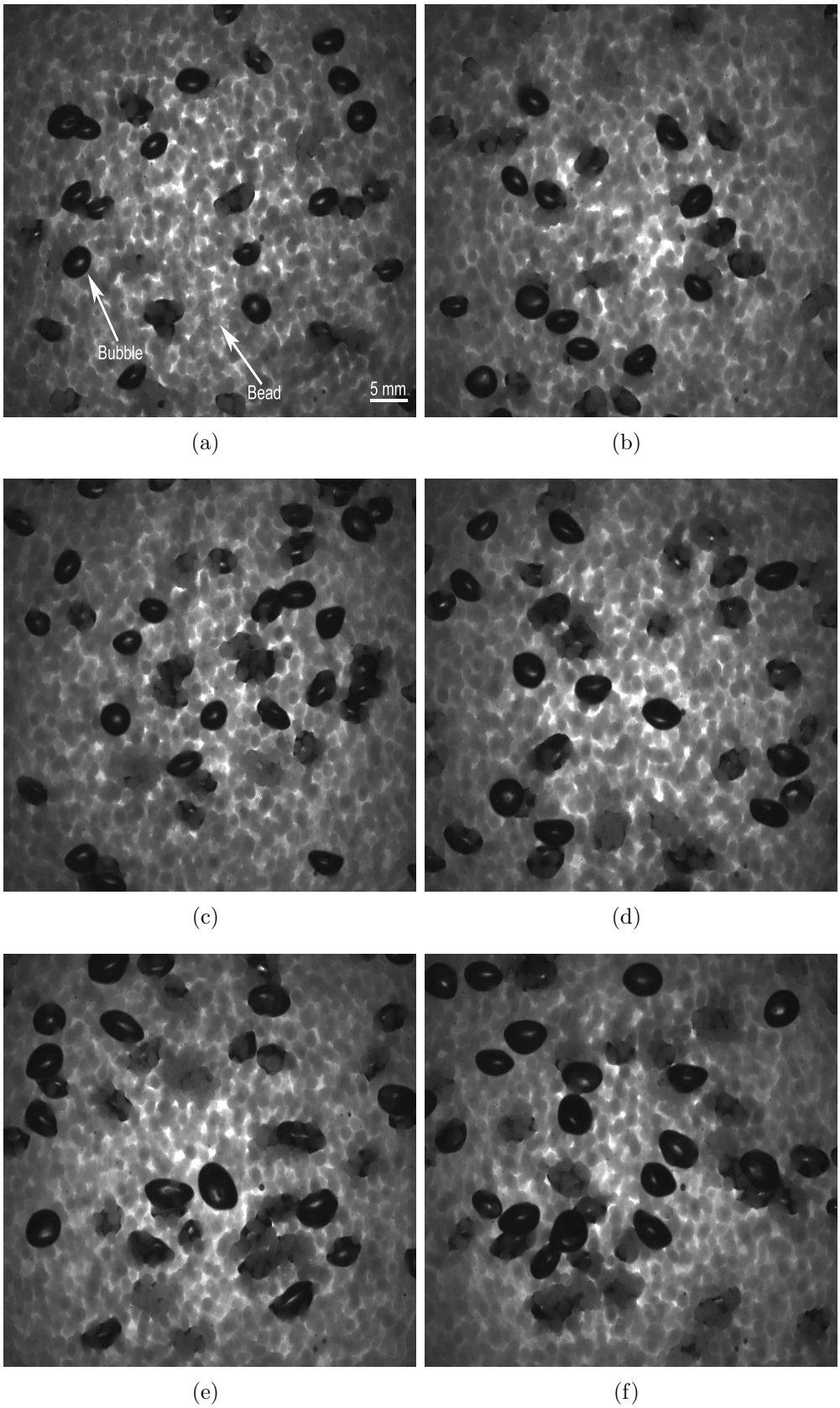

Figure 2.33. Examples of images of air-water-calcium alginate 5 $vol\%$ ($d_{eq} = 1.2\ mm$) system: (a) $u_G = 1.5\ mm/s$ (b) $u_G = 1.7\ mm/s$ (c) $u_G = 2.0\ mm/s$ (d) $u_G = 2.2\ mm/s$ (e) $u_G = 2.5\ mm/s$ (f) $u_G = 2.7\ mm/s$.

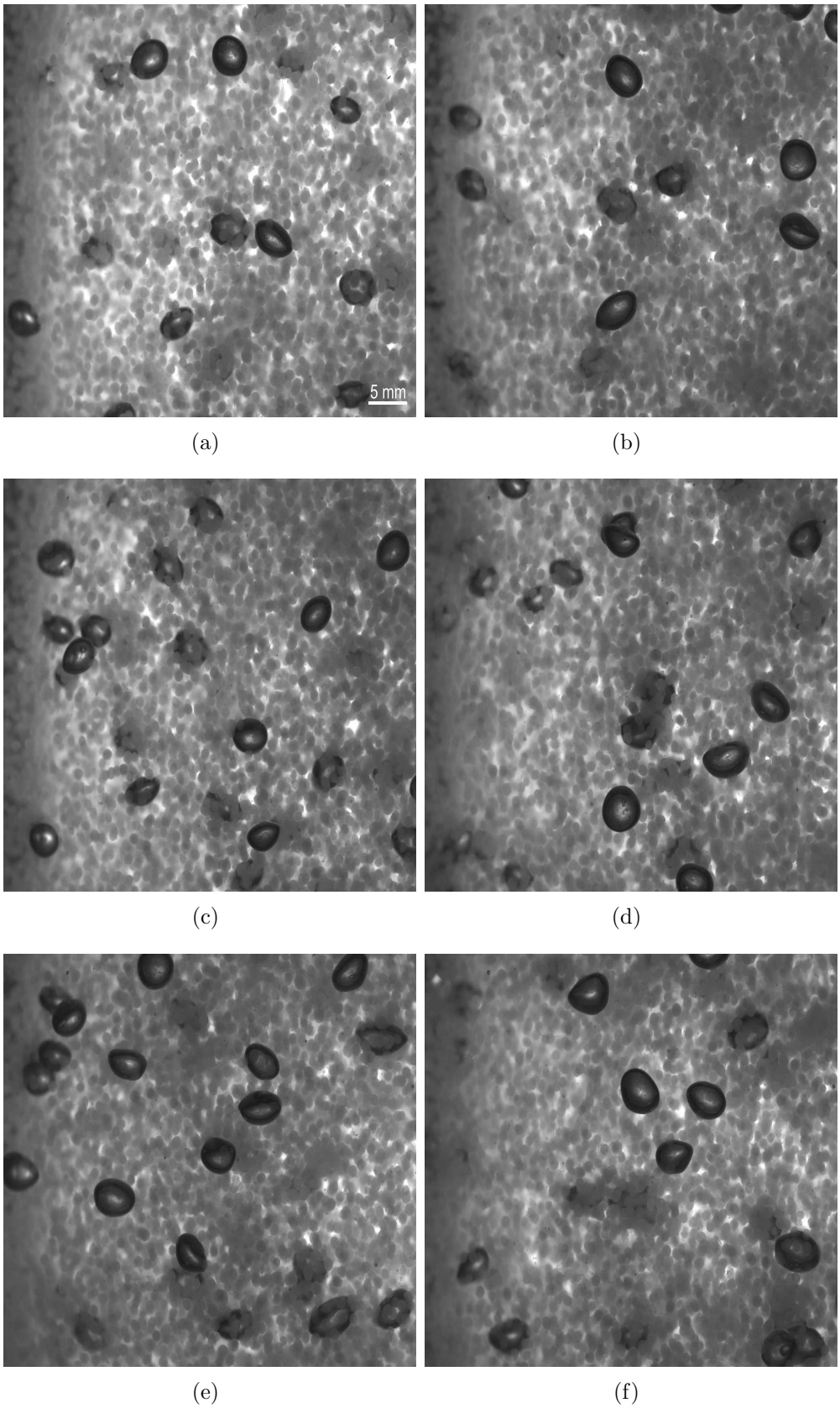

Figure 2.34. Examples of images of air-water-calcium alginate 10 $vol\%$ ($d_{eq} = 1.2\ mm$) system: (a) $u_G = 1.5\ mm/s$ (b) $u_G = 1.7\ mm/s$ (c) $u_G = 2.0\ mm/s$ (d) $u_G = 2.2\ mm/s$ (e) $u_G = 2.5\ mm/s$ (f) $u_G = 2.7\ mm/s$.

in the pure liquid. In this case, however, the concentration of the particles is much smaller (from 0 to 0.25%) and the particles are fibers of varying size, shape and thickness, giving rise to a very different situation from the one presented in this work. Fig. 2.36 shows images of bubbles for different superficial gas velocities and solids loading, for the smaller solid size tested. The images of bubbles presented in Fig. 2.36 support the conclusions referred above.

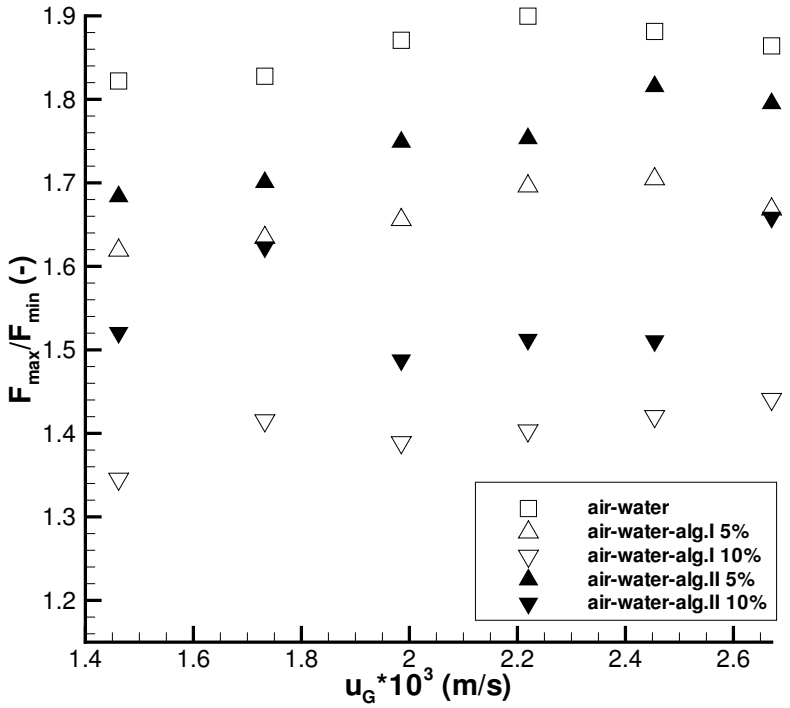

Figure 2.35. F_{max}/F_{min} for the different experimental conditions.

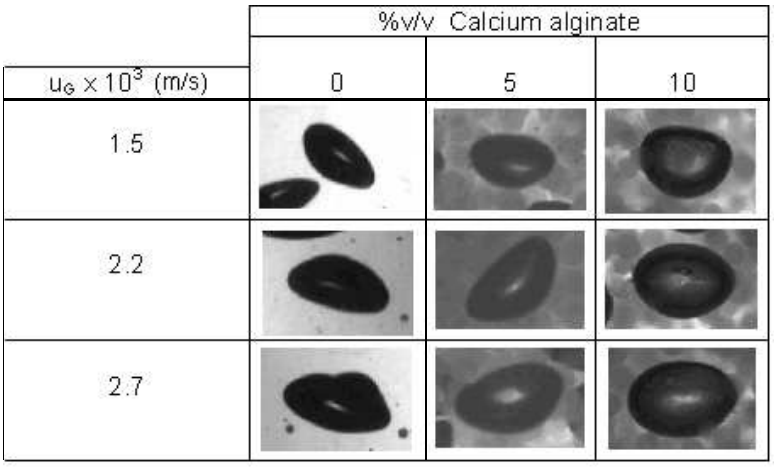

Figure 2.36. Bubble examples for different superficial gas velocities and solid concentrations ($d_p = 1.2\ mm$).

For all runs, several average bubble descriptors were obtained by image analysis, namely the projected area (S) and the Feret diameters (F). The bubbles were classified as elongated or flattened spheroids, and the respective superficial area and volume calculated according to the equations listed in Table 2.3 (Pereira, 1997), where $2r_1$ corresponds to the maximum Feret diameter and $2r_2$ to the minimum Feret diameter.

Table 2.3. Superficial area and volume of elongated and flattened spheroids

Spheroid	Superficial area	Volume
Elongated	$A_{\text{sup}} = 2\pi r_2^2 + 2\pi r_1^2 \sin^{-1}\left(\frac{r_2}{r_1}\right)$	$V = \frac{4}{3}\pi r_1 r_2^2$
Flattened	$A_{\text{sup}} = 2\pi r_1^2 + \pi r_1 r_2 \ln\left(\frac{r_1+r_2}{r_1-r_2}\right)$	$V = \frac{4}{3}\pi r_1^2 r_2$

2.3.8 Gas-liquid interfacial area and gas holdup

The specific interfacial area (or gas-liquid interfacial area), a, is calculated using the following equation:

$$a = \frac{N_b A_{\text{sup}}}{V_L} \tag{2.22}$$

where N_b is the number of bubbles in the column at a certain instant of time, A_{sup} is the mean superficial area of the bubbles and V_L is the liquid volume. The bubbles superficial area and volume are determined by the method described in the previous subsection 2.3.7. The rise velocity of the bubbles is calculated from the expression for the velocity of ellipsoidal bubbles presented in Wesselingh and Bollen (1999) and is used to determine N_b (see Appendix B).

Fig. 2.37 shows the experimental g-l interfacial area for air-water system compared with the correlated values. As expected (Kim and Kim, 1990; Vázquez et al., 2000a; Quicker et al., 1984), interfacial area increases with superficial gas velocity. This happens even as the bubbles become larger, since the number of bubbles formed increases, and in this bubble size range the rise velocity is nearly constant, therefore the total superficial area also increases. Comparing with literature correlations, experimental data shows good agreement with the Quicker et al. (1984) correlation (see eq. 2.23), especially for low superficial gas velocities, with a mean absolute deviation of 7%.

Fig. 2.38 shows the results for the two calcium alginate sizes used. The experimental results are reproducible with an average relative error of 4%. The solids effect is not constant. For the smaller particles one notices a significant decrease of interfacial area at the higher solids loading. This may be due to an increase of bubble coalescence leading to a decrease in the total superficial area (Zahradnik et al., 1992; Kim and Kim, 1990; Patwari et al., 1986). Yagi and Yoshida (1974) reported a similar effect in systems containing dead yeast cells and Yang et al. (2001) suggested that the bubble coalescence rate increase and consequent interfacial area decrease, can be ascribed to the increase of the system apparent viscosity. Both for the larger and smaller particles at reduced concentration, the solid effect is negligible on the occurrence of the bubble coalescence phenomenon. Quicker et al. (1984) proposed the following correlation for g-l interfacial area which takes into account the effective viscosity μ^* of a suspension,

$$a = 651 u_G^{0.87} {\mu^*}^{-0.24}. \tag{2.23}$$

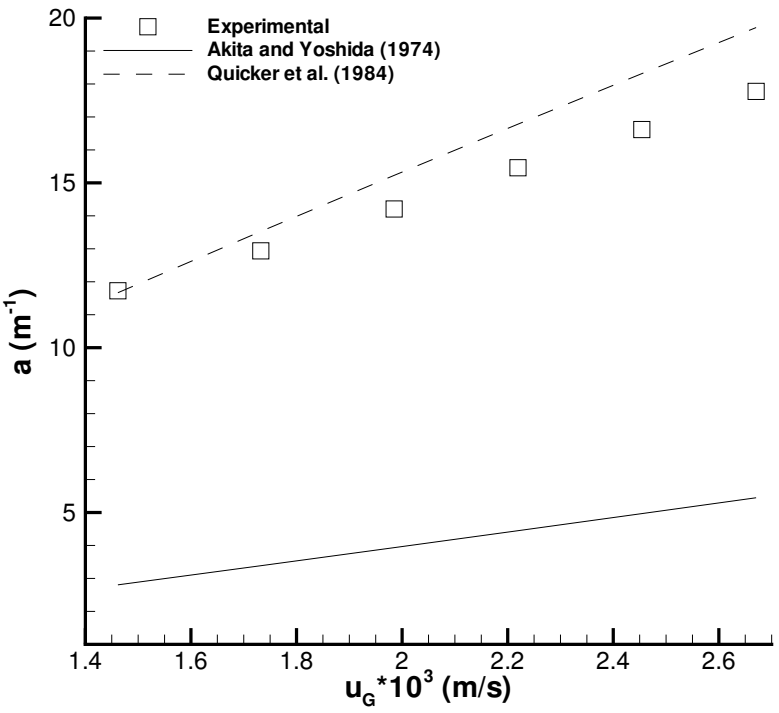

Figure 2.37. Experimental gas-liquid interfacial area and same of the literature correlations for air-water system.

And Einstein (1906) derived an expression which linearly relates the effective viscosity and the particles concentration as follows:

$$\frac{\mu^*}{\mu_f} = 1 + 2.5f \tag{2.24}$$

where μ^* is the effective viscosity of the particle-fluid mixture, μ_f is the viscosity of the fluid and f the volumetric concentration of the particles. For 5% and 10% of calcium alginate beads, the effective viscosity is 0.00113 $Pa.s$ and 0.00125 $Pa.s$, respectively. Good agreement was found between experimental and correlated values, for both concentrations of larger particles and for 5 $vol\%$ of smaller particles, mainly for low superficial gas velocities. However, for 10 $vol\%$ of smaller beads, the experimental and correlated values difference is clear and might be related to the μ^* expression which does not consider the particle size influence.

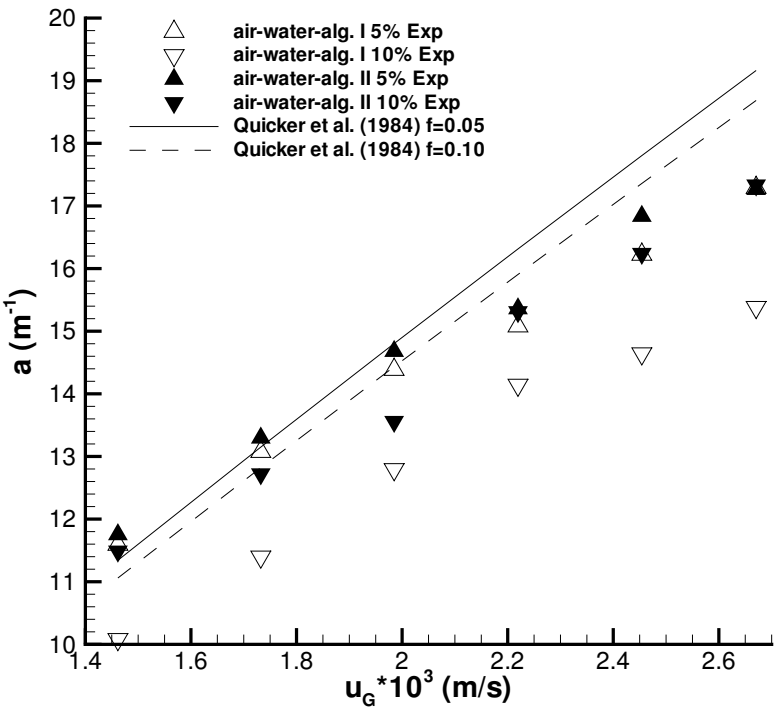

Figure 2.38. Experimental gas-liquid interfacial area and literature correlation for air-water-calcium alginate beads systems (alg.I - $d_p = 1.2\ mm$, alg.II - $d_p = 2.1\ mm$).

The gas holdup (e_G) was not measured experimentally since very low values were expected. However, as the gas-liquid interfacial area and bubble diameter were obtained experimentally for air-water and air-water-calcium alginate systems, the experimental gas holdup could be determined from the relation (Shah et al., 1982),

$$a = \frac{6e_G}{d_b}\ . \tag{2.25}$$

Experimental air-water e_G values were compared with e_G calculated from correlations found in literature (Shah et al., 1982). Some of these correlations are plotted in Fig. 2.39. The gas holdup increases with the superficial gas velocity and the experimental and correlated values are not far. The mean absolute deviation between the experimental and Mersmann (1978) correlation results is 11%. Also in Shah et al. (1982) review one can find a gas holdup correlation for air-water-solids systems. In this correlation (Beovich and

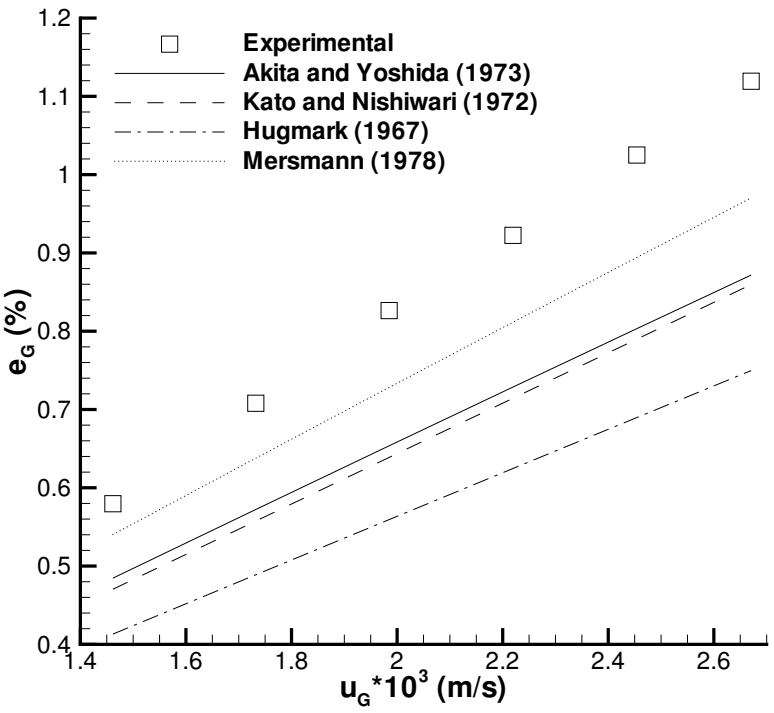

Figure 2.39. Experimental gas holdup and literature correlations for air-water system.

Watson (1978)), e_G is a function of superficial gas velocity, particle diameter and bubble column diameter. In Figs. 2.40 and 2.41, experimental air-water-calcium alginate beads e_G values are plotted together with e_G correlation of Beovich and Watson (1978). Fig. 2.40 indicates the good agreement between experimental and correlated values obtained for air-water-calcium alginate beads ($d_p = 1.2\ mm$) (mean absolute deviation 6%). For air-water-calcium alginate beads ($d_p = 2.1\ mm$), the correlated e_G reasonably agrees with the experimental gas holdup (mean absolute deviation 12%). The experimental e_G for air-water, air-water-calcium alginate beads ($d_p = 1.2\ mm$) and air-water-calcium alginate beads ($d_p = 2.1\ mm$) are comparable. This confirms the visual observation on which no significant changes on the gas holdup were detected.

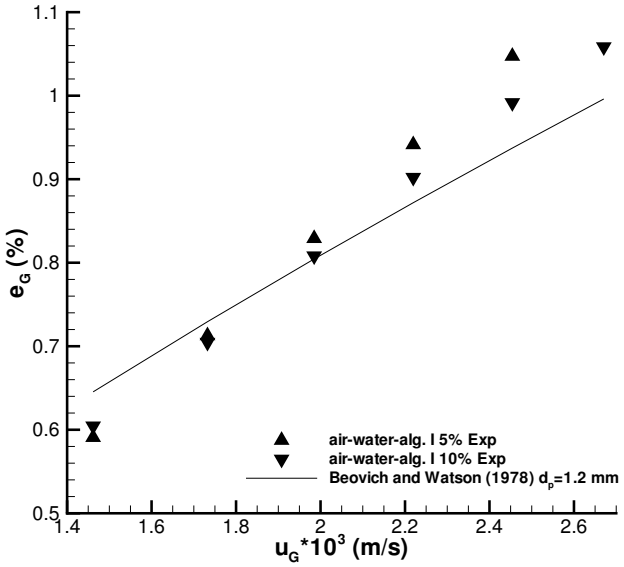

Figure 2.40. Experimental gas holdup and literature correlation for air-water-alg.I system.

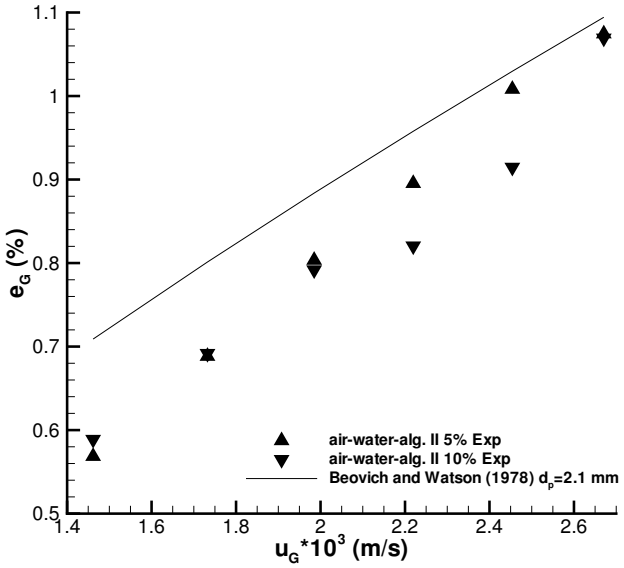

Figure 2.41. Experimental gas holdup and literature correlation for air-water-alg.II system.

2.3.9 Liquid side mass transfer coefficient

The experimental liquid side mass transfer coefficient, k_L, can now be calculated from the values of k_La and a previously determined. The experimental k_L values for air-water system were compared with values determined from the literature correlations but a poor agreement was obtained (Fig. 2.42).

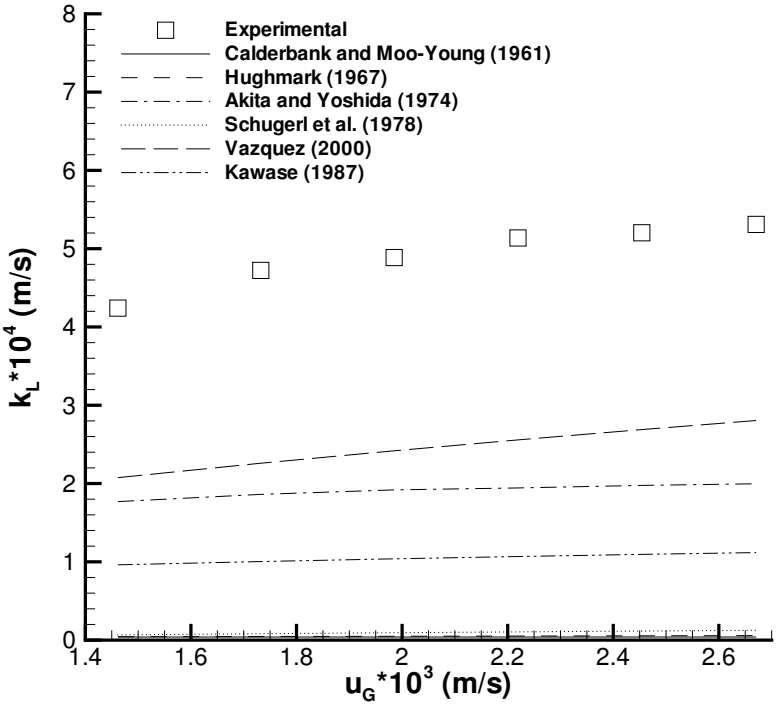

Figure 2.42. Experimental liquid side mass transfer coefficient and literature correlations for air-water system.

The experimental k_L is much higher than the correlated values and the differences in the experimental conditions might explain these significant discrepancies.
Fig. 2.43 presents the results for the two calcium alginate sizes studied here. The k_L values reflect the previously reported values of k_La and a. One notices a conjugate effect of the solid size and concentration on k_L. The more pronounced effect occurs for the smaller particles and at higher concentrations. In this case, the significant k_L decrease can be attributed to the increase of the effective viscosity of the bed with the presence of solids,

since k_L is inversely proportional to viscosity (Yang et al., 2001).

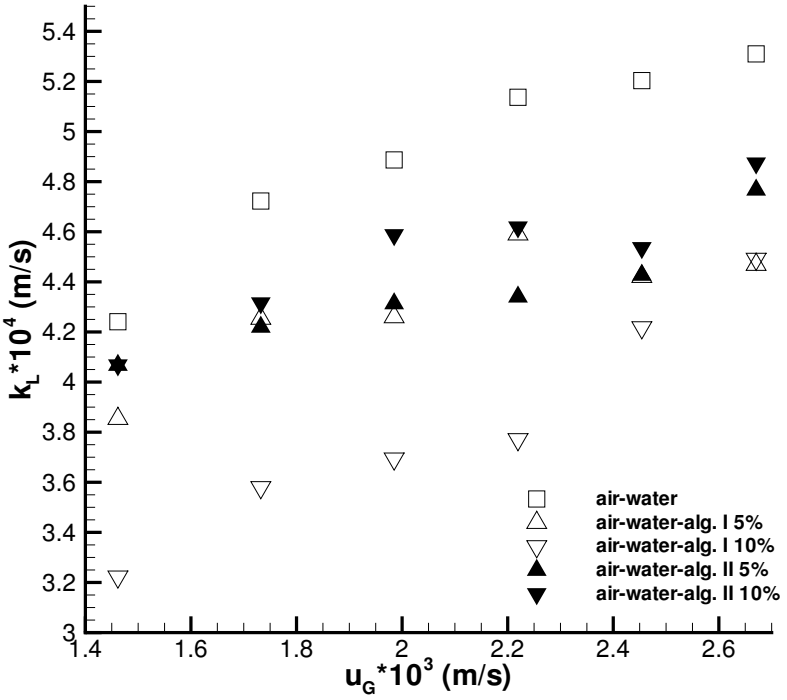

Figure 2.43. Experimental liquid side mass transfer coefficients for air-water and air-water-calcium alginate systems (alg.I - $d_p = 1.2\ mm$, alg.II - $d_p = 2.1\ mm$).

Taking into account the previous analyses, one can examine how a and k_L contribute to the k_La behaviour.

For the smaller particles, the k_La variation is due to the simultaneous variation of a and k_L in the same direction. The presence of solids lowers the interfacial area and the mass transfer coefficient and the effect is more pronounced at the higher solid concentration. For higher superficial gas velocities the solid concentration seems to have a less significant effect. For the larger particles, the k_La variation is essentially due to the k_L variation, which shows a negligible dependence on the solids concentration. The effect of the solids on the interfacial area is negligible, and the effect on the mass transfer coefficient seems to be more pronounced for increasing gas velocities.

2.4 Conclusions

The gas-liquid mass transfer process was investigated in a three-phase bubble column. The main propose was to analyze the effect of certain solid properties on the gas-liquid mass transfer. The solid characteristics under study were the solid type, loading and size. At certain operating conditions, the individualization of the effect of those solid characteristics on the volumetric mass transfer coefficient k_La components, the liquid side mass transfer coefficient k_L and the gas-liquid interfacial area a, was achieved. In order to do that, a bubble column was designed and an adequate experimental facility was built up. The volumetric mass transfer coefficient k_La was determined by the dynamic method and the gas-liquid interfacial area a and other bubble characteristics were determined through an image analysis technique. This technique was found to be suitable and practical especially for air-water and air-water-calcium alginate beads systems under the operating conditions used, since the calculated values of the specific interfacial area are reproducible. However, image analysis revealed limitations for other three-phase systems, mainly at higher solid loadings and superficial gas velocities.

Experimental k_La values for air-water system were compared with correlations from the literature and a very good agreement was found with the Deckwer et al. (1974) correlation. In the experiments with calcium alginate beads as solid phase, the solids present a negative effect on k_La. This effect depends on the solid concentration for the smaller particles, while for the larger particles that is not so evident. The effect of particle size on k_La is significant for the higher solid concentration, but for the smaller solid concentration, particle size has no remarkable effect. The bubble shape is also affected by the presence of the solid phase. The bubbles become more rounded as the solid concentration increases and as the solid size decreases. The effect of the solid phase on k_La was studied separately for its components, a and k_L. The image analysis results show that, for the higher solid concentration and the smaller particle size, the solids decrease the total interfacial area a, while for the other situations no significant effect occurs. This suggests the occurrence of bubble coalescence in the former case. Calculating k_L from the experimental values of a and k_La, one can conclude that k_L increases with the superficial gas velocity and is affected negatively by the presence of solids. The effect of solid concentration is important for the smaller particles.

Finally, one can infer that the k_La variation is due to the simultaneous variations of a and k_L in the same direction for smaller particles, while for the larger particles that

variation is almost only due to the k_L variation. An empirical correlation of the type: $k_La = a_1 u_G^{a_2}(1+d_p)^{a_3}(1-e_S)^{a_4}$ was developed, being the parameters a_1, a_2, a_3 and a_4 dependent on the solid type. For air-water-calcium alginate systems, a good agreement was found between experimental and correlated values.

Two sets of experiments were conducted with polystyrene beads as solid phase, one with "new" polystyrene beads and another with "washed" polystyrene beads. For each set, three solid sizes (P124 $d_p = 1100\ \mu m$; P324 $d_p = 769.8\ \mu m$ and P424 $d_p = 591.2\ \mu m$) were investigated, for solid loadings up to 30 $vol\%$. It was found that the k_La increases with the superficial gas velocity u_G and this dependence generally flattens for increasing solid content. When the solid loading increases, the k_La values decrease. Two empirical correlations of the same type as above were proposed, one for "new" and another for "washed" polystyrene beads, and a good agreement between correlated and experimental data was verified for the "washed" polystyrene beads. Comparing the experimental results of the two sets, one verifies that the k_La values for the systems with "new" polystyrene beads were considerably lower than for systems with "washed" polystyrene beads, attesting the negative effect of fine polystyrene particles on k_La. Comparing the experimental k_La values for the three sizes of "washed polystyrene beads", one concludes that the effect of solid size on k_La is not constant but, in general, k_La decreases as the solid size decreases.

Mass transfer experiments in a three-phase slurry of 9.6 μm hollow glass spheres showed a dual effect of solids loading on k_La. For low solids loading ($\leq\sim 3\ vol\%$) the k_La increases as the solid content increases and then decreases with further solid additions.

Chapter 3

Flow Regime Transition in bubble columns

3.1 Introduction

3.1.1 Flow regimes and regime transition

In the bubble column reactors there are two principal flow regimes (Deckwer, 1992; Kastanek et al., 1993; Molerus, 1993): the homogeneous and the heterogeneous. Depending on the gas distributor, column dimensions and properties of the phases, both regimes can be obtained in the same equipment varying the gas input (Zahradnik et al., 1997).

The **homogeneous regime** (HoR) (also: laminar, dispersed, uniform or bubbly flow regime) is produced by plates with small and closely spaced orifices at low gas flow rates. The bubbles generated at the plate rise undisturbed, almost vertically or with small-scale axial and transverse oscillations. These are small with practically the same size and almost spherical bubbles. Coalescence and bubble break-up are negligible and there is no large-scale liquid circulation in the bed (Ruzicka et al., 2001b; Zahradnik et al., 1997). Thus, liquid velocity (Hills, 1974; Lapin and Lubbert, 1994) and voidage (Kumar et al., 1997) long-time radial profiles are flat (see Fig. 3.1).

The **heterogeneous regime** (HeR) (also: turbulent, circulation, clustered or churn-turbulent regime) is produced by plates with small and closely spaced orifices at high gas

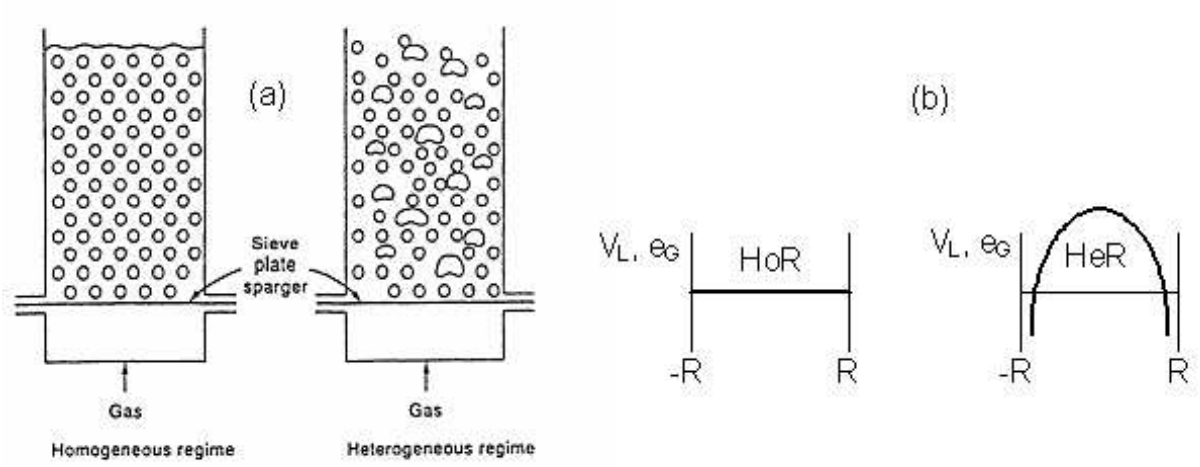

Figure 3.1. (a) Dispersion behaviour in the homogeneous and heterogeneous flow regimes (Zahradnik et al., 1997). (b) Time-averaged radial profiles of liquid velocity and voidage.

flow rates and also by plates with large orifices at any gas flow rate (pure heterogeneous regime). This regime is characterized by a wide bubble size distribution, due to generation of large and highly non-uniform bubbles. Bubble coalescence is promoted and macro-scale circulations of the liquid phase are present (Ruzicka et al., 2001b; Zahradnik et al., 1997). Therefore, long-time radial profiles of liquid velocity (v_L) and voidage (e_G) are no more flat, but roughly parabolic along the column radius (R) with a maximum at the center (Franz et al., 1984) (see Fig. 3.1).

The **homogeneous-heterogeneous regime transition** is a slow process and is indicated by an increasing number of coherent structures (circulations) of increasing size and intensity in the bubble bed. The transition is intermittent (in space and time) and both regimes coexist in the bubble column (Ruzicka et al., 2001b). The transition begins when the HoR loses its stability. The nature of this instability is not fully understood and is intensively studied. The two main regimes can be identified from the character of the experimental voidage-superficial gas velocity graph ($e_G - u_G$). The homogeneous voidage increases progressively with gas velocity (convex graph) while heterogeneous voidage follows a rational function (concave graph) and the transition branch connects the convex and concave graphs (Ruzicka et al., 2001b) (see Fig. 3.2). Regime transition experiments have been performed for a long time, being the voidage and gas flow rate dependence measured (Zahradnik et al., 1997) and correlated (Shah et al., 1982). The regime transition was alre-

ady identified by analyzing pressure signals, liquid velocity signals and using the drift-flux concept. Some models have also been proposed based on the different basis: bubble drag force, gas phase slip velocity, energy balance of the g-l mixture, concept of large and small bubbles and hydrodynamic coupling between gas and liquid phases (Ruzicka et al., 2001b).

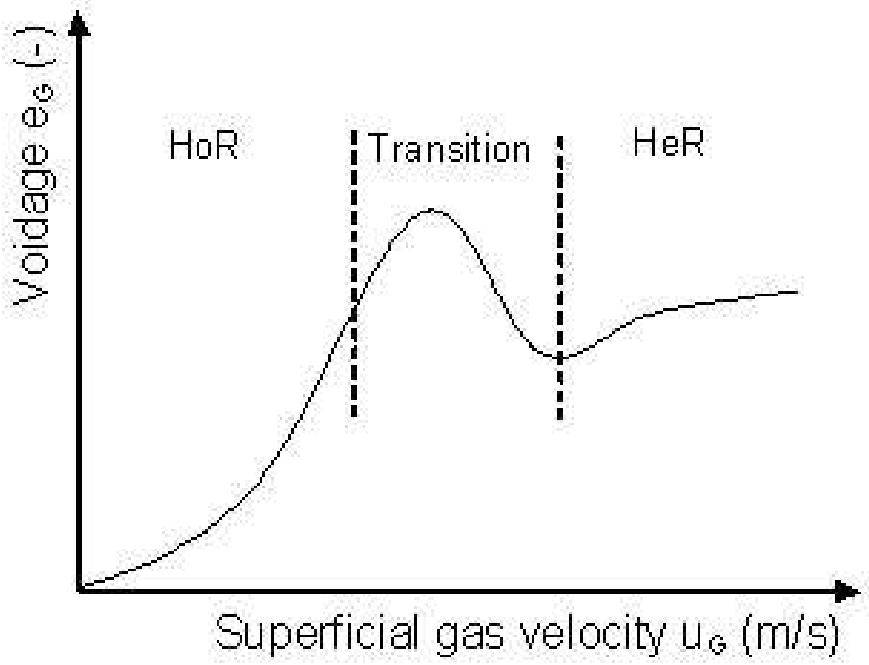

Figure 3.2. Dependence of voidage on superficial gas velocity.

Bubble column reactors have different behaviour in homogeneous and heterogeneous regimes, thus, the dependencies of the rates of mass, heat and momentum transfer on the design and operating parameters (such as reactor geometry, gas and liquid flow rates and proprieties of the contacting phases) are also very different. Therefore, for a rational reactor design and operation it is of crucial importance to know the range of parameters over which a certain regime prevails (Zahradnik et al., 1997). This naturally leads to the stability issue and to the regime transition conditions. In previous studies focused on the regime transition, two stability theories were suggested by Ruzicka and co-workers: one kinematic, based on the concept of the Darwinian drift of bubbles (Ruzicka et al., 2001b), and the second, more elaborated, dynamic, based on the analogy with the Rayleigh-

Benard instability in thermal convection (Ruzicka and Thomas, 2003). The latter yields a stability criterion for the homogeneous regime in terms of the following parameters: column dimensions, effective viscosity of bubbly mixture, hydrodynamic diffusivity of bubbles. The latter two have a clear physical meaning, but their concepts are not yet well developed, especially at intermediate Re. Experiments were also performed to validate particular aspects of the stability criterion, namely, the effect of column dimensions (Ruzicka et al., 2001a) and liquid viscosity (Ruzicka et al., 2003, 2005) and the effect of the presence of the solid phase (Mena et al., 2005c), which is not explicitly involved in the above theories. In spite of all these efforts, many basic questions concerning the effect of important design and operational parameters and system properties on regime stability and on flow regime transition remain unanswered. These knowledge gaps restrict the ability to design and operate gas-liquid and gas-liquid-solid contacting and reacting systems.

3.1.2 Effect of surfactants on regime transition

Surfactants or surface-active compounds are solutes which change the behaviour of the gas-liquid interface in comparison with the pure solvent. Aliphatic alcohols and electrolytes (namely inorganic salts) are important groups of surface-active additives, due to their common industrial application.

In the literature, two different kinds of studies can be found: one about the **effect of surfactants on bubble coalescence** in aqueous media and coalescent viscous solutions (Zahradnik et al., 1995, 1999a,b) and another concerning the **effect of surfactants on gas holdup and HoR stability in bubble columns** (Zahradnik et al., 1995, 1997, 1999b).

Zahradnik et al. (1999a) tested the influence of the presence of alcohols and electrolytes on bubble coalescence. They found that the inhibitory effect of aliphatic alcohols increased with the length of their carbon chain. The effects of the two surfactant groups on bubble coalescence in viscous coalescent media (Newtonian and non-Newtonian) were quite different. Alcohols reduced significantly the coalescence and could totally suppress it. The addition of electrolyte to saccharose solutions had no effect, while electrolyte transition concentration (the concentration corresponding to 50% coalescence) in xanthan solutions was clearly higher than that observed in aqueous solutions. Zahradnik et al. (1999b) focused their attention only on the effect of the addition of alcohols on bubble coalescence

and gas holdup in viscous saccharose solutions. Coalescence results were similar to those presented in Zahradnik et al. (1999a). Bubble column experiments showed a significant increase of gas holdup with the increase of alcohol concentration. The increase in holdup was more pronounced for larger carbon chain alcohols, which is in agreement with the bubble coalescence results. Furthermore, the effect of alcohol addition also increased as the viscosity of the media increased. The surfactant addition foments the radial uniformity of the flow and gas holdup profiles in viscous saccharose solutions and compensates the negative liquid viscosity effect on the formation and stability of the HoR in bubble columns. A study of the effect of electrolytes on bubble coalescence and gas holdup is presented in Zahradnik et al. (1995). They reported that it is possible to link bubble coalescence experiments with the gas holdup experiments. Therefore, only with the former it should be possible to predict the behaviour of a gas-liquid system in a bubble column, concerning for instance the effect of an electrolyte on gas holdup. Gas holdup experiments have shown that the $e_G(u_G)$ dependence does not depend on the electrolyte type. Moreover, in HeR the influence of the electrolyte concentration is small, due to strong turbulence predominance, while in HoR and transition regime the shape of $e_G(u_G)$ curve is very sensitive to the electrolyte content and presents a maximum considerably higher than the gas holdup values for air-water system. A similar result can be found in Zahradnik et al. (1997). Also, in that study is reported that the stability of the HoR is significantly enhanced by the presence of surfactants and it is observed an increase in the difference between the $e_G(u_G)$ in HoR and in HeR.

Krishna et al. (1999) studied the influence of surface tension reducing agents (surfactants) on flow regime transition. Firstly, they observed that the gas holdup increased considerably with small increases of ethanol concentration. Furthermore, increasing the ethanol concentration, the gas holdup at regime transition increases, representing a delay of the regime transition. Finally, they suggested that the surface effects strongly influence the bubble coalescence phenomena.

Summarizing, the effect of surfactants on bubble coalescence and gas holdup have been investigated in the past (Zahradnik et al., 1995, 1997, 1999a,b). However, the information on the influence of surfactants on $HoR - HeR$ flow regime transition is still far from being satisfactory (Krishna et al., 1999). Indeed, a quantitative and detailed study on the influence of surfactant properties (type, concentration) on parameters which define the

regime transition, such as e_{G_C} and u_{G_C}, is clearly needed.

3.1.3 Effect of viscosity on regime transition

There are many works in the literature about the effect of the liquid viscosity on the gas holdup in the **heterogeneous flow regime (HeR)**. Usually, it is reported that the gas holdup decreases with increasing liquid viscosity, which is normally ascribed to the presence of large population of big and fast bubbles with short retention time (Deckwer, 1992; Kastanek et al., 1993; Zahradnik et al., 1997). The viscous media not only induce the formation of big bubbles at the gas distributor (Deckwer, 1992; Kastanek et al., 1993; Kuncova and Zahradnik, 1995), but also promote bubble coalescence (Shah et al., 1982; Kastanek et al., 1993; Kuncova and Zahradnik, 1995; Zahradnik et al., 1997) and suppress bubble breakup (Shah et al., 1982). The decrease of gas holdup is described by various correlations containing the viscosity effect. They are generally of the form $e_G \sim \mu^n$ and different values of n can be found: -0.053 and -0.16 (Kastanek et al., 1993) and -0.05 (Deckwer, 1992). There are also studies reporting controversial effects of the viscosity (Deckwer, 1992; Kastanek et al., 1993) and both increase and decrease of the gas holdup have been observed. Kuncova and Zahradnik (1995) measured the gas holdup under heterogeneous conditions and found a maximum at $\mu \simeq 3\ mPa.s$, followed by a sustained decrease in voidage with increasing viscosity up to $\mu \simeq 30\ mPa.s$. Highly viscous beds have been also investigated and for $\mu > 30\ mPa.s$, the formation and accumulation of the small bubbles is considerable and results in further increase of the total gas holdup with increasing viscosity (Kawalec-Pietrenko, 1992). Summarizing, the viscosity effect on the heterogeneous gas holdup can be roughly described as follows: the gas holdup increases for $\mu < 3\ mPa.s$, decreases for $3 < \mu < 30\ mPa.s$, and then increases for $\mu > 30\ mPa.s$. This suggests that the viscosity plays a dual role. At low viscosity, the larger drag forces reduce the bubble rise speed and increase the gas holdup. Nevertheless, these forces are not strong enough to promote the bubble coalescence. At higher viscosity, the coalescence and polydispersity prevails over the drag reduction and the uniformity is broken by big bubbles. The small bubbles formation is responsible for the increase of gas holdup with viscosity for highly viscous beds.

Results about the effect of the liquid viscosity on the **homogeneous flow regime**

(HoR) and its stability are not abundant in the literature. Usually, an adverse effect is expected as a result of deterioration of the uniformity by the strong variation in bubble sizes caused mainly by the coalescence (Deckwer, 1992; Kastanek et al., 1993). Experience with bubble columns points out that the HoR is much more sensitive to the phases properties than the HeR (Kastanek et al., 1993). Available experimental results show that the homogeneous gas holdup decreases with increasing viscosity. Moreover, it was also observed that in sufficiently viscous liquids (roughly at $\mu > 8\ mPa.s$), the HoR can be totally suppressed and the HeR occurs even with 'homogeneous plates' (fine and closely spaced orifices) at low gas flow rates. Therefore, the flow regime in viscous batches is virtually independent of the geometry of the gas distributor, which might be important for the design of real equipment. The gas holdup decrease with increasing viscosity suggests that the stability of the HoR is reduced (Kuncova and Zahradnik, 1995; Zahradnik et al., 1997). However, this is just a conjecture that has to be proved experimentally. A parameter which directly relates the stability with viscosity must be experimentally measured. This parameter can be the critical gas holdup or the critical gas flow rate. Furthermore, there also are two theoretical studies refering to the HoR stability: one developed by Shnip et al. (1992) and another by Ruzicka and Thomas (2003). In the former study, the viscosity disappears along the derivations and does not enter in the stability criterion. In the latter study, Ruzicka and Thomas (2003) developed a stability concept for uniform dispersed layers. The Rayleigh number was introduced for bubbly layers and gives a stability criterion in terms of the critical gas holdup. This criterion predicts a stabilizing effect of viscosity on the HoR, with a linear increase of the critical gas holdup with viscosity ($e_{G_C} \sim \mu$), which contradicts the general expectation.

3.1.4 Effect of solids on regime transition

Numerous research groups dealing with bubble columns (Kantarci et al., 2005), airlift reactors (Freitas and Teixeira, 2001), bubbly flows (Douek et al., 1997), flotation columns (Ityokumbul et al., 1995), pulp slurry columns (Xie et al., 2003) and fluidized beds (De Lasa et al., 1984; Thompson and Worden, 1997) are interested in the complex three-phase system. Since they operate the equipments under different conditions, the results are not always comparable. One obvious difference is the liquid throughput, which is typically zero in bubble columns, often nonzero in flotation and always nonzero in fluidized beds

and bubbly flows. Another difference is in the solid particles, regarding their size, shape, material and surface properties. Big wettable beads are likely to produce different effects from those produced by fine hydrophobic particles of a catalyst, or by flexible and sticky fibres in pulp suspensions in paper industry. Despite the intense research, the knowledge about the possible effects of solids on gas-liquid systems is far from being satisfactory. Even less understood are the physical mechanisms underlying their known macroscopic effects. Often, the results are ambiguous or even contradictory, partly because they are compared under aforementioned different operating conditions, partly due to the complex nature of the solid influence, where many aspects have to be taken into account.

The presence of solids affects the gas-liquid mixture in many different ways: bubble formation (Yoo et al., 1997; Luo et al., 1998; Fan et al., 1999), bubble rise (Luo et al., 1997a; Fan et al., 1999), axial (Gandhi et al., 1999) and radial (Warsito et al., 1997; Warsito and Fan, 2001) profiles, mixing and dispersion, mass transfer (Quicker et al., 1984; Sada et al., 1985; Joly-Vuillemin et al., 1996; Mena et al., 2005a), and gas holdup and flow regimes (Zhang et al., 1997; Mena et al., 2005c). Unfortunately, it seems that there is no authoritative review available, covering in detail this broad area, where the reader could be referred to. However, some particular aspects have been reviewed (Fan et al., 1999). References having a relevance for the present study, the effect of solids on voidage and flow regimes in bubble columns, are given.

Most of the published works report that the gas holdup generally decreases with increasing solid concentration (Banisi et al., 1995a,b; Reese et al., 1996; De Swart et al., 1996; Jianping and Shonglin, 1998; Fan et al., 1999; Krishna et al., 1999; Zon et al., 2002). Equivalently, the mean bubble speed must increase with solids. This is usually attributed to an increase in bubble coalescence caused by the solids, which results in bigger and faster bubbles (Jianping and Shonglin, 1998; Krishna et al., 1999; Zon et al., 2002). An apparent shift in the bubble population from small to large bubbles is documented (De Swart et al., 1996). Furthermore, a reduction of bubble breakup (Gandhi et al., 1999) and an increase of mixture viscosity (Luo et al., 1997a; Tsuchiya et al., 1997; Jianping and Shonglin, 1998; Fan et al., 1999) are suggested as alternative probable reasons. Another possibility can be the reduction of the space available for the g-l mixture in presence of solids. Effects of hydrodynamic interactions between bubbles and solids are considered too. The relative importance of several possible mechanisms (coalescence, mixture density and viscosity, radial

profiles, wake effects) causing the decrease of gas holdup in a particular flotation system has been evaluated (Banisi et al., 1995b).

On the other hand, an interesting dual effect of solids on gas holdup has also been observed (Sada et al., 1986a,b; Garcia-Ochoa et al., 1997; Xie et al., 2003; Banisi et al., 1995a), indicating the presence of two counteracting physical mechanisms. With fine 7 μm wettable solids, Sada et al. (1986a) found a maximum in the (gas holdup)-(solid content) dependence at about $C_S \approx 5\%$, where the unexpected increase is explained by the suppression of coalescence due to the presence of solids in the liquid film between bubbles. A similar result is found also in their sequel paper (Sada et al., 1986b). Zon et al. (2002) confirmed that the hydrophobic particles reduce the gas holdup and Banisi et al. (1995a) found no apparent difference between hydrophilic and hydrophobic particles. The dual effect was observed also for pulp slurry (Xie et al., 2003). Occasionally, under certain conditions, a negligible effect of solids on voidage is also reported (Ityokumbul et al., 1995).

The effect of the particle size on gas holdup was also investigated in the past. Usually, a decrease of e_G is reported but sometimes, an increase is also detected (Banisi et al., 1995a). A negligible effect can be found too (Fan et al., 1999). Garcia-Ochoa et al. (1997) working with glass beads observed, first, a slight increase and then a decrease of the gas holdup with increasing particle diameter, $e_{G,85\mu m} > e_{G,38\mu m} > e_{G,air-H_2O} > e_{G,160\mu m}$. Also, experiments with pyrite particles suggest that the presence of very fine particles (≈ 1 μm) may increase the gas holdup due to rigidification of bubbles, hindering bubble coalescence. Regarding the complicated relations between holdup, solids size and content, i.e. the character of the function $e_G = e_G(d_p, C_S)$, Banisi et al. (1995a) suggest a consensus: small amounts of fine particles (suppressing coalescence) and large amounts of big particles (break up of large bubbles) tend to increase the gas holdup (reduce mean bubble speed). Otherwise a decrease of e_G can be expected (e.g. big amounts of small particles, medium particles at moderate content, small amounts of big particles).

In spite of all the efforts aimed at the gas holdup studies, the information about the effect of solids on the flow regimes is very scarce. Often, no attempt is made to specify the prevailing flow regime during the experiment. Sometimes, the type of the regime is assessed. For instance, Reese et al. (1996) find advanced transition for pulp slurry.

There are also few studies where the transition point is determined. Krishna et al. (1999) used the homogeneous drift-flux model for the critical point (beginning of the transition) and demonstrated, by two experimental points, that the presence of 14% of fine silica ($d_p = 40\ \mu m$) in ethanol dramatically reduces the critical values of gas flow rate and gas holdup, hence destabilizing the uniform regime. It follows that the knowledge regarding the flow regimes and their transitions in three-phase systems is indeed far from satisfactory. It lacks both data and its interpretation in terms of the underlying physical processes. The propose of this study is to contribute to this subject and examine the effect of solid particles on homogenous regime stability. In order to do that, two kinds of experiments are done: the basic regime transition study (macro-scale) and an auxiliary visualization study (micro-scale). The results show that the homogeneous regime is stabilized by low solid load, but destabilized by high solid load.

3.2 Experiments and data treatment

3.2.1 Experimental technique and errors

The measurements were performed in a cylindrical plexiglas bubble column of 0.14 m diameter (Fig. 3.3). The column was equipped with a 3 mm brass perforated plate with 0.5 mm orifices, 10 mm pitch, and relative free area 0.2%. This plate ensures the generation of the homogeneous, transition and heterogeneous bubbling regimes. Such a plate is a typical gas distributor for production of the uniform bubbly layers for stability studies. The typical bubble size in the HoR was $4 - 5\ mm$, with the following features: terminal speed $U_0 \approx 0.2\ m/s$, $Re \approx 10^3$, $We \approx 2.7$, $Eo \approx 3.4$, $Mo \approx 2.6 \times 10^{-11}$. The dimensionless numbers were determined using the following physico-chemical properties values: $\rho_L \approx 1000\ kg/m^3; \rho_G \approx 1\ kg/m^3; \mu_L \approx 0.001\ Ns/m^2; \sigma_L \approx 0.073\ N/m$ and $g \approx 9.8\ m/s^2$. Compressed filtered air from laboratory lines was the gas phase in all experiments.

In the study of the **influence of surfactants on the regime transition**, the liquid phases were aqueous solutions of $CaCl_2$ (prepared with distilled water) with concentrations between 0 and 0.1 mol/l. The $CaCl_2$ concentrations values are presented in Table 3.1.

In the study of the **influence of viscosity on the regime transition**, the liquid

phases were aqueous solutions of glycerol (prepared with distilled water) with viscosity between 1 and 5 $mPa.s$. Preliminary experiments were performed with the eight following values of viscosity, corresponding solution A to distilled water (see Table 3.2).

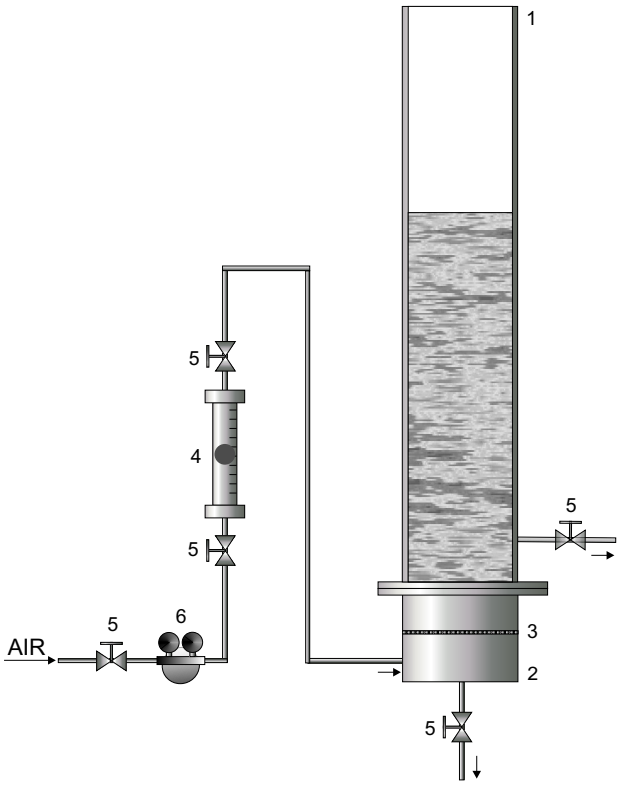

Figure 3.3. Scheme of the experimental set-up (1: Bubble column, 2: Gas chamber, 3: Perforated plate, 4: Rotameters, 5: On/Off valves, 6: Pressure reducer).

More detailed experiments on the effect of viscosity on regime transition were then conducted also with glycerol solutions for the viscosity range $0.946 - 5.480\ mPa.s$. Several glycerol solutions were tested and their viscosities were experimentally determined with a capillary viscometer (see Table 3.3). Glycerol was chosen as the viscosity providing agent, since it has a simple Newtonian rheology and, as a non-polar solute, has negligible surface activity (Zahradnik et al., 1997).

In the study of the **influence of solids on the regime transition**, distilled water was the liquid phase. Calcium alginate beads, roughly spherical particles, with equivalent diameter $d_p = 2.1\ mm$ and density $\rho_p = 1023\ kg/m^3$ were the solid phase (see subsection

Table 3.1. Aqueous $CaCl_2$ solutions

Solution	$CaCl_2$ **(mol/l)**
DW (Dist. Water)	0
TW (Tap Water)	0.00126
A	0.0052
B	0.0102
C	0.0207
D	0.0315
E	0.0415
F	0.0513
G	0.062
H	0.072
J	0.08
K	0.09
I	0.103

Table 3.2. Aqueous glycerol solutions

Solution	A	B	C	D	E	F	G	H
μ **(mPa.s)**	1	1.53	2.05	2.52	3.04	3.48	3.96	5.02

2.2.3). The choice of the phases corresponds to our interest in three-phase airlift reactors with immobilized biomass. The solids are well-defined completely wettable objects with reasonable rigidity. Furthermore, they do not form agglomerates and are big enough not to affect the surface properties of the gas-liquid interface. The following nine values of solid loading were used: 0 (water), 1, 3, 5, 10, 15, 20, 25 and 30 $vol\%$.

The clear liquid height was $h_0 = 0.4\ m$ for all experiments (no liquid throughput). The dependence of the voidage e_G on the gas flow rate Q_G was measured three times and then averaged. The superficial gas velocity varied in the range $u_G = 0 - 0.1\ m/s$, which covers the HoR and part of the transition regime. The gas flow rate was read from a rotameter. For the more detailed experiments (of viscosity and solids effect), the 37 measuring points covered densely the range from $u_G = 0.0144$ to $0.0722\ m/s$, where the transition points were located, with the step of $1.8\ mm/s$. The gas holdup was determined from the bed expansion. The estimated error of the voidage results is less than 5%. The claimed 5% is the upper limit for voidage error in the range measured (HoR + part of transitional

Table 3.3. Viscosities of the aqueous glycerol solutions

% Gly	μ**(mPa.s)**	**% Gly**	μ**(mPa.s)**
0	0,957	6	1,091
0,2	0,946	10	1,216
0,4	0,949	15	1,402
0,6	0,957	20	1,634
0,8	0,955	25	1,958
1	0,960	30	2,263
1,5	0,972	35	2,739
2	0,985	40	3,329
2,5	0,995	45	4,224
3	1,017	50	5,480
4	1,041		

regime). When the layer is uniform, the surface is stable and horizontal, and the interface can be located with precision of 1 mm (resolution of the ruler). For layers with $h \approx$ 40-55 cm (voidage 0-30%) this gives an error 0.25-0.18% in h for the homogeneous range up to the critical point, which causes a comparable error in measuring e_G, since e_G is a function of h. Going further into the transition regime, the surface starts to wave and the uncertainty increases. The surface position was determined as the mean value over certain number of periods of the oscillations, providing enough data to obtain the deviation within the claimed 5% range. These data, however, are well beyond the transition point and are shown only for depicting the trend of the $e_G - u_G$ dependence for larger u_G. One assumes that the reading of the gas flow rate from the rotameter was precise. As for the critical values, the simultaneous application of several methods gives the uncertainty in its determination within one experimental data point. So the error in u_{G_C} is the discrete step size in u_G, i.e., 0.0018 m/s, which amounts to 2.5 - 6.7% with the typical values of u_{G_C} being 0.027 - 0.072 m/s (viscosity study - Fig. 3.23(b)). Since the data points were connected with a continuous line, the actual precision in the determination of u_{G_C} is much higher and these 6.7% represent the upper limit. The error in e_{G_C} comprises the error on the measurement of e_G and the error on the determination of the transition point on the e_G-coordinate. The error on the measurement of e_G is the above mentioned value, less than 1%. The error on the determination of the transition point relates to the difference between the neighbouring data points. Considering the 6% glycerol experiment, which

represents the larger e_G increase, the e_G changes from 0 to 0.62 within 37 measuring points (Fig. 3.16). So, the mean step in e_G is 0.017, which amounts to 3% with the value of e_{G_C} being 0.53 (Fig. 3.23(a)). Since the data points were connected with a continuous line, the actual precision in the determination of e_{G_C} is much higher and the 3% represents the upper limit.

3.2.2 Evaluation of the critical point

For each experiment, the dependence $e_G = e_G(u_G)$ was the primary data. The critical point could be found as the inflexion point of the data graph, but its direct determination by this method is difficult and inaccurate. Therefore, the data evaluation was based on the drift flux model by Wallis (1969), which is based on the concept of bubble slip speed (U). The following example for aqueous glycerol solution of 2% exposes the data evaluation process.

The layer height (h) was experimentally measured and plotted against the superficial gas velocity (u_G) (Fig. 3.4).

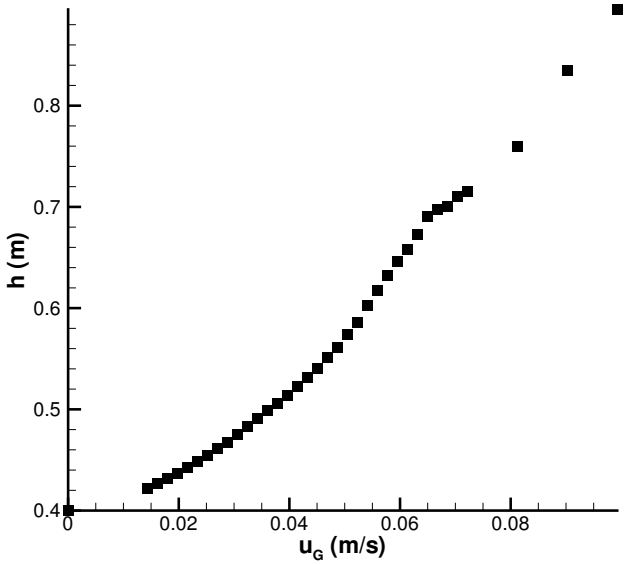

Figure 3.4. Layer height as a function of superficial gas velocity.

The gas holdup was determined by the relation,

$$e_G = \frac{h - h_0}{h} \tag{3.1}$$

and plotted against the superficial gas velocity u_G (Fig. 3.5). The experimental bubble

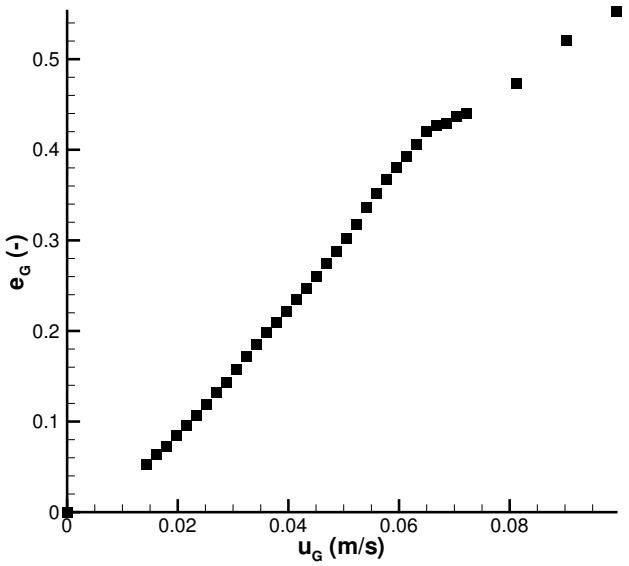

Figure 3.5. Dependence of gas holdup on superficial gas velocity.

slip speed was obtained by the relation that expresses the mass conservation of gas phase

$$e_G = \frac{u_G}{U} \tag{3.2}$$

and it was plotted against the superficial gas velocity $u_G(m/s)$ (Fig. 3.6).
The theoretical bubble slip speed U_{theo} was calculated by the formula derived for the homogeneous regime (Ruzicka et al., 2001b),

$$U_{theo} = U_0 \left(1 - \frac{a' \cdot e_G}{1 - e_G}\right) \tag{3.3}$$

The values of the bubble terminal velocity U_0 and the bubble drift coefficient a' can be extracted from the experimental data $e_G(u_G)$ by putting equation 3.2 into equation 3.3

and linearizing equation 3.3:

$$\frac{u_G}{e_G} = U_0 - (a' \cdot U_0) \cdot \frac{e_G}{1 - e_G} \tag{3.4}$$

From the $U = U(u_G)$ graph it is possible to define the linear region where the homogeneous regime prevails (see white marks from Fig. 3.6) and considering only this region, the values of U_0 and a' can be obtained by plotting Eq. 3.4 (Fig. 3.7). The theoretical slip speed

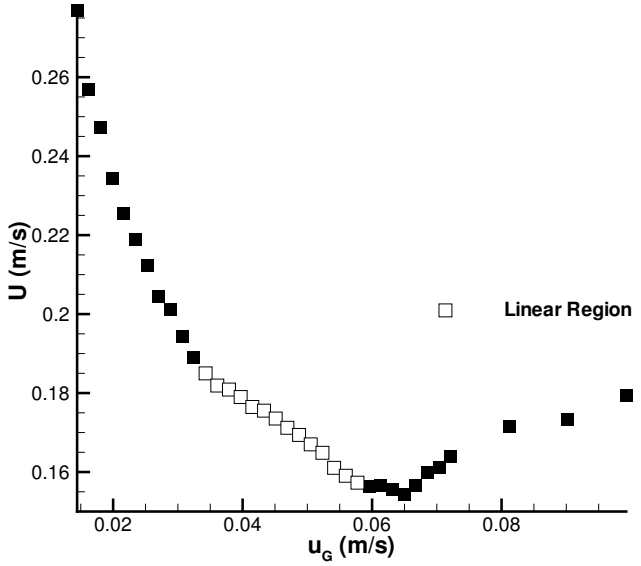

Figure 3.6. Slip speed graph.

U_{theo} can now be determined by Eq. 3.3 and the theoretical drift flux j_{theo} can be obtained by the following expression (Wallis, 1969):

$$j_{theo} = e_G \cdot (1 - e_G) \cdot U_{theo} \tag{3.5}$$

The experimental drift flux j_{exp} is calculated from the experimental data, substituting Eq. 3.2 in Eq. 3.5,

$$j_{exp} = (1 - e_G) \cdot u_G \tag{3.6}$$

In order to obtain the critical point (U_{G_C}, e_{G_C}) where the homogeneous regime loses stability and the transition begins, it was used the drift flux plot, on which the experimental

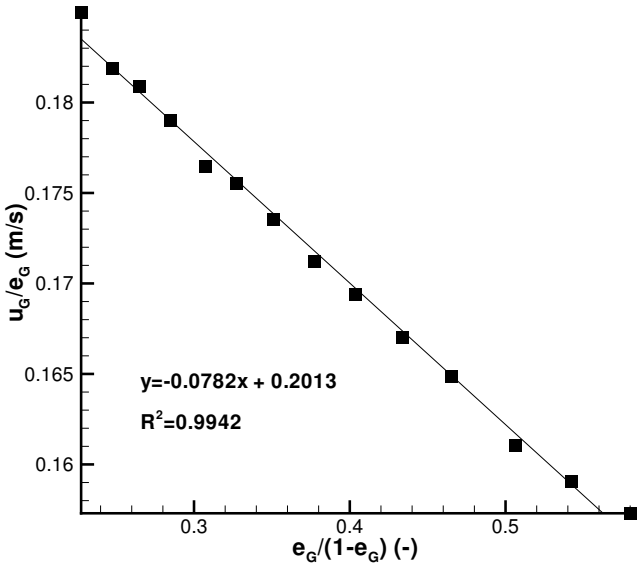

Figure 3.7. Determination of the bubble terminal velocity U_0 and the bubble drift coefficient a'.

and theoretical drift flux are plotted against the gas holdup (Fig. 3.8). The critical value is the point where the experimental data j_{exp} separate from the theoretical curve j_{theo} for the HoR. From the analysis of the graph of Fig. 3.8 and of the three following graphs (Figs. 3.9,3.10,3.11) the critical values could be obtained more accurately.

In this example $e_{G_C} = 0.37$ and $u_{G_C} = 0.058\ m/s$. This procedure was followed for all experiments. The values of the critical superficial gas velocity (u_G) and critical voidage (e_{G_C}) were taken as the quantitative measures of the homogeneous regime stability.

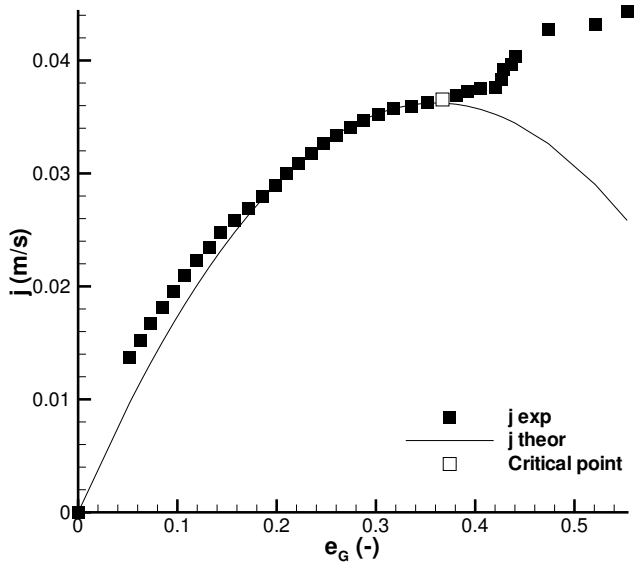

Figure 3.8. Drift flux plot (j versus e_G).

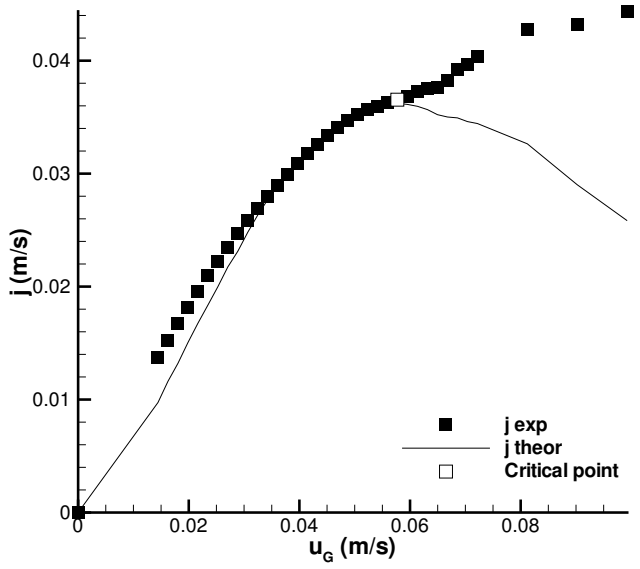

Figure 3.9. Drift flux plot (j versus u_G).

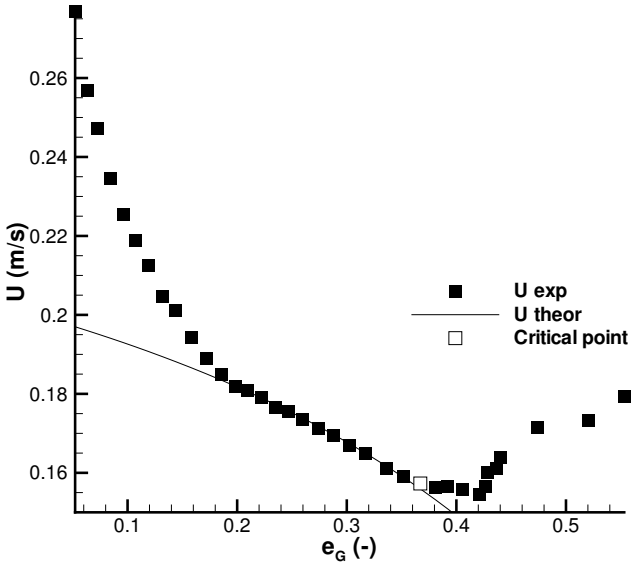

Figure 3.10. Slip velocity graph (U versus e_G).

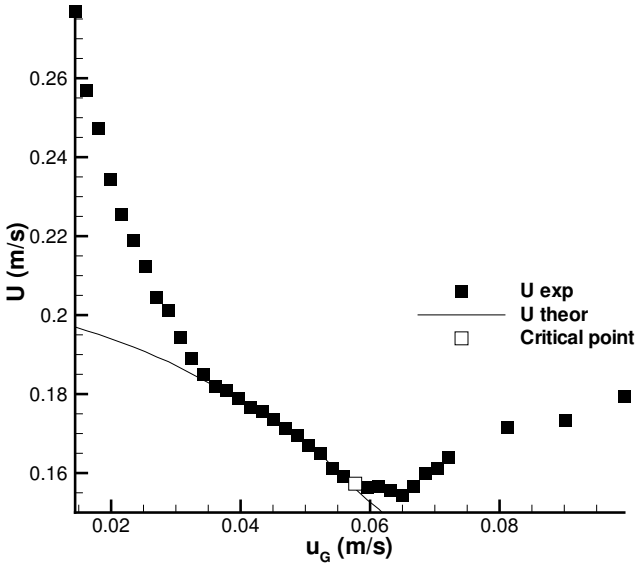

Figure 3.11. Slip velocity graph (U versus u_G).

3.2.3 Criteria for transition

There are not many stability criteria available for the HoR in gas-liquid systems. Even less is known about the criteria for gas-liquid-solid systems. Those criteria we are aware of are discussed below:

(i) The simplest and sometimes most effective is the **rule of thumb**, which states that the transition in water-air system under normal conditions begins somewhere around 0.03 m/s and is completed around 0.1 m/s. Thus, the u_{G_C} is expected to be within this interval, but depends on its definition: some authors take the critical point at the maximum of the $e_G(u_G)$ graph, others at the beginning or the end of the transition. We prefer to take the critical point at the beginning of the transition range where the instability starts (see Fig. 3.2). For instance, in Krishna's simple and flexible model designed mostly for practical purposes, it is estimated $u_{G_C} \approx 0.09\ m/s$ (Krishna et al., 1991). Empirical criteria of this kind usually come from long-term experience and are reliable, but not very precise.

(ii) Other kind of criteria are **empirical or semiempirical correlations** for the criticals. They are based on experimental data, thus should be both reliable and precise. Their basic weakness is that they lack the universal character. They usually refer to the particular situations under which the data were collected, and reflect particular effects of certain parameters only. Unfortunately, there are not many of them available. One such criteria was given by Wilkinson et al. (1992), who suggested the following correlation for the critical voidage,

$$e_{G_C} = 0.5 \exp\left(-193 \rho_G^{-0.61} \mu^{0.5} \sigma^{0.11}\right), \tag{3.7}$$

based on data collected from the literature as well as from their own experiments. The critical superficial gas velocity u_{G_c} is given by e_{G_C}/u_s, where u_s is the speed of so-called small bubbles that are responsible for the prevailing part of the uniform voidage,

$$u_s = 2.25 \left(\frac{\sigma}{\mu}\right) \left(\frac{\sigma^3 \rho_L}{g\mu^4}\right)^{-0.273} \left(\frac{\rho_G}{\rho_L}\right)^{0.03}, \tag{3.8}$$

where, ρ_G is the gas density, μ the liquid viscosity, σ the surface tension, ρ_L the liquid density, and g the gravity. Another example is the criterion due to Reilly et al. (1994), coming from an assumption of a specific form of the relation between the gas momentum

flux and the voidage. This criterium is based on data obtained in a 0.15 m diameter column with water and non-aqueous liquids in the form:

$$e_{G_C} = 0.59 B_1^{1.5} \left(\frac{\rho_G^{0.96} \sigma^{0.12}}{\rho_L} \right) \tag{3.9}$$

$$u_{G_C} = \left(\frac{\sigma^{0.12}}{2.84 \rho_G^{0.04}} \right) e_{G_C} \left(1 - e_{G_C}\right) \tag{3.10}$$

where B_1 is an empirical parameter that depends on the kind of liquid ($B_1 \approx 4$).

(iii) The third kind of criteria are based on an underlying **theoretical concept**. Their reliability relies on reliable closures used in the analysis. Depending on their predictive value, they belong to two classes.

A posteriori criteria are used for evaluation of the critical point from data already measured. Two common examples are the slip speed concept and the drift-flux model, used also for our data. The former is based on the empirical fact that, in uniform bed, the bubble speed decreases with bubble concentration (hindrance), while the latter is based on the mass conservation of the phases. Both cases strongly rely on robust closures for the slip speed.

A priori criteria are more ambitious and take the form of relations for the criticals. They belong to two qualitatively different groups:

The first group is based on strictly *one-dimensional (1D) models of the flow*. These have been developed for externally driven $g - l$ flows, flow regimes and their stability, in long and narrow pipes of cooling circuits in nuclear power plants where the liquid speed is large (bubbly flows). These models were adopted to investigate fluidized beds and bubble columns. There are several studies devoted to $1D$ bubble columns (e.g. León-Becerril and Liné (2001)). These models are generally not suitable for bubble columns due to their completely different conditions: internally (buoyancy) driven flow, short and wide containers, low liquid speed. The effect of the horizontal extent of the column and the presence of the boundaries on all sides prevents us from treating the bubble columns as a infinitely long $1D$ systems with flat radial profiles.

The second group is based on *two-dimensional (2D) models of the flow* and we are currently aware about two examples:

In the first, Shnip et al. (1992) performed linear stability analysis of relatively simple

governing equations for gas-liquid flow and obtained an implicit stability criterion for the homogeneous regime in the form:

$$\frac{2g}{\Delta P J' U_0} < \left(\frac{\pi}{D_C}\right) \frac{\sinh(\pi A')}{\cosh(\pi A') - 1} \ , \tag{3.11}$$

where ΔP relates to the pressure drop across the plate and J' equals $U + e(\delta U/\delta e)$; both quantities must be obtained from some closure relations, usually empirical. D_C is the column diameter and A' the column aspect ratio h_0/D_C. To obtain the critical values, Eq. 3.11 must be solved for e_{G_C}, upon substituting $U(e_G)$, using, for instance, the expression proposed by Richardson and Zaki (1954). Note that the effect of the viscosity is absent in Eq. 3.11 and can enter only via the closure for U.

In the second, Ruzicka and Thomas (2003) undertook a different approach, based on the analogy between the buoyancy-driven instability of uniform dispersed layers and the Rayleigh-Benard instability in thermal convection. In both cases, the original homogeneous state is broken by onset of large-scale circulations when increasing the energy input into the system. The Rayleigh number is the order parameter. This generic physical concept yields the following explicit stability criterion:

$$e_G < e_{G_C} = \frac{\mu^* \kappa}{\rho g} \left(\frac{k_1}{h_0^3} + \frac{k_2}{h_0^{3-c_1} D_C^{c_1}}\right), \tag{3.12}$$

where μ^* is the effective dynamic viscosity of the bubbly mixture and κ is the hydrodynamic diffusivity of the bubbles, which must be closed. k_1, k_2 and c_1 are empirical parameters that depend on the columns size (Ruzicka et al., 2001a). For the bubble column used in this study ($D_C = 0.14\ m$, $h_0 = 0.4\ m$), Eq. 3.12 reads

$$e_{G_C} = 2.11 \times 10^5 \mu^* \kappa \ , \tag{3.13}$$

which predicts a linear increase of the stability with the viscosity and diffusivity. Estimating these two, $\mu^* \approx \mu \approx 10^{-3}\ Pa.s$ and $\kappa \approx (bubble\ size) \times (bubble\ speed) \approx 0.005\ m \times 0.2\ m/s = 10^{-3}\ m^2/s$, we have for tap water a constant value $e_{G_c} = 0.211$. All the above concepts relate to g-l systems and do not explicitly contain the effect of solids. However, this effect can be indirectly involved, through the dependence of certain quantities on the solid content. These can be either the constitutive properties of the multiphase system (density, viscosity, diffusivity, etc.), or closure relations for the pressure drop, slip speed,

etc. Thus, the g-l criteria can, in principle, be used for the data obtained in the solids effect study.

There are also studies devoted to the flow regime identification in true three-phase g-l-s systems, mainly for liquid-fluidized beds. The main difference from bubble columns is essentially the non-zero liquid speed, since the liquid passes through the system. For instance, Zhang et al. (1997) classify up to seven different flow regimes of the three-phase flow and present correlations for the boundary lines separating them in the parameter plane. Most of these regimes do not occur in a typical bubble column (e.g. slug, bridging, annular). Since these flow maps are applicable only for a certain size of column (width 0.0826 m, height 2 m), type of distributor ($2-mm$ orifices) and height of the measurement probe (0.65 m), they can not be used in our case.

Indeed, as Krishna et al. (1993) mentioned, there is a need to understand better the flow regime transitions and the development of a unified theory of multiphase flow regime transitions would be useful and enlightening. Also, regarding the g-l-s systems, as stated by Fan et al. (1999), the studies of the regime transition in three-phase fluidized beds and slurry bubble columns are still very scarce. The present study is a contribution to fill in this gap.

3.2.4 Visualization experiments

Auxiliary visualization experiments were performed in order to investigate the three phase systems in more detail, namely the pattern of the bubble-particle interactions. The aim of those experiments was to obtain arguments to support some possible mechanisms responsible for the trends observed in the regime transition experiments. The measurements were performed in a cylindrical plexiglas bubble column of 0.07 m diameter and 0.84 m high. At the bottom, the column was equipped with one 0.3 mm inner diameter needle for the generation of bubbles of similar size as those obtained in the main experiments. Compressed air from laboratory lines, passing through a microvalve, was the gas phase. The liquid phase was tap water. The same calcium alginate beads ($d_{eq} = 2.1\ mm$), as those used in the main regime transition experiments, were used as solid phase. In some experiments, a narrow glass tube (6 or 14 mm diameter) was placed into the column to enable frequent and intense contact between bubbles and particles. Two cameras were used for the visualization. First, a commercial analogue Panasonic S-VHS-C movie camera

NV-S99E, connected to a Panasonic video cassette recorder NV-HS1000EGC and a Sony Trinitron monitor. Second, high-speed digital system Kodak EKTAPRO, with speed up to 10 000 frames per second. The images were downloaded from the fast memory unit through a SCSI interface to a PC. The pictures were taken from two different places in the column: at the bottom and 0.255 m high. Different situations were studied namely the behaviour the of bubbles in the gas-liquid system and the effect of particle-bubble interactions in the gas-liquid-solid system.

3.3 Results and discussion

In this section are presented the results from the studies of the effect of different properties on flow regime transition and HoR stability. The three subsections below correspond to the three properties investigated: surfactants, viscosity and solid phase.

3.3.1 Surfactants

Primary data: voidage-superficial gas velocity

The plots of the $e_G(u_G)$ graphs are shown in Fig. 3.12. For $CaCl_2$ concentrations up to 0.03 mol/L, the data presented in Fig. 3.12(a) show a considerable increase of the gas holdup with increasing $CaCl_2$ concentrations, mainly for higher superficial gas velocities. On the other hand, at larger $CaCl_2$ concentrations ($\geq$ 0.03 mol/L), the gas holdup dependencies for different electrolyte concentrations are similar (Fig. 3.12(b)).

Main result: stability

The critical values of the voidage e_{G_C} and superficial gas velocity u_{G_C} are plotted against the $CaCl_2$ concentration in Fig. 3.13. This figure shows that for low salt concentrations ($|CaCl_2| \leq 0.03\ mol/L$) the HoR is clearly stabilized due to the $CaCl_2$ addition. However, further increases of salt concentration do not change the critical values of gas holdup and superficial gas velocity (e_{G_C}, u_{G_C}). This suggest that from a certain $CaCl_2$ concentration on, the flow regime transition is independent of the electrolyte concentration. Qualitatively, the behaviour of the gas holdup in Fig. 3.12 and the critical voidage in Fig. 3.13(a) are similar: both increase first and then level off for a certain $CaCl_2$ concentration. The

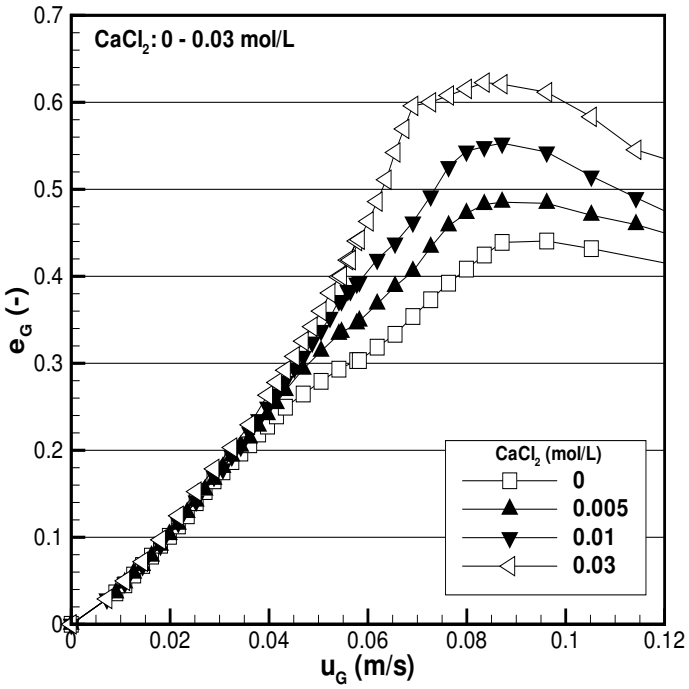

(a)

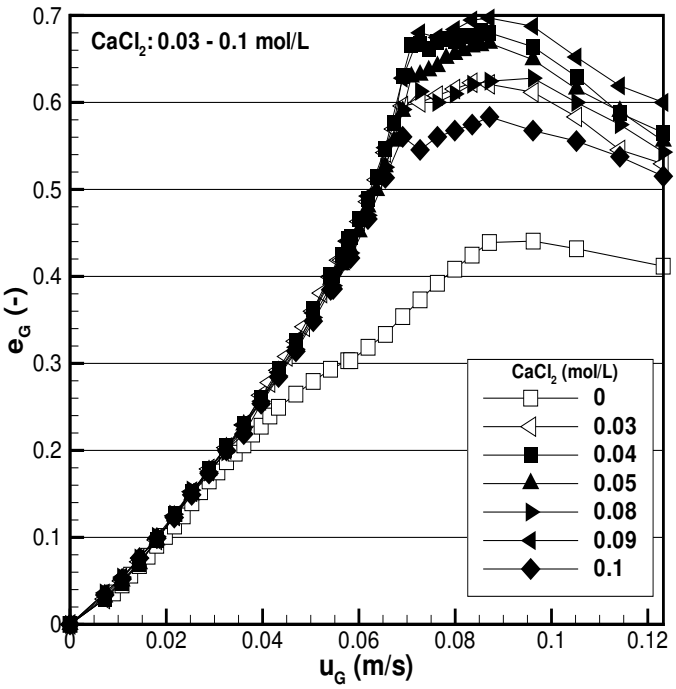

(b)

Figure 3.12. Primary data: voidage e_G vs superficial gas velocity u_G. (a) $|CaCl_2| = 0 - 0.03\ mol/L$ and (b) $|CaCl_2| = 0.03 - 0.1\ mol/L$.

increase of e_{G_C} in the $|CaCl_2| = 0 - 0.03\ mol/L$ range can be fitted with a straight line:

$$e_{G_C} = 12.83 + 0.15 \cdot |CaCl_2| \qquad (R_{xy} = 0.98). \tag{3.14}$$

Discussion

The experimental results demonstrated that the gas holdup (e_G) is positively influenced by the presence of the electrolyte $CaCl_2$, for salt concentrations up to 0.03 mol/L and higher superficial gas velocities. Above that concentration the $e_G(u_G)$ dependencies did not change much with further salt additions. This trend is similar to that observed by Zahradnik et al. (1995) for the different aqueous solutions of electrolyte tested ($NaCl$, KCl, Na_2SO_4, $MgSO_4$, KI, $BaCl_2$ and $CaCl_2$). As an example, they presented the e_G dependence on u_G for $BaCl_2$ solution and from that graph it is possible to see that for $|BaCl_2| > 0.02\ mol/L$ the e_G practically does not depend on the salt concentration. Note that this electrolyte concentration value is comparable to that observed in our case ($|CaCl_2| \approx 0.03\ mol/L$). However, the maximum e_G values observed in our work ($e_{G_{max}} \approx 0.7$) are considerably higher than those observed by Zahradnik et al. (1995) ($e_{G_{max}} \approx 0.4$) for all the electrolytes investigated. Zahradnik et al. (1995) also performed coalescence measurements under strict conditions of bubble contact. It was verified that the concentration corresponding to 50% of coalescence (transition concentration) was 0.056 mol/L for $CaCl_2$ solutions. In those experiments it was found that at a certain salt concentration the bubble coalescence was suddenly almost suppressed. Again, this concentration value $|CaCl_2| = 0.056\ mol/L$ is comparable to our characteristic salt concentration ($|CaCl_2| \approx 0.03\ mol/L$), which means that a parallel can be established between coalescence and voidage measurements. For $CaCl_2$ concentration below $\approx 0.03\ mol/L$, the bubble coalescence is gradually suppressed due to the salt additions, which enhances the stability of the homogeneous flow regime. The $|CaCl_2| \approx 0.03\ mol/L$ is the limit salt concentration, above which the $e_G(u_G)$ dependence is weakly affected and the critical values of gas holdup and superficial gas velocity (e_{G_C} and u_{G_C}) are practically constant, $e_{G_C} \approx 0.6$ and $u_{G_C} \approx 0.07\ m/s$.

The ability for most inorganic electrolytes to inhibit the bubble coalescence above a critical concentration has been normally attributed to: Gibbs-Marangoni effect/surface elasticity, hydration repulsive forces, electrical repulsive forces and a reduction in the hy-

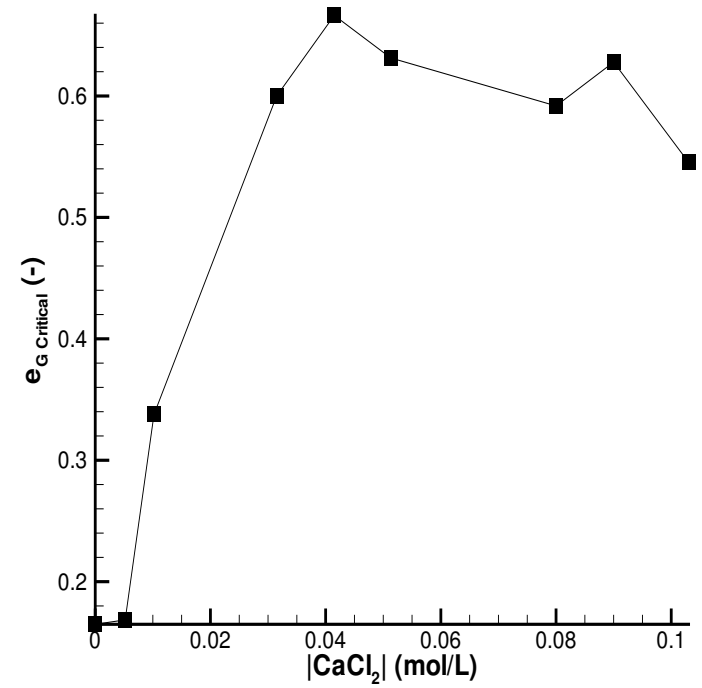

(a)

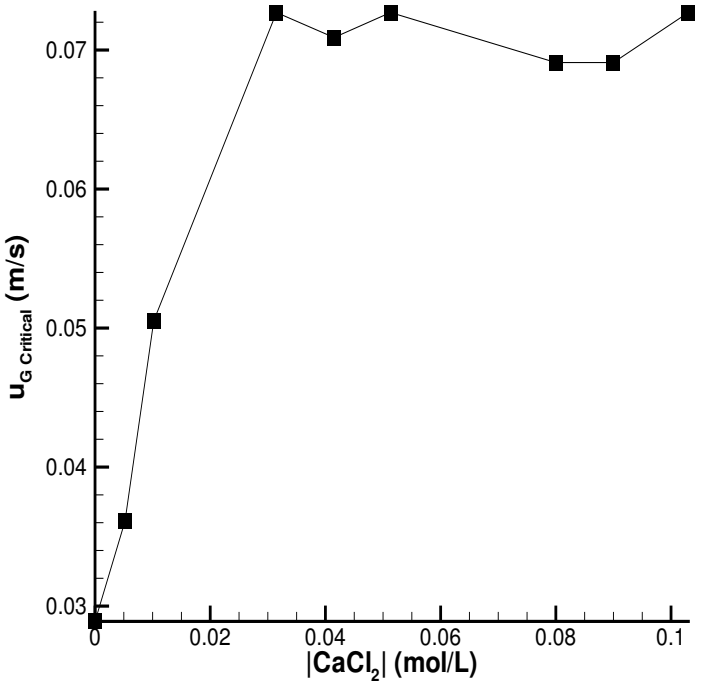

(b)

Figure 3.13. Main result: homogeneous regime stability measured by critical values of (a) voidage e_{G_C} and (b) superficial gas velocity u_{G_C}.

drophobic attraction. The Gibbs-Marangoni effect results from the surface tension gradients formed during expansion or contraction of bubbles. Weissenborn and Pugh (1996) indicated that for the electrolyte solutions tested (including $CaCl_2$), the change in surface tension gradients caused by electrolytes at the transition concentration are too weak to cause significant Gibbs-Marangoni effects. The hydration repulsive forces may be operative between bubbles if the film thickness is $\sim 5\ nm$ or smaller. However, this is possible only at high electrolyte concentrations ($> 1\ mol/L$), which is not our case. Moreover, Weissenborn and Pugh (1996) also presented the film rupture thicknesses for two coalescing bubbles attached to capillaries in various electrolyte solutions and found that they were much larger than the distances over which van der Waals, electrostatic or hydration forces have a considerable strength. Thus, at the rupture thickness, these forces are too weak and can not explain any attraction or repulsion between coalescing bubbles in electrolyte solutions. The attractive hydrophobic force may also be responsible for the inhibition of bubble coalescence in electrolyte solutions, however the evidences collected up to now, do not give us a solid support to this idea. Finally Weissenborn and Pugh (1996) suggested that the mechanism of the interfacial attraction between bubbles may be due to perturbations of water structure which may be related to the effect of the electrolyte concentration on dissolved gas concentration. These last assumptions need however experimental support.

Our experimental work aimed the quantitative evaluation of the $Ho - He$ flow regime transition of air-$CaCl_2$ solutions in a bubble column. Further experiments should be performed in order to evaluate in more detail specially the salt concentration region where the stabilization of the critical parameters occurs. Moreover, the influence of electrolyte type on regime transition should be examined, testing other electrolytes has liquid phase. Microscopic studies on the possible mechanisms underlying the effect of electrolytes on gas holdup and HoR stability must be continued, namely those concerning the forces involved on the bubble coalescence process.

3.3.2 Viscosity

Preliminary Experiments

The investigation of the influence of liquid viscosity on the $Ho - He$ flow regime transition was started with preliminary experiments. In these experiments, a 0.5 $mPa.s$ viscosity

step was considered. The experimental data $e_G(u_G)$ displayed in Fig. 3.14 suggest that for the viscosity range $(0 - 5\ mPa.s)$, three different regions might be found:

- $1 < \mu < 1.5$ small gas holdup increase
- $1.5 < \mu < 2.5$ decreasing gas holdup
- $2.5 < \mu < 5$ constant gas holdup

Since this increase in gas holdup for low liquid viscosities is not commonly observed, more detailed experiments, with smaller viscosity steps, were then performed.

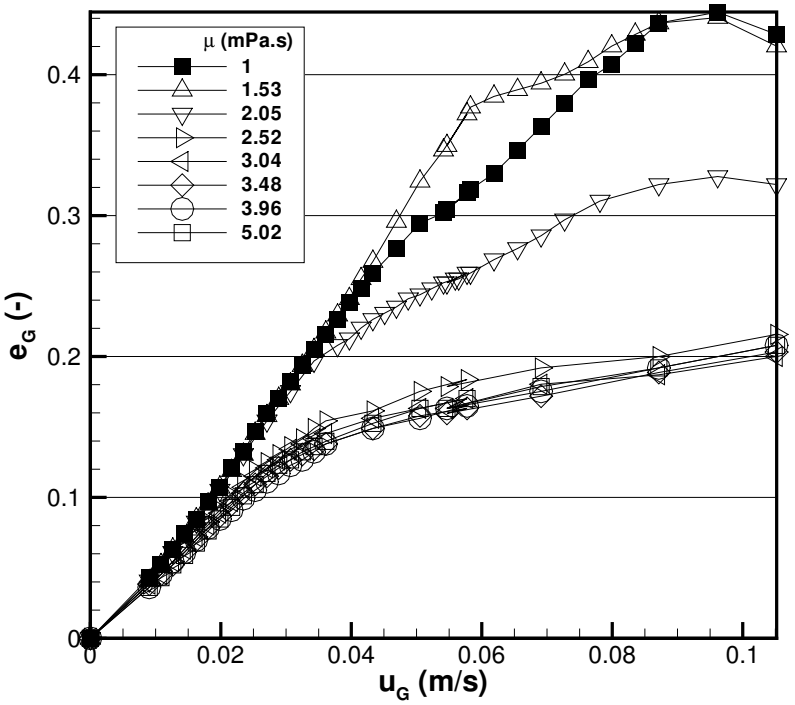

Figure 3.14. Voidage e_G vs superficial gas velocity u_G. Viscosity range: 1-5 $mPa.s$.

The critical values of voidage e_{G_C} and superficial gas velocity u_{G_C} are displayed versus the liquid viscosity in Fig. 3.15. Both Figs. 3.15 (a) and (b) show an increase of the critical values with the viscosity for low viscosity and then a decrease followed by a plateau. The

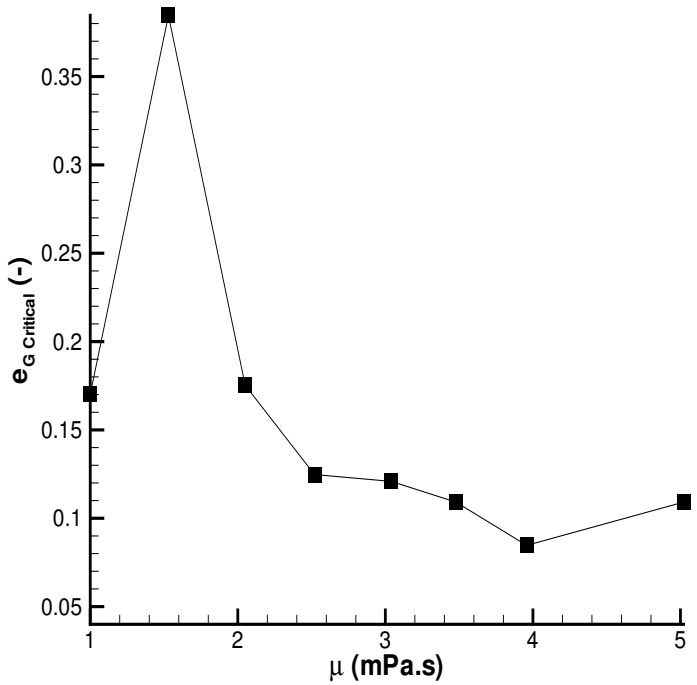

(a)

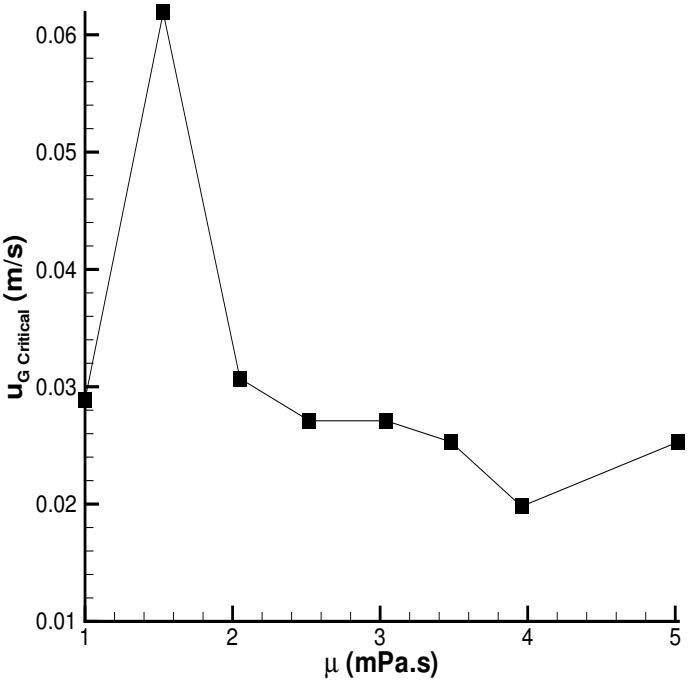

(b)

Figure 3.15. Homogeneous regime stability measured by critical values of (a) voidage e_{G_C} and (b) superficial gas velocity u_{G_C}.

qualitative behaviour of the gas holdup in Fig. 3.14 and the critical gas holdup in Fig. 3.15 is similar. These preliminary results suggest that low liquid viscosity may stabilize the HoR, but detailed and careful measurements must be conducted. The results of those experiments are presented below.

Detailed Experiments

Primary data

A detailed investigation of the viscosity effect on regime transition was performed and experiments with 21 solutions of different and close viscosities were conducted. The dependence of the gas holdup e_G on superficial gas velocity u_G is presented in Fig. 3.16. In Fig. 3.16a, the voidage increases with the viscosity in the range of 0-6% of glycerol ($\mu = 0.946 - 1.091 mPa.s$). On the other hand, in 3.16b, the voidage decreases as viscosity increases in the range 6-50% of glycerol ($\mu = 1.091 - 5.480\ mPa.s$). Note that a change of about 10% in the input (viscosity) may cause about 90% change in the output (voidage), which is noticeable. The dual effect of viscosity on the gas holdup for low viscosities is surprising and indicates the presence of two competing mechanisms, one stabilizing and the other destabilizing the uniform two-phase system.

The quantitative change of voidage with viscosity is displayed in Fig. 3.17. For low superficial gas velocities (0.02 and 0.03 m/s), the gas holdup is not influenced by the viscosity. Then, for increased superficial gas velocities, the gas holdup shows a sharp increase for low viscosities, followed by a slow recovery.

The experimental bubble slip speed, calculated from Eq. 3.2, is plotted in Fig. 3.18. As expected, the dependence $U(u_G)$ is opposite than that observed for $e_G(u_G)$. Fig. 3.18a shows that, for low viscosities ($\mu = 0.946 - 1.091\ mPa.s$), by increasing the viscosity the bubble slip speed decreases. For the viscosity range $\mu = 1.091 - 5.480\ mPa.s$, the bubble slip speed is enhanced by the viscosity, mainly for higher superficial gas velocities (see Fig. 3.18b).

The bubble retention time (τ) was determined by the following expression:

$$\tau = \frac{h_0}{u_G} \cdot \frac{e_G}{1 - e_G}. \tag{3.15}$$

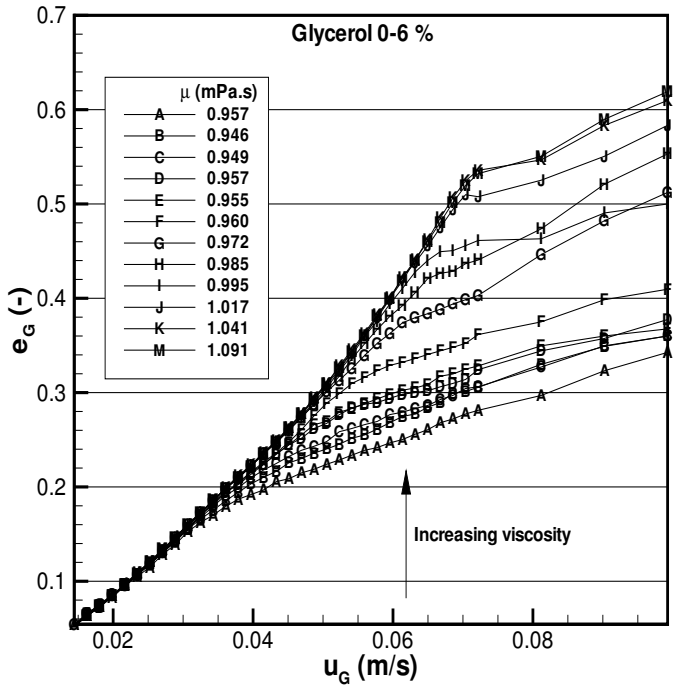

(a)

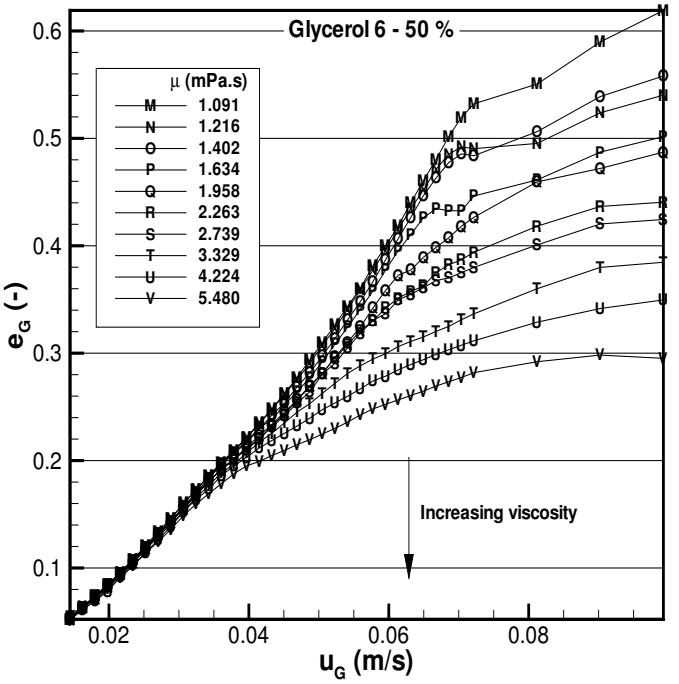

(b)

Figure 3.16. Primary data: voidage e_G vs superficial gas velocity u_G. Viscosity range: 0.946-5.480 $mPa.s$.

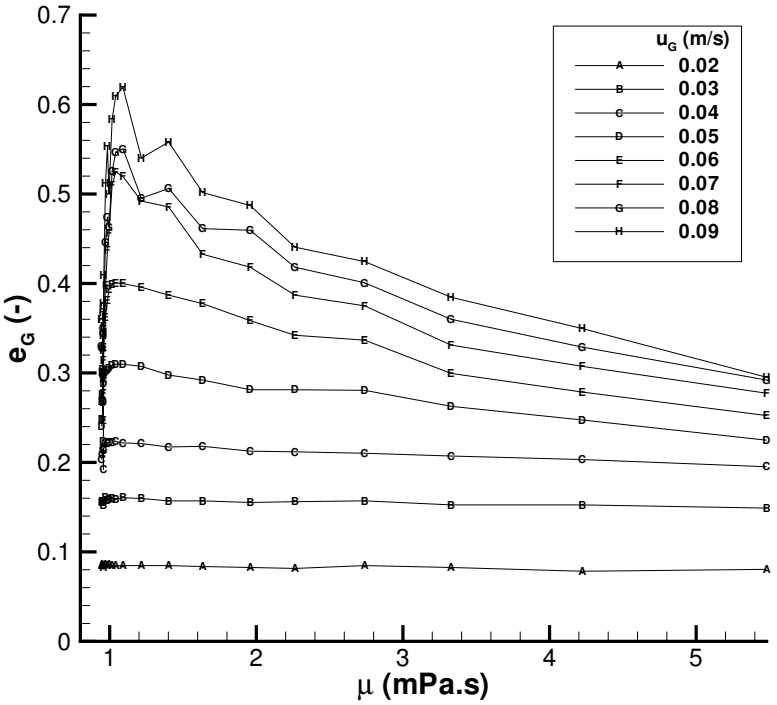

Figure 3.17. Primary data: voidage e_G vs liquid viscosity μ.

An example of retention time (τ), is plotted in Fig. 3.19, for 0% and 6% glycerol solutions. For low superficial gas velocities ($u_G < 0.03\ m/s$), the retention times presented here are comparable. However, for $u_G > 0.03\ m/s$, the retention time for distilled water (0% glycerol) is roughly constant, while the retention time for 6% glycerol solution exhibits a considerable increase with the superficial gas velocity.

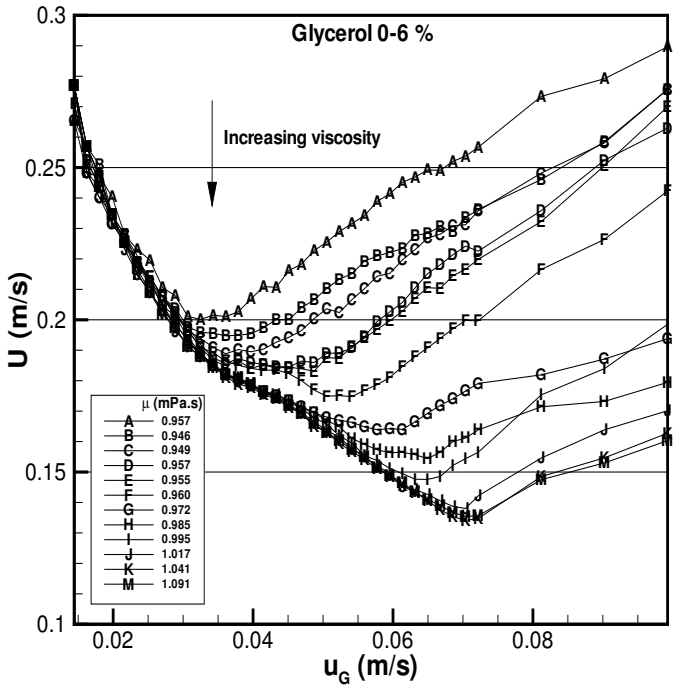

(a)

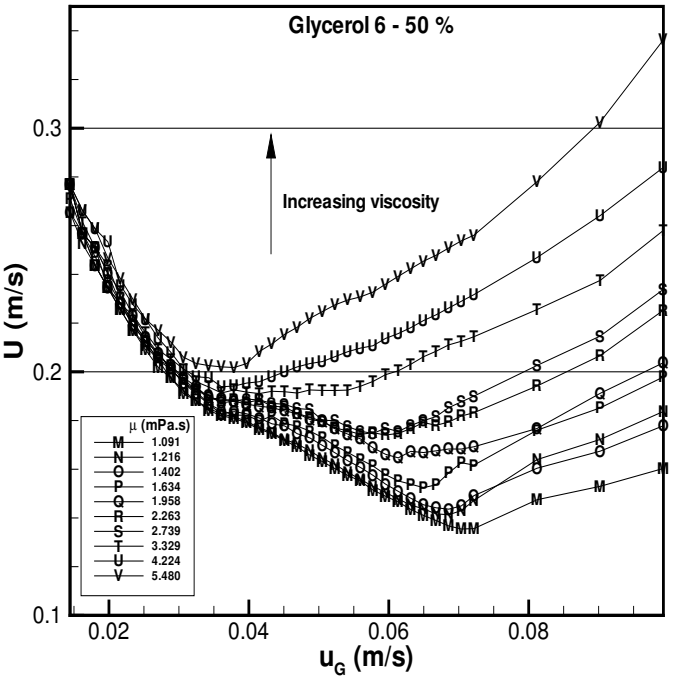

(b)

Figure 3.18. Primary data: slip speed U vs superficial gas velocity u_G. Viscosity range: 0.946-5.480 $mPa.s$.

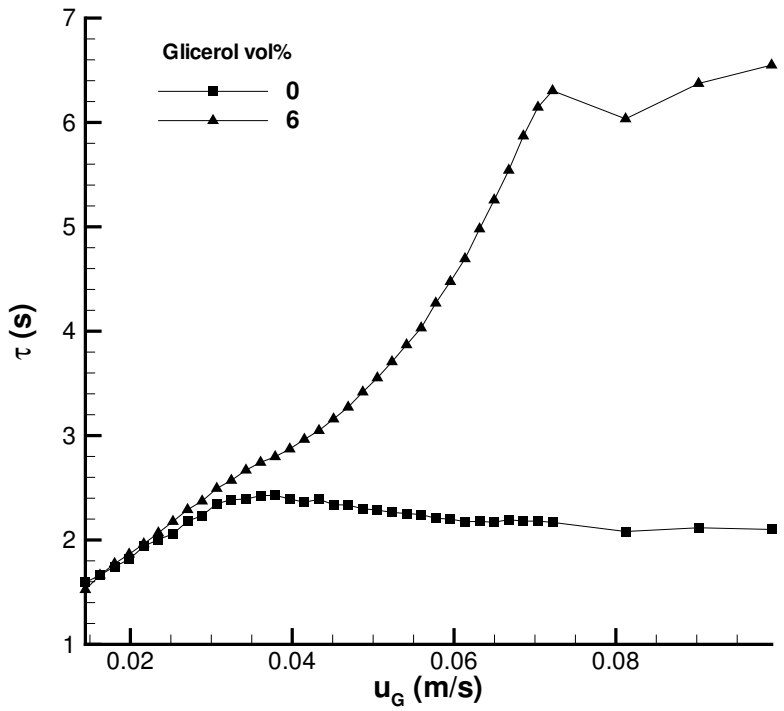

Figure 3.19. Primary data: retention time τ vs superficial gas velocity u_G, for 0 and 6 $vol\%$ of glycerol.

Secondary data

As already explained in subsection 3.2.2, the evaluation of the critical values of voidage and superficial gas velocity (e_{G_C} and u_{G_C}) was based on the drift flux model (Wallis, 1969), which in turn is based on the bubble slip speed concept. The expression used to determine the theoretical bubble slip speed U_{theo} was deducted by Ruzicka et al. (2001b) for the homogeneous flow regime (Eq. 3.3). The parameters of that expression (a' and U_0) have a clear physical meaning: a' is the Darwinian bubble drift coefficient (a' = drift volume/bubble volume), with the drift volume being the amount of liquid carried by each bubble. This parameter represents the strength of coupling between the gas and liquid phases. U_0 is the bubble terminal velocity and represents the velocity scale of the motion of the gas phase in HoR. The dependence of the parameters a' and U_0 on liquid viscosity

is displayed in Fig. 3.21. One can see that both a' and U_0 suffer a deep decline at the beginning, for very dilute glycerol solutions, followed by a slower recovery.

The "theoretical" bubble slip speed U_{theo} can also be given by other formulas, for instance the Richardson and Zaki (1954) formula (U_{R-Z}) for uniform sedimentation:

$$U_{R-Z} = U_0 \cdot (1 - e_G)^p \,, \tag{3.16}$$

where the exponent p is a purely empirical parameter and was plotted in Fig. 3.20 as a function of liquid viscosity. The parameter p presents the same trend as parameters a' and U_0. Both Richardson and Zaki (1954) and Ruzicka et al. (2001b) formulas for bubble slip speed in the HoR are depicted in Fig. 3.22 for air-water system. In this example, one observes that these formulas originate comparable results, and consequently the critical values of voidage and superficial gas velocity (e_{G_C} and u_{G_C}) will also be similar.

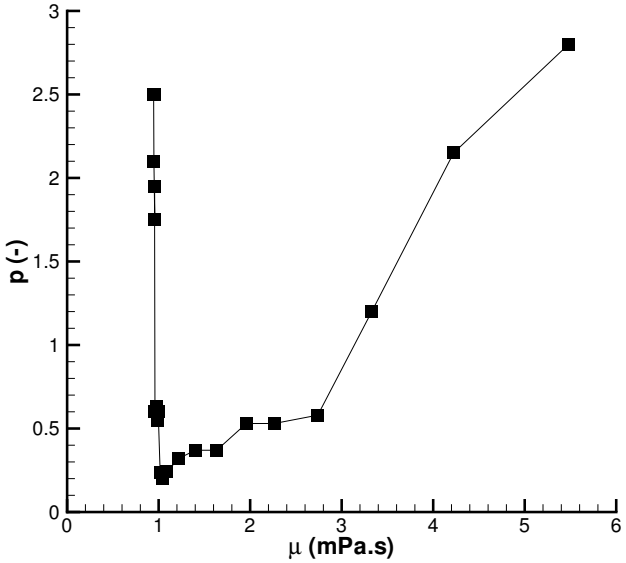

Figure 3.20. Secondary data: Richardson-Zaki exponent p vs liquid viscosity μ.

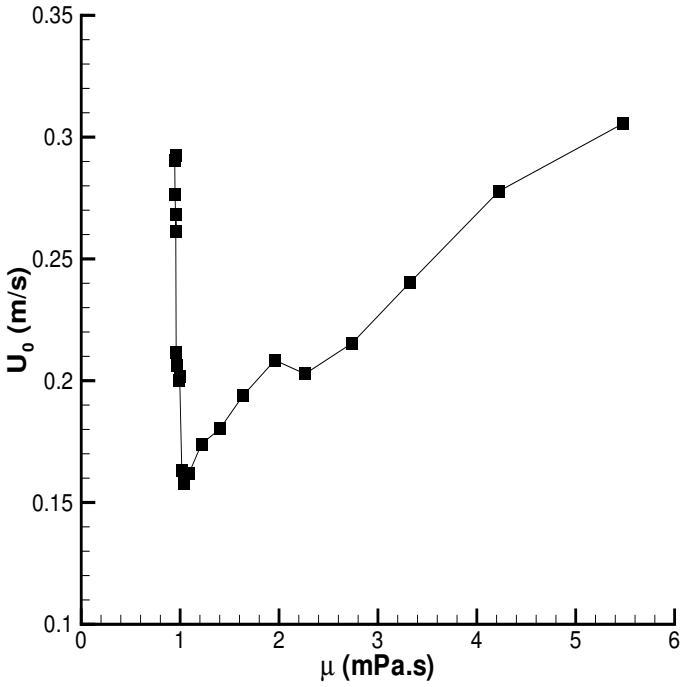

(a)

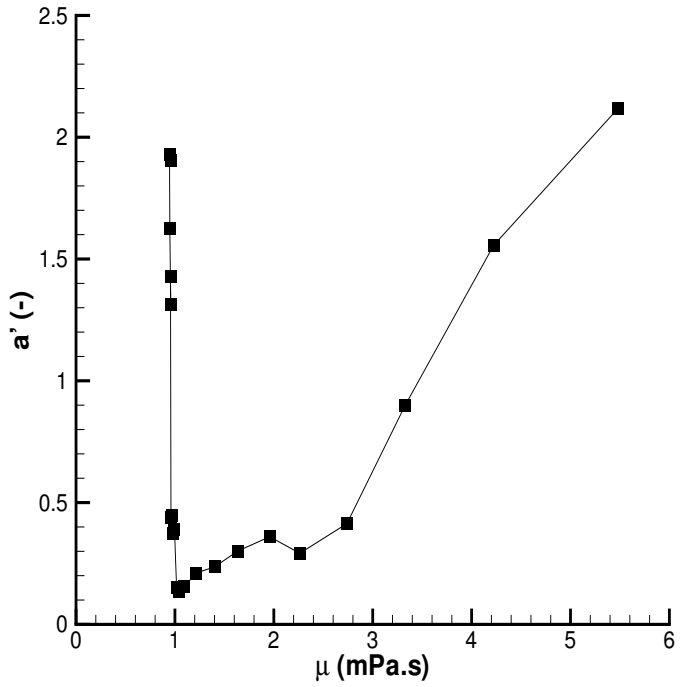

(b)

Figure 3.21. Secondary data: Slip speed parameters (a) terminal bubble velocity U_0 and (b) bubble drift coefficient a'.

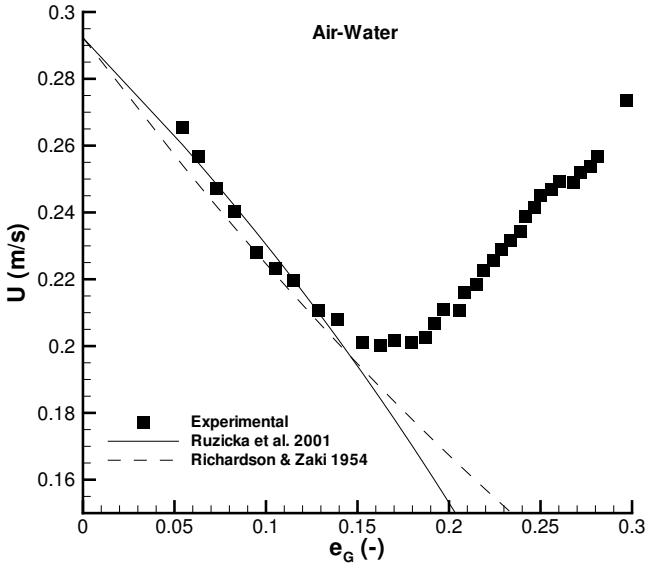

Figure 3.22. Secondary data: Comparison between Ruzicka et al. (2001b) (Eq. 3.3) and Richardson and Zaki (1954) (Eq. 3.16) formulas for the bubble slip speed U. Example for air-water system.

Main result

The critical values of gas holdup e_{G_C} and superficial gas velocity u_{G_C} are plotted versus the liquid viscosity μ in Fig. 3.23. These critical values were taken as the quantitative measure of the uniform bed stability. For low viscosities ($\mu = 0.946 - 1.091\ mPa.s$), increasing the viscosity stabilizes the bubble bed, which is an unexpected result. For larger viscosity ($\mu = 1.091 - 5.480\ mPa.s$), the bubble bed is destabilized, as expected. Thus, the viscosity might have a dual effect on the stability of the HoR, first stabilization and then destabilization.

The behaviour of the gas holdup in Fig. 3.16 and the critical gas holdup in Fig. 3.23(a) is similar, since both present a maximum with respect to the liquid viscosity.
The stabilization occurs in a very narrow viscosity range ($\mu = 0.946 - 1.091\ mPa.s$), where the degree of stability increases by approximately three times due to a viscosity change of only about 10%. The increasing part of the $e_{G_C}(\mu)$ dependence can be fitted with a

straight line (see Fig. 3.24):

$$e_{G_C} = 4.43\mu - 4.03 \qquad (R_{xy} = 0.96). \tag{3.17}$$

As far as we know, there is only a theoretical prediction for the stabilizing effect of viscosity, which is the one derived by Ruzicka and Thomas (2003) (see Eq. 3.12 in subsection 3.2.3). This expression gives a stability criterion and predicts a linear increase of e_{G_C} with viscosity. In the case of this study, Eq. 3.12 reduces to the following relation (see subsection 3.2.3):

$$e_{G_C} \approx 0.211\mu. \tag{3.18}$$

This prediction (Eq. 3.18) is plotted together with the experimental results in Fig. 3.23(a). The descending branch of $e_{G_C}(\mu)$ dependence allows an exponential fit (Fig. 3.23(a)):

$$e_{G_C} = 0.74 \exp(-0.35\mu) \qquad (R_{xy} = 0.99). \tag{3.19}$$

The decreasing part of the $u_{G_C}(\mu)$ dependence allows also an exponential fit (Fig. 3.23(b)):

$$u_{G_C} = 0.095 \exp(-0.24\mu) \qquad (R_{xy} = 0.98). \tag{3.20}$$

These empirical correlations are presented to quantify the trends observed in our narrow range of data, rather than to be used for design and scale-up of real equipment.

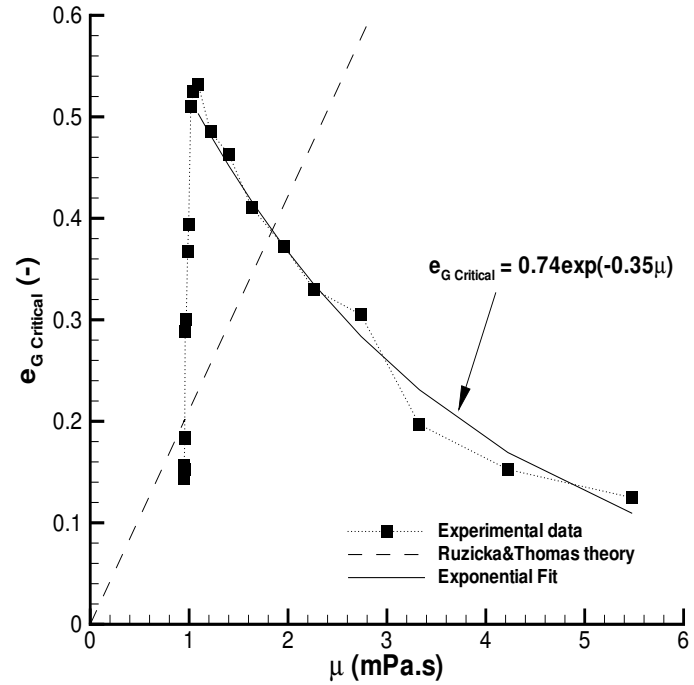

(a)

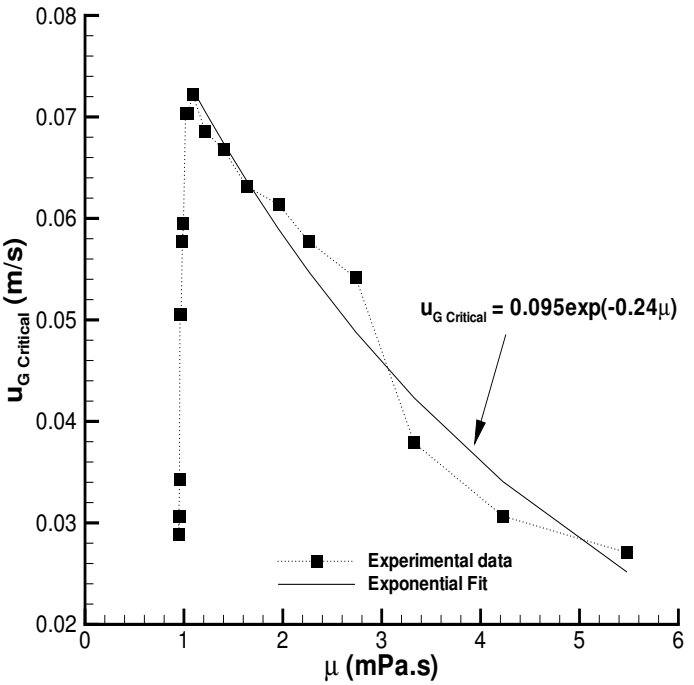

(b)

Figure 3.23. Main result: homogeneous regime stability measured by critical values of (a) voidage e_{G_C} and (b) superficial gas velocity u_{G_C}.

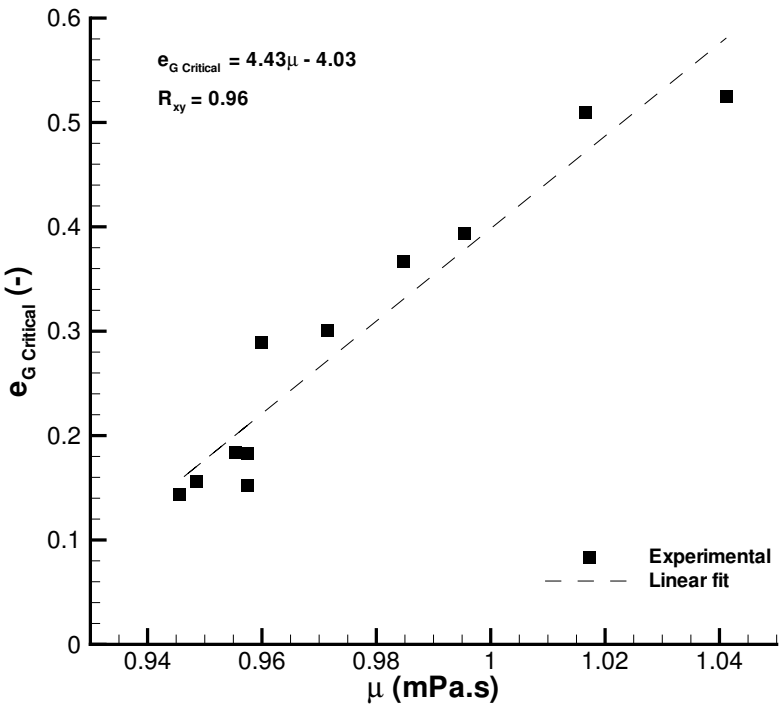

Figure 3.24. Main result: Linear fit of critical voidage e_{G_C} for low viscosities.

Discussion

The effect of liquid viscosity on flow regime transition and HoR stability was experimentally investigated. It was found that around the viscosity $\mu = 1.091\ mPa.s$, which corresponds to 6% of glycerol, the dependencies of parameters such as e_G, U, e_{G_C} and u_{G_C} on viscosity are drastically changed. Primary results indicate that for low viscosities ($\mu = 0.946 - 1.091\ mPa.s$) the gas holdup increases and further viscosity increments ($\mu = 1.091 - 5.480\ mPa.s$) result in a decay of the gas holdup (Fig. 3.16). These results reveal that viscosity may have a dual effect on the gas holdup, which is surprising for low viscosity solutions. Two competing mechanisms should be behind this behaviour: one of them increasing and the other decreasing the gas holdup. The liquid viscosity has a crucial influence on the bubble coalescence process, which necessarily influences key parameters such as bubble size, gas-liquid interfacial area, gas holdup and ultimately the flow regime transition. Note that the bubble coalescence may occur at the gas distributor and also du-

ring the bubble rise through the column. It is commonly admitted that coalescence occurs in three steps: bubble collision, liquid film drainage and rupture. When two bubbles collide, the liquid film formed by the amount of liquid trapped between them begins to drain until it becomes thin enough to break, leading to a coalesced bubble. Bubble coalescence is also a function of the contact time between two bubbles which depends on the bubble rise velocity, which in turn is a function of bubble size and turbulence intensity (Mouza et al., 2005).

At low viscosity, an increase in liquid viscosity will increase the film resistance, hindering film drainage during the thinning process and thus inhibiting the bubble coalescence. Since the bubble coalescence rate decreases with the viscosity (at the viscosity range $\mu = 0.946 - 1.091\ mPa.s$), the mean bubble size is reduced and consequently the bubble slip velocity decreases (Fig. 3.18(a)) and the overall gas holdup increases (Fig. 3.16(a)). This gas holdup increase can also be explained by the increase in the bubble retention time in the column with the liquid viscosity, for low viscosities (see Fig. 3.19). Increased drag forces reduce the bubble rise speed so the bubbles stay longer in the column during their rise and consequently the gas fraction will necessarily increase.

Equivalently, the bubble bed uniformity is positively affected by the liquid viscosity. Our HoR stability measures, the critical gas holdup and the superficial gas velocity (e_{G_C},u_{G_C}), clearly indicate that the bubble bed is stabilized for low viscosities (see increasing branch in Fig. 3.23). In qualitative agreement with this unexpected result is the stability theoretical concept developed by Ruzicka and Thomas (2003), which predicts a stabilizing effect of viscosity on the HoR. By this criterium, the critical gas holdup increases linearly with the viscosity. However the predicted e_{G_C} increase is less pronounced than the one observed in our experiments.

On the other hand, for the viscosity range $\mu = 1.091 - 5.480\ mPa.s$, one observes that the viscosity increase reduces the gas holdup. A decrease of the turbulence in the liquid phase enhances the large bubble formation by coalescence. Therefore, the uniformity of the bubble bed is deteriorated by strong variation in the bubble sizes. As the big bubbles rise faster than the smaller ones, the mean slip velocity will increase (Fig. 3.18(b)) and consequently the gas holdup will decrease with the viscosity increase (Fig. 3.16(b)). The stability of the HoR is reduced and consequently the flow regime transition occurs earlier. This is unequivocally illustrated in Fig. 3.23 that shows the decreases of the critical gas holdup and the superficial gas velocity (e_{G_C},u_{G_C}) with the viscosity increase, for liquid

viscosities higher than 1.091 $mPa.s$.

Not many works can be found in literature concerning the effect of viscosity on HoR stability. Generally, an adverse influence was observed (Deckwer, 1992; Kastanek et al., 1993). Kuncova and Zahradnik (1995) and Zahradnik et al. (1997) found that the gas holdup decreases with increasing viscosity and suggested that the stability of the HoR would be reduced. However, no quantitative measurements were performed in order to support their suspicions. Wilkinson et al. (1992) combined the simple modelling concept of Krishna et al. (1991) with a dimension analysis approach to various gas holdup data collected from the literature. They chose an empirical exponential formula to describe the viscosity effect and found a decrease of the critical holdup $e_{G_C} \propto \exp\left(-const \cdot \mu^{0.5}\right)$. More recently, Mouza et al. (2005) measured gas holdup and bubble sizes of air-glycerol solutions and investigated the $HoR - HeR$ regime transition. In agreement with our findings, they also suggested that the viscosity may play a dual role, first inhibiting the bubble coalescence for low viscosities and then enhancing the coalescence for further increase of viscosity. Their remarks were supported by bubble size distributions, whose shapes give indications about the bubble coalescence. Their critical voidages were comparable, but they observed that an increase in liquid viscosity shifts the transition to higher velocities, thus stabilizing the HoR.

3.3.3 Solids

Primary data: voidage-superficial gas velocity

The plot of the $e_G(u_G)$ is shown in Fig. 3.25. For low solid content, $C_S \leq 5\%$, the data presented in Fig. 3.25(a) show a significant increase in the voidage with increasing solid loading, namely for higher u_G. On the other hand, at larger content ($C_S \geq 5\%$), the voidage displays a substantial reduction (Fig. 3.25(b)). This dual effect of the solid particles on the gas holdup is interesting, since it indicates the presence of two competing mechanisms, one stabilizing and another destabilizing the uniform three-phase system. This result also reconciles the contradictory findings reported in the literature. The quantitative change of voidage with solid content is documented in Fig. 3.26a. The corresponding variation in the mean speed of the gas phase is shown in Fig. 3.26b. Note that the data in Fig. 3.26 belong to the transition regime ($u_G = 0.1\ m/s$), where the bubble speed is enhanced by the liquid circulations.

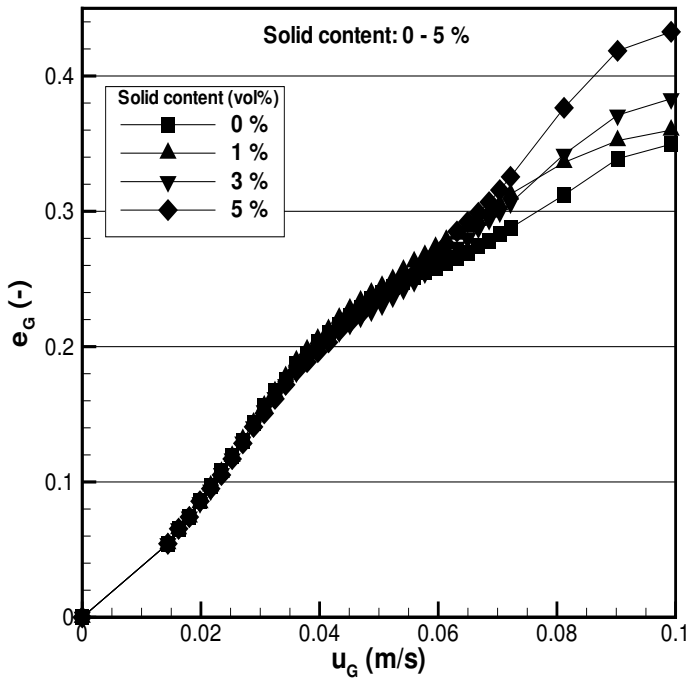

(a)

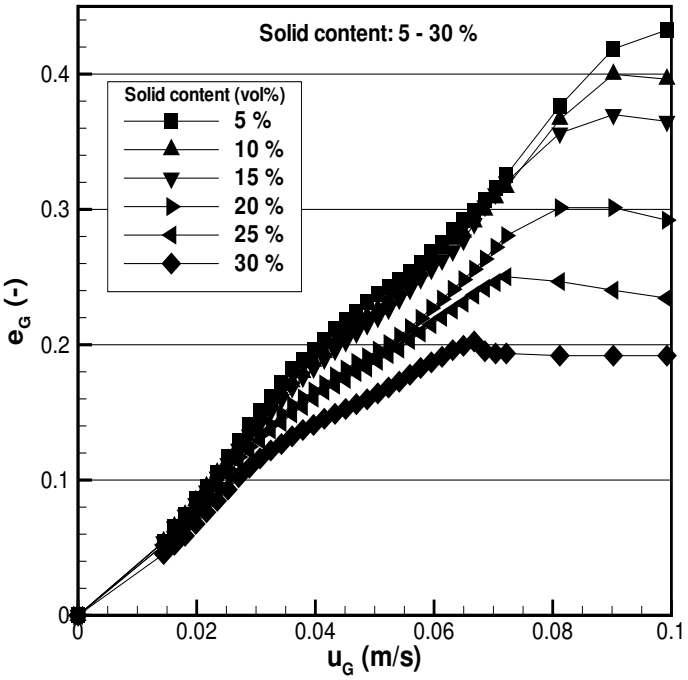

(b)

Figure 3.25. Primary data: voidage e_G vs superficial gas velocity u_G. (a) solid content 0-5 *vol*% and (b) solid content 5-30 *vol*%.

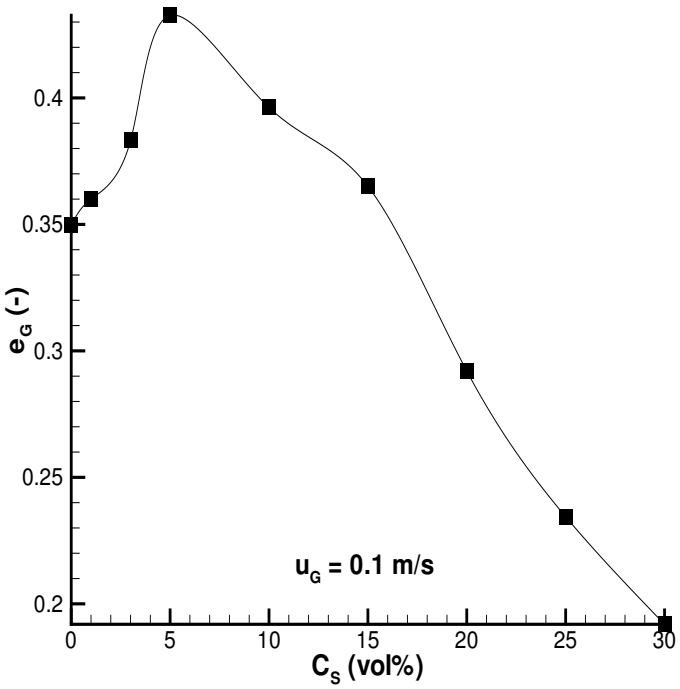

(a)

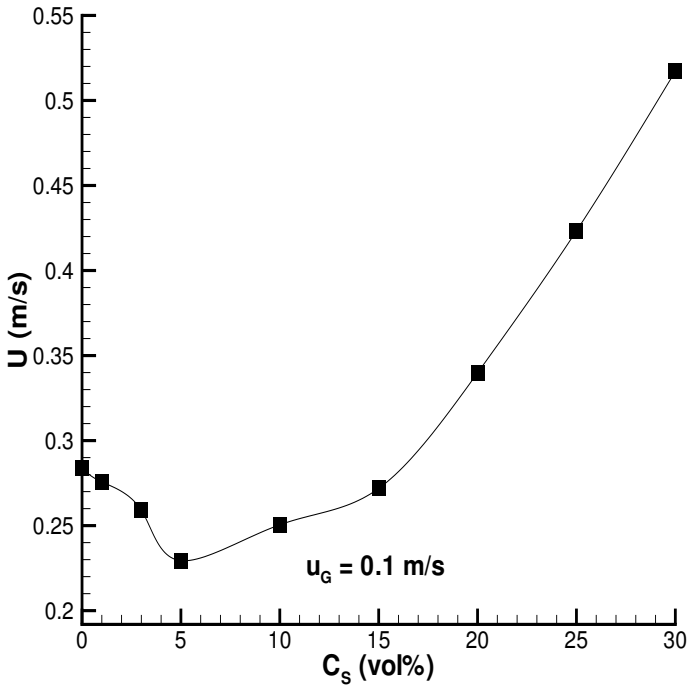

(b)

Figure 3.26. Primary data: effect of solid content C_S on (a) voidage e_G and (b) mean bubble speed U.

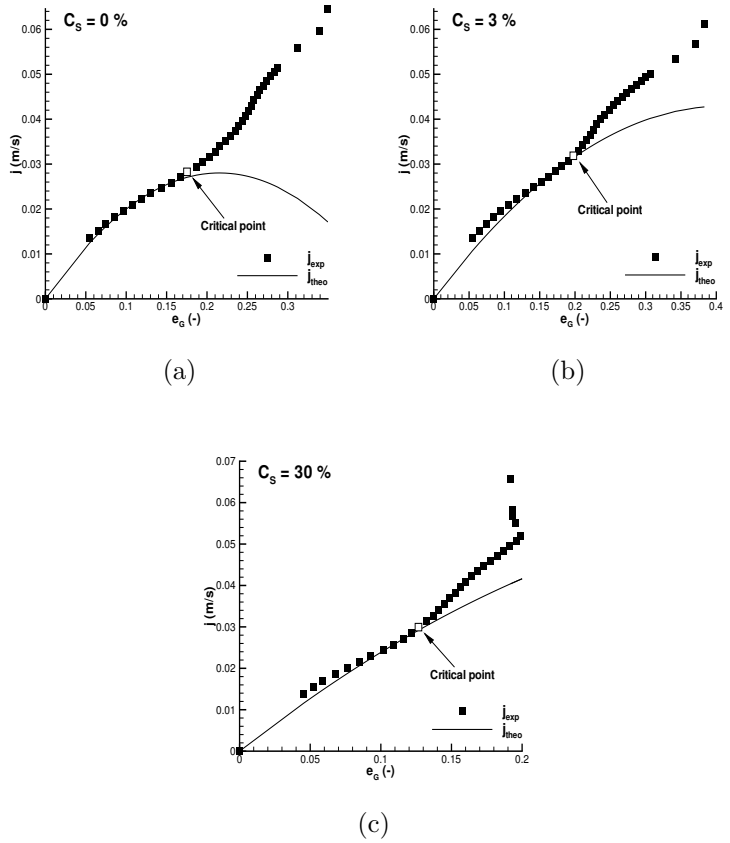

Figure 3.27. Secondary data: drift flux plot of drift flux j vs voidage e_G (a) $C_S = 0\%$, (b) $C_S = 3\%$ and (c) $C_S = 30\%$.

Secondary data: drift flux plot

Three examples of the determination of the critical point based on the drift-flux model are presented in Fig. 3.27. The data are shown in the co-ordinates voidage e_G - drift flux j, according to Eqs. 3.5 and 3.6. It is clearly seen where the experimental data depart from the uniformity theoretical line (transition point). For solid content $C_S = 3\%$ (Fig. 3.27(a)), the experimental data separate from the theoretical curve later than for $C_S = 0\%$ (Fig. 3.27(b)) (distilled water), which suggests stabilization of the HoR for low solid loading. On the other hand, for $C_S = 30\%$ (Fig. 3.27c), the separation happens earlier, suggesting destabilization of the HoR for high solid contents.

Main result: stability

The critical values of the voidage (e_{G_C}) and superficial gas velocity (u_{G_C}) are plotted versus the solid content C_S in Fig. 3.28. The picture unequivocally demonstrates the ambiguous effect of the solid particles on the stability of the HoR. The stabilization occurs at low solid load ($C_S \leq 3\%$), and the destabilization at higher load ($C_S > 3\%$). Qualitatively, the behaviour of the voidage in Fig. 3.25 and the critical voidage in Fig. 3.28 are similar: both have a maximum with respect to the solid content. Quantitatively, there is a small discrepancy: the maximum is at $C_S = 3\%$ in Fig. 3.28, and at $C_S = 5\%$ in Fig. 3.25. This suggests that the shapes of the $e_G(u_G)$ graphs are not universal in the following sense: there are exceptions to the expected rule - the larger the voidage, the larger the critical voidage. The absolute values of the criticals in Fig. 3.28 may seem rather low, $u_{G_C} \approx 0.035 - 0.04\ m/s$ and $e_{G_C} \approx 0.13 - 0.2$. This is because they represent the beginning of the regime transition process.

The stabilization effect amounts to 13% of increase in e_{G_C} and 11% of increase in u_{G_C}, relative to the g-l air-water system. The increase of e_{G_C} between $C_S = 0\%$ and 1% can be described by a modified Eq. 3.13,

$$e_{G_C} = 1.75 \times 10^5 \mu^* \kappa \, (1 + 2.23 f) \tag{3.21}$$

where the original critical voidage, 0.211, of g-l system with tap water was replaced by a somewhat lower value, 0.175, for distilled water, with $f = C_S/100$ being the solid volume fraction. Eq. 3.21 should not be considered a reliable correlation; it only demonstrates how to incorporate the stabilizing effect of solids into the stability criterion, Eq. 3.12, and indicates the magnitude of the solids effect. The destabilization trend, represented by the descending branch in Fig. 3.28(a), can be well fitted to a straight line:

$$e_{G_C} = 0.21 - 0.25 f \qquad (R_{xy} = 0.987)\ . \tag{3.22}$$

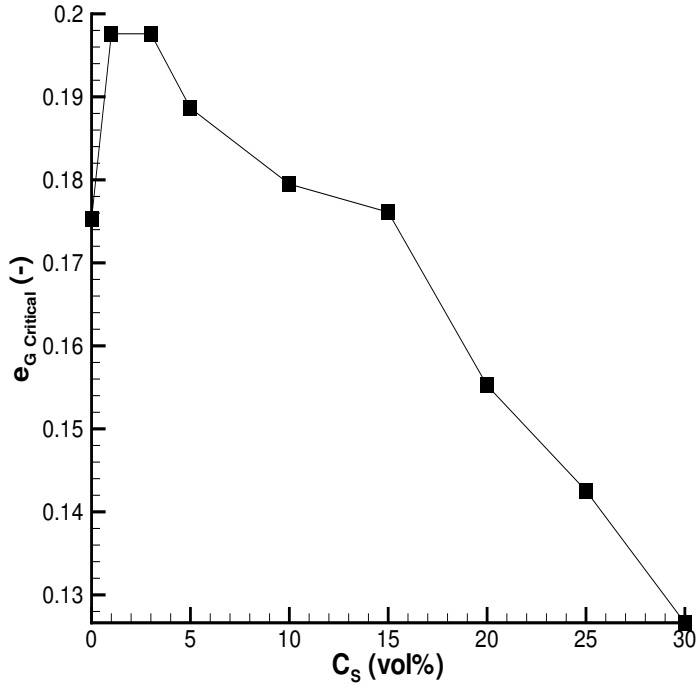

(a)

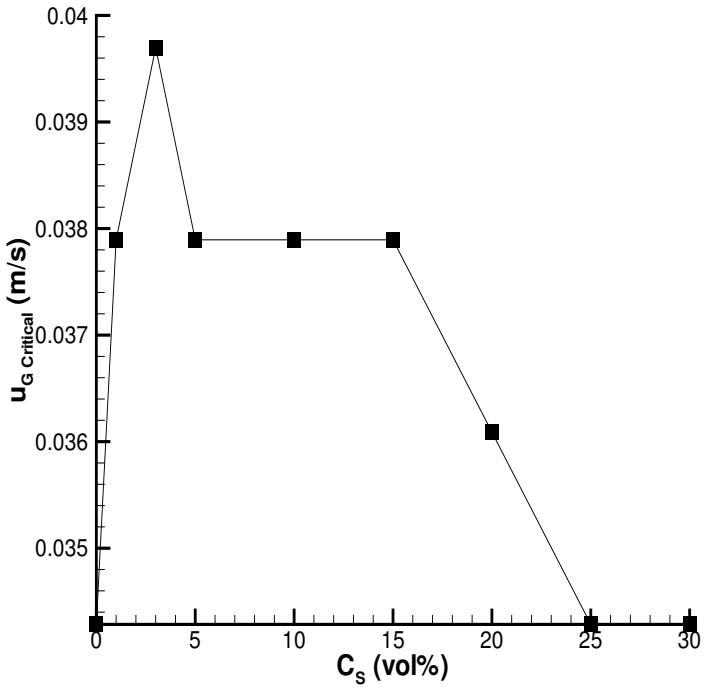

(b)

Figure 3.28. Main result: homogeneous regime stability measured by critical values of (a) voidage e_{G_C} and (b) superficial gas velocity u_{G_C}.

Discussion

The purpose of this discussion is to provide some suggestions regarding the explanation of the observed dual effect of the solids: first increase and then decrease of both the gas holdup e_G and the critical gas holdup e_{G_C}, and hence the increase and decrease of the HoR stability. Correspondingly, by Eq. 3.2, the presence of solids first reduces and then increases the mean bubble rise speed.

The suspended solids should be regarded as a new phase, and the original set of equations for the g-l system should be expanded to the g-l-s system. The difference between the solutions of the respective sets of governing equations is precisely the effect of solids, which is hard to predict. Therefore, we resorted to make a list of particular effects known from the literature, suggesting possible ways in which the presence of solids can affect the behaviour of the bubble bed. First, the corresponding physical mechanisms are explained, then the magnitude of the effect in case of our experimental data is assessed. In quantitative evaluations, the following relations between the gas holdup and the quantities that can be directly affected by the solids can be used: $e_G \propto 1/U$ by Eq. 3.2, $U \propto U_0$ by Eq. 3.3, $U_0 \propto ((\rho_L - \rho_g)d_b/\rho_L C)^{0.5} \approx (d_b/C)^{0.5}$, since $\rho_L \gg \rho_G$, so that with an error of order $O(10^{-3})$ the bubble speed does not explicitly depend on liquid density, $C \propto 1/Re$, $Re = \rho_L d_b U_0/\mu$ and consequently, $e_G \propto \mu^{0.5}$. Since the possible effects depend on the solid loading, they are evaluated at the point where the stability diagrams in Fig. 3.28 change their trends, i.e., at $C_S \approx 3\%$, or at solid volume fraction $f \approx 0.03$.

(i) The first effect is the **steric effect**, consisting in the simple fact that the solids occupy a certain space of the column. Consequently, the bubble concentration is different whether it is based on g-l or g-l-s volume. At any given u_G, the effective bubble concentration e_G^*, based on the g-l volume, is by a factor $1/(1-f)$, larger than the common voidage e_G used here and based on the g-l-s volume. Thus, the true critical value $e_{G_C}^*$ is also reached sooner, at lower gas input, hence there is destabilization. This effect can be particularly strong at large f, i.e., at high solid loadings. In our case, when the solid content is $C_S \approx 3\%$, this destabilizing effect is weak, $1/(1-f) \approx 1.03$, i.e., about 3%. However, at large C_S of 20-30%, this effect can contribute to the instability (descending branch in Fig. 3.28(a)).

(ii) The second effect is the **density effect**. Although the density itself should not affect the single bubble rise, the influence of solids can be estimated in terms of the effective (mixture, apparent) density:

$$\rho^* = (1 - f)\,\rho_L + f\rho_p \ . \tag{3.23}$$

The concept of effective density, hence buoyancy, applies only when the size d of a body (here a bubble) immersed in a dispersion is much larger than the size d_p of the dispersed particles. The quantitative criterium for the body and the particles of similar shapes is: $d > dp/f^{1/3}$. In our case, with almost neutrally buoyant dispersed particles ($\rho_p = 1023\ kg/m^3$), the solid-liquid density difference is as small as $O(10^{-2})$, so an effect of the same magnitude is expected due to the effective density, if applicable. Evaluation of the criterium for the applicability of the concept of effective density for $d = d_b \approx 0.004\ m$ and $d_p \approx 0.002\ m$, and for the characteristic solid loading $f \approx 0.03$ and maximum solid loading $f = 0.3$, one obtains $0.004 > 0.0064$ and $0.004 > 0.003$, respectively. This means that the concept is inappropriate at low solid content and only very weakly applies at large solid content. One conclude that the possible density effect is very minute.

(iii) The third effect is the **viscosity effect**. It relates to one particular change of the liquid flow field caused by the presence of solids. Each particle in the flow presents a new boundary surface with the no-slip condition, where the liquid velocity must accommodate to zero. Therefore, additional velocity gradients arise and the viscous dissipation increases. This is reflected in the effective (mixture, apparent) viscosity μ^* of a suspension, which is larger than that of a pure fluid and increases with the particle content. Consequently, the free rise speed of a buoyant body is reduced, not because of higher friction at the surface (it experiences the pure fluid), but due to the higher capacity of the flow to absorb the energy released by the body motion. Therefore, the concept of effective viscosity applies generally, whenever the dispersed particles are present, and regardless of their relative sizes or shapes comparing to the immersed body. With bubbles, the reduction of bubble rise speed results in larger gas holdup at the same gas input ($e_G \propto 1/U_0$), hence stabilization. On the other hand, the bubble coalescence is promoted in viscous media, bigger and fast bubbles are formed, which results in lower gas holdup, hence destabilization. Thus, the viscosity plays a dual role in the stability of uniform bubble bed. There are many studies

devoted to elaborating formulas for μ^* (e.g. Tsuchiya et al. (1997); N.-S. Cheng (2003)). A common form is a power series $\mu^*/\mu = 1 + b_1 f + b_2 f^2 + b_3 f^3 + ...$, with the coefficients b_1, b_2, b_3 of $O(10^0)$. The resulting figure can be modified by the fact that the effective viscosity increases with particle size and particle density. In our case, we had relatively large particles, however spherical and almost neutrally buoyant. At low solid loading, with typical $f \approx 0.03 \approx O(10^{-2})$, the viscosity effect is of the same leading-order $O(10^{-2})$: using the standard value $b_1 = 2.5$ it gives $\mu^*/\mu = 1.075$. Since $e_G \propto \mu^{0.5}$, the effect of gas holdup is $e_G^*/e_G \approx 1.037$, i.e., about $3-4\%$. This effect (reduction of bubble speed) can contribute to the increase of stability in Fig. 3.28. At high solid load, with $f \approx 0.2-0.3$, this effect is of $O(10^{-1})$ in viscosity, giving $\mu^*/\mu \approx 1.75$. This may not be enough to promote a massive coalescence, so that another effect must be responsible for the decrease of stability in Fig. 3.28.

(iv) The fourth effect concerns the **physical chemistry of surfaces**. Depending on the interfacial properties of the g-l-s system (hydro-philicity/phobicity, wettability, etc.), particles tend to increase or reduce their concentration near the g-l interface. The deposition at the bubble surface affects the original slip boundary condition. Stabilization of the surface then causes higher drag, hence lower rise speed. Bubble shape oscillations can also be affected, and the result in terms of bubble speed is difficult to assess. The concentration differences along the interface can serve as a driving force for various processes and complicated electrokinetic phenomena can be found. Changes in the interfacial properties affect the tendency to coalescence and breakup. These effects will be strong in the case of small particles, much smaller than the bubbles. In our case, the particles are big (comparable with bubble size) and completely wettable, thus, no interface effects are expected.

(v) The fifth effect concerns the **bubble size at detachment**, when the bubbles are formed in a suspension. In systems with a small effect of particle inertia, the influence of solids is negligible (Yoo et al., 1997), which is also our case. On the other hand, in the opposite case, the bubble size generally increases due to additional downward forces exerted by settling solids on the growing bubble (Luo et al., 1998). At low gas flow rates (lower than necessary for complete suspension) the solids settle on the plate and the bubbles coalesce there (Ityokumbul et al., 1995). In our case, with neutrally buoyant particles ($\rho_p \approx \rho_L$), we did not observe intensive particle settling so we conclude that this effect can

be neglected.

(vi) The sixth effect relates to **bubble rise velocity in suspension**. The contribution of effective viscosity is treated in (iii). Here, the effect of direct bubble-particle interactions is considered. Generally, the presence of particles reduce the bubble speed (Luo et al., 1997a), due to the hydrodynamic forces and mutual collisions. Both effects delay the bubble motion. One aspect of the retardation is the hindrance effect from particles to bubbles. This effect can be expressed in the form of a power series, $U_0^*/U_0 = 1 + B_1' f + B_2' f^2 + ...$, with the coefficients of $O(10^0)$ (e.g. Bly and Worden (1992)). Taking $B_1' \approx 5$ and $f \approx 0.03$, one obtains a 15% effect. Another effect is the lateral bubble motion induced and/or enhanced by collisions with the solid particles. The buoyant potential energy of a bubble is partitioned into more degrees of freedom to the detriment of the vertical velocity component. This results in a net reduction of the mean rise speed. In our case, the solids effect on

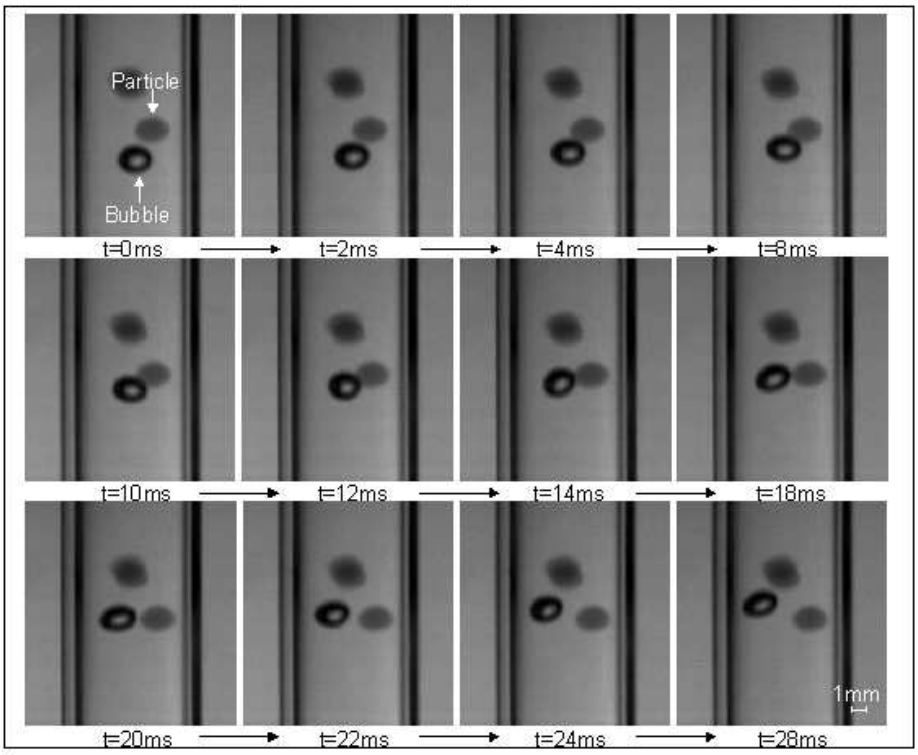

Figure 3.29. Bubble deflection from the vertical direction after collision with a solid particle.

bubble rise is documented by the auxiliary visualization experiments focused on a simple

situation. Fig. 3.29 shows a typical collision event, where a bubble is deflected from its original trajectory after the contact with a particle. These events were frequent in the bubble column and can contribute to the increase of stability in Fig. 3.28. Other phe-

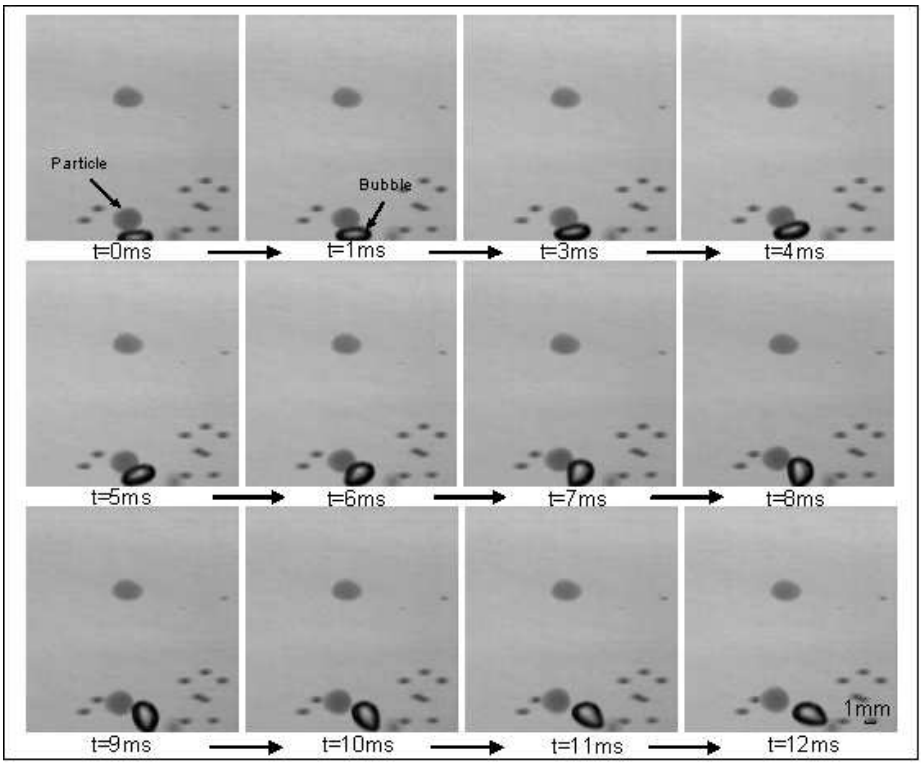

Figure 3.30. Bubble rotation caused by collision with a solid particle.

nomena may result from the bubble-particle contact: bubble rotation (see Fig. 3.30) and bubble shape oscillation (see Fig. 3.31) and both may reduce the bubble rise velocity. Preliminary estimates indicate that the speed reduction could be of 5-15%. Consequently, the hydrodynamic gas-solid interactions at low C_S can be important in stabilizing the bubble bed by reducing the vertical component of the bubble speed.

(vii) The seventh effect relates to **bubble coalescence in suspension**. This is usually considered to be the reason for the destabilizing effect of the solid phase. The properties of the solids are very important here. Depending on their size, density and surface properties (wettability), they can both suppress and promote the coalescence. The detailed mechanism of this phenomena has not been fully understood yet. In our case, during the

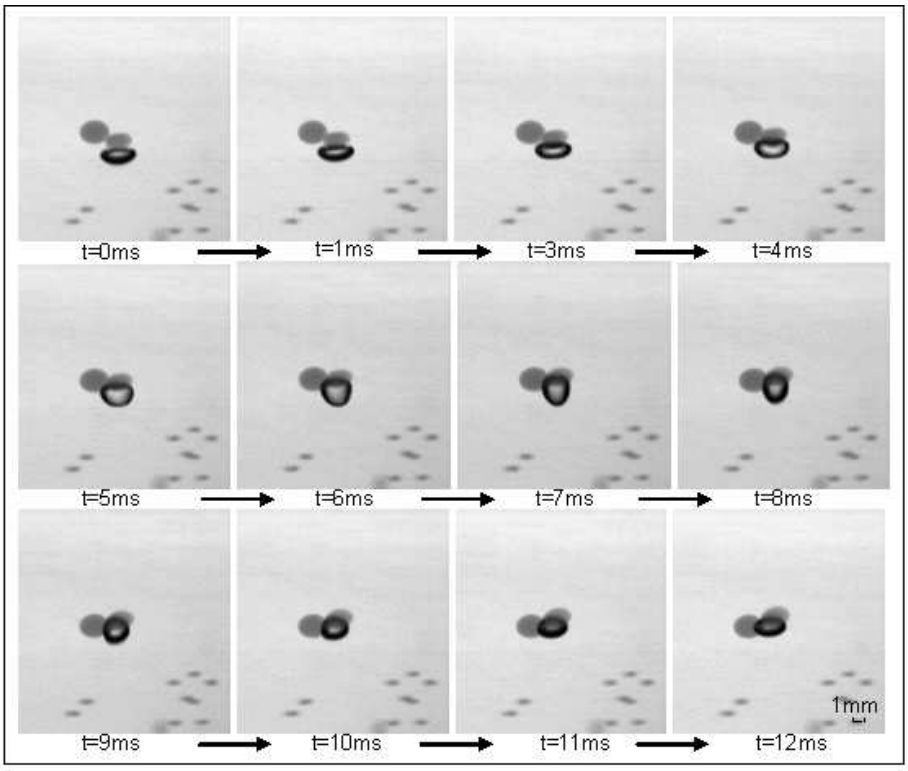

Figure 3.31. Bubble shape oscillation caused by collision with two solid particles.

visualization experiments we observed an increase in the number of coalescing events with increasing solid content. Fig. 3.32 shows a typical situation where the rise of two bubbles is hindered by a small cloud of solids so that they remain in contact for a long enough time to complete the coalescence process. We did not succeed in assessing this effect quantitatively.

(viii) The last possible effect mentioned here relates to **spatial inhomogeneities in the distribution of solid particles**. The homogeneity of the three-phase bed can be broken by nonuniformities originated in any of the two dispersed phases. When pronounced radial profiles develop in the solid phase, the flow regime transition can occur even if the bubbles are uniformly distributed. On the other hand, a statistically uniform distribution of solids can act against the clustering tendency of the gas phase, hence stabilizing the bed. Thus, interactions between two phenomena should be considered: (1) fluidization (sedimentation) of solids by liquid and (2) generation of bubbly layer, both uniform at low gas input and solid load. The mechanism of breakage of the uniformity in both cases is believed to

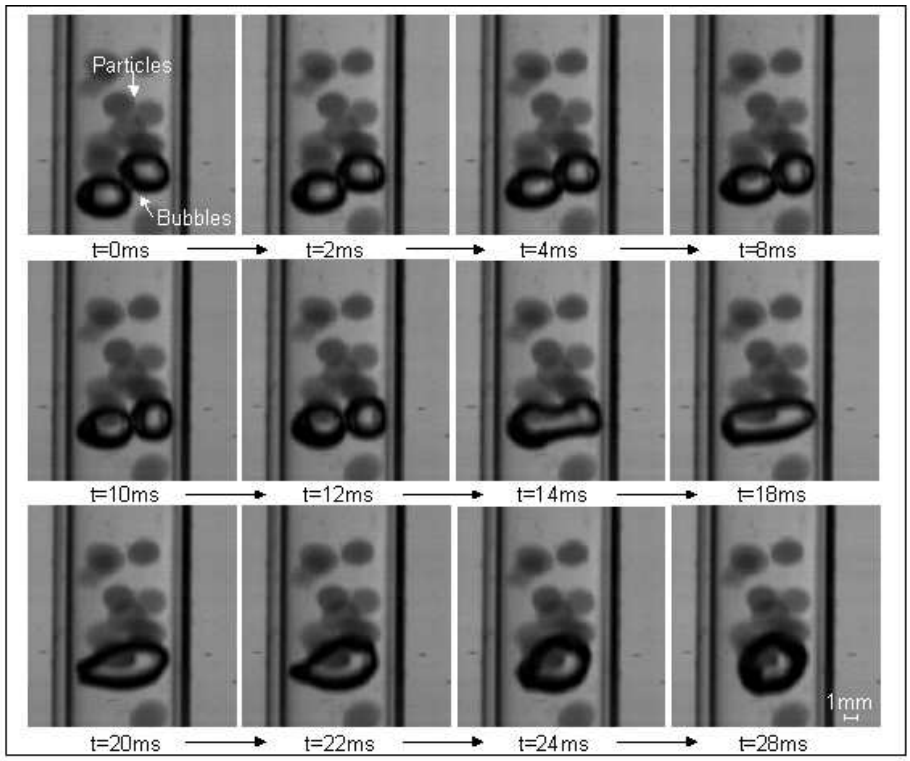

Figure 3.32. Bubble coalescence induced by collision with a swarm of solid particles.

be the advection of randomly formed buoyant clusters that introduces the large-scale motions and circulations. The clustering tendency of the dispersed phases finds its long-term expression in the nonuniform spatial profiles. In our case, with particles and bubbles of comparable sizes, we can presume a comparable tendency to the formation of clusters as a result of the action of hydrodynamic forces. Since the g-l density difference $\approx O(10^3)$ is much larger than the s-l difference $\approx O(10^{-2})$, the clusters of solids can generate only very small destabilizing buoyant energy, when compared to the buoyant energy generated by the clusters of bubbles. Therefore, we assume that the nonuniformity starts in the gas phase first.

Note that, qualitatively, the same dual effect on the stability of the homogeneous flow regime exerted by the presence of solids has been found for another important parameter - the liquid viscosity. Small viscosity stabilizes the uniform bubble bed while large viscosity destabilizes the bed. The underlying physical mechanism is currently under study (see subsection 3.3.2).

Summarizing, several effects can influence the stability of the HoR in three-phase systems. The most relevant effects in the present study are the steric effect, the viscosity effect, the bubble rise velocity in suspension, the bubble coalescence and the clustering tendency of the dispersed phases.

3.4 Conclusions

The aim of this study was to analyze the influence of relevant operating parameters on the flow regime transition and on the stability of the homogeneous flow regime in bubble columns. The parameters studied were: the presence of a surfactant (electrolyte) in the liquid phase, the viscosity of the liquid and the presence of a solid phase. The effect of these parameters was investigated separately.

The study of the influence of the electrolyte was performed using as liquid phase $CaCl_2$ solutions for the concentration range 0-0.1 mol/L. In the viscosity effect research, glycerol aqueous solutions, in the viscosity range 0.946-5.480 $mPa.s$ (0-50% of glycerol), were the liquid phases. And, in the solids effect investigation, calcium alginate beads ($d_p = 2.1\ mm$) were used was solid phase, for solid loading up to 30 $vol\%$.

In all these studies, the gas holdup (e_G) was measured by bed expansion, for increasing superficial gas velocities. These measurements were performed varying the key parameter (electrolyte concentration, viscosity and solid content). The $HoR - HeR$ flow regime transition was then determined by the Drift flux plot Wallis (1969), which is based on the concept of bubble slip speed. The theoretical bubble slip speed was calculated by the formula derived for the homogeneous regime (Ruzicka et al., 2001b). The critical values of gas holdup and superficial gas velocity (e_{G_C} and u_{G_C}) were our measures of the stability of the homogeneous flow regime.

To complement the solids effect study, auxiliary experiments in a smaller size bubble column were performed. These were focused mainly on the bubble-particle interactions and on the behaviour on bubbles rising through a liquid-solid bed.

In the study of the electrolyte influence on regime transition, a considerable increase of e_G was observed as $CaCl_2$ concentration increases up to 0.03 mol/L. The e_{G_C} and u_{G_C} also presented increases for that concentration range, showing that the regime transition is delayed, hence stabilizing the HoR. The $|CaCl_2| \approx 0.03\ mol/L$ is the limit electrolyte

concentration, above which the $e_G(u_G)$ dependence is weakly affected and e_{G_C} and u_{G_C} are almost constant.

This study presents also experimental results on the effect of the liquid viscosity on the stability of the HoR. One observed that at a certain viscosity ($\mu = 1.091\ mPa.s$), corresponding to 6% of glycerol, the dependencies of e_G, U (bubble slip speed), e_{G_C} and u_{G_C} on viscosity are completely changed. At low viscosities ($\mu = 0.946 - 1.091\ mPa.s$), the e_G increases with viscosity and further viscosity increases ($\mu = 1.091 - 5.480\ mPa.s$) result in a decrease of e_G. This suggests that viscosity may have an ambiguous effect on the e_G, that is surprising for low viscosity solutions. Moreover, at low viscosities ($\mu = 0.946 - 1.091\ mPa.s$), the bubble bed uniformity is positively affected by the viscosity, since e_{G_C} and u_{G_C} increase with viscosity, indicating that the bubble bed is stabilized at this viscosity range. This unexpected result is in agreement with the stability theoretical concept developed by Ruzicka and Thomas (2003), which predicts a stabilizing effect of viscosity on the HoR. One the other hand, for the viscosity range $\mu = 1.091 - 5.480\ mPa.s$, the stability of the HoR is reduced and consequently the flow regime transition occurs earlier, which is indicated by the decreases of the e_{G_C} and u_{G_C} as the liquid viscosity increases.

Finally, in the study of the effect of the solid phase on the $HoR - HeR$ flow regime transition, it was found that both e_G and critical values increased with the solid content at low solid loading (approximately $C_S = 0 - 3\ vol\%$), and decreased at higher loading ($C_S > 3\ vol\%$). The HoR was thus first stabilized and then destabilized. Therefore, as well as the liquid viscosity, the presence of the solids has a dual effect on the bubble bed stability. The most relevant mechanisms that can influence the stability of the HoR in three-phase systems are: steric effect, viscosity effect, bubble rise velocity in suspension, bubble coalescence and clustering tendency of the dispersed phases. Some of those effects were documented by auxiliary visualization experiments, that indicated the importance of hydrodynamic bubble-particle interactions.

Chapter 4

Local gas-phase characteristics in three-phase systems

4.1 Introduction

Many research groups working with bubble columns (Jianping and Shonglin, 1998), slurry columns (Reese et al., 1996; Warsito et al., 1999; Li and Prakash, 2000; Xie et al., 2003), fluidized beds (De Lasa et al., 1984; Thompson and Worden, 1997), airlift reactors (Freitas and Teixeira, 2001), bubbly flows and flotation columns, are interested in the complex gas-liquid-solid systems. Their wide application in various industrial processes such as chemical, petrochemical, biochemical and environmental is a strong evidence of their increasing importance. Despite all the research efforts, the knowledge about the effects of solids on gas-liquid system and the respective physical mechanisms are not yet clarified. The presence of the solid phase can influence the gas-liquid mixture in different ways such as bubble rise and formation, radial (Warsito and Fan, 2001) and axial profiles, mixing and dispersion, gas holdup and flow regimes (Zhang et al., 1997; Mena et al., 2005c) and mass transfer (Sada et al., 1985; Joly-Vuillemin et al., 1996; Mena et al., 2005a). A clear understanding of the hydrodynamics of the gas-liquid-solid (g-l-s) systems is needed to improve the design and operation of the processes involving these systems.

However, the operation and design of g-l and g-l-s reactors still relies, to a large extent, on empirical rules and correlations, which in turn are based on measurements performed under relevant conditions to industry. Modern approaches like computer fluid dynamics (CFD), which are used to help in the design of multiphase reactors, need also data on local

and transient flow characteristics to build physical models. Therefore, reliable measuring techniques are required for a rational design and description of multiphase reactors. The measuring techniques can be divided into non-invasive and invasive. There are many non-invasive techniques available to investigate the hydrodynamics of multiphase reactors. They can be used to measure global reactor characteristics, such as pressure drop, gas and liquid holdup, and to measure local characteristics like gas and liquid velocity or bubble size. However, there are many practical situations where non-invasive techniques are ineffective, particulary at nearly industrial operating conditions such as: particular physico-chemical phase characteristics, opaque walls (as for image analysis), high gas holdup (as for Laser Doppler Anemometry or Particle Image Velocimetry). Also, the non-invasive techniques are often not easy to apply and very expensive. Therefore, the invasive techniques are indeed very useful and examples of invasive probes are: the needle probe, the heat transfer probe, the ultrasound probe and the pitot tube. The needle probes are very thin and sharp ended. They are settled to face the flow direction, in order to pierce as many bubble as possible. Two main types of needle probes can be distinguished: optical fibre probes and the impedance probes (Boyer et al., 2002).

Phase detection probes are, in fact, frequently used in the investigation of gas-liquid two-phase flows (Cartellier, 1998) and more recently also in three-phase flows (Yang et al., 2001; Schweitzer et al., 2001; Boyer et al., 2002; Wang et al., 2003). Nowadays optical probes are able to measure not only phase concentrations but also bubble velocities, size distribution (Liu et al., 1998), mean interfacial area, mean Sauter diameter (Leung et al., 1995; Kiambi et al., 2001) and to identify flow regimes (Kozma, 1995). This information is of crucial importance to the description and modelling of multiphase flows. These characteristics, combined with their relatively simple operating principle and use, turn the intrusive phase detection probes very attractive for industry and research.

In the present work, the local structure of the multiphase flow is investigated with a monofiber optical probe in order to determine the variations of bubble flow properties along the column cross section. Auxiliary visualization experiments were performed to improve the post-treatment of the optical probe data and to understand the optical probe signal in three phase systems.

4.2 Experimental

4.2.1 Experimental conditions

The measurements were carried out in a cylindrical plexiglas bubble column of 0.072 m diameter and 0.5 m height. The column was equipped with a perforated plate with 0.6 mm orifices and relative free area ratio (φ) 1%. Compressed air from laboratory lines was the gas phase and tap water was the liquid phase. Calcium alginate beads, roughly spherical particles, with equivalent diameter $d_p = 2.1\ mm$ and density $\rho_p = 1023\ kg/m^3$ were the solid phase. The following solid loadings were used: 0, 5, 10, 15, 20, 25 and 30 $vol\%$. The clear liquid height was $h_0 = 0.295\ m$ for all experiments (no liquid throughput). Experiments were done for the following four superficial gas velocities 1.6, 2.7, 3.8 and 4.6 cm/s. The gas flow rate was read simultaneously from a rotameter and a mass flow meter.

4.2.2 Optical probe response for three phase systems

One question that remained unanswered since the beginning of the optical probe experiments was why in three-phase systems the signal showed peaks with higher amplitudes, besides the peaks of normal amplitudes (as in two phase flows). To investigate if the former peaks represent bubbles or solids, a parallel study was performed. In order to do that a high speed camera was synchronized with the optical probe data acquisition. The optical probe was located 28 cm high and at the center of the column. Using a pre-trigger, it was possible to start the image recording before the first high amplitude event was detected. The images were grabbed at 1000 $frames/s$ (see Fig. 4.1).

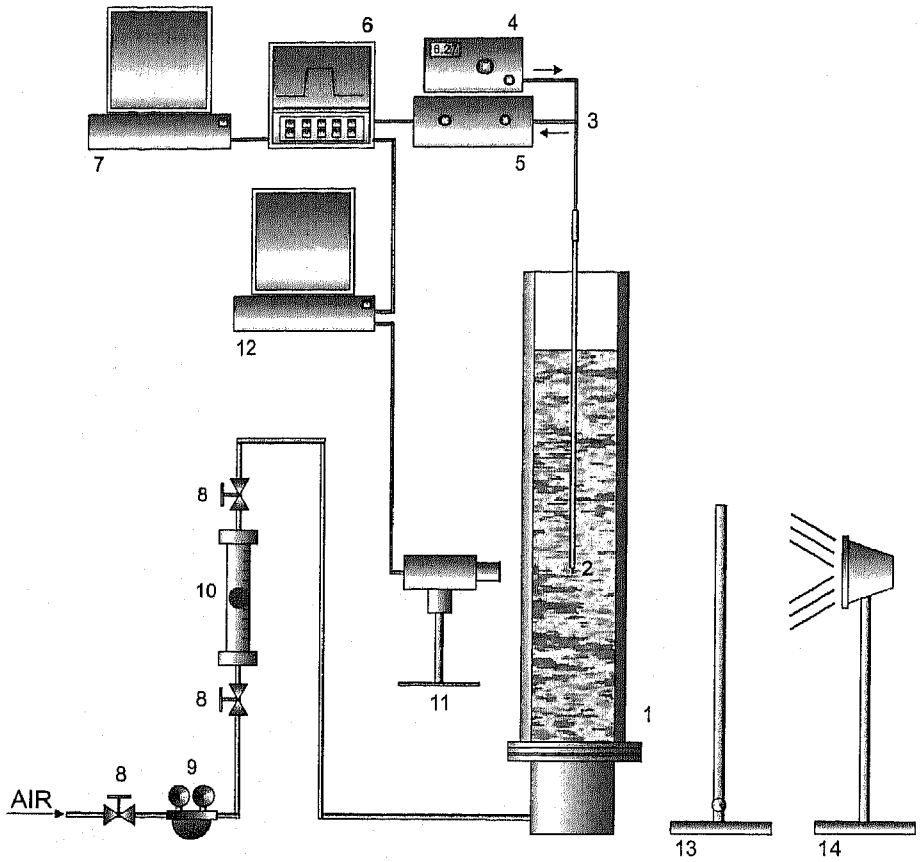

Figure 4.1. Experimental set-up for investigation of the optical probe response in three phase systems (1: Bubble column, 2: Optical probe, 3: Y junction, 4: Light emitter, 5: Light receiver and converter, 6: Oscilloscope, 7: PC1, 8: On/off valve, 9: Pressure reducer, 10: Rotameter, 11: High speed camera, 12: PC2, 13: Diffuser glass, 14: Halogen lamp).

4.2.3 Optical Probe Measurements

A monofiber optical probe, manufactured at Laboratoire des Ecoulements Géophysiques et Industriel (LEGI), Grenoble-France, is used to locally detect the presence of the gas phase in a multiphase system. A monochromatic light is transmitted through an optical fibre to the sensing conical tip. When the tip is dipped into a gas phase, the light is mainly reflected and travels back to the detector through a Y junction and is converted into an electrical signal. When the tip is immersed in a liquid environment, the light is scattered and almost no light is reflected back to the emitter/receiver device leading to a weak electric signal (Boyer and Cartellier, 1999). These electric signals are observed in a oscilloscope (see Fig. 4.2).

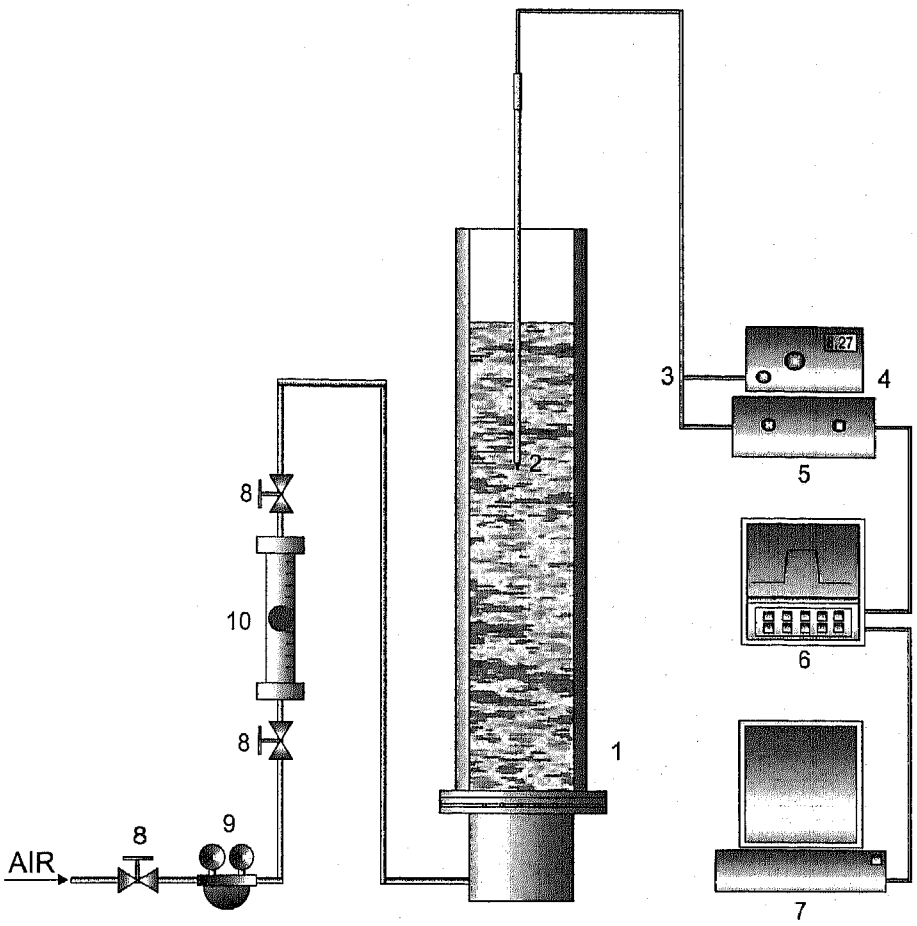

Figure 4.2. Experimental set-up for optical probe measurements (1: Bubble column, 2: Optical probe, 3: Y junction, 4: Light emitter, 5: Light receiver and converter, 6: Oscilloscope, 7: PC, 8: On/off valve, 9: Pressure reducer, 10: Rotameter).

The typical signal obtained by this probe when a bubble is pierced in a multiphase flow is shown in Fig. 4.3. The on-line acquisition data was done using the software $So2\_4$ developed at LEGI. This allowed to record, for each experiment, the rising time ($t_m = t_D - t_C$), the residence time ($t_G = t_B - t_A$), the arriving time (t_a) and the amplitude of the signal. These raw data are used to determine several gas phase characteristics, such as gas holdup and bubble velocity. The sampling rate was 100 KHz and the duration of the acquisition 300 s. The optical probe was located 28 cm from the gas sparger and measurements were performed varying the radial position.

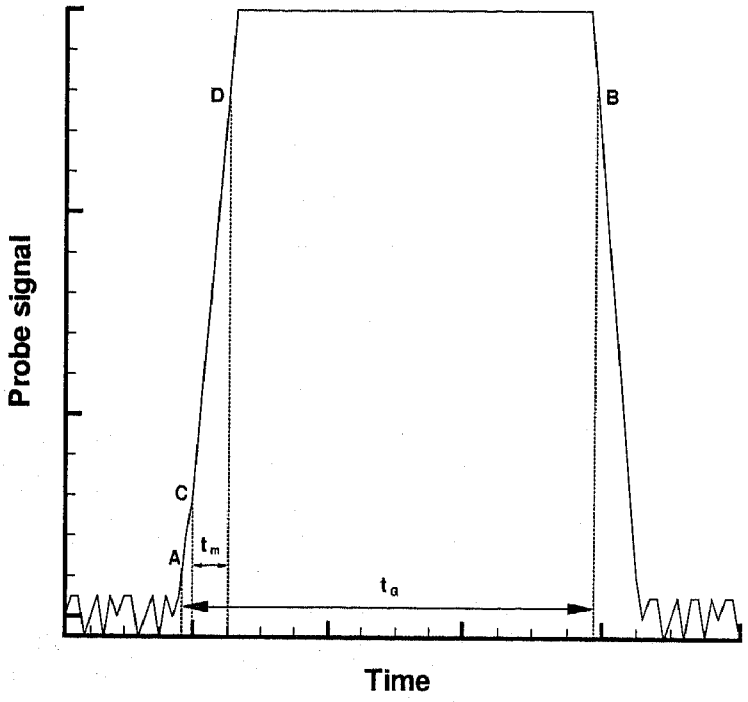

Figure 4.3. Typical signal of a bubble signature. t_G - residence time, t_m - rising time.

4.2.4 Visualization Measurements

To obtain the bubble sphericity, images were grabbed with a black and white digital video camera, which was connected to the PC through RS232. Sets of images (768x512 *Pixels*) were recorded for varying superficial gas velocities and solid loadings, for the same conditions used in the optical probe measurements. Backlight through a diffusing glass was found to be the most suitable lightning system (see Fig. 4.4). Due to the complexity of these three-phase systems (high solid loadings and void fractions) it was not possible to apply an automatic image treatment and this procedure had to be done "manually".

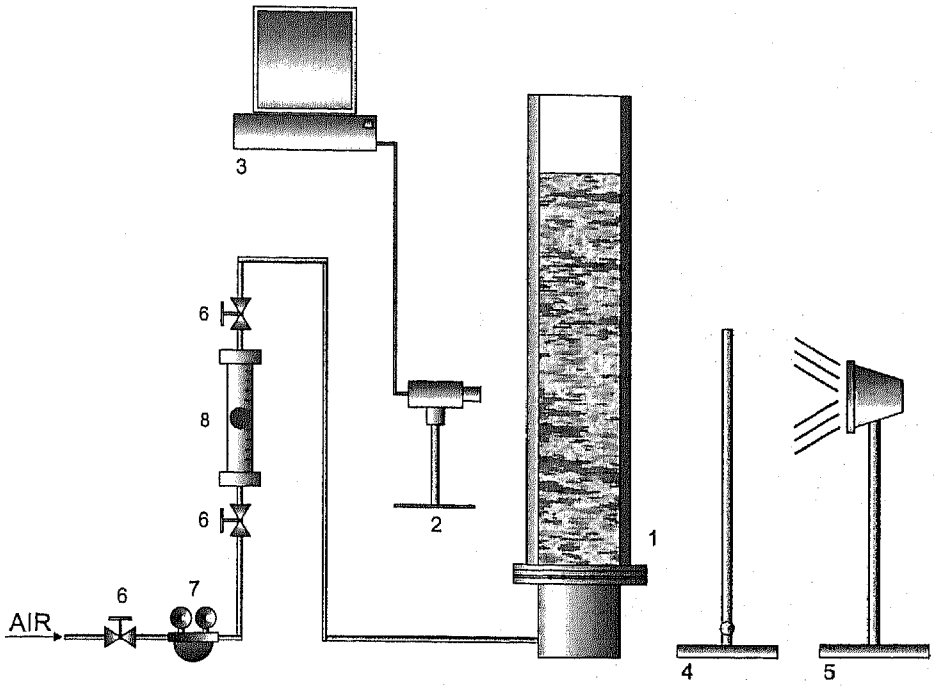

Figure 4.4. Experimental set-up for visualization measurements (1: Bubble column, 2: Digital camera, 3: PC, 4: Diffuser glass, 5: Halogen lamp, 6: On/off valve, 7: Pressure reducer, 8: Rotameter).

4.3 Results and discussion

4.3.1 Validity of the optical probe response for three phase systems

This study aimed to clarify whether the high intensity probe signals, observed in three phase systems, represent bubbles or solid particles in contact with the optical probe tip. A high speed camera, recording at 1000 fps, was synchronized with the optical probe signal acquisition in order to ascribe a certain probe signal to the respective event (see Fig. 4.1). A pre-trigger enables to start the image recording before the first high amplitude signal is detected. Several tests were performed, varying the solid loading, the superficial gas velocity and the trigger level. The results presented here correspond to an experiment performed at $u_G = 1.6\ cm/s$, 5 $vol\%$ of solids and trigger level of 2 V.

In Fig. 4.5 a typical probe signal is presented and the respective high speed camera image sequences are shown in Fig. 4.6.

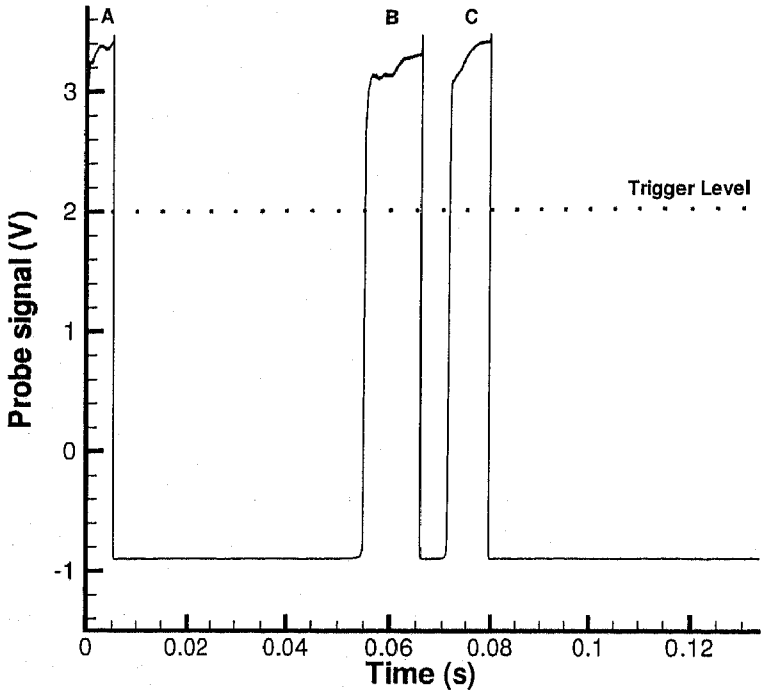

Figure 4.5. High amplitude signal observed for bubbles after probe tip hitting by a solid: A - solid piercing (seq A1-A3 in Fig. 4.6). B and C - bubble piercing (seq B1-B3 and C1-C3 in Fig. 4.6).

When a calcium alginate particle is pierced by the optical probe, the probe tip is contaminated with small solids which attach to the probe. This results in a high amplitude signal which is immediately detected by the probe (see signal A in Fig. 4.5 and sequence A1-A3 in Fig. 4.6). Due to the probe tip contamination, the next bubble piercings also exhibit high amplitude ($\approx$ 3.4 V), comparing to the normal amplitude ($\approx$ 1.3 V) for bubble detection (see signals B and C in Fig. 4.5 and sequences B1-B3 and C1-C3 in Fig. 4.6). The long time probe signal acquisition shown in Fig. 4.7 demonstrates that the high amplitude signal, resulting from a solid piercing, is kept for the next bubble piercing and then the signal stabilizes (for $t = 4.618$ s) at the typical bubble detection values.

It is important to mention that since the high amplitude signals represent bubbles (except the first one which reflects a particle piercing), they are considered for the gas holdup profiles. But as their amplitude is much higher than the regular amplitudes, the

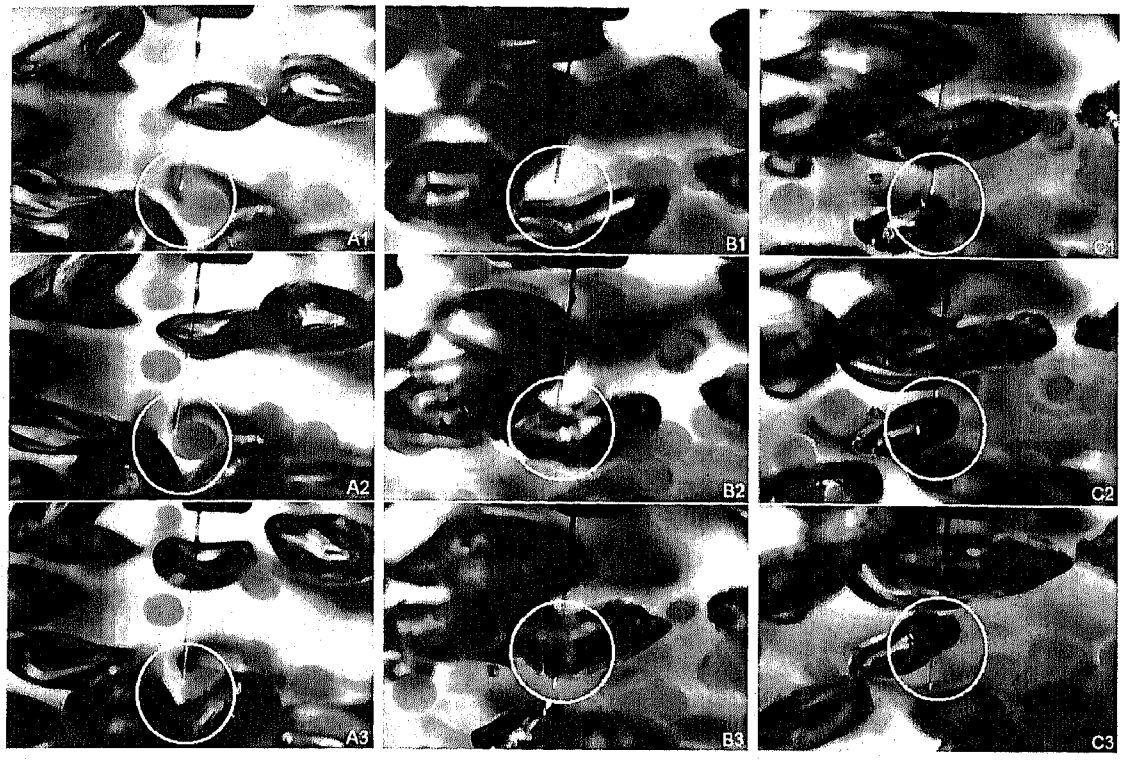

Figure 4.6. High speed camera image sequences of particle and bubble piercing: A1-A3 particle piercing; B1-B3 bubble piercing; C1-C3 bubble piercing.

calibration curve of the probe is no longer valid, and in the calculation of the parameters where bubble rising velocity is involved, these peaks must be rejected. Experiments with polystyrene spheres as solid phase were also carried out and no high intensity peaks were observed. This supports the contamination description since only soft and wettable particles, like calcium alginate beads, can contaminate the probe, and this phenomenon was not observed for the polystyrene rigid spheres.

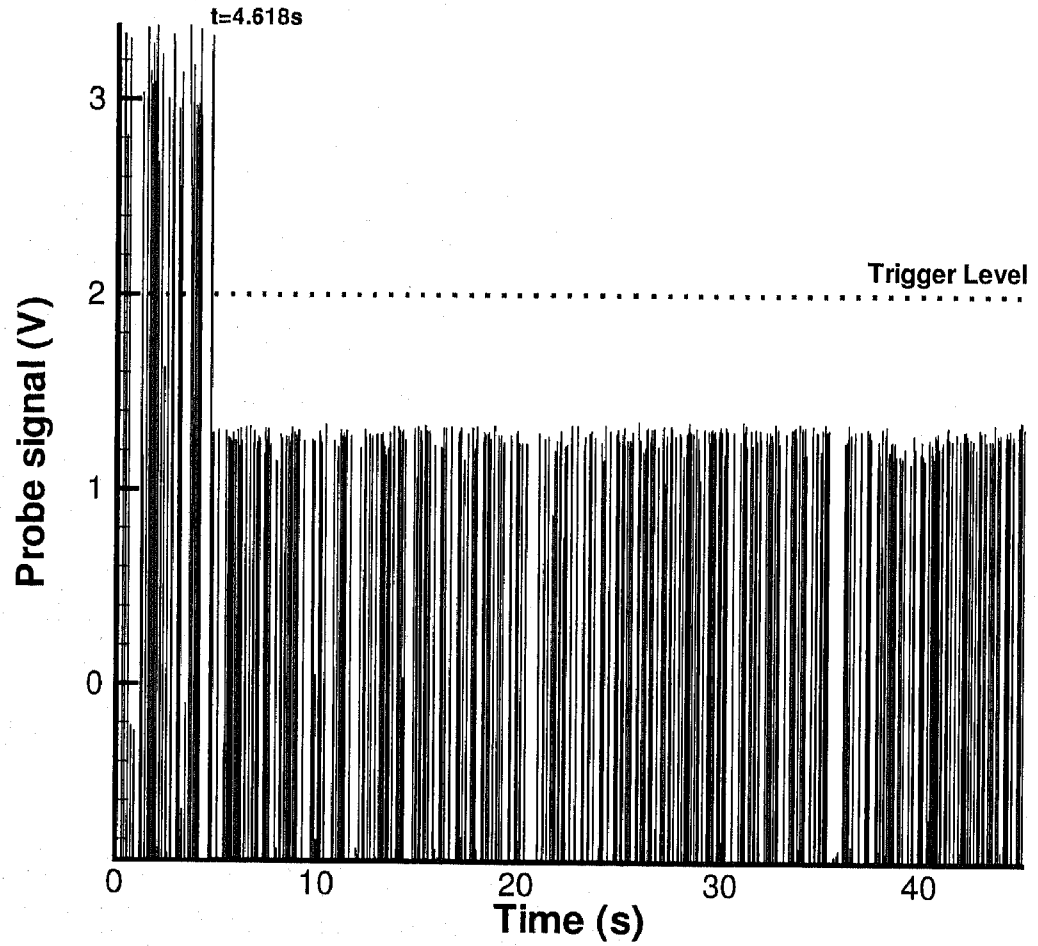

Figure 4.7. Probe signal during particle and bubble piercing (long time acquisition).

4.3.2 Optical Probe results

Gas holdup

As mentioned before, one of the parameters obtained in the optical probe measurements is the residence time t_G, which represents the time the optical probe is in contact with the gas phase, when a bubble is pierced by the probe. The local gas holdup (e_G) is defined as the ratio the sum of these times t_G over the total acquisition time (t_{acq}):

$$e_G = \frac{\sum t_G}{t_{acq}} \tag{4.1}$$

The local gas holdup profiles were measured for the range of superficial gas velocities from 1.6 to 4.6 cm/s and for solid loadings up to 30 $vol\%$ (Fig. 4.8). The profiles displayed are radial profiles, being r the radial probe position and R the bubble column radius.

The graphs plotted in Fig. 4.8 show that the gas holdup profiles are strongly affected by the presence of solids. As the gas velocity increases, the influence of solid loading is even more relevant. For lower solid loadings ($C_S = 0 - 20$ $vol\%$), the gas holdup profiles are flat and exhibit an increase near the wall. This increase can be attributed to the wall peaking effect, and this effect is more pronounced for lower gas velocities. It is mentioned in Deckwer (1992) that the wall effects are important for $D_C/d_b < 20$, and, in this case, $D_C/d_b = 0.072/0.005 = 14.4$ which confirms our previous expectations. From 20% of solids content, the profiles exhibit a negative parabolic curve with the maximum at the center. The flat gas holdup radial profile is typical for the homogeneous flow regime (HoR) while the parabolic dependence is typical for the heterogeneous flow regime (Ruzicka et al., 2001a). This radial profile change clearly shows a transition of flow regimes due to the increase of the solids loading. For solids content between 0 and 20 $vol\%$, the homogeneous regime prevails while for higher solids concentrations the heterogeneous regime is dominant. So, the local gas holdup profiles, obtained by the optical probe experiments, can be useful in the identification of the flow regimes and its transition.

The integration of the local gas holdup profile over the column cross section provides the mean gas holdup ($e_{G_{mean}}$):

$$e_{G_{mean}} = \frac{1}{\pi R^2} \int_0^R e_G 2\pi r dr. \tag{4.2}$$

In the previous chapter (Chapter 3), the voidage-superficial gas velocity dependencies were obtained by bed expansion and the flow regime transition was studied for the same three-phase systems (air-water-calcium alginate beads). In Fig 4.9, the black squares represent the critical points, where the flow regime transition begins, obtained in the regime transition study presented in the previous chapter (see subsection 3.3.3 for details). This figure shows that the gas holdups obtained in both studies are in good agreement, which validates the optical probe technique for the voidage measurements in multiphase systems.

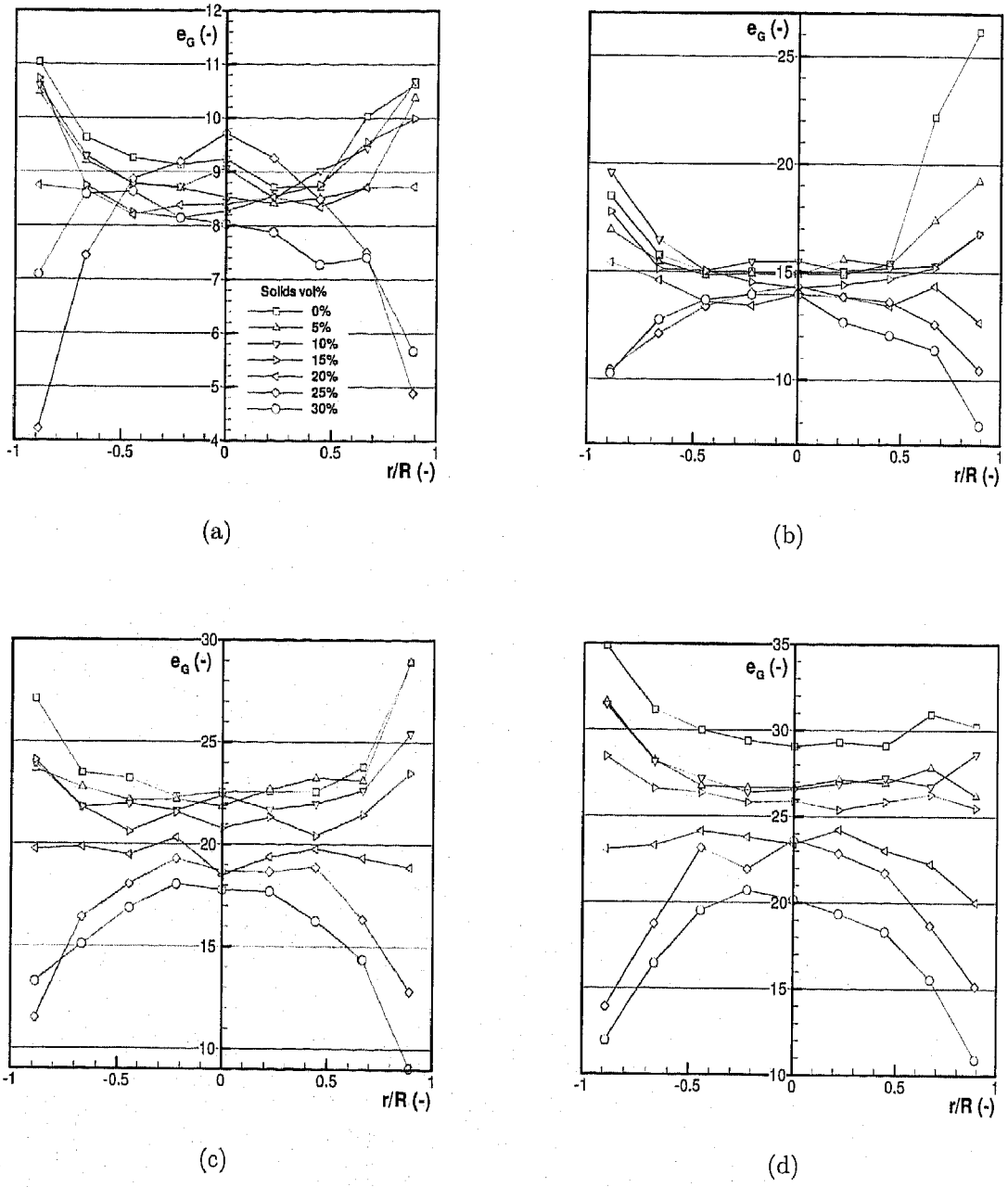

Figure 4.8. Radial gas holdup profile for: (a) $u_G = 1.6\ cm/s$; (b) $u_G = 2.7\ cm/s$; (c) $u_G = 3.8\ cm/s$; (d) $u_G = 4.6\ cm/s$. The symbols depicted in (a), for $vol\%$ of solids, are valid for the other subfigures.

From 0 to 20 $vol\%$ of solids, it is considered in the present study that the homogeneous regime prevails, which is in agreement with the previous study, except for the higher

superficial gas velocity ($u_G = 4.6\ cm/s$), for which it was previously considered that the transition had already occurred. For 25 and 30 $vol\%$ of solids, the heterogeneous regime is present for all u_G, while in the previous study the homogeneous-heterogeneous flow regime transition still occurs. These differences are certainly attributed to differences in the bubble column dimensions and in the gas distributor (see table 4.1).

Table 4.1. Comparison of experimental conditions between the regime transition study (Chapter 3) and the present study.

	$D_{column}(m)$	$d_{holes}\ (mm)$	$\varphi(\%)$
Reg. transition study (Chapter 3)	0.14	0.5	0.2
Present study	0.072	0.6	1

In the present study the column diameter is almost half of the one previously used and the column is now equipped with a gas distributor with bigger holes and higher relative free area (φ). Thus, bubble interactions and consequently bubble coalescence are promoted, and therefore, bigger and faster bubbles are formed enhancing liquid circulations and instability, which are responsible for the heterogeneous regime. In Fig. 4.10, the mean gas holdup increases almost linearly with the superficial gas velocity, as expected.

The increase of the solid content decreases the gas holdup, and this effect is stronger for higher superficial gas velocities. This result is in agreement with previous works (Lu et al., 1995; Banisi et al., 1995a; De Swart et al., 1996; Reese et al., 1996; Thompson and Worden, 1997; Jianping and Shonglin, 1998; Gandhi et al., 1999; Luo et al., 1999; Fan et al., 1999). In the present study, the gas holdup was also measured by bed expansion. In Fig. 4.11, a comparison between the mean gas holdup obtained from the optical probe measurements and the overall gas holdup measured by bed expansion is presented. A good agreement between the two techniques is observed validating the measurements conducted with the monofiber optical probe. The maximum and mean deviations between the results obtained with the two different techniques are of 22% and 7%, respectively.

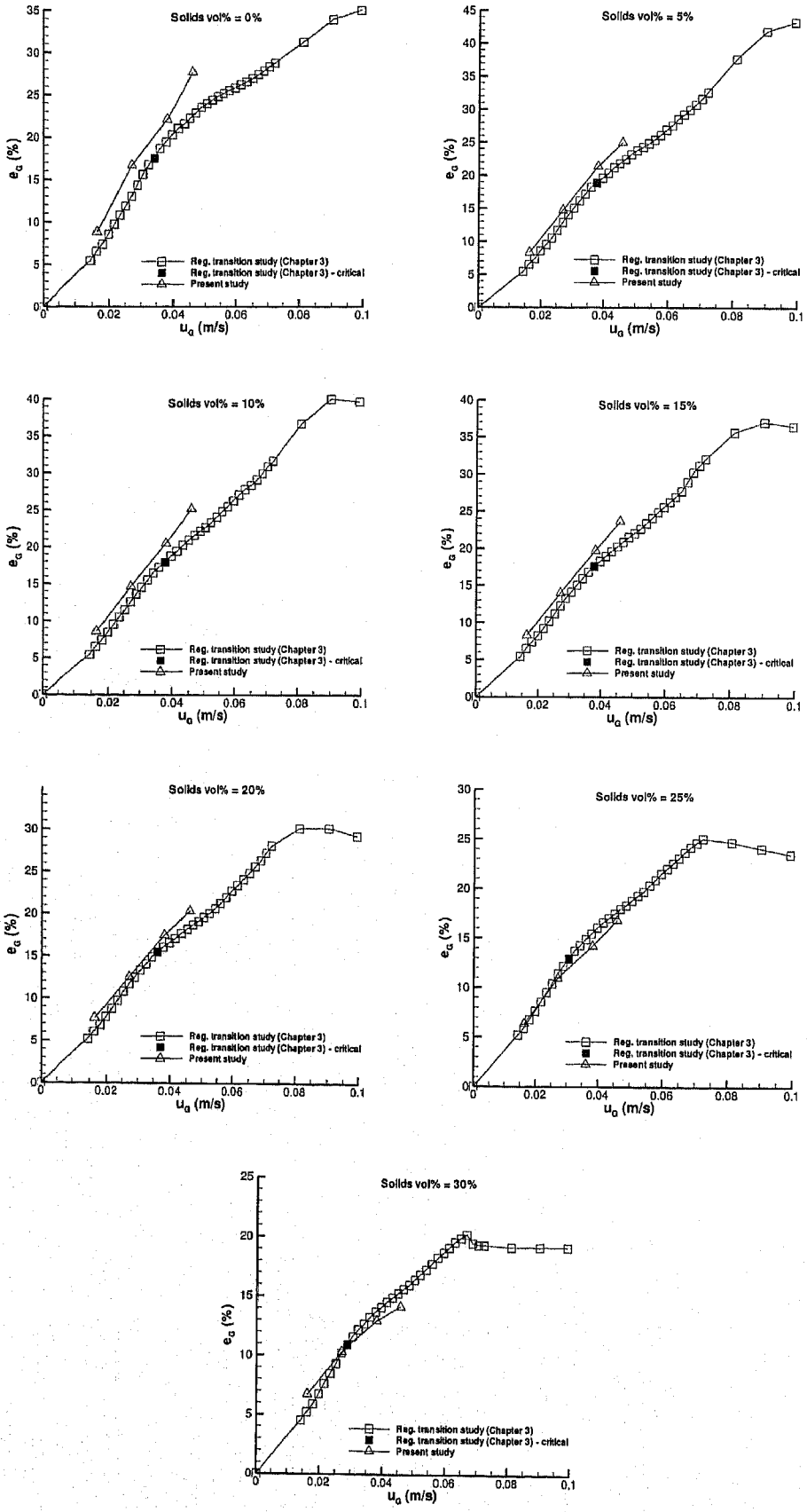

Figure 4.9. Comparison between the present study and regime transition study presented in Chapter 3.

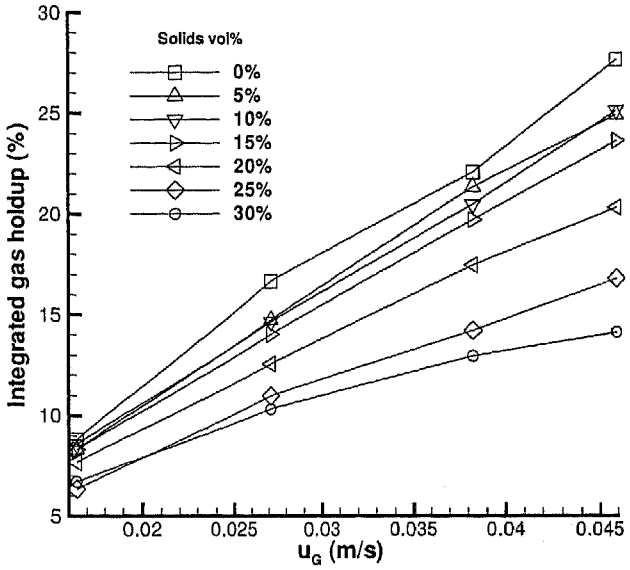

Figure 4.10. Integrated gas holdup as a function of superficial gas velocity.

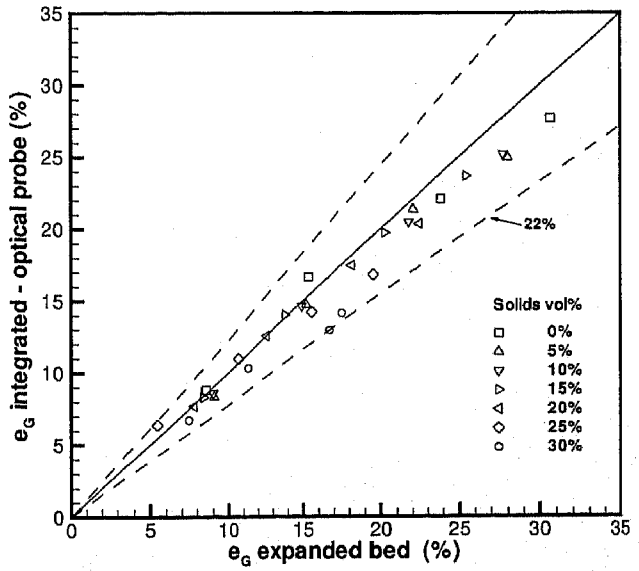

Figure 4.11. Comparison between gas holdup obtained by optical probe and by bed expansion.

Bubble rise velocity and bubble flow

The bubble velocity is determined using a correlation between the rising time (t_m) and the bubble velocity. This correlation is given by the probe calibration where the bubble velocity is estimated by a power function of t_m ($v_b = C'.t_m^{D'}$). The calibration curve found for this particular optical probe is presented in Fig. 4.12.

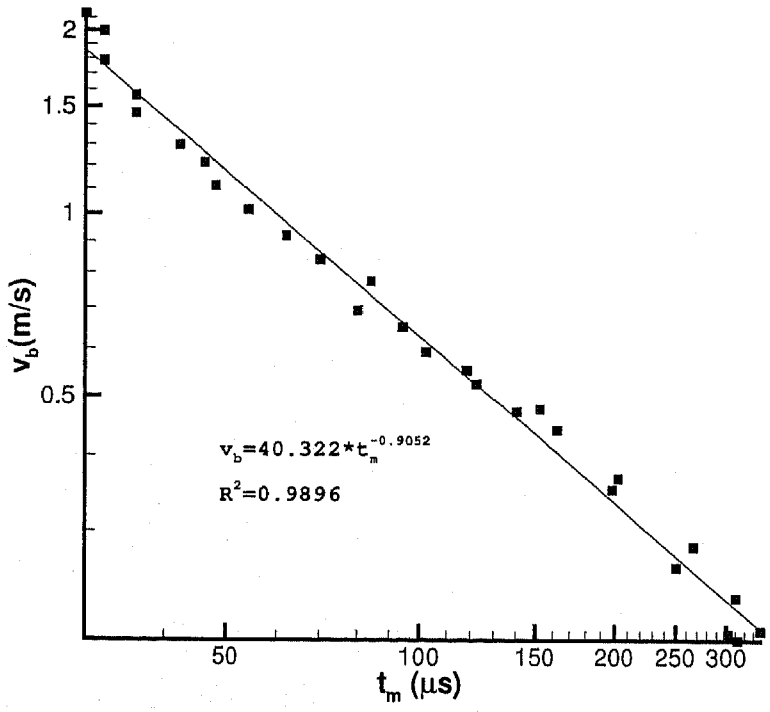

Figure 4.12. Calibration curve of the monofiber optical probe.

Fig. 4.13 shows the bubble rise velocity profiles for the superficial gas velocities studied here. There are unstable circulating cells inside the flow, with bubbles going downwards (which are not taken into account by the probe), causing disturbances on the instantaneous bubble velocity measurements. The bubble rise velocity profiles are influenced by the solid loading. As the solid content increases, the profiles change progressively from flat to non-uniform. One of the possible mechanisms that may be responsible for this behavior is the bubble coalescence. As observed in a previous chapter, the introduction of a third phase promotes bubble interactions due to bubble-particle collisions. The bubble

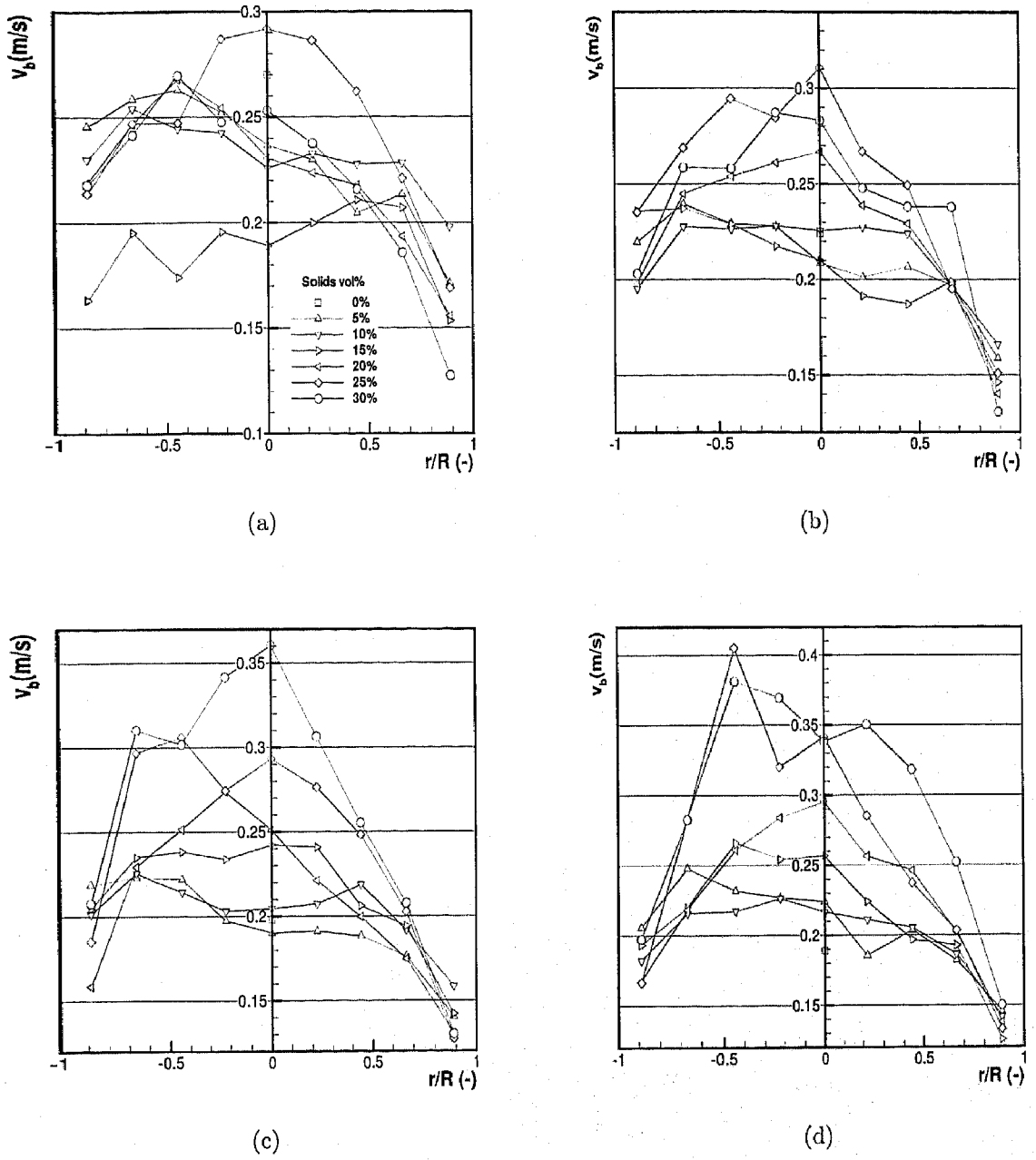

Figure 4.13. Bubble rise velocity profile for: (a) $u_G = 1.6\ cm/s$; (b) $u_G = 2.7\ cm/s$; (c) $u_G = 3.8\ cm/s$; (d) $u_G = 4.6\ cm/s$. The symbols depicted in (a), for *vol*% of solids, are valid for the other subfigures.

coalescence rate is then increased, resulting in bigger bubbles which rise faster and mainly through the center of the column, yielding in a parabolic radial bubble velocity profile. Li

and Prakash (2000) also observed an increase of bubble rise velocity with solids loading and Wang et al. (2003) denoted a slight change on the radial rise velocity profile as the solids loadings increased.

Since the average gas holdup (e_G) and bubble rise velocity (v_b) are known along the column cross section, the bubble flow rate (Q_b) can be computed as follows,

$$Q_b = \int_0^R e_G v_b 2\pi r dr \tag{4.3}$$

In Fig. 4.14 the measured values of the bubble flow rate are compared with real gas flow rates (measured by a rotameter).

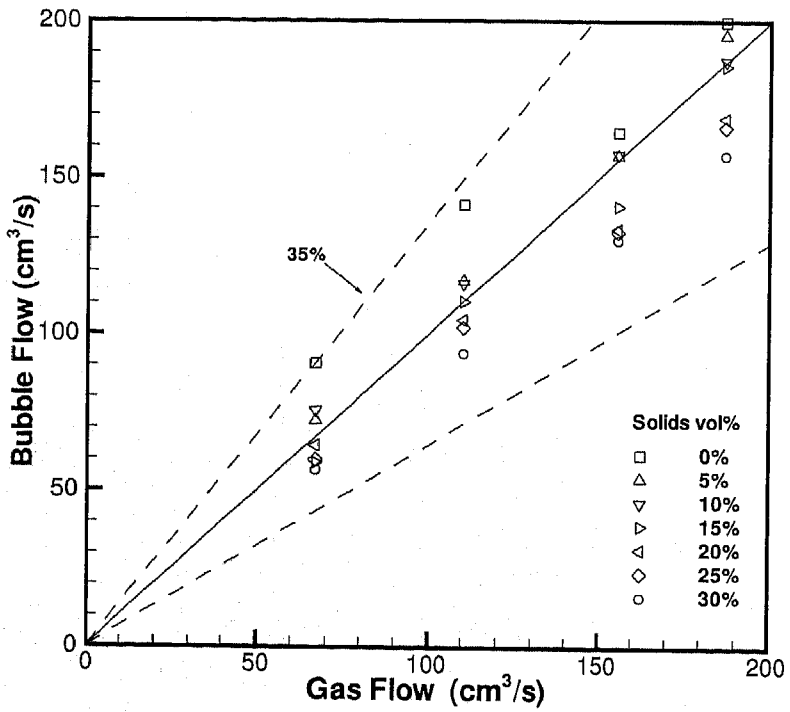

Figure 4.14. Comparison between bubble flow and gas flow.

A good agreement was found between bubble flow and gas flow, which validates both gas holdup and bubble rise velocity local measurements with the monofiber optical probe. The maximum and mean deviations between bubble flow and gas flow is of 35% and 10%,

respectively. The structure of the flow is complex with contra-rotative, non-stationary cells and the probe only detects bubbles on their upward motion. Nevertheless, the results obtained on the averages quantities are consistent with other results showed in the previous chapter and were well validated by independent measurements.

Gas-liquid interfacial area

The gas-liquid interfacial area (a) can be determined locally as,

$$a = 4\bar{f}'\overline{\left(\frac{1}{v_b}\right)}, \tag{4.4}$$

where f' is the bubbles frequency, which is defined as the ratio of the detected bubbles number ($n_{det.bubbles}$) over the total acquisition time (t_{acq}):

$$f' = \frac{n_{det.bubbles}}{t_{acq}} \tag{4.5}$$

and v_b is the bubble rise velocity. The integration of the local interfacial areas over the column cross section provides the mean interfacial area, a_{mean}:

$$a_{mean} = \frac{1}{\pi R^2}\int_0^R a 2\pi r dr. \tag{4.6}$$

It can be seen in Fig. 4.15 that the mean gas-liquid interfacial area is almost constant for solid concentrations up to 20 $vol\%$ and then decreases for further increases of solid loading.

This decrease is more pronounced for higher superficial gas velocities. This result is consistent with the results presented above, in particular, for the gas holdup radial profiles from which it was suggested that at 20 $vol\%$ a flow regime transition occurs. The knowledge of the gas-liquid interfacial area is essential to clearly understand the gas-liquid mass transfer behavior of three-phase systems. In Chapter 2, the gas-liquid interfacial area was determined for the same three-phase system and for concentrations up to 10 $vol\%$. In that case, visualization experiments were performed, followed by automatic image processing. It was observed that the interfacial area was not influenced by the solids particles, which agrees with the results of the present study.

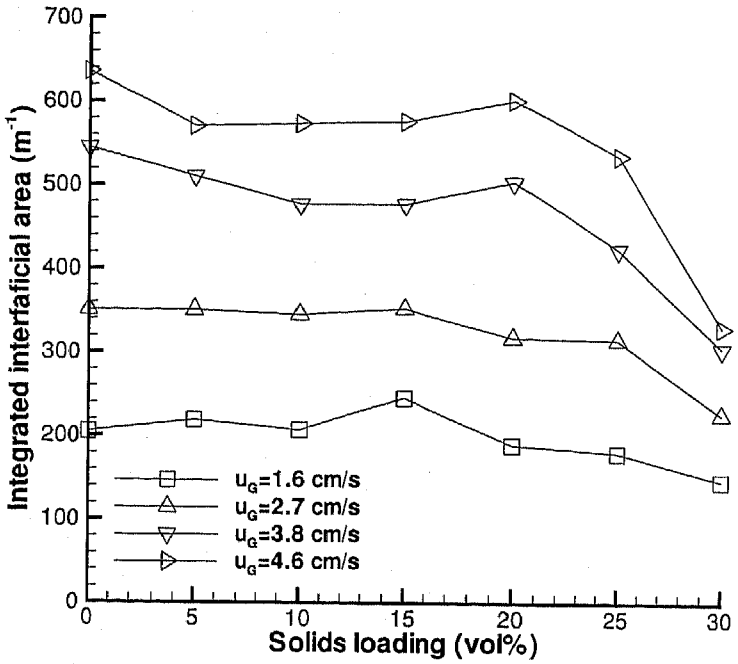

Figure 4.15. Interfacial area as a function of solids loading.

4.3.3 Visualization results - Bubble sphericity

For the same conditions of the optical probe measurements, images were recorded and treated in order to determine the bubble sphericities (Sp). Examples of images of air-water-calcium alginate beads systems recorded with the standard video camera are shown in Fig. 4.16. The minimum and maximum bubble lengths were obtained and the mean sphericity calculated from the ratio of these two quantities.

It can be seen in Fig. 4.17 that the bubble sphericity increases with superficial gas velocity and solid loading. A similar behavior was already observed in Chapter 2. A remarkable increase of sphericity is noted for the higher two solid concentrations, which is, once again, consistent with the gas holdup and interfacial area results. As the bubble coalescence rate increases, bigger and rounder bubbles are formed, increasing the bubbles sphericity, modifying the gas holdup profile and reducing the gas-liquid interfacial area. The flow regime is consequently affected and the turbulent or heterogeneous flow regime becomes predominant.

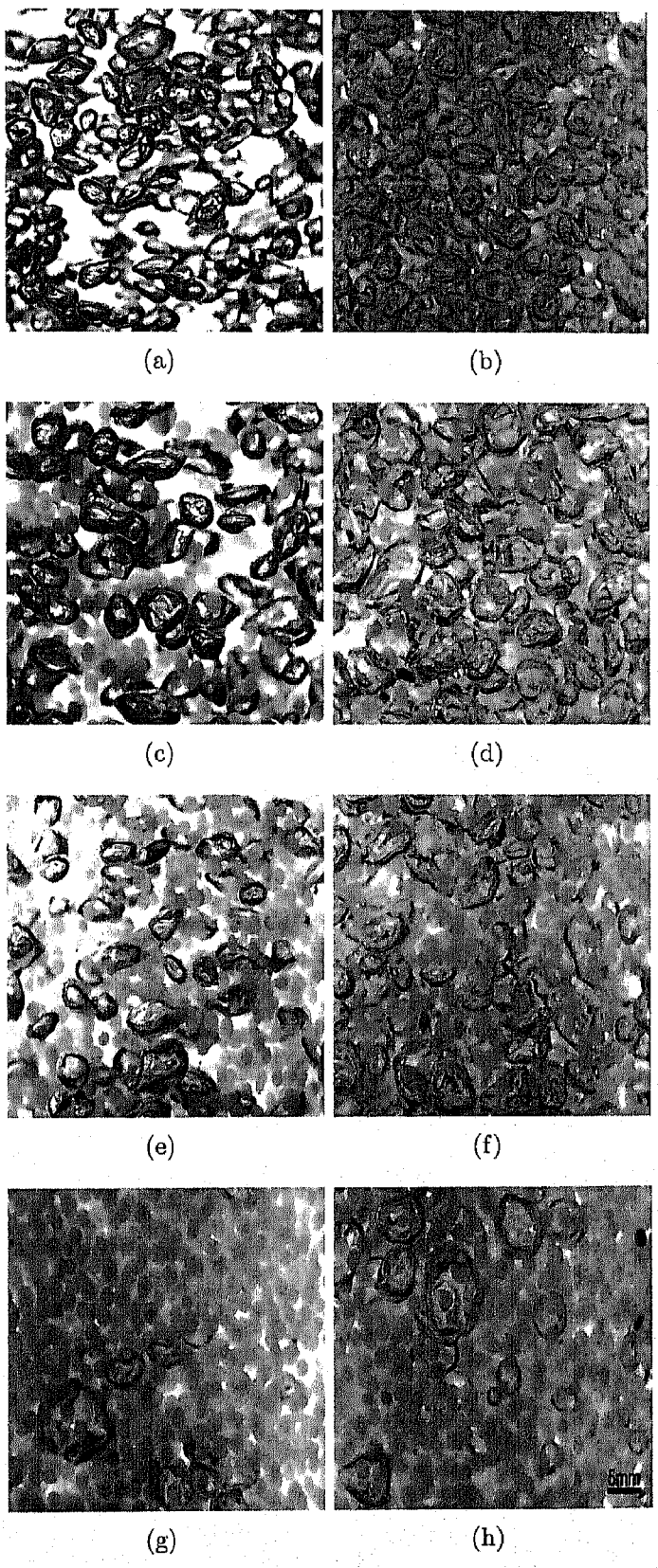

Figure 4.16. Examples of images of air-water-calcium alginate systems: (a) $u_G = 1.6\ cm/s$; $C_S = 0\ vol\%$ (b) $u_G = 4.6\ cm/s$; $C_S = 0\ vol\%$ (c) $u_G = 1.6\ cm/s$; $C_S = 10\ vol\%$ (d) $u_G = 4.6\ cm/s$; $C_S = 10\ vol\%$ (e) $u_G = 1.6\ cm/s$; $C_S = 20\ vol\%$ (f) $u_G = 4.6\ cm/s$; $C_S = 20\ vol\%$ (g) $u_G = 1.6\ cm/s$; $C_S = 30\ vol\%$ (h) $u_G = 4.6\ cm/s$; $C_S = 30\ vol\%$.

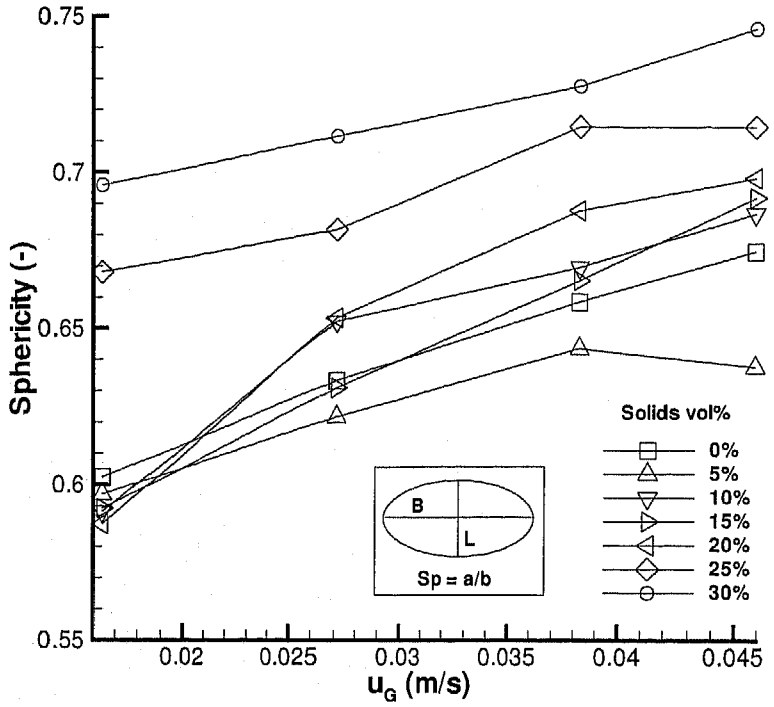

Figure 4.17. Bubble sphericity as a function of superficial gas velocity.

4.4 Conclusions

Local measurements of the gas-phase characteristics were performed in a three-phase bubble column, using a monofiber optical probe.

In spite of its fragile appearance, the probe proved to be very resistent even operating under hard solid concentrations and gas flow rate conditions. Frequently used in two-phase flows, the probe presented a remarkable performance, demonstrating that it can also be a useful tool for the three-phase flow studies.

The experimental results show that the radial gas holdup profile is affected by the presence of the solid phase and the mean gas holdup decreases with the solid content increase. It is observed that up to 20 *vol*% of solid concentration a flat gas holdup profile occurs, with an increase close to the wall. For solid concentrations higher than 20 *vol*%, a negative parabolic gas holdup profile is observed, suggesting an homogeneous-heterogeneous flow regime transition.

Bubble rise velocity radial profiles were also determined and changes from flat to non-uniform profile, due to increasing solid content, were observed.

The gas-liquid interfacial area remains constant for solid concentrations lower than 20 *vol%* and then decreases for higher concentrations. The optical probe technique was validated by independent measurements.

In visualization experiments, it was found that the bubble sphericity increases with the solid concentration, mainly for higher solid contents.

Bubble coalescence is probably the most important mechanism underlying the effect of solids (mainly for higher loadings) on gas phase properties in multiphase systems.

Chapter 5

General conclusions and suggestions for future work

5.1 General conclusions

The mass transfer and the hydrodynamics of three-phase bubble columns were experimentally investigated. The main purpose of this work was to study the influence of relevant phase characteristics on the gas-liquid mass transfer process and on the hydrodynamic behaviour of bubble columns, where three phases (gas, liquid and solid) are in contact. As the effect of the presence of a solid phase was not, so far, exhaustively investigated, most of this work was focused on the properties of the solid phase. The solids properties taken in account were: the type, the loading and the size. Attention was also given to the liquid phase. In particular, the effect of its viscosity and the presence of surfactants was characterized. Basically, three main studies were performed, the first devoted to the mass transfer in three-phase systems, the second to the flow regime transition and homogeneous regime stability in two-phase and three-phase flows, and the third focused on local measurements of gas phase characteristics in a three-phase bubble column.

In the first study, the influence of solid type, loading and size on mass transfer was analyzed. The individualization of the effect of those solid characteristics on the volumetric mass transfer coefficient (k_La) components (the liquid side mass transfer coefficient k_L and the gas-liquid interfacial area a) was achieved within certain operating conditions. k_La was determined by the dynamic method and a as well as other bubble characteristics were

determined through an image analysis technique, especially developed for that purpose. This technique proved to be suitable and practical for air-water and air-water-calcium alginate beads systems under the operating conditions used. However, image analysis revealed limitations for other three-phase systems, mainly when higher solid loadings and superficial gas velocities are used. Three types of solids were used: calcium alginate beads (d_p = 1.2 and 2.1 mm), "new" and "washed" polystyrene spheres (d_p = 1100, 769.8 and 591.2 μm) and hollow glass spheres (d_p = 9.6 μm).

In the experiments with calcium alginate beads as solid phase, the solids loading decreases k_La, mainly for the smaller solids. As solid size decreases k_La also decreases, due to simultaneous variations of a and k_L in the same direction, mainly for higher solid contents. The bubble shape is also affected by the presence of the solid phase.

In the experiments with polystyrene beads as solid phase, it was found that the k_La increases with the superficial gas velocity (u_G) and this dependence generally flattens for increasing solid content. When solid loading increases, the k_La values decrease. One verified that the k_La values for the systems with "new" polystyrene beads were considerably lower than for the "washed" polystyrene beads, confirming the negative influence of fine polystyrene particles on k_La. Comparing the experimental k_La values for the three sizes, we conclude that the effect of solid size on k_La is not constant but, in general, k_La decreases as the solid size decreases, as in the air-water-calcium alginate beads systems.

Experiments in a three-phase slurry of 9.6 μm hollow glass spheres showed a dual effect of these fine solids loading on k_La, demonstrating that k_La can also be enhanced by the presence of the solid phase.

In the second study, the influence of important operating parameters on the flow regime transition and on the stability of the homogeneous flow regime (HoR), was studied. The gas holdup (e_G) was measured by bed expansion. The $HoR - HeR$ flow regime transition was determined by the Drift flux plot (Wallis, 1969), which is based on the concept of bubble slip speed. The critical values of gas holdup and superficial gas velocity (e_{G_C} and u_{G_C}) were the experimentally obtained parameters used to characterize the stability of the HoR. To complement the solids effect study, auxiliary visualization experiments, focused mainly on the bubble-particle contact and on the behaviour of bubbles rising through a liquid-solid bed, were performed with a standard and a high speed camera.

In the study of the electrolyte influence on regime transition, a considerable increase

of e_G, e_{G_C} and u_{G_C} was observed as the $CaCl_2$ concentration increased up to 0.03 mol/L, showing that the regime transition is delayed, hence stabilizing the HoR. That salt concentration is the limit, above which the $e_G(u_G)$ dependence is weakly affected and e_{G_C} and u_{G_C} are practically constant.

The study of the viscosity effect on regime transition, showed the surprising result, that at low viscosities ($\mu = 0.946 - 1.091\ mPa.s$), the uniform bubble bed is stabilized, since both e_{G_C} and u_{G_C} increase with viscosity.

Finally, in the study of the solid phase effect on the flow regime transition, it was found that both e_G and critical values increased with the solid content at low solid loading (approximately $C_S = 0 - 3\ vol\%$), and decreased at higher loading ($C_S > 3\ vol\%$). Thus, the HoR was first stabilized and then destabilized. So, as for the liquid viscosity, the presence of solids has a dual effect on the bubble bed stability. Various possible physical mechanisms underlying this dual effect were discussed. Auxiliary visualization experiments indicated the importance of hydrodynamic bubble-particle interactions.

In the third study, local measurements of the gas-phase characteristics were performed in a three-phase bubble column, using a monofiber optical probe. In spite of its fragile appearance, the probe proved to be very resistant even operating under hard solid concentrations and gas flow rate conditions, showing that it can be a very powerful tool in the three-phase flow study.

Experimental results showed that the mean gas holdup decreases with the solid content increase. For solid contents up to 20 $vol\%$, a flat gas holdup profile occurs, with an increase close to the wall, while for loadings higher than 20 $vol\%$, a negative parabolic gas holdup profile was observed, suggesting a $HoR - HeR$ flow regime transition. Bubble rise velocity radial profiles changed from flat to non-uniform due to increasing solid content. The gas-liquid interfacial area remains unchanged for solid concentrations lower than 20 $vol\%$, decreasing for higher concentrations. The optical probe technique was validated by independent measurements. Visualization experiments revealed that the bubble sphericity increases with the solid concentration, mainly for higher solid contents.

In this work, advances were made, namely in techniques and results, concerning the effect of solid phase on the mass transfer and on the hydrodynamics of the complex gas-liquid-solid systems.

An innovative image analysis technique was specially developed for the study of bubble characteristics in two- and three-phase systems. The monofiber optical probe was successfully used in three-phase flows, demonstrating a huge potential. The high speed camera revealed to be a very promising technique in the fundamental study of the bubble-bubble and bubble-particle hydrodynamic interactions.

Therefore, progresses have been made, in this thesis, on the comprehension of the complicated gas-liquid-solid systems. The results obtained can be very useful for improving the design and operation of the industrial equipment that works with these kind of systems. Moreover, better performances can be achieved in the physical and chemical processes involving gas-liquid-solid systems.

5.2 Suggestions for future work

Since the research in this field is far from being complete, some future work suggestions are given here, which follow the stream line of the present work.

The characterization of the global hydrodynamics of three-phase contactors should be continued. Particularly, the study of the gas holdup dependence on relevant solid characteristics such as surface properties (hydrophobicity), shape, size and loading; and the investigation of the influence of those solid characteristics on flow regime transition. Different types of solids, with unquestionable importance for industry, such as bacteria and yeasts, should be investigated. In order to identify and clarify the mechanisms underlying the global hydrodynamics results, two complementary investigations may be conducted. One, on a macroscale, is the characterization of the local hydrodynamics of three-phase flows, which could be performed using a monofiber optical probe. And another, on a microscale, is the fundamental study of the bubble-bubble and bubble-particle interactions, namely, the study of the mechanisms involved on the bubble coalescence phenomenon and on the attachment of particles to the bubble surface. These studies would, certainly, help to understand the solids effects on gas-liquid mass transfer process.

Appendix A

Image Analysis

In this appendix, the parameters used to describe the objects within an image are presented and defined. Also, the image processing commands applied in the image analysis automatic treatment are described. Finally, examples of images of different gas-liquid and gas-liquid-solid systems are presented.

A.1 Image descriptors

In this section, the parameters used to characterize the objects of an image are presented. The characterization retrieves object important information, concerning its position, size and shape.

Barycenter X

Abscissa of the object gravity center.

Barycenter Y

Ordinate of the object gravity center.

Projected area (S)

Theoretically, the area of an object X in 2 dimensions is defined in the continuous case as:

$$S(X) = \int_X dxdy \tag{A.1}$$

But here, the area is defined in the discrete case and is approximated by the number of pixels inside X:

$$S(X) = \sum_{ij} g\left(x_i, y_j\right) \tag{A.2}$$

where,
$g(x_i, y_j) = 1$, if the pixel is inside the object X
$g(x_i, y_j) = 0$, if the pixel is outside the object X

Feret diameters

The Feret diameter represents the straight distance between two parallel tangents to the object (Fig. A.1). The position of the tangents is determined by the angle θ between the tangents and the abscissa axis. The angles are previously selected in the $0^o - 180^o$ range (Fig. A.1).

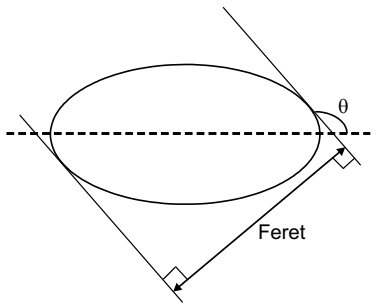

Figure A.1. Feret diameter.

Maximum Feret diameter (F_{max})

F_{max} is the maximum straight distance between two parallel tangents to the object (Fig. A.2).

Minimum Feret diameter (F_{min})

F_{min} is the minimum straight distance between two parallel tangents to the object (Fig. A.2).

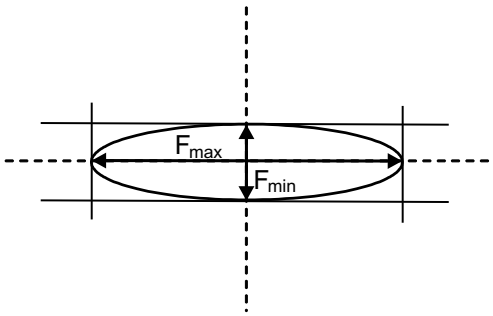

Figure A.2. Maximum and minimum Feret diameters.

Maximum Feret diameter+90^o ($F_{max} + 90^o$)

$F_{max} + 90^o$ is the Feret diameter positioned 90^o from the maximum Feret diameter (Fig. A.3).

Equivalent diameter (d_{eq})

d_{eq} is the diameter of the circle with the same area as the projected area of the object (Fig. A.4).

Analytically, the equivalent diameter is expressed as,

$$d_{eq} = 2\sqrt{\frac{S}{\pi}} \ . \tag{A.3}$$

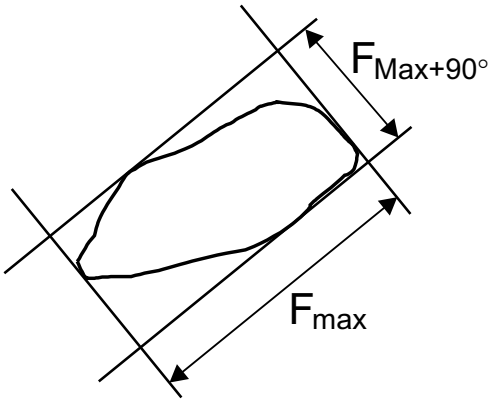

Figure A.3. Maximum Feret diameter+90^o.

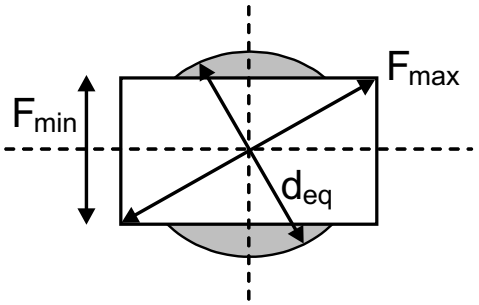

Figure A.4. Equivalent diameter.

Elongation parameters

Two parameters can be defined: the elongation (F_{max}/F_{min}) and the aspect ratio (F_{max}/d_{eq}) (Fig. A.5).

Circularity (Circ)

This parameter measures the elongation and rugosity of an object (Fig. A.6). The circularity is determined by the following expression:

$$Circ = \frac{P^2}{4\pi S} \tag{A.4}$$

where P is the perimeter of the object.

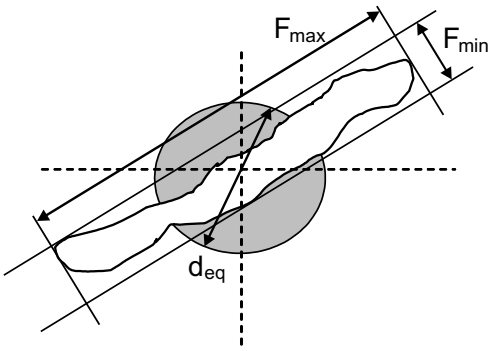

Figure A.5. Elongation parameters.

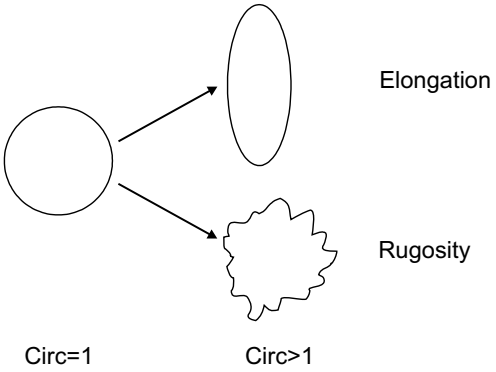

Figure A.6. Circularity.

Convex bounding polygon (CBP)

First, n equally spaced points are selected in the border of the object and then $n-1$ straight lines depart from each point to the remaining points. These lines will cover the cavities that might exist, involving the object in an 'envelope' (Fig. A.7). In the example shown in Fig. A.7, the straight lines were drawn only from two points, but actually this procedure is done for all selected points.

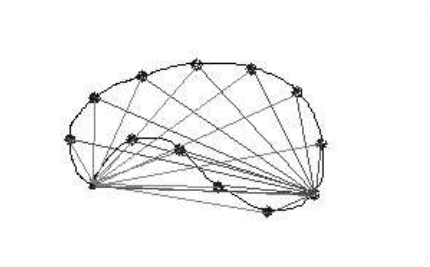

Figure A.7. Convex bounding polygon.

Robustness

Successive erosions are performed until the object disappears. The robustness Ω_1 of the object is the normalized number of erosions,

$$\Omega_1 = \frac{2\omega_1}{\sqrt{S}} \tag{A.5}$$

where ω_1 is the number of erosions needed to totally erase the object.

Biggest concavity

All the cavities of the object are obtained if the difference between the convex bounding polygon and the object (C.B.P. - Obj) is done (Fig. A.8). Successive erosions are performed in the resulting image and the number of erosions needed to erase it is defined, after normalization, as the biggest concavity Ω_2 of the object,

$$\Omega_2 = \frac{2\omega_2}{\sqrt{S}} \tag{A.6}$$

where ω_2 is the number of erosions necessary to erase the object 'CBP-Obj'.

Concavity Index (CI)

The concavity index is determined by the following ratio,

$$C.I. = \frac{S_{Obj}}{S_{CBP}} \tag{A.7}$$

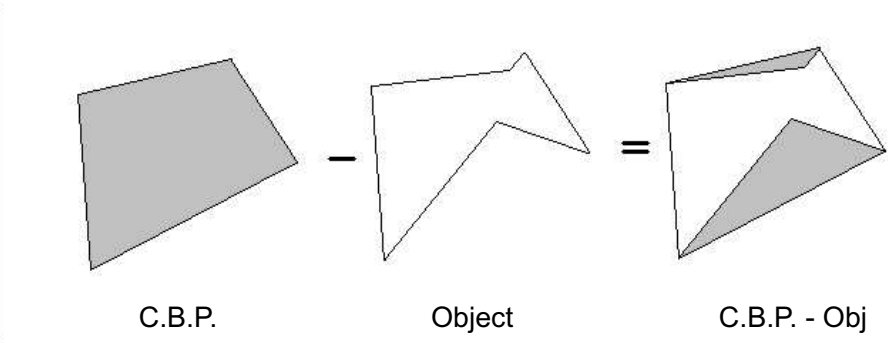

Figure A.8. Biggest concavity.

where S_{Obj} and S_{CBP} are the projected area of the object and of the convex bounding polygon, respectively.

Sphericity (Sp)

The sphericity is the roundness of a 3-dimensional object. Since our images retrieve only two dimensions of the objects, and assuming that the objects are elliptical, we define sphericity as:

$$Sp = \frac{L}{B} \tag{A.8}$$

where L is the minor axis and the B is the major axis of an elliptical object (Fig. A.9).

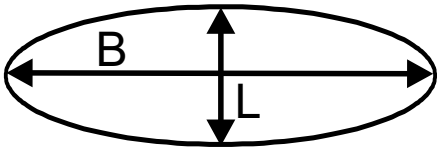

Figure A.9. Bubbles sphericity.

A.2 Image Processing

In this section, the image processing tools used to automatically treat the images are illustrated.

Binarization

The binarization transforms a grey-level image into a binary image. This method is used when the relevant image information is only in a certain grey-level region. In a binary image the value 1 is ascribed to the pixels of interest and the value 0 (background) to the rest.

- **Threshold**
  The threshold originates a binary image between two levels (λ_1,λ_2), which are defined by the user. In the final binary image all the pixels whose grey-level is between λ_1 and λ_2 is ascribed the value 1 and all the others the value 0 (Figs. A.10 and A.11).

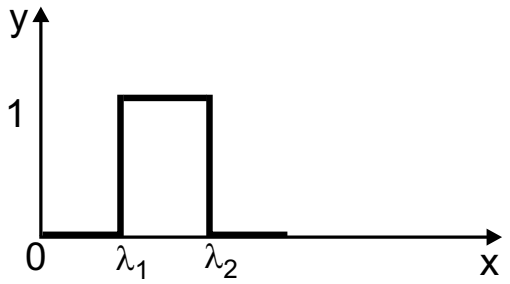

Figure A.10. Threshold.

- **Label**
  The image is scanned from top to bottom and from left to right. Each pixel of the same object takes the same value and a different value is ascribed to each object. Thus the objects can be distinguish and the number of objects can be assessed (Fig. A.12).

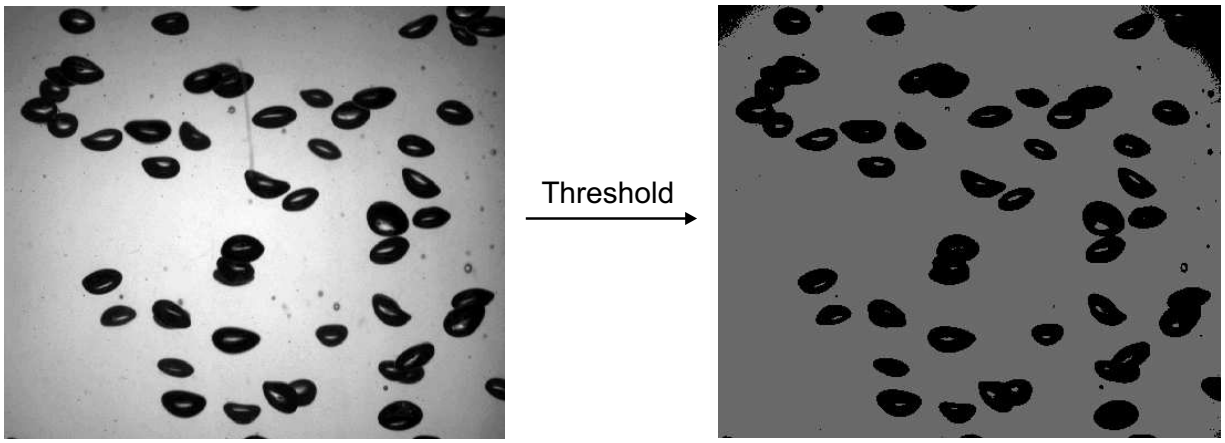

Figure A.11. Example of threshold.

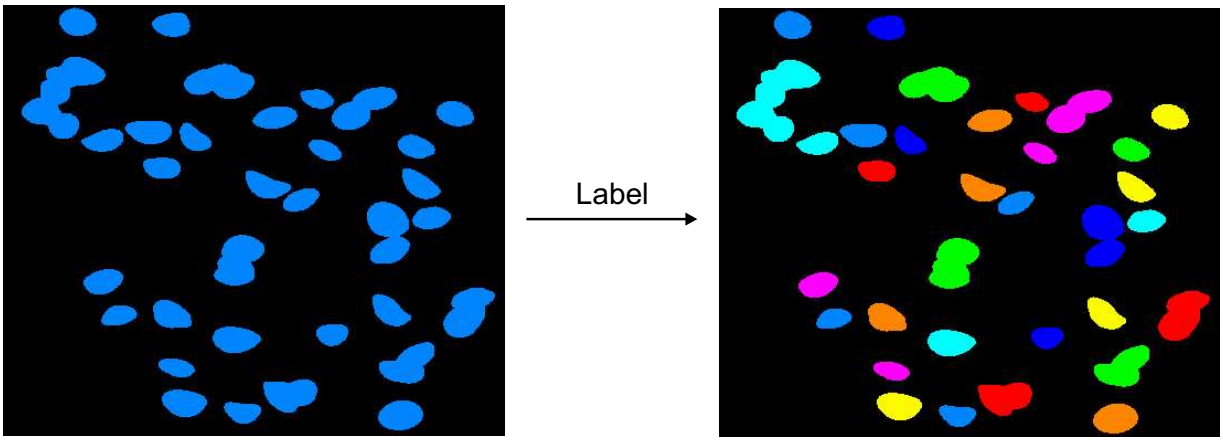

Figure A.12. Example of label.

Morphology

- **Hole fill**
  All the holes inside the objects are filled (Fig. A.13).

- **Border kill**
  All the objects touching the image frame are eliminated (Fig. A.14).

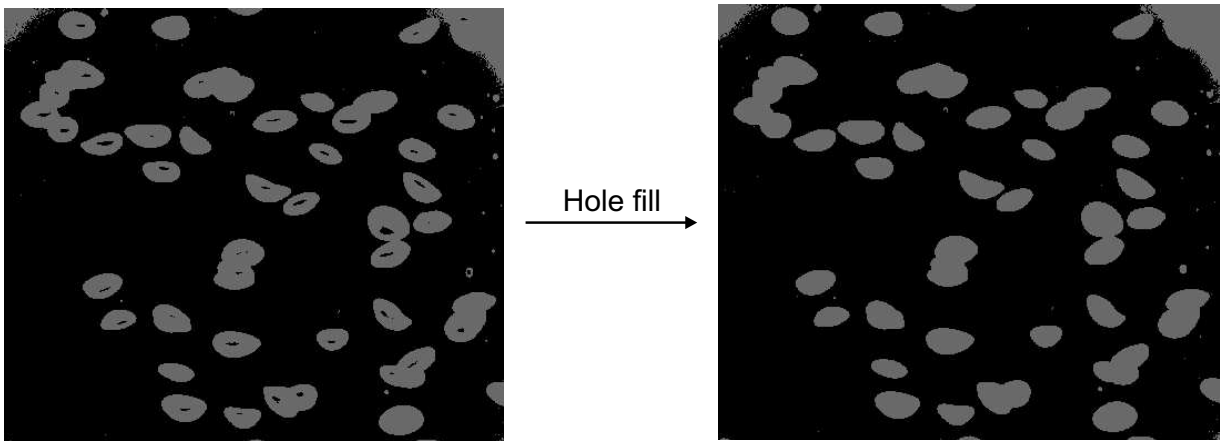

Figure A.13. Example of hole fill.

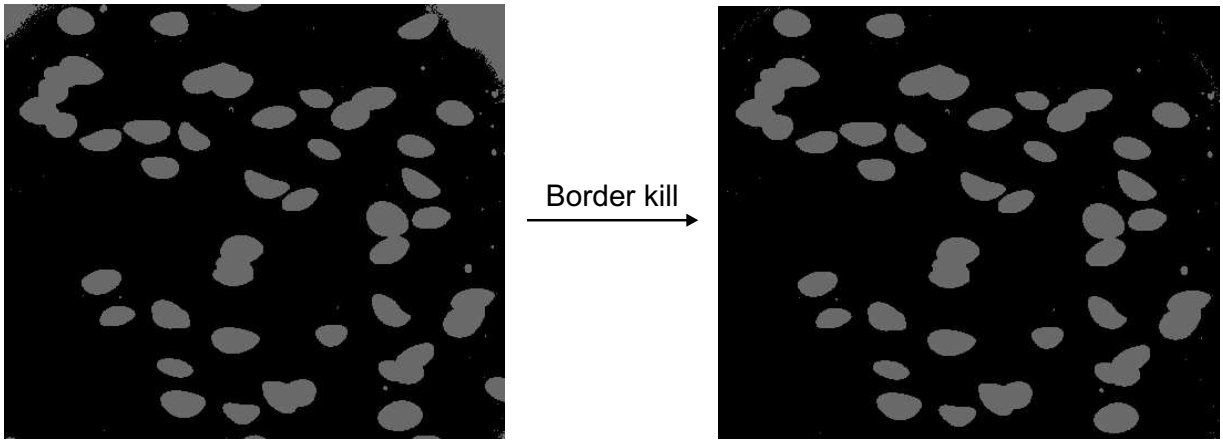

Figure A.14. Example of border kill.

The morphologic transformations are based on a structuring element (E) characterized by a certain shape, size and center position. Each pixel in an image is compared with E by moving E so that its center hits the pixel. Depending on the type of transformation, the pixel value is reset to the value or the average value of one or more of its neighbours. Different structuring elements can be found, but the most common for a square grid is the quadrangular, in which each pixel has 8 neighbour pixels (Fig. A.15).

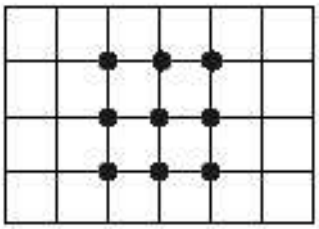

Figure A.15. Structuring element.

Erosion

In an erosion, the pixels within the structuring element are set to the minimum value of that element. In a binary image, erosion removes isolated points and small particles, shrinks other particles, eliminates peaks at the object border and separates some particles. A simple erosion of order 1 is presented in Fig. A.16. In this case, the structuring element operates only once.

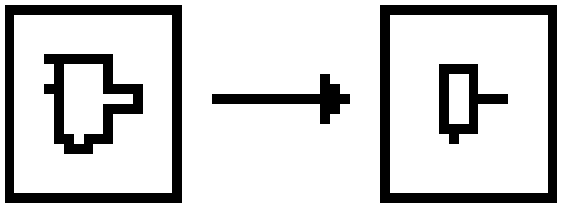

Figure A.16. Erosion of order 1.

However, sometimes is necessary to execute stronger erosions, for instance, to remove undesirable small particles. In this case, an erosion of order higher than one is performed, with the structuring element operating repeatedly (see Fig. A.17).

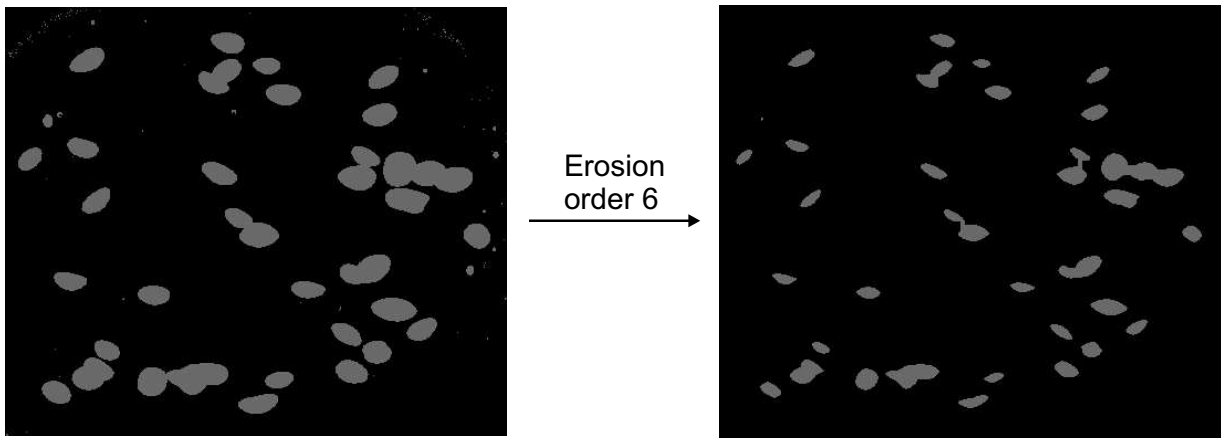

Figure A.17. Erosion of order 6.

Dilation

Dilation is the opposite of erosion. In dilation, the pixels of structuring element are set to the maximum within that element. Dilation fills the small holes inside the particles, enlarges objects and may connect neighbouring particles. Depending on the intensity of desired dilation, one can dilate once (*order* 1) or successive times (*order* > 1) (see Fig. A.18).

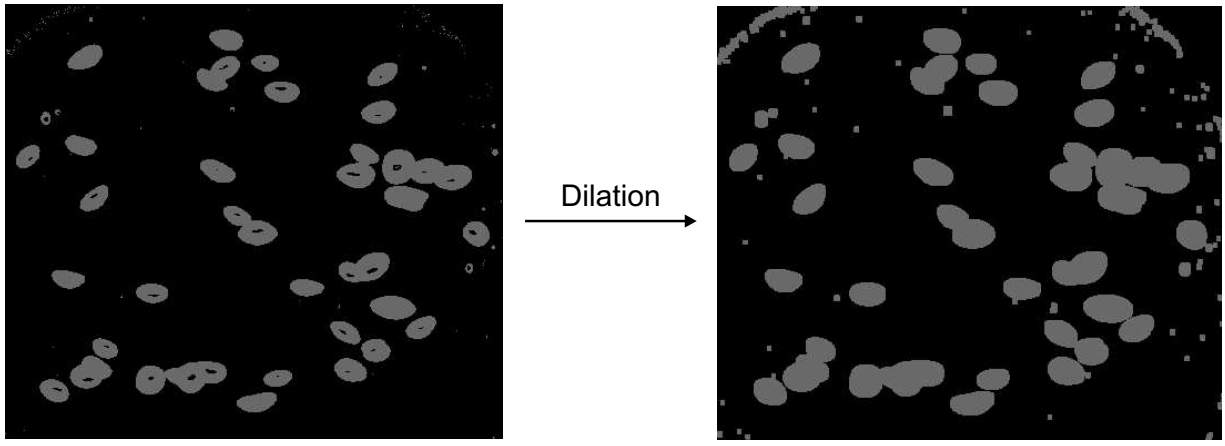

Figure A.18. Dilation of order 4.

Reconstruction

The principle of reconstruction is to rebuild an image starting from markers, recovering only the objects which contain a marker. In this process, successive dilations are executed on the image with markers, and each dilation is followed by an interception with the original image until convergence is reached. Reconstruction retrieves the original shape of the particles obtained after erosion, which eliminates small objects. Therefore, the eroded objects are used as markers (see Fig. A.19).

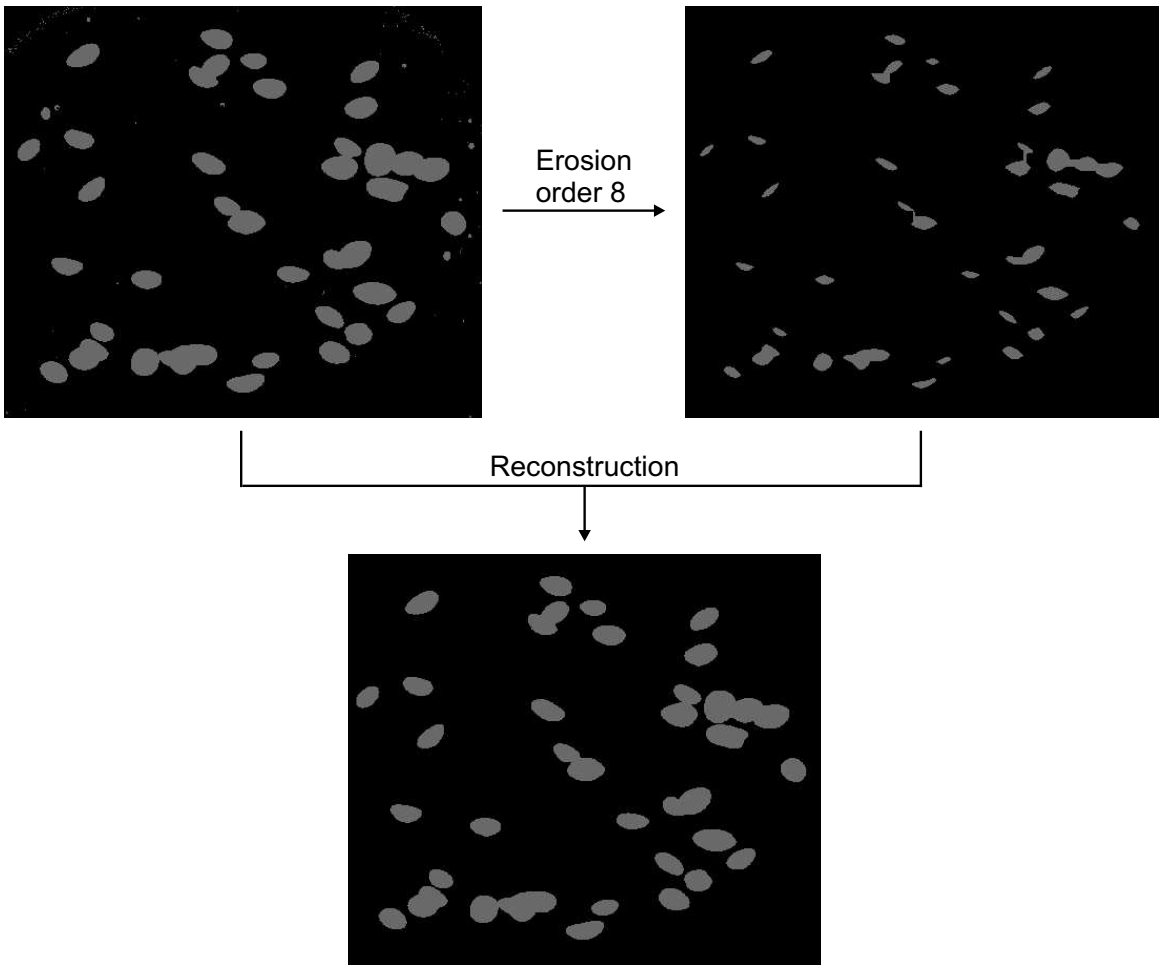

Figure A.19. Example of reconstruction.

Ultimate

Ultimate searches for the last points obtained by erosion. This enables to count the number of convex particles, even if they touch each other, as long as the pseudo-center of each particle does not intersect other particles. The principle of this operation is to perform successive erosions in the image until all particles disappear and to reconstruct each eroded image. At each step, the original image is subtracted to the reconstructed image and the last points of each object are obtained (Fig. A.20).

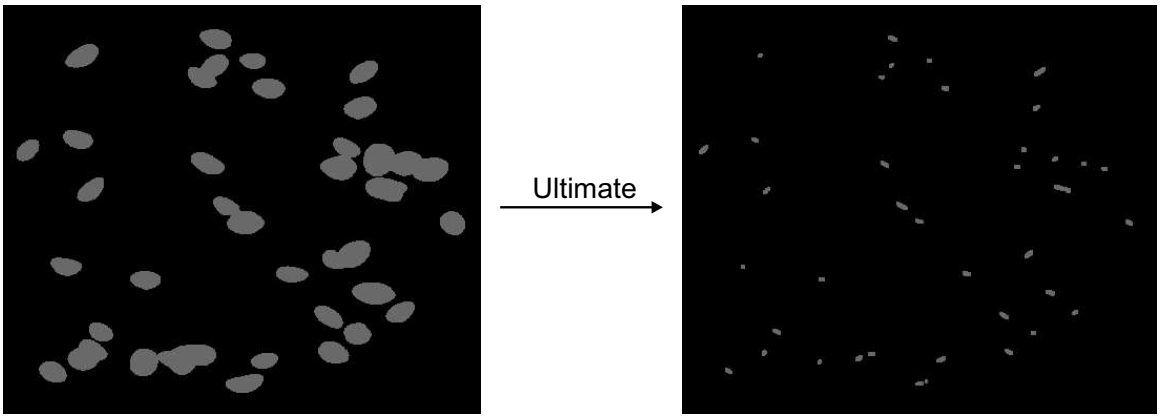

Figure A.20. Example of ultimate.

A.3 Images of different systems

In this section some examples of images of different systems tested are presented. Some of those sets of images represent cases in which the image treatment was tried, but was found to be inappropriate.

Image A.21 shows an air-water-glycerol ($\mu = 5\ cP$) system at different superficial gas velocities. In this case, as in every gas-liquid system at low or moderate gas velocities, the automatic image processing is a good technique for determining the characteristics of the bubbles. The processing of those images revealed that the main bubble characteristics of this system were very close to those found for air-water systems, which means that, for those conditions, the viscosity effect on air bubbles would not have been very significant.

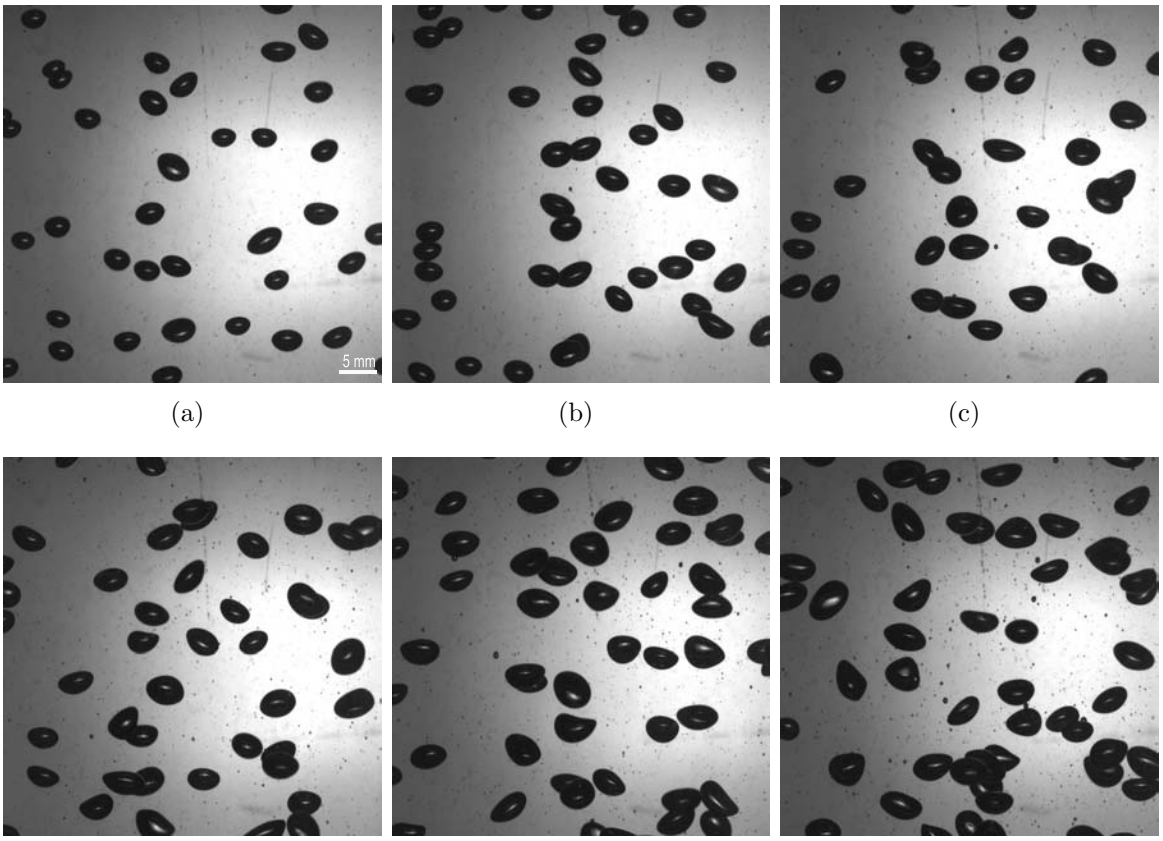

Figure A.21. Examples of images of air-water-glycerol ($\mu = 5\ cP$) system: (a) $u_G = 1.5\ mm/s$ (b) $u_G = 1.7\ mm/s$ (c) $u_G = 2.0\ mm/s$ (d) $u_G = 2.2\ mm/s$ (e) $u_G = 2.5\ mm/s$ (f) $u_G = 2.7\ mm/s$.

Examples of images of air-water-pvc system (0.5 $wt\%$; $160 < d_p < 180\ \mu m$) are shown in Fig. A.22. In spite of the bubbles being visible in the pictures, their automatic treatment was not possible. This is because the background grey-level is not uniform, being often very close to bubble grey-level, which makes the bubble isolation difficult. Note that the amount of solids is quite low (0.5 $wt\%$), but their small size ($160 < d_p < 180\ \mu m$) turns their presence noticeable.

In Fig. A.23 images of air-water-ion exchange resin system (1 $vol\%$; $d_p = 0.8\ mm$) are presented. The automatic processing was not conducted due to similar reasons as mentioned above for air-water-pvc system. The complete solid particle suspension was only achieved for the higher superficial gas velocities and in those cases the solid population was too high for a viable automatic image treatment. Several tests were also conducted at

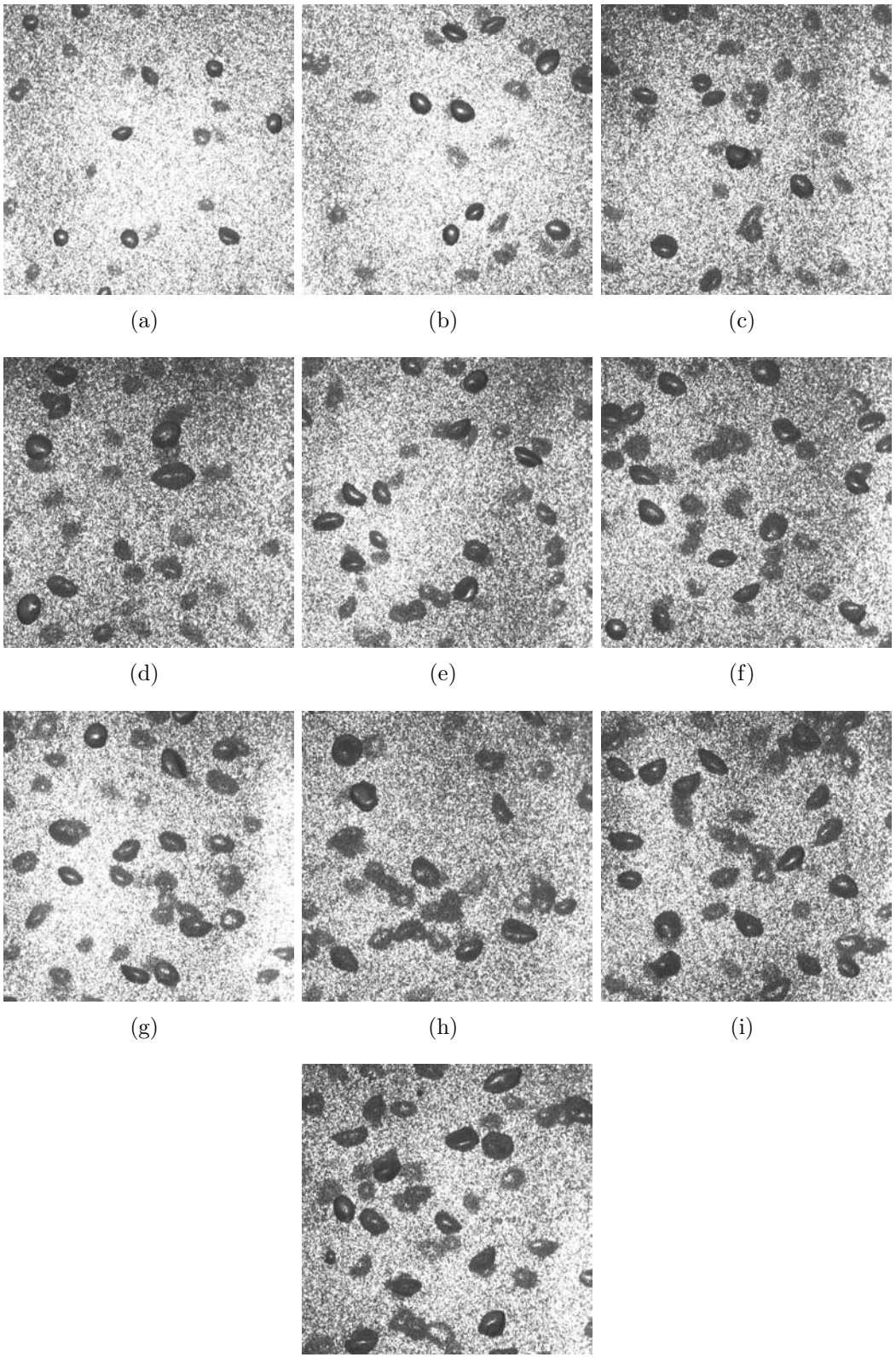

Figure A.22. Examples of images of air-water-pvc system (0.5 $wt\%$; $160 < d_p < 180$ μm): (a) $u_G = 0.4$ mm/s (b) $u_G = 0.6$ mm/s (c) $u_G = 0.9$ mm/s (d) $u_G = 1.2$ mm/s (e) $u_G = 1.5$ mm/s (f) $u_G = 1.7$ mm/s (g) $u_G = 2.0$ mm/s (h) $u_G = 2.2$ mm/s (i) $u_G = 2.5$ mm/s (j) $u_G = 2.7$ mm/s.

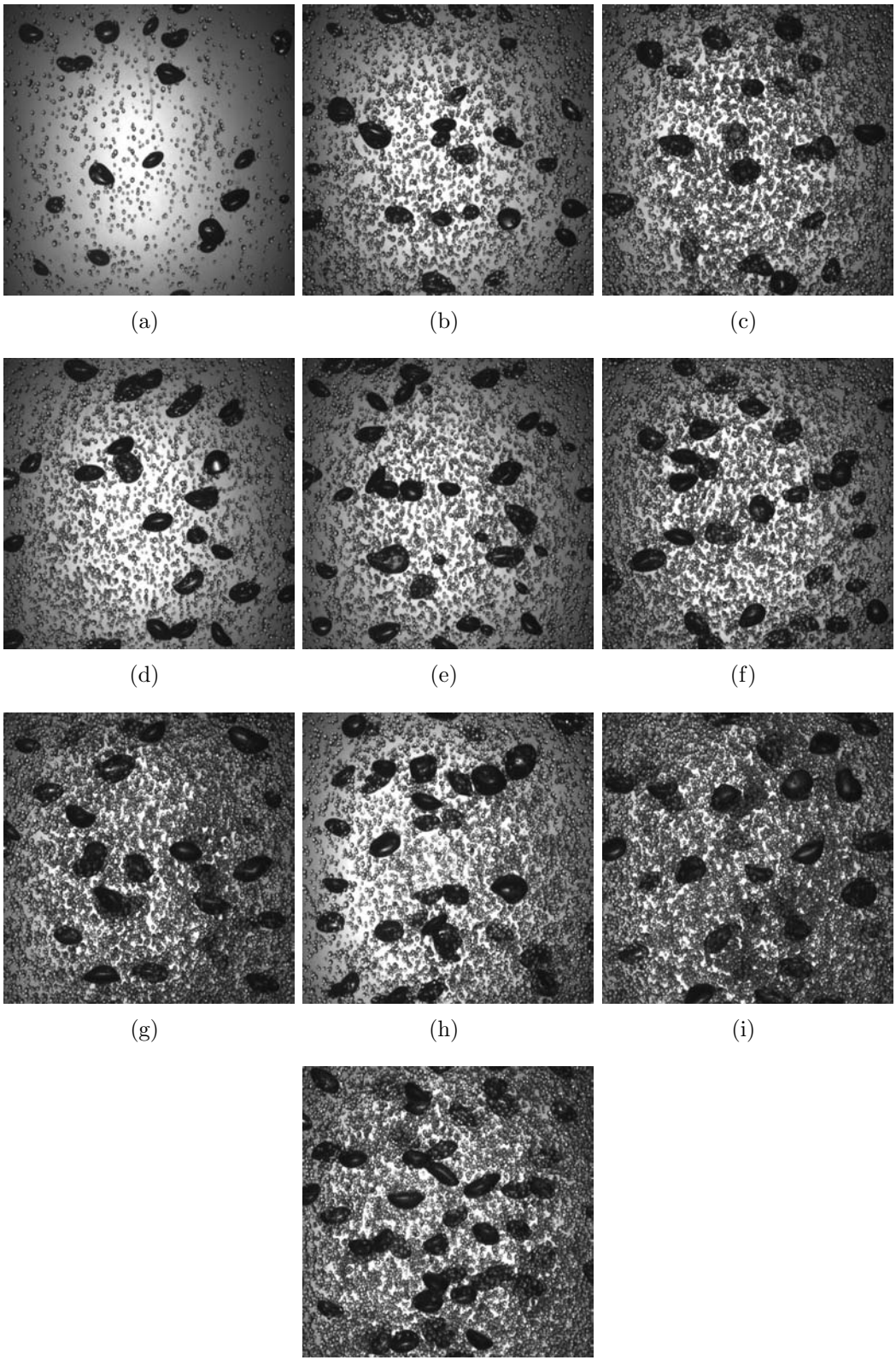

Figure A.23. Examples of images of air-water-ion exchange resin system (1 $vol\%$; $d_p = 0.8\ mm$): (a) $u_G = 0.4\ mm/s$ (b) $u_G = 0.6\ mm/s$ (c) $u_G = 0.9\ mm/s$ (d) $u_G = 1.2\ mm/s$ (e) $u_G = 1.5\ mm/s$ (f) $u_G = 1.7\ mm/s$ (g) $u_G = 2.0\ mm/s$ (h) $u_G = 2.2\ mm/s$ (i) $u_G = 2.5\ mm/s$ (j) $u_G = 2.7\ mm/s$.

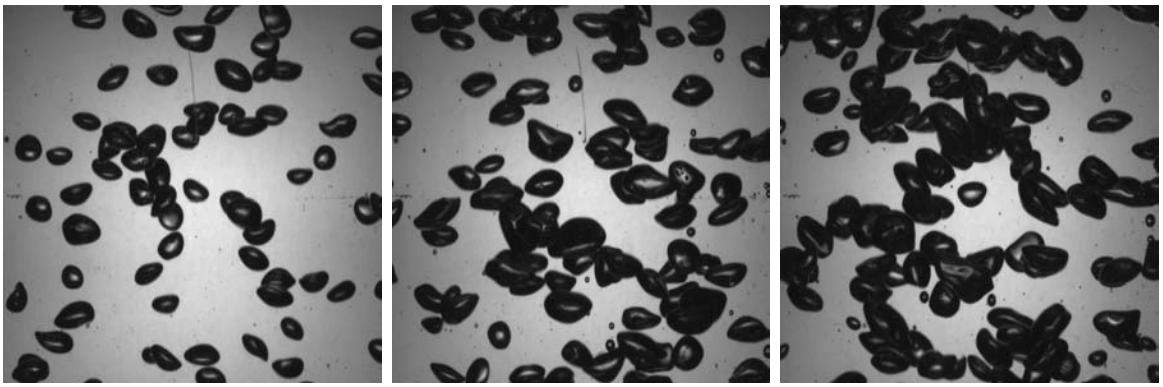

(a) (b) (c)

Figure A.24. Examples of images of air-water system ("high" superficial gas velocities): (a) $u_G = 3.4\ mm/s$ (b) $u_G = 6.6\ mm/s$ (c) $u_G = 8.7\ mm/s$.

higher superficial gas velocity range ($1.4 < u_G < 8.7\ mm/s$). Fig. A.24 shows examples of images of air-water system at this "high" superficial gas velocity range. Specially from the picture (c), one may conclude that the image processing seems problematic. Indeed, from this picture one can see isolated bubbles, but the majority of the bubbles are overlapped, which unables their treatment. Bigger bubbles are more likely to overlap, so we can predict an underestimation of the mean bubble size, since only smaller bubbles would be considered to the treatment and bigger bubbles would be rejected. Examples of images of air-water-calcium alginate system 5 $vol\%$ ($d_{eq} = 2.1\ mm$) at the same "high" superficial gas velocity range are presented in A.25. In addition to the limitation mentioned above for air-water system at this u_G range, this system has also the presence of solids as factor that has to be taken into account. The visibility of the bubbles is reduced due to the presence of calcium alginate beads. In spite of the bubbles and the beads have different grey-levels, the beads overlapping turns them darker, which complicates the image processing.

Fig. A.26 shows examples of images of air-water-calcium alginate system 5 $vol\%$ ($d_{eq} = 1.2\ mm$) at "high" superficial gas velocities. The limitations presented before for air-water-calcium alginate system 5 $vol\%$ ($d_{eq} = 2.1\ mm$) are still valid for this system. Moreover, since the particle size is smaller, for the same $vol\%$, the number of particles increases which reduces the bubbles-background contrast.

Fine particles were also tested as solid phase and examples of images of air-water-alumina (Al_2O_3) system (0.5 $wt\%$; $\bar{d}_p = 78\ \mu m$) at "high" superficial gas velocities can

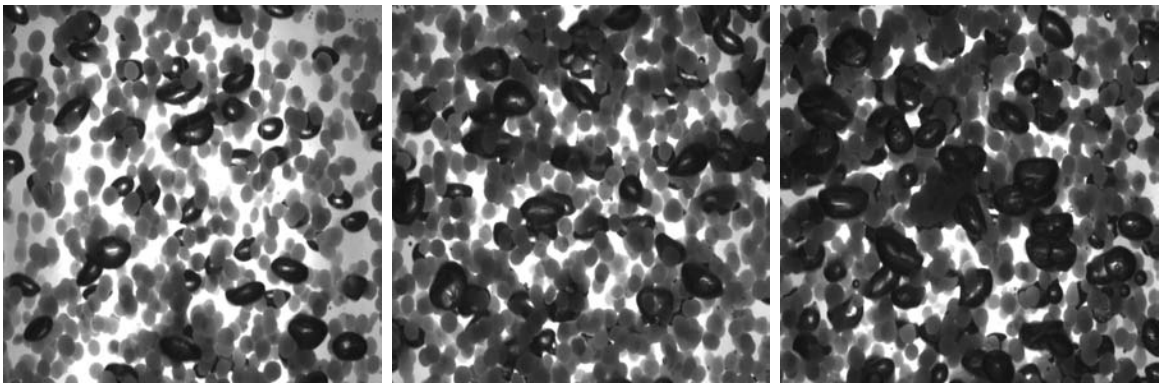

(a) (b) (c)

Figure A.25. Examples of images of air-water-calcium alginate system 5 $vol\%$ ($d_{eq} = 2.1\ mm$) ("high" superficial gas velocities): (a) $u_G = 3.4\ mm/s$ (b) $u_G = 6.6\ mm/s$ (c) $u_G = 8.7\ mm/s$.

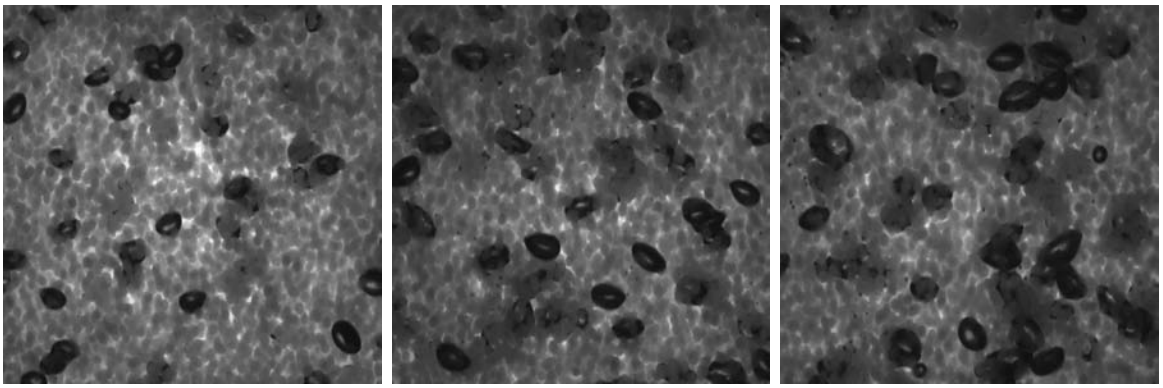

(a) (b) (c)

Figure A.26. Examples of images of air-water-calcium alginate system 5 $vol\%$ ($d_{eq} = 1.2\ mm$) ("high" superficial gas velocities): (a) $u_G = 2.4\ mm/s$ (b) $u_G = 4.2\ mm/s$ (c) $u_G = 5.8\ mm/s$.

be seen in Fig. A.27. Even with very low solid content (0.5 $wt\%$), the automatic image processing is still unpracticable mainly due to the overlapping of bubbles and difficulties in the detection of bubble border because of the non-uniformity of the background.

Finally, in Fig. A.28 one shows examples of images of air-water-gibbsite ($Al(HO)_3$) system (0.5 $wt\%$; $\bar{d}_p = 86\ \mu m$), at "high" superficial gas velocities. As this system is very similar to the air-water-alumina system, obviously the image processing limitations are identical. Note that the images presented in this section are the 'best' images selected among the sets of 70-100 images recorded.

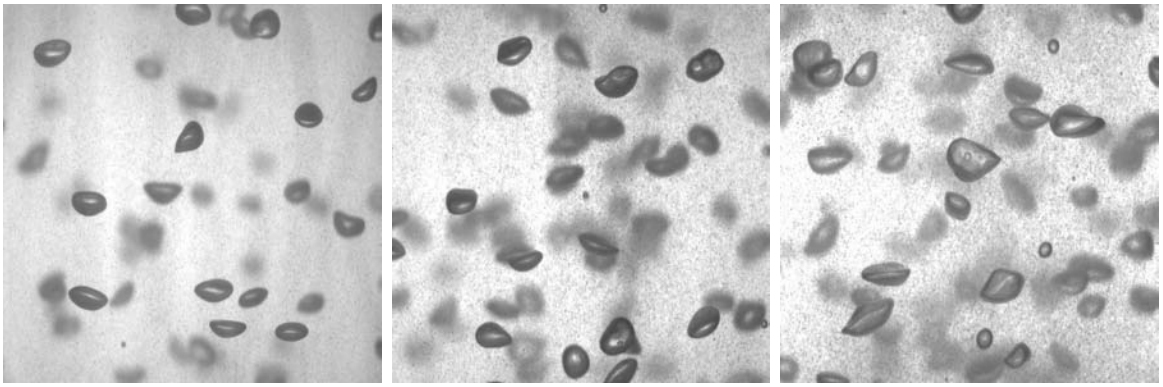

(a) (b) (c)

Figure A.27. Examples of images of air-water-alumina (Al_2O_3) system (0.5 $wt\%$; $\bar{d}_p = 78\ \mu m$) ("high" superficial gas velocities): (a) $u_G = 2.4\ mm/s$ (b) $u_G = 4.2\ mm/s$ (c) $u_G = 5.8\ mm/s$.

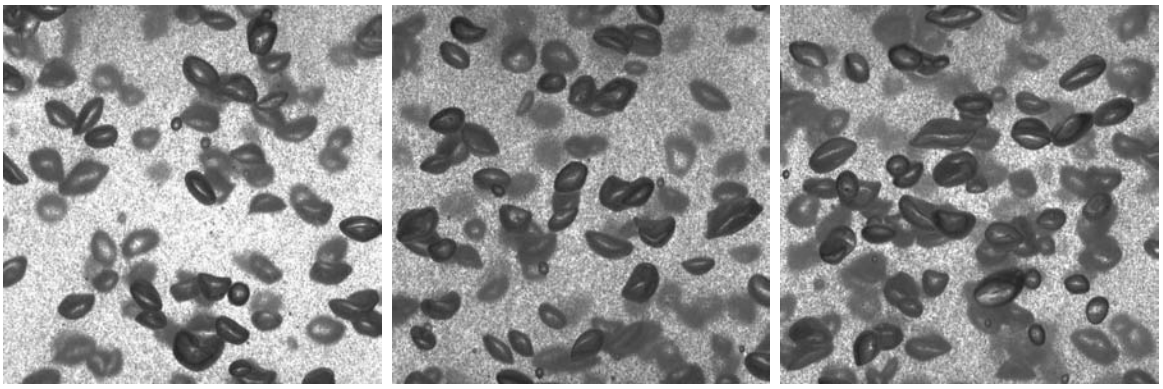

(a) (b) (c)

Figure A.28. Examples of images of air-water-gibbsite ($Al(HO)_3$) system (0.5 $wt\%$; $\bar{d}_p = 86\ \mu m$) ("high" superficial gas velocities): (a) $u_G = 5.8\ mm/s$ (b) $u_G = 7.3\ mm/s$ (c) $u_G = 8.7\ mm/s$.

Appendix B

Determination of gas-liquid interfacial area

In this appendix, the procedure for the determination of the gas-liquid interfacial area found in subsection 2.3.8 is presented.

This involves the calculation of the rise velocity of ellipsoidal bubbles v_b (Wesselingh and Bollen, 1999) which is, then, used to obtain the number of bubbles N_b in the column at a certain instant of time.
From the image analysis experiments one obtains the values of mean superficial area of the bubbles A_{sup} and of the mean bubble volume V_b. The bubble equivalent diameter d_b is that of a sphere with the same volume,

$$d_b = \left(\frac{6V_b}{\pi}\right)^{1/3}. \tag{B.1}$$

The reference diameter, d_{ref}, which only depends on physical properties of the contacting phases and on the gravity aceleration, g, is given by:

$$d_{ref} = \left(\frac{\mu^2}{\rho_L g\left(\rho_L - \rho_G\right)}\right)^{1/3} \tag{B.2}$$

and the dimensionless diameter can now be obtained ($d^{\%} = d_b/d_{ref}$).
The dimensionless interfacial tension $\sigma^{\%}$ also has to be determined. Once again, first, the

reference interfacial tension is given by the expression:

$$\sigma_{ref} = \left(\frac{g\left(\rho_L - \rho_G\right)\mu^4}{\rho_L^2} \right)^{1/3} \tag{B.3}$$

and the dimensionless interfacial tension by $\sigma^{\%} = \sigma/\sigma_{ref}$, with σ being the interfacial air-water tension. The dimensionless velocity of ellipsoidal bubbles $v^{\%}$ is obtained by the following equation:

$$v^{\%} = \left(\frac{31\sigma^{\%^{2/3}}}{d^{\%}} + 0.51 d^{\%} \right)^{0.5} . \tag{B.4}$$

After determining the reference bubble velocity, v_{ref}, as,

$$v_{ref} = \left(\frac{g\left(\rho_L - \rho_G\right)\mu}{\rho_L^2} \right)^{1/3} \tag{B.5}$$

one may obtain the bubble rise velocity ($v_b = v^{\%} \cdot v_{ref}$). The rising time ($t_s$) of a bubble through the column can be expressed as the ratio between the clear liquid height h_0 and the bubble rise velocity v_b:

$$t_S = \frac{h_0}{v_b} \tag{B.6}$$

and the number of bubbles N_b in the column at a certain instant is given by the relation:

$$N_b = \frac{Q_G t_s}{V_b}. \tag{B.7}$$

Finally, the gas-liquid interfacial area a represents the total superficial area of the bubbles ($N_b \cdot A_{\text{sup}}$) per unit of liquid volume in the bubble column (V_L):

$$a = \frac{N_b A_{\text{sup}}}{V_L} . \tag{B.8}$$

Appendix C

Solubility of oxygen in freshwater

Dissolved Oxygen (mg/l)
(at normal atmospheric pressure, 760 mm Hg)

T (°C)	0.0	0.1	0.2	0.3	0.4	0.5	0.6	0.7	0.8	0.9
0	14.62	14.58	14.54	14.50	14.46	14.42	14.39	14.35	14.31	14.27
1	14.23	14.19	14.15	14.11	14.07	14.03	14.00	13.96	13.92	13.88
2	13.84	13.80	13.77	13.73	13.70	13.66	13.62	13.59	13.55	13.52
3	13.48	13.44	13.41	13.38	13.34	13.30	13.27	13.24	13.20	13.16
4	13.13	13.10	13.06	13.03	13.00	12.97	12.93	12.90	12.87	12.83
5	12.80	12.77	12.74	12.70	12.67	12.64	12.61	12.58	12.54	12.51
6	12.48	12.45	12.42	12.39	12.36	12.32	12.29	12.26	12.23	12.20
7	12.17	12.14	12.11	12.08	12.05	12.02	11.99	11.96	11.93	11.90
8	11.87	11.84	11.81	11.79	11.76	11.73	11.70	11.67	11.65	11.62
9	11.59	11.56	11.54	11.51	11.49	11.46	11.43	11.41	11.38	11.36
10	11.33	11.31	11.28	11.25	11.23	11.21	11.18	11.15	11.13	11.11
11	11.08	11.06	11.03	11.00	10.98	10.96	10.93	10.90	10.88	10.86
12	10.83	10.81	10.78	10.76	10.74	10.71	10.69	10.67	10.65	10.62
13	10.60	10.58	10.55	10.53	10.51	10.48	10.46	10.44	10.42	10.39
14	10.37	10.35	10.33	10.30	10.28	10.26	10.24	10.22	10.19	10.17
15	10.15	10.13	10.11	10.09	10.07	10.05	10.03	10.01	9.99	9.97
16	9.95	9.93	9.91	9.89	9.87	9.85	9.82	9.80	9.78	9.76
17	9.74	9.72	9.70	9.68	9.66	9.64	9.62	9.60	9.58	9.56
18	9.54	9.52	9.50	9.48	9.46	9.44	9.43	9.41	9.39	9.37
19	9.35	9.33	9.31	9.30	9.28	9.26	9.24	9.22	9.21	9.19
20	9.17	9.15	9.13	9.12	9.10	9.08	9.06	9.04	9.03	9.01
21	8.99	8.98	8.96	8.94	8.93	8.91	8.89	8.88	8.86	8.85
22	8.83	8.81	8.80	8.78	8.77	8.75	8.74	8.72	8.71	8.69
23	8.68	8.66	8.65	8.63	8.62	8.60	8.59	8.57	8.56	8.54
24	8.53	8.51	8.50	8.48	8.47	8.45	8.44	8.42	8.41	8.39
25	8.38	8.36	8.35	8.33	8.32	8.30	8.28	8.27	8.25	8.24
26	8.22	8.20	8.19	8.17	8.16	8.14	8.13	8.11	8.10	8.08
27	8.07	8.05	8.04	8.02	8.01	7.99	7.98	7.96	7.95	7.93
28	7.92	7.90	7.89	7.87	7.86	7.84	7.83	7.81	7.80	7.78
29	7.77	7.75	7.74	7.73	7.71	7.70	7.69	7.67	7.66	7.64
30	7.63	7.61	7.60	7.59	7.57	7.56	7.55	7.54		

T (°C)	Dissolved Oxygen (mg/l)	*T* (°C)	Dissolved Oxygen (mg/l)
31	7.5	41	6.5
32	7.4	42	6.4
33	7.3	43	6.3
34	7.2	44	6.2
35	7.1	45	6.1
36	7.0	46	6.0
37	6.9	47	5.9
38	6.8	48	5.8
39	6.7	49	5.7
40	6.6		

Note: correction for barometric pressure B (mm Hg) multiply by $B/760$; correction for salinity S (chloride, mg/l) multiply by $[1 - (S/100{,}000)]$.

Figure C.1. Solubility of oxygen in freshwater (Velz, 1970).

Bibliography

Albal, R. S., Shah, Y. T., Schumpe, A., 1983. Mass transfer in multiphase agitated contactors. Chem. Eng. J. 27, 61–80.

Alper, E., Deckwer, W. D., Danckwerts, P. V., 1980. Comparison of effective interfacial areas with the actual contact area for gas absorption in a stirred cell. Chem. Eng. Sci. 35, 1263–1268.

Alvarez, E., Sanjurjo, B., Cancela, A., Navaza, J. M., 2000. Mass transfer and influence of physical properties of solutions in a bubble column. Chem. Eng. Res. Des. 78, 889–893.

Banisi, S., Finch, J. A., Laplante, A. R., Weber, M. E., 1995a. Effect of solid particles on gas holdup in flotation columns - i. measurement. Chem. Eng. Sci. 50, 2329–2334.

Banisi, S., Finch, J. A., Laplante, A. R., Weber, M. E., 1995b. Effect of solid particles on gas holdup in flotation column - i. measurement. Chem. Eng. Sci. 50, 2329–2334.

Bly, M., Worden, R., 1992. The effects of solids density and void fraction on the bubble rise velocity in a liquid-solid fluidized bed. Chem. Eng. Sci. 47, 3281–3288.

Boyer, C., Cartellier, A., 1999. Bubble velocity and size estimation using a single optical probe in a gas/liquid flow across a fixed bed reactor. ECCE 2 - Montpellier.

Boyer, C., Duquenne, A.-M., Wild, G., 2002. Measuring techniques in gas-liquid and gas-liquid-solid reactors. Chem. Eng. Sci. 57, 3185–3215.

Camacho, F., Molina, E., Valdés, F., Andujar, J. M., 1991. Influence of operating and physical variables on interfacial area determination. AIChE J. 37, 1196–1204.

Cartellier, A., 1998. Measurement of gas phase characteristics using new monofiber optical probes and real time signal processing. Nucl. Engng. Design 184, 393–408.

Chandrasekaran, K., Sharma, M. M., 1977. Absorption of oxygen in aqueous solutions of sodium sulfide in the presence of activated carbon as catalyst. Chem. Eng. Sci. 32, 669–671.

Cussler, E. L., 1984. Diffusion - Mass Transfer in Fluid Systems. Cambridge University Press.

Dagaonkar, M. V., Heeres, H. J., Beenackers, A. A. C. M., Pangarkar, V. G., 2002. The application of fine TiO2 particles for enhanced gas absorption. Chem. Eng. J. 4109, 1–9.

De Lasa, H., Lee, S. L. P., Bergougnou, M. A., 1984. Bubble measurement in three-phase fluidized beds using a u-shape optical fiber. Can. J. Chem. Eng. 62, 165–169.

De Swart, J. W. A., Van Vliet, R. E., Krishna, R., 1996. Size, structure and dynamics of "large" bubbles in a two-dimensional slurry bubble column. Chem. Eng. Sci. 51, 4619–4629.

Deckwer, W. D., 1992. Bubble column reactors. J. Wiley Chichester.

Deckwer, W. D., Burckhart, R., Zoll, G., 1974. Mixing and mass transfer in tall bubble columns. Chem. Eng. Sci. 29, 2177–2188.

Deckwer, W.-D., Schumpe, A., 1987. Bubble columns - the state of the art and current trends. Int. Chem. Eng. 27, 405–422.

Dhanuka, V. R., Stepanek, J. B., 1980. Simultaneous measurement of interfacial area and mass transfer coefficient in three phase fluidized beds. AIChE J. 26, 1029–1038.

Douek, R., Hewitt, G., Livingston, A., 1997. Hydrodynamics of vertical co-current gas-liquid-solid flows. Chem. Eng. Sci. 52, 4357–4372.

Dudley, J., 1995. Mass transfer in bubble columns: A comparison of correlations. Wat. Res. 29, 1129–1138.

Einstein, A., 1906. A new determination of molecular dimensions. Ann. Phys. 19, 289–306.

Fan, L.-S., Yang, G. Q., Lee, D. J., Tsuchiya, K., Luo, X., 1999. Some aspects of high-pressure phenomena of bubbles in liquids and liquid-solid suspensions. Che. Eng. Sci. 54, 4681–4709.

Franz, K., Borner, T., Kantorek, H. J., Buchholz, R., 1984. Flow structures in bubbly columns. Ger. Chem. Eng. 7, 365–374.

Freitas, C., 2002. Biorreactores multifásicos - caracterização hidrodinâmica e de transferência de massa. Ph. D. Thesis, University of Minho, Portugal.

Freitas, C., Teixeira, J. A., 2001. Oxygen mass transfer in a high solids loading three-phase internal-loop airlift reactor. Chem. Eng. J. 84, 57–61.

Gandhi, B., Prakash, A., Bergougnou, M., 1999. Hydrodynamic behaviour of slurry bubble column at high solids concentrations. Powder Technol. 103, 80–94.

Garcia-Ochoa, J., Khalfet, R., Poncin, S., Wild, G., 1997. Hydrodynamics and mass transfer in a suspended solid bubble column with polydispersed high density particles. Chem. Eng. Sci. 52, 3827–3834.

Hills, J. H., 1974. Radial non-uniformity of velocity and voidage in a bubble column. Trans. Int. Chem. Eng. 52, 1–9.

Hwang, S. J., Lu, W. J., 1997. Gas-liquid mass transfer in an internal-loop airlift reactor with low density particles. Chem. Eng. Sci. 52, 853–857.

Ityokumbul, M., Kosaric, N., Bulani, W., 1995. Effect of solids and frother on gas hold-up and liquid mixing in a flotation column. Mineral Eng. 8, 1369–1380.

Jianping, W., Shonglin, X., 1998. Local hydrodynamics in a gas-liquid-solid three-phase bubble column reactor. Chem. Eng. J. 70, 81–84.

Joly-Vuillemin, C., de Bellefon, C., Delmas, H., 1996. Solid effects on gas-liquid mass transfer in three-phase slurry catalytic hydrogenation of adiponitrile over raney nickel. Chem. Eng. Sci. 51, 2149–2158.

Jourdain, C., 2002. Les spheroids tumoraux multicellulaires - analyse par traitment d'image, chimiosensibilité, encapsulation de cellules tumorales humaines. M. Sc. Thesis, Centre Alexis Vautrin, Vandoeuvre-Lès-Nancy, France.

Kantarci, N., Borak, F., Ulgen, K. O., 2005. Bubble column reactors. Process Biochem. 40, 2263–2283.

Kastanek, F., Zaharadnik, J., Kratochvil, J., Cermak, J., 1993. Chemical Reactors for Gas-Liquid Systems. Ellis Horwood, Chichester, UK.

Kawalec-Pietrenko, B. T., 1992. Time-dependent gas hold-up and bubble size distributions in a gas-highly viscous liquid-solid system. Chem. Eng. J 50, B29–B37.

Kawase, Y., Hashimoto, N., 1996. Gas hold-up and oxygen transfer in three-phase external-loop airlift bioreactors: Non-newtonian fermentation broths. J. Chem. Tech. Biotechnol. 65, 325–334.

Kiambi, S. L., Duquenne, A. M., Bascoul, A., Delmas, H., 2001. Measurements of local interfacial area: Application of bi-optical fibre technique. Chem. Eng. Sci. 56, 6447–6453.

Kim, J. O., Kim, S. D., 1990. Gas-liquid mass transfer in a three-phase fluidized bed with floating bubble breakers. Can. J. Chem. Eng. 68, 368–375.

Kozma, R., 1995. Studies of the relationship between the statistics of void fraction fluctuations and the parameters of two-phase flows. Int J. multiphase flow 21, 241–251.

Krishna, R., Ellenberger, J., Hennephof, D. E., 1993. Analogous description of the hydrodynamics of gas-solid fluidized bed and bubble columns. Chem. Eng. J. 53, 89–101.

Krishna, R., Ellenberger, J., Maretto, C., 1999. Flow regime transition in bubble columns. Int. Comm. Heat Mass Transfer 26, 467–475.

Krishna, R., Wilkinson, P. M., Dierendonck, L., 1991. A model for gas holdup in bubble columns incorporating the influence of gas density on flow regime transitions. Chem. Eng. Sci. 46 , 2491–2496.

Kumar, S. B., Moslemian, D., Dudukovic, M., 1997. Gas-holdup measurements in bubble columns using computed tomography. A.I.Ch.E. J. 43, 1414–1425.

Kuncova, G., Zahradnik, J., 1995. Gas holdup and bubble frequency in a bubble column reactor containing viscous saccharose solutions. Chem. Eng. Proc. 34, 25–34.

Lapin, A., Lubbert, A., 1994. Numerical simulation of the dynamics of two-phase gas-liquid flows in bubble columns. Chem. Eng. Sci. 49, 3661–3674.

Lee, S.-Y., Tsui, Y. P., 1999. Succeed at gas/liquid contacting. Chem. Eng. Prog. 95, 23–49.

León-Becerril, E., Liné, A., 2001. Stability analysis of a bubble column. Chem. Eng. Sci. 56, 6135–6141.

Leung, W., Revankar, S., Ishii, Y., Ishii, M., 1995. Axial development of interfacial area and void concentration profiles measured by double-sensor probe method. Int. J. Heat Mass Transfer 38 (3), 445–453.

Li, H., Prakash, A., 2000. Influence of slurry concentrations on bubble population and their rise velocities in a three-phase slurry bubble column. Power tech. 113, 158–167.

Liu, W., Clark, N. N., Karamavruç, A. I., 1998. Relationship between bubble size distributions and chord-length distribution in heterogeneously bubbling systems. Chem. Eng. Sci. 53 (6), 1267–1276.

Lu, W., Hwang, S., Chang, C., 1995. Liquid velocity and gas holdup in three-phase internal loop airlift reactors with low-density particles. Chem. Eng. Sci. 50, 1301–1310.

Luo, X., Lee, D. J., Lau, R., Yang, G., Fan, L.-S., 1999. Maximum stable bubble size and gas holdup in high-pressure slurry bubble columns. AIChE J. 45, 665–680.

Luo, X., Yang, G., Lee, D., L.S., F., 1998. Single bubble formation in high pressure liquid-solid suspensions. Powder Technol. 100, 103–112.

Luo, X., Zhang, J., Tsuchiya, K., Fan, L., 1997a. On the rise velocity of bubbles in liquid-solid suspensions at elevated pressure and temperature. Chem. Eng. Sci. 52, 3693–3699.

Mena, P. C., Pons, M. C., Teixeira, J. A., Rocha, F. A., 2005a. Using image analysis in the study of multiphase gas absorption. accepted for publication in Chem. Eng. Sci.

Mena, P. C., Rocha, F. A., Teixeira, J. A., Cartellier, A., Sechet, P., 2005b. Measurement of gas phase characteristics using a monofiber optical probe in a three-phase flow. Submitted to Int. J. Multiphase Flow.

Mena, P. C., Rocha, F. A., Teixeira, J. A., Drahos, J., Ruzicka, M. C., 2005c. Effect of solids on homogeneous-heterogeneous flow regime transition in three-phase bubble columns. Chem. Eng. Sci. 60, 6013–6026.

Midoux, N., Morsi, B. I., Purwasasmita, M., Laurent, A., Charpentier, J. C., 1984. Interfacial area and liquid side mass transfer coefficient in trickle bed reactors operating with organic liquids. Chem. Eng. Sci. 39, 781–794.

Molerus, O., 1993. Principles of Flow in Disperse Systems. Chapman & Hall, London.

Mouza, A. A., Dalakoglou, G. K., Paras, S. V., 2005. Effect of liquid properties on the performance of bubble column reactors with fine pore spargers. Chem. Eng. Sci. 60, 1465–1475.

N.-S. Cheng, A. W.-K. L., 2003. Exponential formula for computing effective viscosity. Powder Technol. 129, 156–160.

Nguyen-Tien, K., Patwari, A. N., Schumpe, A., Deckwer, W. D., 1985. Gas-liquid mass transfer in fluidized particle beds. AIChE J. 31, 194–201.

Nicolella, C., Van Loosdrecht, M., Van der Lans, R., Heijnen, J., 1998. Hydrodynamic characteristics and gas-liquid mass transfer in a biofilm airlift suspension reactor. Biotechnol. Bioeng. 60, 627–635.

Nirdosh, I., Garred, L. J., Baird, M. H. I., 1998. Low-cost experiments in mass transfer. part 3 - mass transfer in a bubble column. Chem. Eng. Edu., 138–141.

Ozkan, O., Calimli, A., Berber, R., Oguz, H., 2000. Effect of inert solid particles at low concentrations on gas-liquid mass transfer in mechanically agitated reactors. Chem. Eng. Sci. 55, 2737–2740.

Patwari, A. N., Nguyen-Tien, K., Schumpe, A., Deckwer, W. D., 1986. Three-phase fluidized beds with viscous liquid: Hydrodynamics and mass transfer. Chem. Eng. Commun. 40, 49–65.

Pereira, I., 1997. Estudos de transferência de oxigénio em colunas de borbulhamento. Ph.D. thesis, Faculdade de Engenharia, Universidade do Porto, Portugal.

Perry, R. H., Green, D., 1984. Perry's Chemical Engineers' Handbook. McGraw-Hill.

Pons, M. N., Vivier, H., Dodds, J., 1997. Particle shape characterization using morphological descriptors. Part. Part. Syst. Char. 14, 272–277.

Quicker, G., Schumpe, A., Deckwer, W. D., 1984. Gas-liquid interfacial areas in a bubble column with suspended solids. Chem. Eng. Sci. 39, 179–183.

Randall, E. W., Goodall, C. M., Fairlamb, P. M., Dold, P. L., O'Connor, C. T., 1989. A method for measuring the sizes of bubbles in two- and three-phase systems. J. Phys. E: Sci. Instrum. 22, 833–837.

Reese, J., Jiang, P., Fan, L., 1996. Bubble characteristics in three-phase systems used for pulp and paper processing. Chem. Eng. Sci. 51, 2501–2510.

Reilly, I., Scott, D., de Bruijn, T. J. W., MacIntyre, D., 1994. The role of gas phase momentum in determining gas holdup and hydrodynamic flow regimes in bubble column. Can. J. Chem. Eng. 72, 3–12.

Richardson, J. F., Zaki, W. N., 1954. Sedimentation and fluidization: Part i. Trans. IChem. 32, 35–53.

Ruzicka, M. C., Drahos, J., Drahos, M., Fialova, M., Thomas, N. H., 2001a. Effect of bubble column dimensions on flow regime transition. Chem. Eng. Sci. 56, 6117–6124.

Ruzicka, M. C., Drahos, J., Mena, P. C., Teixeira, J. A., 2003. Effect of viscosity on homogeneous-heterogeneous flow regime transition in bubble columns. Chem. Eng. J. 96, 15–22.

Ruzicka, M. C., Mena, P. C., Rocha, F. A., Teixeira, J. A., Drahos, J., 2005. Small viscosity can estabilize uniform bubble bed. in preparation.

Ruzicka, M. C., Thomas, N. H., 2003. Buoyancy-driven instability of bubbly layers: Analogy with thermal convection. Int. J. Multiphase flow 29, 249–270.

Ruzicka, M. C., Zahradnik, J., Drahos, J., Thomas, N. H., 2001b. Homogeneous-heterogeneous regime transition in bubble columns. Chem. Eng. Sci. 56, 4609–4626.

Sada, E., Kumazawa, H., Lee, C., Fujiwara, N., 1985. Gas-liquid mass transfer characteristics in a bubble column with suspended sparingly soluble fine particles. Ind. Eng. Chem. Process Des. Dev. 24, 255–261.

Sada, E., Kumazawa, H., Lee, C., Iguchi, T., 1986a. Gas holdup and mass transfer characteristics in a three-phase bubble column. Ind. Eng. Process Des. Dev. 25, 472–476.

Sada, E., Kumazawa, H., Lee, C. H., 1983. Chemical absorption in a bubble column loading concentrated slurry. Chem. Eng. Sci. 38, 2047–2051.

Sada, E., Kumazawa, H., Lee, C. H., 1986b. Influences of suspended fine particles on gas holdup and mass transfer characteristics in a slurry bubble column. AIChE J. 32, 853–856.

Schluter, M., Bork, O., Scheid, S., Hovelmann, S., Rabiber, N., 2001. New aspects of hydrodynamics and mass transfer in multiphase flows. Proceedings of the ICMF-2001 (4th International Conference on Multiphase Flow), Tulane University, New Orleans, LA, USA.

Schumpe, A., Deckwer, W.-D., Nigam, K. D. P., 1989. Gas-liquid mass transfer in three-phase fluidized beds with viscous pseudoplastic liquids. Can. J. Chem. Eng. 67, 873–877.

Schweitzer, J.-M., Bayle, J., Gauthier, T., 2001. Local gas hold-up measuments in fluidized bed and slurry bubble column. Chem. Eng. Sci. 56, 1103–1110.

Shah, Y. T., Kelkar, B. G., Godbole, S. P., Deckwer, W. D., 1982. Design parameters estimations for bubble column reactors. AIChE J. 28, 353–379.

Sherwood, T. K., Pigford, R. L., Wilke, C. R., 1975. Mass Transfer. McGraw Hill, Kogakusha.

Shnip, A. I., Kolhatkar, R. V., Joshi, D. S. J. B., 1992. Criteria for the transition from the homogeneous to the heterogeneous regime in two-dimensional bubble column reactors. Int. J. Multiphase Flow 18, 705–726.

Smith, B., Skimore, D., 1990. Mass transfer phenomena in an airlift reactor: Effects of solids loading and temperature. Biotechnol. Bioeng. 35, 483–491.

Sotelo, J. L., Benitez, F. J., Beltran-Heredia, J., Rodriguez, C., 1994. Gas holdup and mass transfer coefficients in bubble columns. 1. porous glass-plate diffusers. Int. Chem. Eng. 34 (1), 82–90.

Terasaka, K., Hullmann, D., Schumpe, A., 1998. Mass transfer in bubble columns studied with an oxygen optode. Chem. Eng. Sci. 53, 3181–3184.

Thompson, V. S., Worden, R. M., 1997. Phase holdup, liquid dispersion, and gas-to-liquid mass transfer measurements in a three-phase magnetofluidized bed. Chem. Eng. Sci. 52, 279–295.

Treybal, R. E., 1968. Mass-Transfer Operations. McGraw-Hill.

Tservistas, M., Koneke, R., Comte, A., Sheper, T., 2001. Oxygen monitoring in supercritical carbon dioxide using a fibre optic sensor. Enzyme and Microbial Technology 28, 637–641.

Tsuchiya, K., Furumoto, A., Fan, L. S., Zhang, J., 1997. Suspension viscosity and bubble rise velocity in liquid-solid fluidized beds. Chem. Eng. Sci. 52, 3053–3066.

Vázquez, G., Cancela, M. A., Reverol, C., Alvarez, E., Navaza, J. M., 2000a. Determination of interfacial areas in a bubble column by different chemical methods. Ind. Eng. Chem. Res. 39, 2541–2547.

Vázquez, G., Cancela, M. A., Riverol, C., Alvarez, E., Navaza, J. M., 2000b. Application of the dankwerts method in a bubble column. effect of surfactants on mass transfer coefficient and interfacial area. Chem. Eng. J. 78, 13–19.

Velz, C., 1970. Applied Stream Sanitation. Wiley Interscience, New York.

W.-H. Hong, H. B., 1989. Gas-liquid mass transfer in bubble-column reactors. Int. Chem. Eng. 29, 388–434.

Wallis, G. B., 1969. One-Dimensional Two-Phase Flow. McGraw-Hill, New York.

Wang, T., Wang, J., Yang, W., Jin, Y., 2003. Experimental study on bubble behaviour in gas-liquid-solid three-phase circulating fluidized beds. Powder technol. 137, 83–90.

Warsito, M.Ohkawa, Maezawa, A., Uchida, S., 1997. Flow structure and phase distributions in a slurry bubble column. Chem. Eng. Sci. 52, 3941–3947.

Warsito, Ohkawa, M., Kawata, N., Uchida, S., 1999. Cross-sectional distributions of gas and solid holdups in slurry bubble column investigated by ultrasonic computed tomography. Chem. Eng. Sci. 54, 4711–4728.

Warsito, W., Fan, L. S., 2001. Measurement of real-time flow structures in gas-liquid and gas-liquid-solid flow systems using electrical capacitance tomography (ECT). Chem. Eng. Sci. 56, 6455–6462.

Weissenborn, P. K., Pugh, R. J., 1996. Surface tension of aqueous solutions of electrolytes: Relationship with ion hydration, oxygen solubility, and bubble coalescence. J. Colloid Interface Sci. 184, 550–563.

Wesselingh, J. A., Bollen, A. M., 1999. Single particles, bubbles and drops: Their velocities and mass transfer coefficients. Trans IChemE 77, 89–96.

Wilkinson, P. M., Spek, A. P., Van Dierendonck, L. L., 1992. Design parameters estimation for scale-up of high-pressure bubble columns. A.I.Ch.E. J. 38, 544–554.

Xie, T., Ghiaasiaan, S., Karrila, S., McDonough, T., 2003. Flow regimes and gas holdup in paper pulp-water-gas three-phase slurry flow. Chem. Eng. Sci. 58, 1417–1430.

Yagi, H., Yoshida, F., 1974. Oxygen absorption in fermenters - effects of surfactants, anti-foaming agents, and sterilized cells. J. Ferment. Technol. 12, 905–916.

Yang, W., Wang, J., Wang, T., Jin, Y., 2001. Experimental study on gas-liquid interfacial area and mass transfer coefficient in three-phase circulating fluidized beds. Chem. Eng. J. 84, 485–490.

Yoo, D., Tsuge, H., Terasaka, K., Mizutani, K., 1997. Behavior of bubble formation in suspended solution for an elevated pressure system. Chem. Eng. Sci. 52, 3701–3707.

Zahradnik, J., Drapal, L., Kastánek, F., Reznickova, J., 1992. Hydrodynamic and mass transfer characteristics of sectionalized aerated slurry reactors. Chem. Eng. and Process. 31, 263–272.

Zahradnik, J., Fialova, M., Kastánek, F., Green, K. D., Thomas, N. H., 1995. The effect of electrolytes on bubble coalescence and gas holdup in bubble column reactors. Trans IChemE 73, 341–346.

Zahradnik, J., Fialova, M., Linek, V., 1999a. The effect of surface-active additives on bubble coalescence in aqueous media. Chem. Eng. Sci. 54, 4757–4766.

Zahradnik, J., Fialova, M., Ruzicka, M., Drahos, J., Kastanek, F., Thomas, N. H., 1997. Duality of the gas-liquid flow regimes in bubble column reactors. Chem. Eng. Sci. 52, 3811–3826.

Zahradnik, J., Kuncova, G., Fialova, M., 1999b. The effect of surface active additives on bubble coalescence and gas holdup in viscous aerated batches. Chem. Eng. Sci. 54, 2401–2408.

Zhang, J. P., Grace, J. R., Epstein, N., Lim, K. S., 1997. Flow regime identification in gas-liquid flow and three-phase fluidized beds. Chem. Eng. Sci. 52, 3979–3992.

Zhang, T., Wang, J., Wang, T., Lin, J., Jin, Y., 2005. Effect of internal on the hydrodynamics in external-loop airlift reactors. Chem. Eng. Process. 44, 81–87.

Zheng, C., Chen, Z., Feng, Y., Hofmann, H., 1995. Mass transfer in different flow regimes of three-phase fluidized beds. Chem. Eng. Sci. 50, 1571–1578.

Zon, M. V. d., Hamersma, P. J., Poels, E. K., Bliek, A., 2002. Coalescence of freely moving bubbles in water by action of suspended hydrophobic particles. Chem. Eng. Sci. 57, 4845–4853.